Università del Salento
DIPARTIMENTO DI FISICA
Dottorato di Ricerca in Fisica - XIX Ciclo

Ph.D Thesis

Nuclear excited states within the Random Phase Approximation theory

Advisor:
Prof. Giampaolo CO'

Coadvisor:
Dott. Chiara MAIERON

Ph.D Student:
Viviana DE DONNO

Lecce, June 2008

"If I have made any valuable discoveries,
it has been owing more to patient attention
than to any other talents."

(Sir Isaac Newton)

Contents

Introduction

This thesis is part of a project aimed to describe the structure of medium-heavy nuclei by using microscopic nucleon-nucleon (NN) interactions, i.e. interactions able to reproduce the properties of two-nucleons systems.

The description of the atomic nucleus in terms of interacting nucleons, based on the solution of the many-body Schrödinger equation, has always been a basic working hypothesis in nuclear structure theory. In this last ten years, however, the validity of this ansatz has been supported, and consolidated, by the success of the calculations which solve the many-body Schrödinger equation without approximations. Remarkable results have been obtained in few body systems where the Schrödinger equation has been solved by various groups with different techniques, and a convergence of the results has been obtained [1]. The Quantum Monte Carlo approach of the Argonne Urbana group has allowed the description of light nuclei up to ^{12}C [2, 3, 4, 5]. The extension of the Quantum Monte Carlo technique to the description of heavier nuclei is hindered by technical, computational, reasons. Recently, a new Monte Carlo approach, where also the spin and isospin configurations are sampled, has been developed [6], and with this approach it will be possible to describe also medium-heavy nuclei.

The results of the microscopic calculations quoted above have established the validity of the working hypothesis that the nucleus can be well described by using as a basic degrees of freedom the nucleons which interact with two-body, and eventually three-body, potentials in a non relativistic framework. This is the starting point of the many-body techniques aiming to solve the many-body Schrödinger equation by doing controlled approximations. The presence of a strong repulsive core of the NN interactions at short internucleonic distances hinders the possibility of a straightforward use of the perturbation theory. Dealing with the short range repulsion of the NN interaction is the main problem of the nuclear many-body theories.

There have been two main approaches to deal with this problem. A first approach works on the interaction which is renormalized by summing an infinite set of diagrams. Then perturbation theory is applied with this new interaction which behaves well at short internucleonic distances. This is the Brueckner theory approach [7, 8]. The second approach works instead on the relative wave function of the interacting nucleonic pair. A short-range correlation function is introduced in order to prevent the two nucleons to approach each other too much. This is the basic idea of the Correlated Basis Function (CBF) theory [9, 10, 11, 12, 13, 14]. Recently the ground state of various doubly magic nuclei, from ^{12}C up to ^{208}Pb, have been investigated by using the CBF theory solved with the Fermi Hypernetted Chain (FHNC) resummation techniques [15].

The presence of the short-range repulsion of the NN potential, which is the source of the so-called short-range correlations, is the main concern in the calculation of the ground state of nuclear systems. However, as soon as one wants to investigate excited states, one immediately finds the need of dealing with collective nuclear modes. These are the source of the so-called long range correlations. The theory most widely used to deal with this type of correlations is the Random Phase Approximation (RPA) [16, 17] which is an effective theory based on effective interactions and effective operators which describe observables. It is possible to formulate a correlated RPA theory [18, 19] which uses microscopic NN interactions and relates bare and effective operators.

As a first step of the project of having a unified description of both ground and excited states of the nucleus based on microscopic NN potentials, we deal in this thesis with the traditional RPA approach. We have, however, considered some peculiarities important for the final aim of the project, often neglected in RPA calculations.

We formulated our RPA equations by considering finite range effective interactions whose form is similar to that of the Argonne-Urbana potentials. We consider the first six interaction channels, which, in the traditional classification of this type of potentials, are the four central channels, plus the tensor and tensor isospin channels.

We have calculated the low-lying excitation spectra of various doubly closed shell nuclei by using a procedure which discretizes the continuum part of the single particle spectrum. As it will be pointed out in sect. 3.1, the description of nuclear excitations above the nucleon emission threshold requires a proper treatment of the continuum. The traditional approaches dealing with the continuum consider only zero-range forces [20, 21, 22], or if they use finite range forces, they calculate only the direct matrix elements terms [23]. A theoretically consistent treatment of finite range forces in RPA requires the evaluation of both direct and exchange matrix elements. This problem is solved by writing the RPA secular equations in coordinate space, and expanding them on a basis [24], [25]. Following the approach of Refs. [25] we used a basis of Sturmian Bessel functions [26, 27, 28, 29, 30].

The techniques we have developed have a wide range of applications. We first studied the low lying spectrum of some double closed shell nuclei. We have done that in the spirit of the Landau-Migdal theory of Finite Fermi Systems (LMFFS), therefore the single particle (s.p.) basis and the interaction have been fixed by fitting some experimental data of the ground state and of some specific excited states of the nuclei under investigation. Because of this phenomenological input, the RPA results obtained within the LMFFS are the best one can expect in terms of comparison with experimental data. The prediction power of this approach is limited to the nuclei where s.p. energies, charge distributions, or at least *rms* charge radii, are known. We used this phenomenological approach to study the intrinsic limitations of the RPA theory, especially by comparing its results with high precision inelastic electron scattering data. In this study we paid special attention to identify effects produced by the tensor terms of the interaction.

We extended the discrete LMFFS approach to describe the low-lying spectrum of some hypernuclei. The goal was the search for collective effects.

Always in the framework of the LMFFS approach we have done continuum RPA calculations for the ^{16}O nucleus. We present the excitation spectra for the total photoabsorption cross sections, for various multipole excitation, including some magnetic ones.

Finally, we present some discrete RPA results obtained by doing fully self-consistent calculations with the finite range Gogny interaction [31, 32]. In this case the s.p. spectrum is generated by Hartree-Fock calculations. The comparison with the results obtained within the LMFFS and with the experimental data gives an idea of the difficulties related to a complete self-consistent approach.

An immediate extension of our work is the calculation of electron and neutrino cross sections in the giant resonance region by using the continuum RPA wave functions. We expect that the finite range of the force and the presence of the tensor terms provide a good description of the magnetic resonances. The comparison between continuum RPA results obtained in the LMFFS approach and the self-consistent ones is another straightforward application of our techniques.

It is evident where we stand in the perspective of the project outlined at the beginning of this introduction. We have completed the work regarding the RPA, and now we are able to make self-consistent calculations, in order to use the same effective NN interaction to describe both ground and excited states. We have to make the link between the microscopic NN hamiltonian and the effective one. We think, however, that before using an effective interaction obtained from microscopic NN potentials, it is necessary to go over the limits of the RPA theory, by considering more complicated excitation modes than the one-particle one-hole ones. This is also indicated by the results obtained by the Darmstadt group which pursue a similar research project, but with different techniques [33, 34, 35, 36, 37].

The thesis is written in order to have different reading levels. The main reading level is that proposed in the natural sequence of the various chapters. Here the basic information necessary to understand the work done, and the results presented is given. Therefore we present first the MF input used in the LMFFS calculations. Then we discuss the discrete RPA equations and in the next chapter we discuss first the stability of the solutions, and then we present results for ^{12}C

^{16}O ^{40}Ca ^{48}Ca ^{90}Zr and ^{208}Pb nuclei. In the next chapter we present our extension of the RPA theory to the study of hypernuclei, and we discuss our results regarding the spectrum of ^{12}C ^{16}O ^{40}Ca ^{90}Zr ^{208}Pb single Λ hypernuclei. We present in Chapter 5 our approach to the solution of the continuum RPA equations, and we show some results obtained for the ^{16}O. Finally we discuss in Chapter 6 the discrete RPA results obtained by using the D1 interaction of Gogny, in fully self-consistent calculations.

For the reader requiring a deeper understanding we put in the appendixes the detailed derivations of the expressions presented in the main body of the thesis. The reader interested to the quantitative results can find a section of summary and conclusions at the end of each chapter where the results are presented.

Chapter 1

The Mean Field basis

A mean field basis is a necessary background of the RPA theory. In fact, in addition to the residual interaction, the solution of the RPA equations requires a set of single particle (s.p.) wave functions and energies which are obtained within a mean field (MF) theory. We describe the nucleus by solving the following eigenvalues equation:

$$H|\Psi\rangle = E|\Psi\rangle, \tag{1.1}$$

where H is the hamiltonian of the system. If we consider only two-body forces, the many-body hamiltonian assumes this form:

$$H = \sum_{i=1}^{A} t(i) + \sum_{i<j=1}^{A} V(i,j), \tag{1.2}$$

where the first term represents the kinetic energy and is a one-body operator, while the second term represents the interaction and is a two-body operator. The indexes i and j indicate the set of quantum numbers which identify a single nucleon and the sums are extended to all nucleons. We add and subtract to the hamiltonian of Eq. (1.2) a one-body mean potential $U(i)$

$$\begin{aligned} H &= \sum_{i=1}^{A} t(i) + \sum_{i=1}^{A} U(i) + \sum_{i<j=1}^{A} V(i,j) - \sum_{i=1}^{A} U(i) = \\ &= \sum_{i=1}^{A} [t(i) + U(i)] + V_{res} = \sum_{i=1}^{A} h(i) + V_{res} = H_0 + V_{res}. \end{aligned} \tag{1.3}$$

In the previous expression H_0 is sum of one-body hamiltonians, and V_{res} is the so-called residual interaction which contains the two-body terms of the many-body hamiltonian H.
In the mean-field model V_{res} is neglected and the many-body system is described by H_0 only. The eigenstates $|\Phi\rangle$ of H_0 are Slater determinants of eigenstates $|\phi_i\rangle$ of the single nucleon hamiltonians $h(i)$:

$$|\Phi\rangle = \frac{1}{\sqrt{A!}} det||\phi_i\rangle|. \tag{1.4}$$

In Eq. (1.3) we have introduced the mean-field potential as an external term of the hamiltonian. The Hartree-Fock theory produces a mean field basis starting from the two-body residual interaction. In our work we have used two types of single particle wave bases. A first type is generated by a Woods-Saxon potential, a second type is produced by Hartree-Fock theory. In this chapter we present some detail of the Woods-Saxon s.p. basis, and we address our attention to some aspect related to the treatment of the continuum in RPA calculations. Details on the HF basis will be given in chapter 6.

^{12}C	U_0(MeV)	U_{SO}(MeV)	a_0(fm)	a_{SO}(fm)	R_0(fm)	R_{SO}(fm)	R_C(fm)
p	-55.00	-4.00	0.50	0.50	2.95	2.95	2.95
n	-55.00	-5.50	0.50	0.50	2.95	2.95	0.00
^{16}O	U_0(MeV)	U_{SO}(MeV)	a_0(fm)	a_{SO}(fm)	R_0(fm)	R_{SO}(fm)	R_C(fm)
p	-52.50	-7.00	0.53	0.53	3.2	3.2	3.22
n	-52.50	-6.54	0.53	0.53	3.2	3.2	0.00
^{40}Ca	U_0(MeV)	U_{SO}(MeV)	a_0(fm)	a_{SO}(fm)	R_0(fm)	R_{SO}(fm)	R_C(fm)
p	-57.50	-11.11	0.53	0.53	4.10	4.10	4.10
n	-55.00	-8.50	0.53	0.53	4.10	4.10	0.00
^{48}Ca	U_0(MeV)	U_{SO}(MeV)	a_0(fm)	a_{SO}(fm)	R_0(fm)	R_{SO}(fm)	R_C(fm)
p	-59.50	-8.55	0.53	0.53	4.36	4.36	4.36
n	-50.00	-7.74	0.53	0.53	4.36	4.36	0.00
^{90}Zr	U_0(MeV)	U_{SO}(MeV)	a_0(fm)	a_{SO}(fm)	R_0(fm)	R_{SO}(fm)	R_C(fm)
p	-55.80	-7.70	0.645	0.73	5.695	5.68	5.695
n	-48.12	-7.70	0.645	0.73	5.695	5.68	0.00
^{208}Pb	U_0(MeV)	U_{SO}(MeV)	a_0(fm)	a_{SO}(fm)	R_0(fm)	R_{SO}(fm)	R_C(fm)
p	-60.40	-6.754	0.79	0.59	7.46	7.20	7.4062
n	-44.32	-6.0844	0.66	0.64	7.46	6.96	0.00

Table 1.1: Values of the Woods-Saxon potential parameters used in our work for the nuclei we have studied

1.1 The Woods-Saxon Potential

The expression of the Woods-Saxon potential used in our work is

$$V(r) = \frac{U_0}{1+e^{\frac{r-R_0}{a_0}}} + \left(\frac{\hbar c}{m_\pi c^2}\right)^2 \frac{1}{r}\frac{U_{SO}}{a_{SO}} \frac{e^{\frac{r-R_{SO}}{a_{SO}}}}{(1+e^{\frac{r-R_{SO}}{a_{SO}}})} \boldsymbol{l}\cdot\boldsymbol{\sigma} - V_C(r) \tag{1.5}$$

where U_0, U_{SO}, the a's and the R's are parameters. With V_C we indicate the Coulomb potential generated by a homogeneous charged sphere.

$$V_C(r) = \begin{cases} (Z-1)\frac{e^2}{r} & \text{if } r > R \\ \frac{(Z-1)e^2}{2R}\left[3-\frac{r^2}{R^2}\right] & \text{if } r \leq R \end{cases} \tag{1.6}$$

for protons and $V_C(r) = 0.0$ for neutrons, with

$$e^2 = 1.44 MeV \cdot fm. \tag{1.7}$$

In Eq. (1.5) we have indicated with m_π the pion mass, and with $\boldsymbol{l}$ and $\boldsymbol{\sigma}$ the angular momentum and the spin operator respectively.
The parameters of the potential have been fixed to reproduce as well as possible the single particle energies near the Fermi surface and the charge distributions. In table 1.1 we show the values of the parameters for the nuclei we have studied: ^{12}C, ^{16}O, ^{40}Ca, ^{48}Ca, ^{90}Zr and ^{208}Pb. In the table we indicate separately the values for protons (p) and neutrons (n).

1.2 Single particle energies and charge distributions

In this section we present proton, neutron and charge distributions obtained by solving the one-body Schrödinger equation with the Woods-Saxon potential. We compare our charge distributions with the empirical ones, extracted from elastic electron scattering experiments [38].

We show in Figs. 1.1-1.6 the proton, neutron and charge distributions of ^{12}C, ^{40}Ca, ^{48}Ca, ^{16}O, ^{90}Zr and ^{208}Pb nuclei.

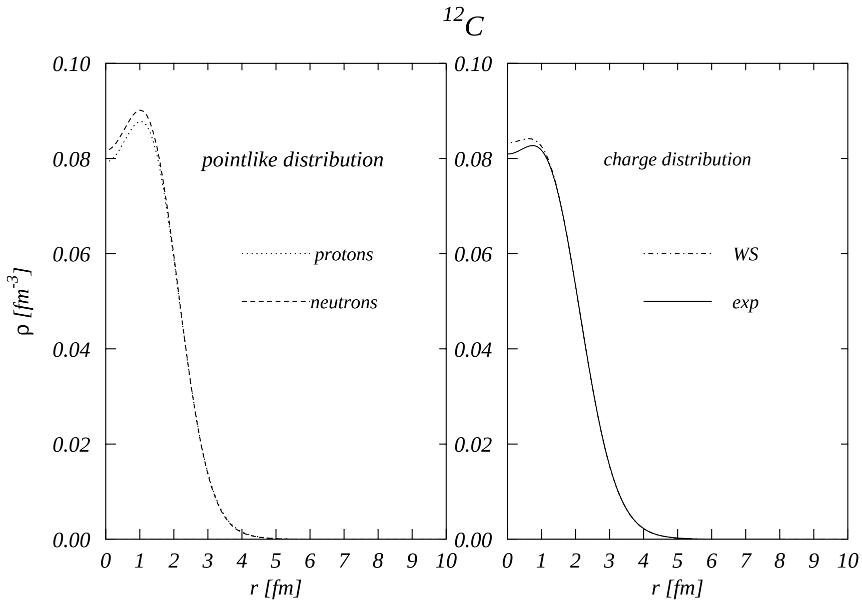

Figure 1.1: Pointlike and charge distributions of ^{12}C.

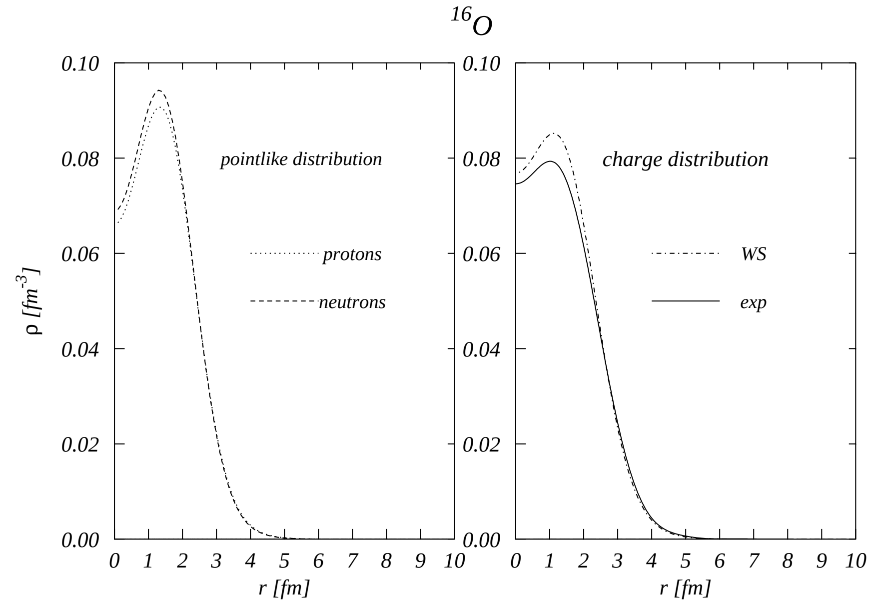

Figure 1.2: Pointlike and charge distributions of ^{16}O.

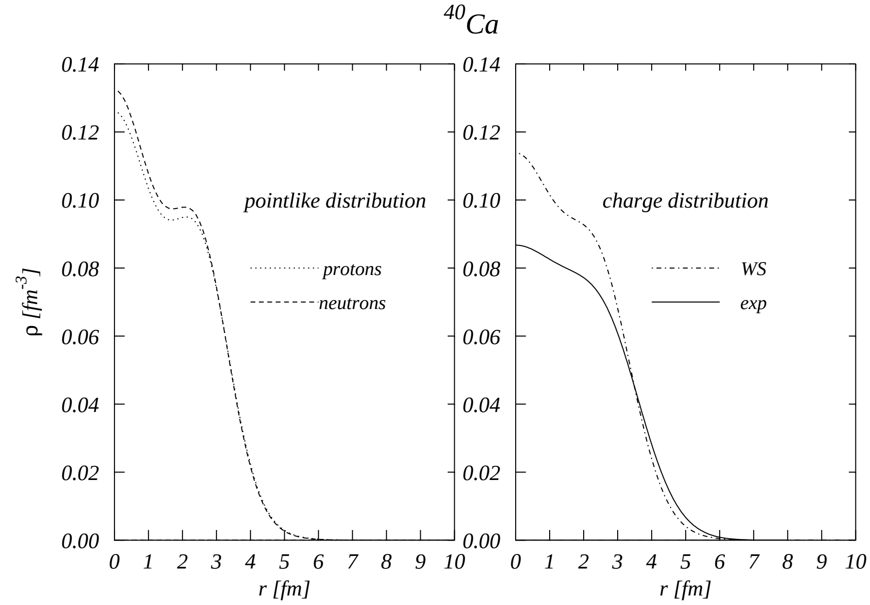

Figure 1.3: Pointlike and charge distributions of ^{40}Ca.

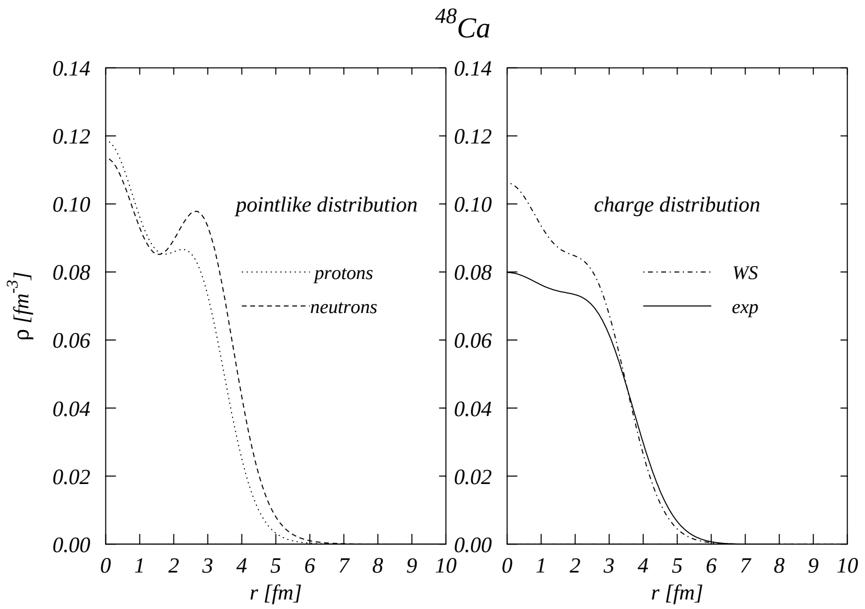

Figure 1.4: Pointlike and charge distributions of ^{48}Ca.

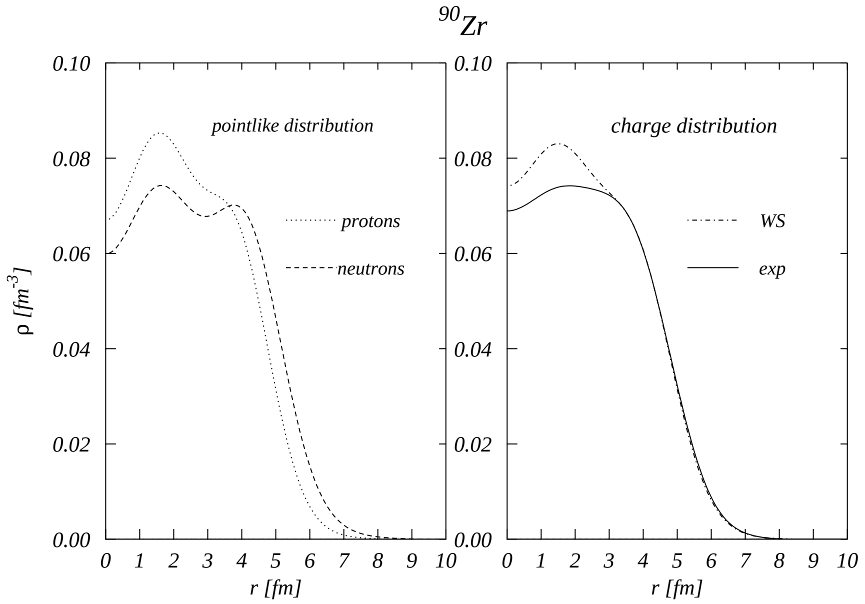

Figure 1.5: Pointlike and charge distributions of ^{90}Zr.

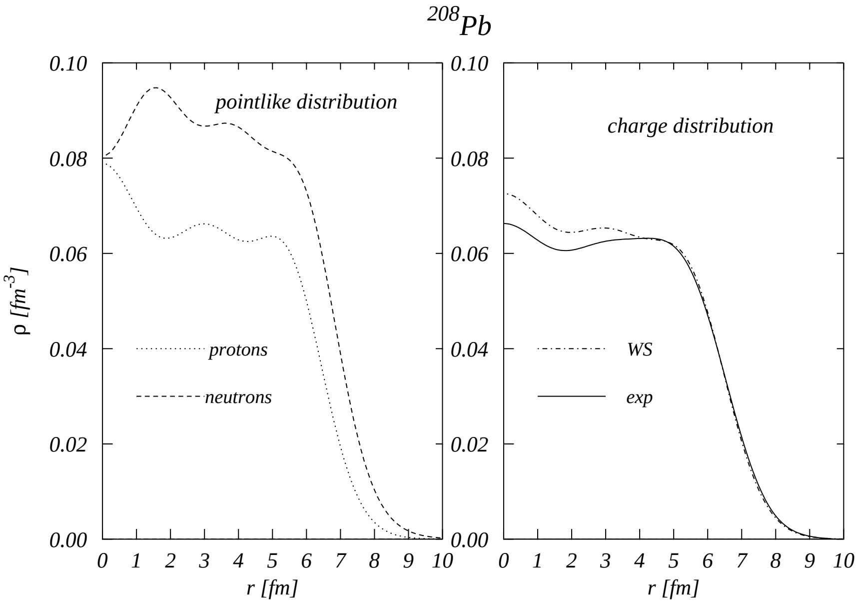

Figure 1.6: Pointlike and charge distributions of ^{208}Pb.

As expected, proton and neutron distributions are very similar in symmetric nuclei as ^{12}C, ^{16}O and ^{40}Ca, despite the differences in the parametrization of the mean-field potentials. There are obvious differences in the asymmetric nuclei ^{48}Ca, ^{90}Zr and ^{208}Pb, where the number of neutrons is larger than that of protons. The theoretical charge distributions agree rather well with the experimental ones at the nuclear surface. Since the larger discrepancies between theoretical and experimental charge distributions are located in the nuclear interior, we show in Tab. 1.2 the values of the distributions at $r = 0$.

Nuclei	WS	Exp
^{12}C	0.083	0.081
^{40}Ca	0.114	0.087
^{48}Ca	0.106	0.080
^{16}O	0.077	0.074
^{90}Zr	0.074	0.069
^{208}Pb	0.072	0.066

Table 1.2: Values in fm^{-3} of the theoretical (WS) and experimental charge density distributions at $r = 0$.

This discrepancy is not related to our specific model, but it has been established to be a limitation of the mean-field description of the nucleus [39].

In Tabs. 1.3 - 1.8 we show the s.p. spectra for the six nuclei under study. We show all, and only, the energies of the bound states, and we compare these energies with the experimental ones, when available. The line in the tables indicates the Fermi level, which separates the occupied states (hole states), from the empty ones (particle states).

^{12}C	j	l	n	E [MeV] WS	Exp
Protons	1/2	0	1	-30.90	-30.90
	3/2	1	1	-15.75	-15.96
	1/2	1	1	-12.95	-1.94
	5/2	2	1	-0.78	
Neutrons	1/2	0	1	-34.04	-34.04
	3/2	1	1	-18.92	-18.72
	1/2	1	1	-15.06	-4.96
	5/2	2	1	-3.88	-1.10
	1/2	0	2	-1.96	-1.86

Table 1.3: S.p. energies in MeV calculated with the Woods-Saxon potential for ^{12}C. The experimental values are taken from [40].

A common feature of our results is that the whole theoretical s.p. spectrum is more compressed than the experimental one. Again, this has been shown to be a general limitation of the mean-field model, [39].

Let us now make a short discussion of the s.p. energy spectrum of each nucleus.

Tab. 1.3 shows that our parametrizations of ^{12}C proton and neutron mean-fields are able to reproduce rather well the energies of the hole states. On the other hand there are remarkable differences with particle state s energies. We observe that for protons the WS s.p. spectrum predicts a bound $1d_{5/2}$ state contrary to the experimental evidence. We notice that the theoretical energies of the $1p_{3/2}$ and $1p_{1/2}$ states, for both proton and neutron cases, are rather close if compared to the roughly $14 MeV$ splitting of the experimental energies. It seems that the spin-orbit term of the potential that gives a splitting of the degenerate levels is too weak to reproduce the exact splitting.

^{16}O	j	l	n	E [MeV] WS	Exp
Protons	1/2	0	1	-29.92	-29.81
	3/2	1	1	-16.93	-18.44
	1/2	1	1	-12.75	-12.11
	5/2	2	1	-3.77	-0.60
	1/2	0	2	-0.90	-0.10
Neutrons	1/2	0	1	-33.98	-34.03
	3/2	1	1	-20.52	-21.81
	1/2	1	1	-16.63	-15.65
	5/2	2	1	-6.84	-4.14
	1/2	0	2	-3.90	-3.27
	3/2	2	1	-0.29	

Table 1.4: The same as Tab. 1.3 for ^{16}O. Experimental values from [40].

In Tab. 1.4 we show the s.p. spectrum of ^{16}O. The agreement with the experimental energies has improved with respect to the ^{12}C case, especially the spin-orbit splitting of the $1p_{1/2}$, $1p_{3/2}$ states is reasonably well reproduced. The $1d_{5/2}$ states of both protons and neutrons are slightly overbound.

^{40}Ca	j	l	n	E [MeV] WS	Exp
Protons	1/2	0	1	-36.00	-36.18
	3/2	1	1	-26.51	-26.62
	1/2	1	1	-23.02	-23.14
	5/2	2	1	-16.19	-14.73
	1/2	0	2	-10.30	-10.33
	3/2	2	1	-8.71	-8.30
	7/2	3	1	-5.31	-1.63
Neutrons	1/2	0	1	-42.57	-42.57
	3/2	1	1	-32.42	-32.42
	1/2	1	1	-29.80	-29.80
	5/2	2	1	-21.37	-21.60
	1/2	0	2	-16.42	-18.20
	3/2	2	1	-15.70	-15.60
	7/2	3	1	-9.76	-8.36
	3/2	1	2	-4.85	-6.20
	1/2	1	2	-2.30	-1.96
	5/2	3	1	-0.82	-4.23

Table 1.5: The same as Tab. 1.3 for ^{40}Ca. Experimental values from [40].

Also for ^{40}Ca (Tab.1.5) we observe a good agreement between the WS energy levels and the experimental data. The $l = 3$ states are not well described. The proton $1f_{7/2}$ is overbound by about $3.5 MeV$. In the neutron case the $1f_{7/2}$ is overbound by $1.5 MeV$, and its spin-orbit partner, the $1f_{5/2}$ state is underbound by about $3.5 MeV$. For this reason the neutron $1f_{5/2}$ state is less bound than the $2p_{1/2}$ state, contrary to the experimental evidence.

Similar considerations can be done for the ^{48}Ca nucleus, Tab. 1.6. In this case, however, the level inversion is present in the proton case, and the $2p_{1/2}$ state is less bound than the $1f_{5/2}$ state, while the opposite is observed experimentally.

^{48}Ca	j	l	n	E [MeV] WS	E [MeV] Exp
Protons	1/2	0	1	-39.70	-39.70
	3/2	1	1	-30.56	-30.56
	1/2	1	1	-28.36	-28.36
	5/2	2	1	-20.34	-20.34
	3/2	2	1	-15.47	-16.17
	1/2	0	2	-15.24	-15.81
	7/2	3	1	-9.37	-9.63
	3/2	1	2	-3.66	-6.54
	5/2	3	1	-1.31	-5.82
	1/2	1	2	-1.08	-6.11
Neutrons	1/2	0	1	-39.19	-39.19
	3/2	1	1	-30.11	-30.11
	1/2	1	1	-28.06	-28.06
	5/2	2	1	-20.11	-20.11
	1/2	0	2	-15.66	-12.55
	3/2	2	1	-15.59	-12.53
	7/2	3	1	-9.51	-9.95
	3/2	1	2	-4.88	-5.24
	1/2	1	2	-2.70	-2.70
	5/2	3	1	-2.17	-2.17

Table 1.6: The same as Tab. 1.3 for ^{48}Ca. Experimental values from [40].

For ^{90}Zr and ^{208}Pb nuclei, we observe a reasonable agreement between the experimental energies around the Fermi surface. This agreement deteriorates for the more bound states.
Our calculations do not bind the proton $3p_{1/2}$ state and the $4s_{1/2}$ and $3d_{3/2}$ neutron states, contrary to the experimental evidence.

In conclusion, a WS potential provides a reasonable description of the s.p. levels for the nuclei under consideration, but with some significant discrepancies with the experimental data regarding some spin-orbit splitting and the binding energies of some specific state.

Since the excitation spectrum of the nucleus is very sensitive to the s.p. spectrum, following the philosophy of the Landau-Migdal theory of finite Fermi systems [43], [44], in our RPA calculations, we substitute the WS s.p. energies with the experimental ones, when available. This is an effective way of considering effects beyond MF, such as particle-phonons coupling.

^{90}Zr	j	l	n	E WS	E Exp
Protons	1/2	0	1	-35.13	-63.96
	3/2	1	1	-29.22	
	1/2	1	1	-28.15	
	5/2	2	1	-22.27	
	3/2	2	1	-19.95	
	1/2	0	2	-18.62	-21.80
	7/2	3	1	-14.49	-17.00
	5/2	3	1	-10.59	-10.80
	3/2	1	2	-9.77	-10.40
	1/2	1	2	-8.36	-8.36
	9/2	4	1	-6.08	-5.17
	5/2	2	2	-1.04	
	7/2	4	1	-0.39	
Neutrons	1/2	0	1	-41.03	
	3/2	1	1	-34.81	
	1/2	1	1	-33.77	
	5/2	2	1	-27.72	
	3/2	2	1	-25.41	
	1/2	0	2	-24.54	
	7/2	3	1	-19.92	
	5/2	3	1	-16.01	
	3/2	1	2	-15.75	
	1/2	1	2	-14.32	
	9/2	4	1	-11.58	-11.57
	5/2	2	2	-7.13	-7.20
	7/2	4	1	-5.88	-5.87
	1/2	0	3	-5.40	
	3/2	2	2	-4.70	-2.90
	11/2	5	1	-2.84	

Table 1.7: The same as Tab. 1.3 for ^{90}Zr. Experimental values from [40].

^{208}Pb	j	l	n	E [MeV] WS	Exp
Protons	1/2	0	1	-33.99	-53.33
	3/2	1	1	-30.30	-46.80
	1/2	1	1	-29.92	-46.50
	5/2	2	1	-25.73	-25.50
	3/2	2	1	-24.81	-24.6
	1/2	0	2	-22.96	-22.70
	7/2	3	1	-20.48	-20.20
	5/2	3	1	-18.75	-18.50
	3/2	1	2	-16.69	-16.40
	1/2	1	2	-15.94	-15.70
	9/2	4	1	-14.65	-14.40
	7/2	4	1	-11.86	-11.51
	5/2	2	2	-10.12	-9.71
	3/2	2	2	-8.64	-8.38
	11/2	5	1	-8.36	-9.37
	1/2	0	3	-8.09	-8.03
	9/2	5	1	-4.27	-3.80
	7/2	3	2	-3.30	-2.90
	13/2	6	1	-1.64	-2.19
	5/2	3	2	-1.01	-0.98
	3/2	1	3	-0.74	-0.69
	1/2	1	3	0.12	-0.16
Neutrons	1/2	0	1	-40.20	-62.89
	3/2	1	1	-36.34	-56.08
	1/2	1	1	-35.87	-34.14
	5/2	2	1	-31.80	-47.89
	3/2	2	1	-30.67	-47.10
	1/2	0	2	-29.56	-43.89
	7/2	3	1	-26.67	-26.70
	5/2	3	1	-24.63	-24.70
	3/2	1	2	-23.34	-23.40
	1/2	1	2	-22.56	-21.77
	9/2	4	1	-21.01	-21.00
	7/2	4	1	-17.86	-17.90
	5/2	2	2	-16.78	-16.80
	3/2	2	2	-15.36	-15.40
	1/2	0	3	-15.01	-15.10
	11/2	5	1	-14.86	-14.90
	9/2	5	1	-10.47	-10.79
	7/2	3	2	-9.96	-9.72
	13/2	6	1	-8.27	-9.01
	5/2	3	2	-7.94	-7.95
	3/2	1	3	-7.77	-8.27
	1/2	1	3	-7.06	-7.38
	9/2	4	2	-3.02	-3.94
	11/2	6	1	-2.59	-3.16
	15/2	7	1	-1.27	-2.52
	5/2	2	3	-0.84	-2.38
	7/2	4	2	-0.56	-1.45
	1/2	0	4	0.02	-1.91
	3/2	2	3	0.15	-1.40

Table 1.8: The same as Tab. 1.3 for ^{208}Pb. Experimental values from [40].

1.3 Continuum with Woods-Saxon potential

The shape of the WS potential implies that the nucleons with energies greater than zero are unbound. We solve the one-body Schrödinger equation with the WS potential by using the traditional Numerov method and by using an expansion on a harmonic oscillator (HO) basis. This second method, described in Appendix A, consists in expanding the radial s.p. wave function on a basis of harmonic oscillator eigenfunctions (A.11) and diagonalizing a matrix whose dimension is the number of expansion coefficients N_{HO}. The solutions of the eigenvalue problem (A.18) (that are the spectrum of the nucleus) are as many as the number of expansion coefficients. This automatically discretizes the continuum. In this method we have to calculate the integrations present in (A.17). These integrations are formally made on the radial coordinate up to ∞, practically only up to a maximum radius: r_{cut}.
A discretization of the continuum spectrum can also be obtained with the Numerov method by imposing bound-state asymptotic boundary conditions beyond r_{cut}.

In this section we analyze the validity of the discretization methods, in view of the use of the s.p. basis in RPA calculations. We start our study by discussing the results obtained with the HO expansion. In Tab. 1.9 we show the energy of the $s_{1/2}$ states of ^{16}O obtained with different numbers of harmonic oscillator expansion coefficient, N_{HO}.

	$N_{HO}=30$	$N_{HO}=25$	$N_{HO}=20$	$N_{HO}=15$	$N_{HO}=10$
1	-29.92	-29.92	-29.92	-29.92	-29.92
2	-0.98	-0.98	-0.98	-0.97	-0.96
3	6.15	6.16	6.17	6.24	7.16
4	16.52	16.55	16.59	16.77	19.32
5	30.65	30.70	30.78	31.13	36.26
6	48.26	48.33	48.47	49.08	58.26
7	69.36	69.47	69.69	70.72	85.88
8	93.89	94.06	94.39	96.07	121.48
9	121.77	122.02	122.52	125.33	165.34
10	152.95	153.31	154.06	158.86	219.77
11	187.39	187.91	189.06	197.19	
12	225.05	225.81	227.67	242.61	
13	265.88	266.96	270.13	295.53	
14	309.76	311.34	316.72	355.24	
15	356.47	358.73	369.04	411.29	
16	405.38	408.34	424.74		
17	453.56	456.46	508.99		
18	487.96	491.16	549.51		
19	523.07	528.89	549.51		
20	564.61	570.95	600.39		
21	595.13	604.17			
22	637.03	647.20			
23	667.61	682.86			
24	709.02	721.40			
25	741.10	772.09			
26	779.51				
27	817.97				
28	850.62				
29	892.08				
30	937.90				

Table 1.9: Energies of $s_{1/2}$ states of ^{16}O obtained by using different numbers of expansion coefficients N_{HO} in the harmonic oscillator basis. The energies are expressed in MeV. The number in the first column is number of nodes minus one.

We can notice that the energies of the first two states, that are bound states, are rather insensitive to the value of N_{HO}. On the contrary the unbound states are very sensitive to N_{HO}. The reasonable value of N_{HO} will be fixed in the next chapter to obtain convergence in RPA results. At this point we can only observe a good convergence of the energies of the first levels (that are interesting for us) when N_{HO} is 30. Up to the 12-th state, the energy difference between $N_{HO} = 30$ or 25 is smaller than 1 part on a thousand, and this can be considered a good accuracy for our goals.

In Tab. 1.9 the number in the first column indicates the number of nodes of the s.p. wave functions minus one, that is the principal quantum number. The discretization method based on the expansion on HO basis allows us to classify the s.p. configuration space in terms of HO major shells. We shall make our discrete RPA calculations by using up to 10 major HO shells. This implies, for example, that we consider up to the $5s_{1/2}$ state.

In Fig. 1.7 we compare the first five $s_{1/2}$ s.p. states obtained by using the HO expansion with various N_{HO}, with those obtained with the Numerov method by imposing asymptotic conditions. We can observe that the s.p. wave function for different value of N_{HO} are in good agreement among them except for s.p. wave function $N_{HO} = 10$ of $4s_{1/2}$ and $5s_{1/2}$ states. This result could be expected by observing the behaviour of the energy eigenvalues in Tab. 1.9. The agreement with the Numerov solution is very good in all cases.

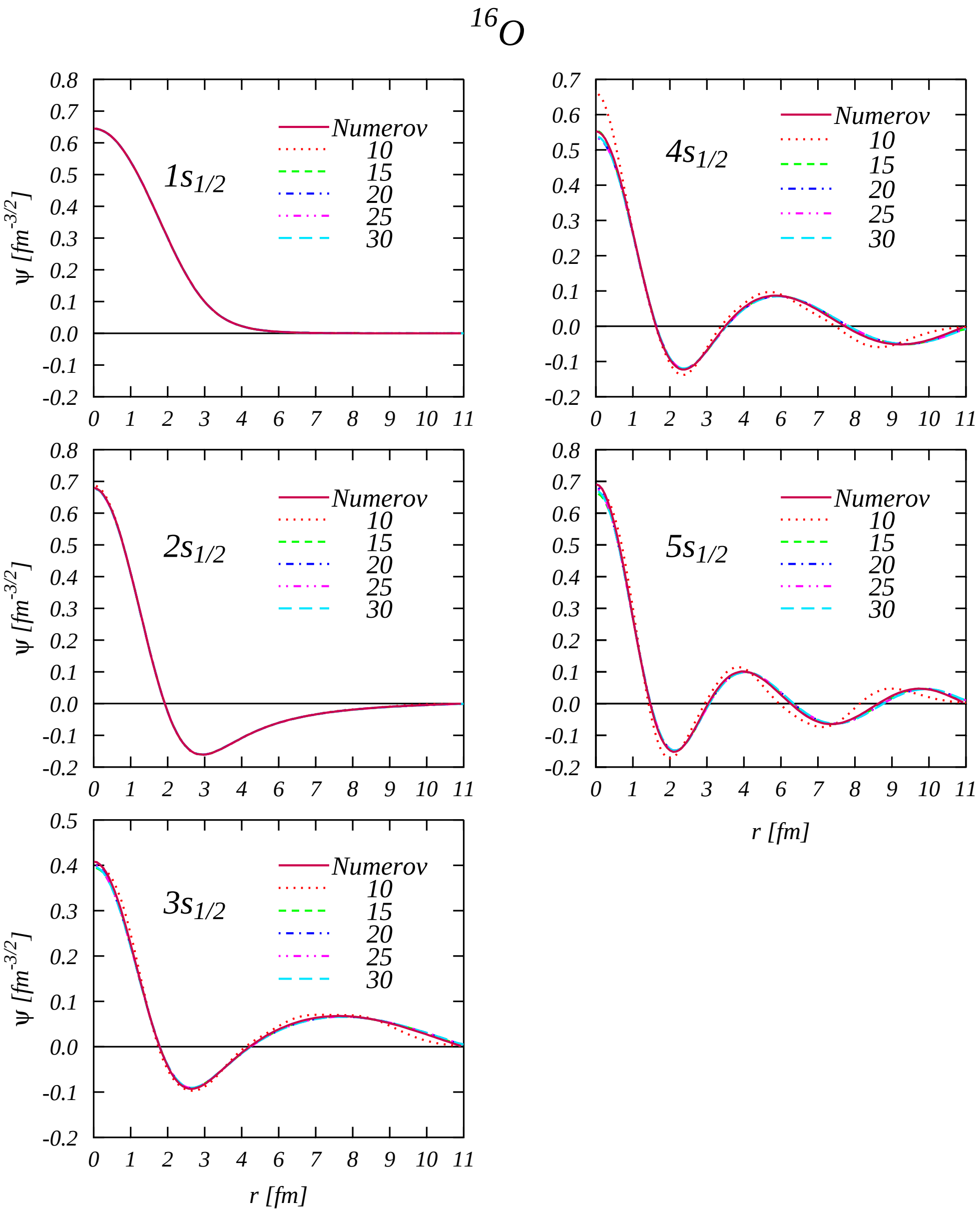

Figure 1.7: S.p. wave functions for $s_{1/2}$ states obtained with different value of N_{HO} compared with the Numerov solution.

In order to test the validity of the discretization of the continuum, we compare the continuum wave functions obtained by solving the one-body Schrödinger equation with scattering boundary conditions, with those obtained with the various discretization methods. An example of this is shown in Fig.1.8 where the proton continuum wave function (c.w.f.) with $l = 0$ and $j = 1/2$ calculated at an energy of $30MeV$, is compared with the discrete $5s_{1/2}$ proton waves. We observe from Tab. 1.9 that $30MeV$ is roughly the energy eigenvalue predicted by the discretization procedure.

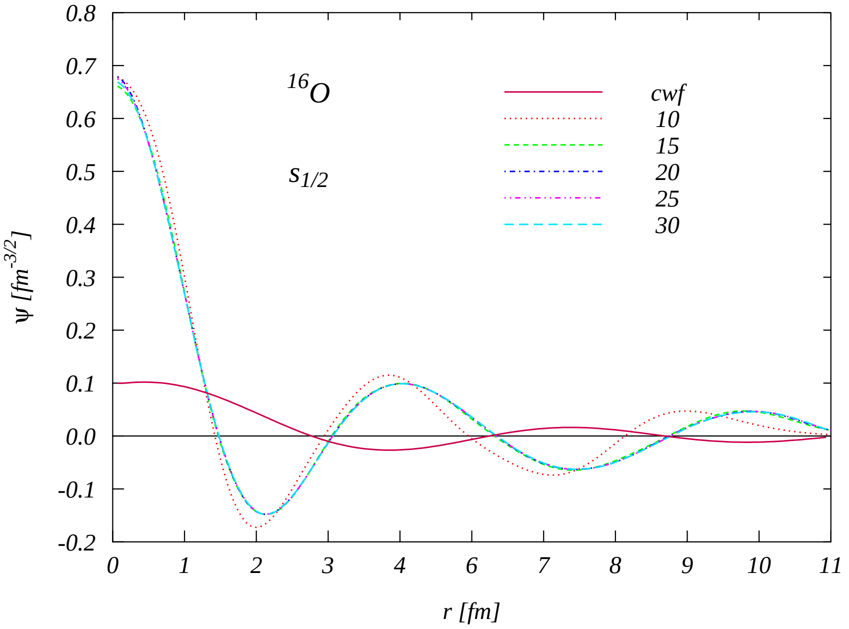

Figure 1.8: Proton continuum wave function with $l = 0$ and $j = 1/2$ calculated for the energy of $30MeV$ compared to the $5s_{1/2}$ discrete waves.

The agreement between c.w.f. and $5s_{1/2}$ discrete wave function is rather poor. The c.w.f. shows only 3 nodes in the figure compared to the 4 nodes of the $5s_{1/2}$ wave functions. The behaviour of the proton $s_{1/2}$ c.w.f. as a function of energy is shown in Fig. 1.9. Only when $E = 45MeV$ the c.w.f. has 4 nodes.

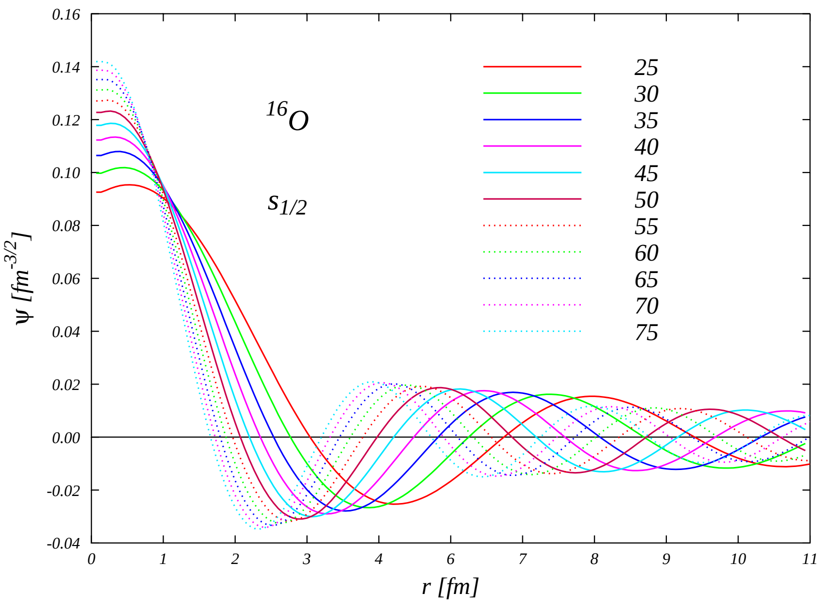

Figure 1.9: Continuum s.p. wave functions for $s_{1/2}$ state obtained with different value of the energy expressed in MeV.

	r_{cut} = 10 fm	r_{cut} = 15 fm	r_{cut} = 20 fm	r_{cut} = 25 fm
1	-30.91	-30.89	-30.86	-30.82
2	0.06	-0.10	-0.09	-0.06
3	7.58	3.03	2.11	2.12
4	20.25	8.26	5.68	5.69
5	37.39	15.77	10.89	10.90
6	58.63	25.36	17.66	17.68
7	83.96	36.88	25.91	25.93
8	113.34	50.30	35.62	35.65
9	146.65	65.62	46.76	46.79
10	183.81	82.85	59.40	59.45

Table 1.10: First ten $s_{1/2}$ states for different value of r_{cut} for ^{12}C. The energies are expressed in MeV.

	r_{cut} = 10 fm	r_{cut} = 15 fm	r_{cut} = 20 fm	r_{cut} = 25 fm
1	-29.92	-29.91	-29.88	-29.85
2	-0.94	-1.00	-0.98	-0.95
3	7.66	3.15	2.24	2.25
4	20.34	8.40	5.81	5.82
5	37.38	15.93	11.04	11.05
6	58.59	25.48	17.81	17.83
7	83.96	36.96	26.04	26.06
8	113.36	50.36	35.71	35.74
9	146.68	65.68	46.84	46.87
10	183.85	82.93	59.47	59.51

Table 1.11: First ten $s_{1/2}$ states for different value of r_{cut} for ^{16}O. The energies are expressed in MeV.

So far we have investigated the sensitivity of our results with respect to the number of the HO coefficients used in the procedure which diagonalizes the WS potential (Appendix A). Now we want to investigate the influence of the box size, or in other words the sensitivity of the s.p. energy values on the maximum radius adopted to make the calculations. We label this value as r_{cut}. In Tabs. 1.10-1.13 we have reported the energies of the first ten $s_{1/2}$ states for different value of the box sizes for ^{12}C, ^{16}O, ^{40}Ca, ^{208}Pb. The number N_{HO} has been kept equal to 30.

A first general remark about the results of these tables is that the spectra shrink with increasing value of r_{cut}. The $n = 10$ s.p. energies are well above $100 MeV$ for all the nuclei for $r_{cut} = 10 fm$, and they become $59 MeV$ in ^{12}C and $25 MeV$ in ^{208}Pb for $r_{cut} = 25 fm$.

The stability of the levels below $n = 5$, those of interest for the RPA calculations, is reached at different values of r_{cut}, depending from the nuclear size. We found convergence at $r_{cut} = 20 fm$ in ^{12}C and ^{16}O, $25 fm$ for ^{40}Ca and ^{48}Ca, and $30 fm$ for ^{90}Zr and ^{208}Pb. In our RPA calculations we have used a value of r_{cut} of $25 fm$.

	$r_{cut} = 10$ fm	$r_{cut} = 15$ fm	$r_{cut} = 20$ fm	$r_{cut} = 25$ fm	$r_{cut} = 30$ fm
1	-36.00	-35.99	-35.98	-35.96	-35.93
2	-10.30	-10.29	-10.26	-10.21	-10.15
3	7.75	4.45	3.13	3.07	3.07
4	18.01	8.79	5.74	5.62	5.63
5	34.17	15.26	9.35	9.14	9.15
6	55.01	24.16	14.21	13.87	13.89
7	79.80	35.35	20.42	19.92	19.94
8	108.48	48.57	27.97	27.31	27.34
9	140.87	63.67	36.78	35.97	36.00
10	176.65	80.62	46.81	45.88	45.92

Table 1.12: First ten $s_{1/2}$ states for different value of r_{cut} for ^{40}Ca. The energies are expressed in MeV.

	$r_{cut} = 10$ fm	$r_{cut} = 15$ fm	$r_{cut} = 20$ fm	$r_{cut} = 25$ fm	$r_{cut} = 30$ fm	$r_{cut} = 35$ fm
1	-33.99	-33.99	-33.99	-33.99	-33.98	-33.98
2	-22.96	-22.96	-22.95	-22.94	-22.92	-22.90
3	-8.06	-8.10	-8.09	-8.07	-8.04	-8.01
4	8.09	7.01	6.98	6.96	6.70	6.70
5	24.34	13.80	9.64	7.48	7.06	7.09
6	43.11	21.68	14.27	10.62	9.51	9.51
7	64.80	31.91	19.77	14.27	12.66	12.66
8	85.31	44.43	26.47	18.52	16.31	16.32
9	99.20	58.83	34.54	23.51	20.55	20.57
10	116.35	75.03	43.79	29.35	25.51	25.53

Table 1.13: First ten $s_{1/2}$ states for different value of r_{cut} for ^{208}Pb. The energies are expressed in MeV.

Chapter 2

The RPA theory

The RPA secular equations can be obtained by using different techniques, for example the equations of motion method [45], [39], the time dependent Hartree Fock [45] or linear response theory [46]. We present here the main points of the derivation based on equations of motion method (major details are presented in Appendix B). The Schrödinger equation to be solved can be expressed as:

$$H|\nu\rangle = \omega|\nu\rangle, \tag{2.1}$$

where H is the many-body hamiltonian describing the system composed by A identical fermions. We indicate with $|\nu\rangle$ an excited state of the system and with $|0\rangle$ the ground state. We use an operator $Q^\dagger_\nu$ defined such as:

$$\begin{aligned} Q^\dagger_\nu|0\rangle &= |\nu\rangle & (2.2)\\ Q_\nu|0\rangle &= 0. & (2.3) \end{aligned}$$

The ground state of the system is defined by Eq. (2.3). The explicit expression of $Q^\dagger_\nu$ in the RPA theory is

$$\begin{aligned} Q^\dagger_\nu &= \sum_{ph}\left[\sum_{\epsilon_p>\epsilon_F}^{0}\left(X^\nu_{ph}(\epsilon_p)a^\dagger_p a_h - Y^\nu_{ph}(\epsilon_p)a^\dagger_h a_p\right) + \right.\\ &\left. + \int_0^\infty d\epsilon_p \left(X^\nu_{ph}(\epsilon_p)a^\dagger_p a_h - Y^\nu_{ph}(\epsilon_p)a^\dagger_h a_p\right)\right] \end{aligned} \tag{2.4}$$

where we have indicated with $a^\dagger_\nu$ and a_ν creation and annihilation operators. We have adopted the convention to indicate the states above Fermi level with the letters m, n, p, q, r and those below Fermi level with h, i, j, k, l. The RPA amplitudes X^ν_{ph} and Y^ν_{ph} are real numbers. The presence of the Y amplitudes indicates that in the RPA ground state correlations beyond the MF are present. We present in Appendix B the derivation of the RPA secular equations which can be expressed in a matrix form as

$$\begin{pmatrix} A & B \\ B^* & A^* \end{pmatrix}\begin{pmatrix} X^\nu \\ Y^\nu \end{pmatrix} = \omega\begin{pmatrix} X^\nu \\ -Y^\nu \end{pmatrix}, \tag{2.5}$$

where we have defined

$$A_{php'h'} = \langle\Psi_0|[a^\dagger_h a_p,[H,a^\dagger_{p'}a_{h'}]]|\Psi_0\rangle \tag{2.6}$$

$$B_{php'h'} = -\langle\Psi_0|[a^\dagger_h a_p,[H,a^\dagger_{h'}a_{p'}]]|\Psi_0\rangle. \tag{2.7}$$

In Occupation Number representation the hamiltonian is written as

$$H = \sum_{\alpha\beta} h_{\alpha\beta}a^\dagger_\alpha a_\beta - \frac{1}{2}\sum_{ijij}\overline{V}_{ijij} + \frac{1}{4}\sum_{\alpha\beta\alpha'\beta'}\overline{V}_{\alpha\beta\alpha'\beta'}N[a^\dagger_\alpha a^\dagger_\beta a_{\beta'}a_{\alpha'}], \tag{2.8}$$

where

$$h_{\alpha\beta} = \langle\alpha|h|\beta\rangle = t_{\alpha\beta} + \sum_i \overline{V}_{\alpha i\beta i}, \tag{2.9}$$

with

$$t_{\alpha\beta} = \langle\alpha|t|\beta\rangle = \int d^3r \phi^*_\alpha(\boldsymbol{r}) \left(-\frac{\hbar^2}{2m}\nabla^2\right) \phi_\beta(\boldsymbol{r}). \tag{2.10}$$

With the symbol $\overline{V}_{ijij}$ we indicate: $V_{ijij} - V_{ijji}$ where

$$V_{\alpha\beta\gamma\delta} = \int d\boldsymbol{r}_1 d\boldsymbol{r}_2 \phi^*_\alpha(\boldsymbol{r}_1)\phi^*_\beta(\boldsymbol{r}_2) v(\boldsymbol{r}_1,\boldsymbol{r}_2)\phi_\gamma(\boldsymbol{r}_1)\phi_\delta(\boldsymbol{r}_2) \tag{2.11}$$

The symbol $N[a^\dagger_\alpha a^\dagger_\beta a_{\beta'} a_{\alpha'}]$ indicates the Normal Ordered Product of annihilation and creation operators. Calculating the explicit expression of (2.6) and (2.7) using (2.8) we obtain the RPA equations in the usual form:

$$(\epsilon_p - \epsilon_h - \omega)X^\nu_{ph} + \sum_{p'h'} \left(v_{ph,p'h'} X^\nu_{p'h'} + u_{ph,p'h'} Y^\nu_{p'h'}\right) = 0 \tag{2.12}$$

$$(\epsilon_p - \epsilon_h + \omega)Y^\nu_{ph} + \sum_{p'h'} \left(v^*_{ph,p'h'} Y^\nu_{p'h'} + u^*_{ph,p'h'} X^\nu_{p'h'}\right) = 0 \tag{2.13}$$

where ϵ indicates the s.p. energy.

The interaction terms v and u are defined as

$$v_{ph,p'h'} = \overline{V}_{ph'hp'} = \langle ph'|V|hp'\rangle - \langle ph'|V|p'h\rangle \tag{2.14}$$

$$u_{ph,p'h'} = \overline{V}_{pp'hh'} = \langle pp'|V|hh'\rangle - \langle pp'|V|h'h\rangle. \tag{2.15}$$

The orthonormalization relation of excited states

$$\langle\nu|\nu'\rangle = \delta_{\nu\nu'}, \tag{2.16}$$

implies the following orthonormalization relation of X and Y amplitudes

$$\sum_{ph}(X^\nu_{ph}X^{\nu'}_{ph} - Y^\nu_{ph}Y^{\nu'}_{ph}) = \delta_{\nu\nu'}. \tag{2.17}$$

2.1 RPA equations in angular momentum coupling

The RPA equations (2.12)- (2.13) are written in a generic representation. Because the states of the nucleus are characterized by total angular momentum and parity, we need to rewrite the RPA equations in angular momentum coupling so that the RPA eigenstates are also eigenstates of the $\boldsymbol{J}^2$ and J_z operators. In this representation the RPA operator has the following expression

$$Q^\dagger_J(j_p, j_h) = \sum_{ph} \left[X^J_{ph} a^\dagger_{j_p m_p} (-1)^{j_h + m_h} a^{j_h - m_h} - Y^J_{ph} a^\dagger_{j_h m_h} (-1)^{j_p + m_p} a_{j_p - m_p}\right] \tag{2.18}$$

where

$$X^J_{ph} = \sum_{m_p m_h} \langle j_p m_p j_h m_h | JM\rangle X_{ph} \tag{2.19}$$

$$Y^J_{ph} = \sum_{m_p m_h} \langle j_p m_p j_h m_h | J - M\rangle (-1)^{J-M} Y_{ph}. \tag{2.20}$$

The operator defined in Eq. (2.18) is an irreducible spherical tensor of rank J and 3rd component M which is not explicitly written, but understood, as indicated by Eqs. (2.19-2.20). We show in Appendix C that the RPA Eqs. (2.12-2.13) in angular momentum coupling assume the form

$$(\epsilon_p - \epsilon_h - \omega)X^J_{ph} + \sum_{p'h'}(v^J_{php'h'}X^J_{p'h'} + u^J_{php'h'}Y^J_{p'h'}) = 0$$

$$(\epsilon_p - \epsilon_h + \omega)Y^J_{ph} + \sum_{p'h'}(v^{*J}_{php'h'}Y^J_{p'h'} + u^{*J}_{php'h'}X^J_{p'h'}) = 0,$$

with

$$\begin{aligned} v^J_{php'h'} &= v^{Jdir}_{php'h'} - v^{Jexch}_{php'h'} \\ &= \sum_K (-1)^{j_h+j_{p'}+K}\hat{K} \left\{ \begin{array}{ccc} j_p & j_h & J \\ j_{p'} & j_{h'} & K \end{array} \right\} \\ &\{\langle j_p j_{h'} K||V_{eff}||j_h j_{p'} K\rangle - (-1)^{j_h+j_{p'}-K}\langle j_p j_{h'} K||V_{eff}||j_{p'} j_h K\rangle \end{aligned} \tag{2.21}$$

and

$$\begin{aligned} u^J_{php'h'} &= u^{Jdir}_{php'h'} - u^{Jexch}_{php'h'} \\ &= (-1)^{j_{h'}-j_{p'}-J} v^J_{phh'p'} \end{aligned} \tag{2.22}$$

where for the angular momentum we used the notation

$$\hat{a} = \sqrt{2a+1}.$$

and the labels *dir* and *exch* indicate the direct and exchange terms of the interaction.

2.2 The interaction matrix elements

In our calculations we want to keep a strict contact with the microscopic NN interaction, of Urbana, Argonne type and also with the effective interactions used in Landau-Migdal theory of finite Fermi systems. For these reasons we consider a finite range residual interaction expressed as

$$\begin{aligned} V_{eff}(r_{12}) &= v_1(r_{12}) + v_2(r_{12})\boldsymbol{\tau_1}\cdot\boldsymbol{\tau_2} + \\ &+ v_3(r_{12})\boldsymbol{\sigma_1}\cdot\boldsymbol{\sigma_2} + v_4(r_{12})\boldsymbol{\sigma_1}\cdot\boldsymbol{\sigma_2}\boldsymbol{\tau_1}\cdot\boldsymbol{\tau_2} + \\ &+ v_5(r_{12})S_{12}(\hat{r}_{12}) + v_6(r_{12})S_{12}(\hat{r}_{12})\boldsymbol{\tau_1}\cdot\boldsymbol{\tau_2}, \end{aligned} \tag{2.23}$$

where $\boldsymbol{\sigma}$ and $\boldsymbol{\tau}$ represent the spin and isospin operators respectively and S_{12} is the tensor operator:

$$S_{12}(\hat{r}) = 3\boldsymbol{\sigma_1}\cdot\hat{r}\boldsymbol{\sigma_2}\cdot\hat{r} - \boldsymbol{\sigma_1}\cdot\boldsymbol{\sigma_2}. \tag{2.24}$$

We calculate the matrix elements by using the effective interaction in momentum space

$$V_{eff}(q) = \int d\boldsymbol{q}e^{i\boldsymbol{q}\cdot\boldsymbol{r}}V_{eff}(r_{12}) \tag{2.25}$$

$$\begin{aligned} V_{eff}(q) &= V_1(q) + V_2(q)\boldsymbol{\tau_1}\cdot\boldsymbol{\tau_2} + \\ &+ V_3(q)\boldsymbol{\sigma_1}\cdot\boldsymbol{\sigma_2} + V_4(q)\boldsymbol{\sigma_1}\cdot\boldsymbol{\sigma_2}\boldsymbol{\tau_1}\cdot\boldsymbol{\tau_2} + \\ &+ V_5(q)S_{12}(\hat{q}) + V_6(q)S_{12}(\hat{q})\boldsymbol{\tau_1}\cdot\boldsymbol{\tau_2}. \end{aligned} \tag{2.26}$$

Past studies of RPA, considering of both phenomenological [44] and self consistent type [47], indicate the need of including a density dependence in the interaction. The physical origin of this density dependence of the interaction is still under discussion.

Following the tradition of the LMFFS we consider a density dependence of the v_1 and v_2 parameters

$$v_{1/2}(r,\rho(r)) = v_{1/2}(r) + v_{\rho/\rho\tau}(r)\rho^{\alpha}(r), \tag{2.27}$$

with

$$\rho(r_{12}) = [\rho(r_1)\rho(r_2)]^{\frac{1}{2}}. \tag{2.28}$$

In the following we shall indicate with the labels 1, 2, 3, 4, 5 and 6 the central, isospin, spin, spin-isospin, tensor, tensor-isospin channel respectively.

Explicit expression for the matrix elements are derived in Appendix D. We give here the final expressions.

For the isospin-independent channels we obtain

$$\begin{aligned} v^{JdirV_1}_{1,php'h'} &= \int dq q^2 \frac{2}{\pi} V_1(q) \int dr_1 r_1^2 R^*_p(r_1) R_h(r_1) j_J(qr_1) \\ & \int dr_2 r_2^2 R^*_{h'}(r_2) R_{p'}(r_2) j_J(qr_2) \\ & \frac{(-1)^{j_p+j_{p'}+1}}{4\pi} \hat{j_p}\hat{j_h}\hat{j_{p'}}\hat{j_{h'}} \begin{pmatrix} j_p & J & j_h \\ \frac{1}{2} & 0 & -\frac{1}{2} \end{pmatrix} \begin{pmatrix} j_{h'} & J & j_{p'} \\ \frac{1}{2} & 0 & -\frac{1}{2} \end{pmatrix} \\ & \xi(l_p + l_h + J)\xi(l_{p'} + l_{h'} + J) \end{aligned} \tag{2.29}$$

$$\begin{aligned} v^{JexchV_1}_{1,php'h'} &= \sum_l \int dq q^2 \frac{2}{\pi} V_1(q) \int dr_1 r_1^2 R^*_p(r_1) R_{p'}(r_1) j_l(qr_1) \\ & \int dr_2 r_2^2 R^*_{h'}(r_2) R_h(r_2) j_l(qr_2) \\ & \frac{(-1)^{j_p+j_{p'}+J+l}}{4\pi} \hat{j_p}\hat{j_h}\hat{j_{p'}}\hat{j_{h'}}\hat{l}^2 \begin{pmatrix} j_p & l & j_{p'} \\ \frac{1}{2} & 0 & -\frac{1}{2} \end{pmatrix} \begin{pmatrix} j_{h'} & l & j_h \\ \frac{1}{2} & 0 & -\frac{1}{2} \end{pmatrix} \\ & \begin{Bmatrix} j_p & j_h & J \\ j_{h'} & j_{p'} & l \end{Bmatrix} \xi(l_p + l_{p'} + l)\xi(l_h + l_{h'} + l) \end{aligned} \tag{2.30}$$

for the central channel, and

$$\begin{aligned} v^{JdirV_3}_{3,php'h'} &= \sum_l \int dq q^2 \frac{2}{\pi} V_3(q) \int dr_1 r_1^2 R^*_p(r_1) R_h(r_1) j_l(qr_1) \\ & \int dr_2 r_2^2 R^*_{h'}(r_2) R_{p'}(r_2) j_l(qr_2) \\ & (-1)^{l+J+l_p+l_{h'}+j_{p'}+j_{h'}} \frac{3}{2\pi} \hat{l}^2 \hat{l_p}\hat{l_h}\hat{l_{p'}}\hat{l_{h'}}\hat{j_p}\hat{j_h}\hat{j_{p'}}\hat{j_{h'}} \\ & \begin{Bmatrix} l_p & \frac{1}{2} & j_p \\ l_h & \frac{1}{2} & j_h \\ l & 1 & J \end{Bmatrix} \begin{Bmatrix} l_{h'} & \frac{1}{2} & j_{h'} \\ l_{p'} & \frac{1}{2} & j_{p'} \\ l & 1 & J \end{Bmatrix} \begin{pmatrix} l_p & l & l_h \\ 0 & 0 & 0 \end{pmatrix} \begin{pmatrix} l_{h'} & l & l_{p'} \\ 0 & 0 & 0 \end{pmatrix} \end{aligned} \tag{2.31}$$

$$\begin{aligned} v^{JexchV_3}_{3,php'h'} &= \sum_l \int dq q^2 \frac{2}{\pi} V_3(q) \int dr_1 r_1^2 R^*_p(r_1) R_{p'}(r_1) j_l(qr_1) \\ & \int dr_2 r_2^2 R^*_{h'}(r_2) R_h(r_2) j_l(qr_2) \\ & \sum_L \frac{3}{2\pi} (-1)^{l_p+l_{h'}+j_{p'}+j_{h'}+l+J+1} \hat{l_p}\hat{l_h}\hat{l_{p'}}\hat{l_{h'}}\hat{j_p}\hat{j_h}\hat{j_{p'}}\hat{j_{h'}}\hat{l}^2\hat{L}^2 \begin{Bmatrix} j_p & j_h & J \\ j_{h'} & j_{p'} & L \end{Bmatrix} \\ & \begin{pmatrix} l_p & l & l_{p'} \\ 0 & 0 & 0 \end{pmatrix} \begin{pmatrix} l_{h'} & l & l_h \\ 0 & 0 & 0 \end{pmatrix} \begin{Bmatrix} l_p & \frac{1}{2} & j_p \\ l_{p'} & \frac{1}{2} & j_{p'} \\ l & 1 & L \end{Bmatrix} \begin{Bmatrix} l_{h'} & \frac{1}{2} & j_{h'} \\ l_h & \frac{1}{2} & j_h \\ l & 1 & L \end{Bmatrix} \end{aligned} \tag{2.32}$$

for the spin channel, and

$$
\begin{aligned}
v_{5,php'h'}^{JdirV_5} = \; & \frac{3\sqrt{30}}{2\pi}(-1)^{j_{p'}+j_{h'}+l_p+l_{h'}}\hat{l_p}\hat{l_h}\hat{l_{p'}}\hat{l_{h'}}\hat{j_p}\hat{j_h}\hat{j_{p'}}\hat{j_{h'}} \\
& \sum_{l_1 l_2}(-1)^{\frac{3}{2}(l_1+l_2)}\hat{l_1}^2\hat{l_2}^2 \begin{pmatrix} l_1 & l_2 & 2 \\ 0 & 0 & 0 \end{pmatrix} \begin{pmatrix} l_p & l_1 & l_h \\ 0 & 0 & 0 \end{pmatrix} \begin{pmatrix} l_{h'} & l_2 & l_{p'} \\ 0 & 0 & 0 \end{pmatrix} \\
& \begin{Bmatrix} l_1 & l_2 & 2 \\ 1 & 1 & J \end{Bmatrix} \begin{Bmatrix} l_p & \frac{1}{2} & j_p \\ l_h & \frac{1}{2} & j_h \\ l_1 & 1 & J \end{Bmatrix} \begin{Bmatrix} l_{h'} & \frac{1}{2} & j_{h'} \\ l_{p'} & \frac{1}{2} & j_{p'} \\ l_2 & 1 & J \end{Bmatrix} \\
& \int dq q^2 \frac{2}{\pi} V_5(q) \int dr_1 r_1^2 R_p^*(r_1) R_h(r_1) j_{l_1}(qr_1) \int dr_2 r_2^2 R_{h'}^*(r_2) R_{p'}(r_2) j_{l_2}(qr_2)
\end{aligned}
\tag{2.33}
$$

$$
\begin{aligned}
v_{5,php'h'}^{JexchV_5} = \; & -\sum_{l_1 l_2} \int dq q^2 V_5(q) \int dr_1 r_1^2 R_p^*(r_1) R_{p'}(r_1) j_{l_1}(qr_1) \int dr_2 r_2^2 R_{h'}^*(r_2) R_h(r_2) j_{l_2}(qr_2) \\
& \frac{3\sqrt{30}}{\pi^2}(-1)^{l_p+l_{h'}+j_{p'}+j_{h'}+l_1+l_2+J} i^{l_1+l_2} \hat{l_p}\hat{l_h}\hat{l_{p'}}\hat{l_{h'}}\hat{j_p}\hat{j_h}\hat{j_{p'}}\hat{j_{h'}}\hat{l_1}^2\hat{l_2}^2 \\
& \begin{pmatrix} l_1 & l_2 & 2 \\ 0 & 0 & 0 \end{pmatrix} \begin{pmatrix} l_p & l_1 & l_{p'} \\ 0 & 0 & 0 \end{pmatrix} \begin{pmatrix} l_{h'} & l_2 & l_h \\ 0 & 0 & 0 \end{pmatrix} \\
& \sum_L (-1)^L \hat{L}^2 \begin{Bmatrix} l_1 & l_2 & 2 \\ 1 & 1 & L \end{Bmatrix} \begin{Bmatrix} j_p & j_h & J \\ j_{h'} & j_{p'} & L \end{Bmatrix} \\
& \begin{Bmatrix} l_p & \frac{1}{2} & j_p \\ l_{p'} & \frac{1}{2} & j_{p'} \\ l_1 & 1 & L \end{Bmatrix} \begin{Bmatrix} l_{h'} & \frac{1}{2} & j_{h'} \\ l_h & \frac{1}{2} & j_h \\ l_2 & 1 & L \end{Bmatrix}
\end{aligned}
\tag{2.34}
$$

for the tensor channel.

The isospin dependent terms can be obtained from the ones reported above by the following substitutions: $V_1 \to cV_2$ for the central channel, $V_3 \to cV_4$ for the spin channel, and $V_5 \to cV_6$ for the tensor channel. Here c is a constant, equal for all channels. For direct terms one has $c = 1$ if ph and $p'h'$ pairs have the same isospin and $c = -1$ otherwise. For the exchange terms $c = 1$ in the first case and $c = 2$ in the second.

In all the above equations we have indicated with $R(r)$ the radial part of the s.p. wave function and with j_l the spherical Bessel function.

2.3 Charge changing excitations

The traditional formulation of the RPA theory for nuclear systems considers excitations where the nucleus does not change its identity. This means that only ph excitations between particles of the same type (proton and neutron) are considered.

The RPA formulation can be extended by considering excitations of ph pairs between unlike particles. In this charge-changing RPA excitations only the isospin dependent terms of the residual interaction (2.23) are active.

The expressions of the matrix elements of these terms are analogous to those of the charge conserving excitations but for an overall constant. The multiplicative constants can be found easily, as we show in Appendix D, and are +2 for the direct terms and −1 for the exchange terms.

2.4 RPA transition matrix element

The matrix element of the one-body operator inducing the transition from the nucleus ground state to the excited state is given by:

$$< J|T_J|0 >= \sum_{ph} \Big[X^J_{ph} < j_p||T_J||j_h > + (-1)^{J+j_p-j_h} Y^J_{ph} < j_h||T_J||j_p > \Big] . \quad (2.35)$$

For the electric excitations the operator T_J is the following:

$$T_J = Q_J = er^J Y_{JM}(\Omega) , \quad (2.36)$$

therefore the matrix elements to be inserted in Eq. (2.35) are

$$< j_f||T_J||j_i >= e\frac{(1+(-1)^{l_i+l_f+J})}{2} \langle f|r^J|i\rangle \frac{\hat{J}\hat{j}_i\hat{j}_f}{\sqrt{4\pi}} (-1)^{j_f-\frac{1}{2}} \begin{pmatrix} j_f & J & j_i \\ -\frac{1}{2} & 0 & \frac{1}{2} \end{pmatrix} \quad (2.37)$$

In the above equation we have used the Wigner 3-j symbol [48].

In the magnetic case we have the magnetic operator:

$$T_J = M_J = \mu_N \{ g_S \boldsymbol{\sigma} + \frac{2g_l}{J+1} \boldsymbol{l} \} \cdot [\boldsymbol{\nabla} r^J Y_{JM}(\Omega)] \quad (2.38)$$

where $g_S = 2\mu_{p/n}$ where μ_N, μ_p and μ_n are magnetic nuclear, proton and neutron momentum respectively, g_l is 1 for protons and 0 for neutrons. The expressions of magnetic momenta are:

$$\mu_N = \frac{e\hbar c}{2mc^2}, \quad \mu_p = 2.79\mu_N \quad \mu_n = -1.91\mu_N \quad (2.39)$$

where e is the elementary charge and m is the proton rest mass, with:

$$\hbar c = 197.32858 MeV \cdot fm \quad (2.40)$$

In the magnetic case the matrix elements to be inserted in Eq. (2.35) are

$$< j_f||T_L||j_i >= \mu_N \frac{(1 = (-1)^{l_i+l_f+J})}{2} \langle f|r^{J-1}|i\rangle \frac{\hat{J}\hat{j}_i\hat{j}_f}{\sqrt{4\pi}} (-1)^{j_f-\frac{1}{2}} \begin{pmatrix} j_f & J & j_i \\ -\frac{1}{2} & 0 & \frac{1}{2} \end{pmatrix} (J-k)[\frac{1}{2}g_S - g_l(1+\frac{k}{J+1})] \quad (2.41)$$

with

$$k = (j_i + \frac{1}{2})(-1)^{l_i+j_i+\frac{1}{2}} + (j_f + \frac{1}{2})(-1)^{l_f+j_f+\frac{1}{2}} \quad (2.42)$$

The radial integrals are defined as

$$\langle f|r^J|i\rangle = \int_o^\infty R_f(r) r^J R_i(r) r^2 dr \quad (2.43)$$

The B-value is the square of the modulus of (2.35) and the photoabsorption cross section is given by:

$$\sigma_T(0 \to J) = 8\pi^3 \frac{J+1}{J} \frac{e^2}{[(2J+1)!!]^2} k^{2J-1} B(EJ : 0 \to J) \quad (2.44)$$

Chapter 3

Discrete RPA calculations

In this chapter we present results of RPA calculations done by using a discrete configuration space.

Following the discussion of chapter 2, we first discuss the limits and validity of the use of a discrete basis, we then present in detail the four different parameterizations of the residual interaction which have been used in our calculations, and, finally, we present results for the low energy spectrum of ^{12}C, ^{16}O, ^{40}Ca, ^{48}Ca, ^{90}Zr and ^{208}Pb nuclei.

For each nucleus we discuss the energies of the low-lying excited states, studying their sensitivity to the different residual interactions employed in the calculation and we analyze the structure of some significant natural and unnatural parity states and their transverse or longitudinal response functions.

In the case of ^{16}O, which is discussed first and studied more extensively, we also analyze further the sensitivity of our results on the discretization procedure.

3.1 Analysis of the continuum discretization with Woods-Saxon potential

The aim of this section is to investigate the validity of the techniques employed to describe the contribution of the continuum in RPA calculations done with a discrete s.p. basis. Here we use as input of the RPA calculations the s.p. wave functions obtained from the diagonalization procedure of the s.p. hamiltonian in HO basis described in chapter 1, where we have already discussed the sensitivity of the s.p. energy values to the box dimensions (r_{cut}) and to the number of HO expansion coefficients N_{HO}. We now extend this discussion to the full RPA results. Besides depending on N_{HO} and r_{cut}, the latter are also sensitive to the size of the configuration space, that is to the number of the s.p. states included in the calculations. In our study all the states below the Fermi surface are taken into account and a truncation is applied only to states above the Fermi surface.

The configuration space used for each nucleus under study is shown in Tab. 3.1, where we indicate the number of states and the corresponding major shells.

With these configuration spaces we made RPA calculations using different values of r_{cut} and N_{HO}. In all these calculations we used the same effective interaction, specifically the LM interaction, presented in the next section. In Fig. 3.1 we show the energy of the lowest 2^+ in ^{12}C and ^{90}Zr and 3^- state in ^{16}O, ^{40}Ca, and ^{208}Pb as a function of N_{HO} for different value of r_{cut}.

The calculations have been done with N_{HO} that varies from 8 to 50 and r_{cut} equal to 10, 15, 20, 25 and 30 fm.

nucleus	proton states		neutron states		total
^{16}O	22	$6\hbar\omega$	22	$6\hbar\omega$	44
^{12}C	22	$6\hbar\omega$	22	$6\hbar\omega$	
^{40}Ca	29	$7\hbar\omega$	29	$7\hbar\omega$	59
^{48}Ca	29	$7\hbar\omega$	29	$7\hbar\omega$	
^{90}Zr	46	$9\hbar\omega$	54	$10\hbar\omega$	100
^{208}Pb	46	$9\hbar\omega$	54	$10\hbar\omega$	

Table 3.1: Configuration space used in our discrete RPA calculations for each nucleus. We indicate the number of states and the corresponding HO major shells.

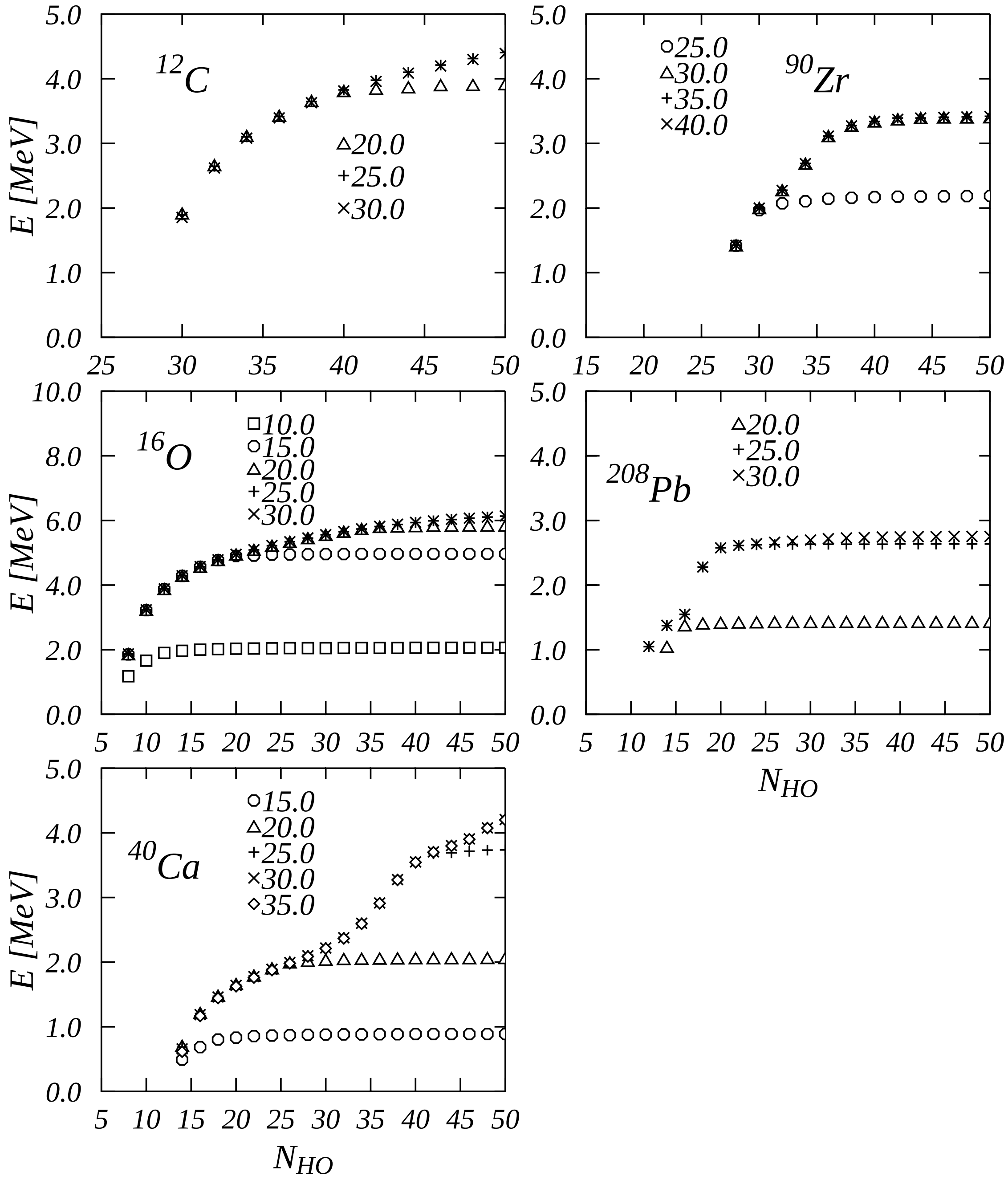

Figure 3.1: Energy of lowest 2^+ state in ^{12}C and ^{90}Zr the lowest 3^- state in ^{16}O, ^{40}Ca, and ^{208}Pb as a function of N_{HO} for different values of r_{cut}. The symbols indicates the different values of r_{cut} which are expressed in fm.

We observe that there is a relation between the values of r_{cut} and N_{HO} which give convergence. If we increase the value of r_{cut} also N_{HO} has to increase. We find that for ^{12}C and ^{16}O r_{cut} equal to 25 fm gives the appropriate convergence, while for ^{90}Zr and ^{208}Pb we need r_{cut} equal to 30 fm. The case of ^{40}Ca is more complicated. A summary of the combinations of r_{cut} and N_{HO} values providing convergence is given in Tab. 3.2. All results presented in this chapter have been obtained by using $r_{cut} = 25fm$ and $N_{HO} = 50$.

	N_{HO}				
$r_{cut}[fm]$	^{12}C	^{16}O	^{40}Ca	^{90}Zr	^{208}Pb
10		14			
15		22	20		
20	40	40	28		16
25	50	50	42	32	22
30	50	50	50	42	36

Table 3.2: Combinations of r_{cut} and N_{HO} giving convergence in the results shown in Fig. 3.1.

So far we have addressed our attention to the lowest energy states, which are the main focus of this chapter, however the value of N_{HO} influences the full excitation spectrum. As an example of this we show in Fig. 3.2 the B-values of the 3^- excitation in ^{16}O obtained with the LM interaction and with $r_{cut} = 25fm$. We observe a reasonable overlap between the solutions obtained with $N_{HO} = 20$ and $N_{HO} = 30$, while the spectrum produced by $N_{HO} = 8$ is very different, especially at the higher energies.

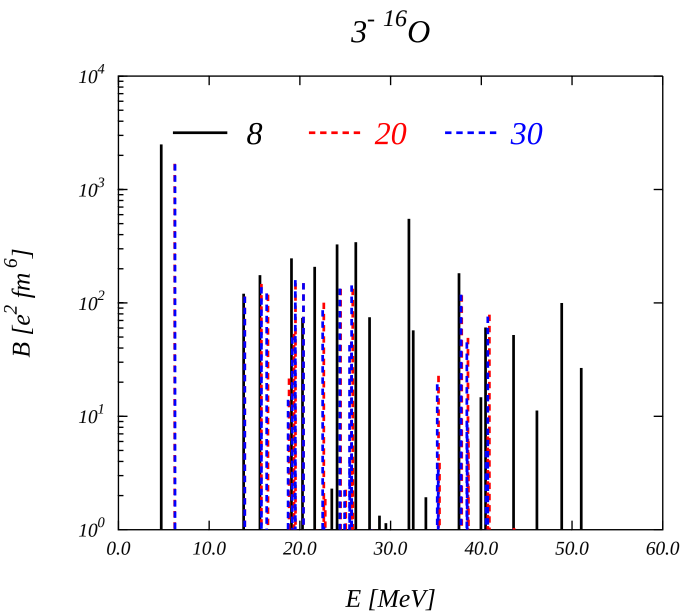

Figure 3.2: B-values of 3^- excitation of ^{16}O for three different values of N_{HO} (8, 20, 30). The calculations have been done with the LM interaction and with $r_{cut} = 25fm$.

Finally we conclude this section by discussing the influence of the size of the configuration space on the results.

As an example we show in Fig. 3.3 the B-values of the 3^- excitation energies. In this figure we compare 3^- spectra obtained with configuration space formed by 44, 58 and 100 states (see Tab. 3.1). The position of the lowest 3^- state is strongly related to the size of the configuration space. There is a reasonable agreement between the three calculations in the region between 15 to 25 MeV. Above 25 MeV the results obtained with 100 states show many more states than the other calculations done.

In concluding this section we observe that the effects of the discretization of the continuum and, especially, of the truncation of the configuration space are partially considered by the use of effective interactions and operators. In fact the effective interactions are fixed by reproducing some chosen nuclear levels or properties calculated with a specific choice of the configuration space and are thus "designed" to work within this choice. This should be considered in the comparison with microscopic interactions and calculations.

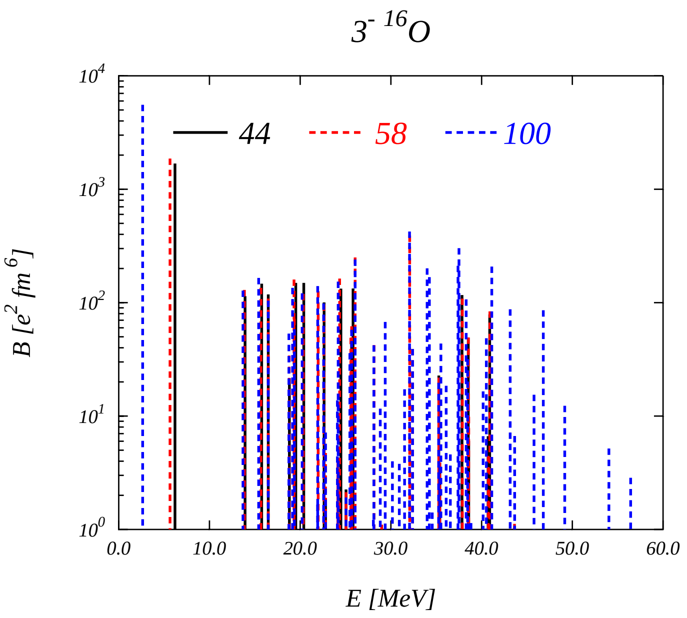

Figure 3.3: B-values of 3^- excitation in ^{16}O for configuration space composed by 44, 58 and 100 states.

3.2 Residual interaction

As already mentioned at the end of previous chapter, RPA is an effective theory and therefore effective hamiltonians and transition operators should be used. Following the philosophy of the LMFFS we choose effective nucleon-nucleon interactions whose parameters have been adjusted to reproduce some special features of the nuclear excitation spectrum. In building the effective interactions we adopted the following criteria. We have chosen a unique set of parameters for all the nuclei studied and for all the six channels of the residual interactions (see Eq. (2.23)), but for the scalar one. In the scalar channel we included a density dependent term, see Eq. (2.27) and (2.28), adjusting its parameters to reproduce energy of some collective low-lying states for each nucleus under consideration. These states are the first 2^+ state in ^{12}C and ^{90}Zr, the lowest energy 3^- states in ^{16}O, ^{40}Ca, and ^{208}Pb. For ^{48}Ca we used the same interactions as for ^{40}Ca. The parameters in the other channels have been chosen to get a reasonable description of the IVGDR, and to reproduce the excitation energies of some magnetic states in ^{208}Pb, namely the 1^+ states at 5.85 and 7.30 MeV, and the two 12^- states at 6.43 and 7.08 MeV. We also cared that the energy of the isoscalar spurious 1^- excitation is below zero.

We build four phenomenological interactions. Two of them are zero-range interactions of Landau-Migdal type, and the other two have finite range. For each type of interaction we consider parameterizations without and with tensor terms. The last ones are identified with a tt label in their names. For the Landau-Migdal interactions the $v(r_{12})$ functions of Eq. (2.23) become constants, therefore

$$V^{LM}_{eff}(r_{12}) = [V_1(\rho) + V_2\boldsymbol{\tau_1}\cdot\boldsymbol{\tau_2} + V_3\boldsymbol{\sigma_1}\cdot\boldsymbol{\sigma_2} + V_4\boldsymbol{\sigma_1}\cdot\boldsymbol{\sigma_2}\boldsymbol{\tau_1}\cdot\boldsymbol{\tau_2} + \\ + V_5 S_{12} + V_6 S_{12}\boldsymbol{\tau_1}\cdot\boldsymbol{\tau_2}]\,\delta(\boldsymbol{r}_1 - \boldsymbol{r}_2). \tag{3.1}$$

where

$$V_1(\rho) = V_1 + V_\rho \rho^\alpha(r_{12}) \tag{3.2}$$

$$\rho(r_{12}) = [\rho(r_1)\rho(r_2)]^{\frac{1}{2}}\,. \tag{3.3}$$

and where we use $\alpha = 1$.

The values of the parameters we have chosen are given in Tab.3.3.

	V_1	V_2	V_3	V_4	V_5	V_6
LM	-918	600	20	200	0	0
LMtt	-918	600	20	200	0	-150

Table 3.3: Parameters of LM and LMtt interactions in $MeV fm^3$

The values we obtain for V_3 and V_4 are similar to those frequently used in the literature [49],[50]. In Tab. 3.4 we show the values of the density dependent parameter that is the same for LM and LMtt. For ^{16}O we constructed two interactions considering configuration spaces composed by 44 and 100 states, respectively.

	^{12}C	^{16}O (44 states)	^{16}O (100 states)	^{40}Ca	^{90}Zr	^{208}Pb
V_ρ	361.0	436.4	457.1	492.3	485.0	599.0

Table 3.4: The values of the density dependent parameter $V\rho$ of the LM and LMtt interactions in $MeV fm^6$.

The other two interactions have finite range, and we identify them as FR and FRtt. They have been constructed by keeping the long range behaviour of the Argonne V18 potential [51] and modifying the short-range behaviour in order to take into account the short-range correlations effects.

For the first four channels we take

$$V^{p=1,4}(r) = \widetilde{V}_{18}^{p=1,4}(r) + \sum_{\mu=1}^{M} a_\mu e^{-b_\mu (r-R_\mu)^2}. \tag{3.4}$$

With M we indicate the number of gaussians used in the channel. For the scalar channel we have used two gaussians in order to obtain an attractive behaviour starting from the repulsive core. The repulsive behaviour is hold in the density dependent term. For the other channels one gaussian is enough to obtain the correct behaviour of the interaction.

We indicate with $\widetilde{V}_{18}^p$ the analogous term of the bare Argonne V18 potential where the short range term have been set to zero.

The tensor channels have been obtained by multiplying the bare $V18$ tensor terms by the scalar short range correlation of [15] indicated by $f(r)$:

$$V^{p=5,6}(r) = V_{18}^{5,6}(r) f(r) \tag{3.5}$$

The $f(r)$ correlation function is shown in Fig. 3.4.

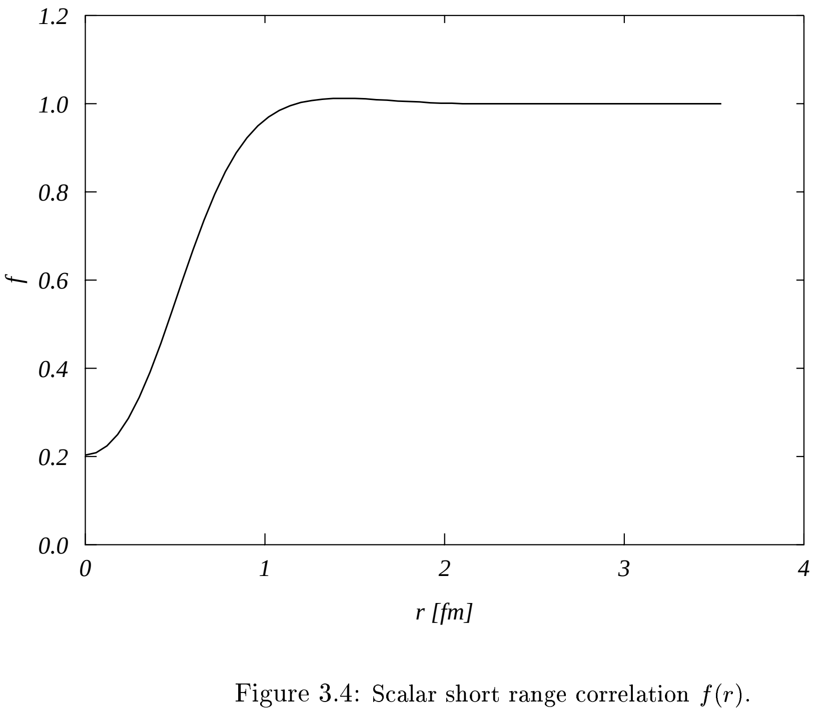

Figure 3.4: Scalar short range correlation $f(r)$.

Finally, the density dependent terms are taken to be gaussians:

$$V_{\rho,\tau}(r) = a_{\rho,\tau} e^{-b_{\rho,\tau} r^2} \tag{3.6}$$

All the fits have been done by considering only the direct terms of the RPA matrix elements, see sect. 2.2. This is the correct procedure for the zero-range LM and LMtt force, but it is an approximation for the other two forces of finite-range type. Our fit procedure considers effectively the contribution of the exchange terms.

The parameters chosen are written in the following table:

	channel	*FR*	*FRtt*
V_1	1	$\widetilde{V}_{18}+$ $a_1 = 600.0$ $b_1 = 4.0$ $R_1 = 0.5$ $a_2 = -200.0$ $b_2 = 20.$ $R_2 = 0.0$	$\widetilde{V}_{18}+$ $a_1 = 600.0$ $b_1 = 4.0$ $R_1 = 0.5$ $a_2 = -200.0$ $b_2 = 20.$ $R_2 = 0.0$
V_2	$\tau_1 \cdot \tau_2$	$\widetilde{V}_{18}+$ $a_1 = 300.0$ $b_1 = 7.0$ $R_1 = 0.5$	$\widetilde{V}_{18}+$ $a_1 = 300.0$ $b_1 = 7.0$ $R_1 = 0.5$
V_3	$\sigma_1 \cdot \sigma_2$	0	0
V_4	$\sigma_1 \cdot \sigma_2 \tau_1 \cdot \tau_2$	$\widetilde{V}_{18}+$ $a_1 = -40.0$ $b_1 = 4.5$ $R_1 = 0.5$	$\widetilde{V}_{18}+$ $a_1 = -40.0$ $b_1 = 4.5$ $R_1 = 0.5$
V_5	S_{12}	0	$\widetilde{V}_{18}$f(r)
V_6	$S_{12}\tau_1 \cdot \tau_2$	0	$\widetilde{V}_{18}$f(r)
V_ρ	V_ρ	$a_\rho(^{12}C) = 133.8$ $a_\rho(^{16}O - 44 states) = 163.4$ $a_\rho(^{16}O - 100 states) = 172.8$ $a_\rho(^{40}Ca) = 194.7$ $a_\rho(^{48}Ca) = 194.7$ $a_\rho(^{90}Zr) = 187.6$ $a_\rho(^{208}Pb) = 240.0$ $b_\rho = 1.0$	$a_\rho(^{12}C) = 133.8$ $a_\rho(^{16}O - 44 states) = 163.3$ $a_\rho(^{16}O - 100 states) = 172.8$ $a_\rho(^{40}Ca) = 194.6$ $a_\rho(^{48}Ca) = 194.6$ $a_\rho(^{90}Zr) = 187.5$ $a_\rho(^{208}Pb) = 240.0$ $b_\rho = 1.0$
$V_{\rho\tau}$	$V_\rho \tau_1 \cdot \tau_2$	$a_\tau(^{12}C) = 90.0$ $a_\tau(^{16}O) = 0.0$ $a_\tau(^{40}Ca) = 32.0$ $a_\tau(^{48}Ca) = 32.0$ $a_\tau(^{90}Zr) = 130.0$ $a_\tau(^{208}Pb) = 130.0$ $b_\tau = 1.0$	$a_\tau(^{12}C) = 20.$ $a_\tau(^{16}O) = 0.0$ $a_\tau(^{40}Ca) = 32.0$ $a_\tau(^{48}Ca) = 32.0$ $a_\tau(^{90}Zr) = 130.0$ $a_\tau(^{208}Pb) = 130.0$ $b_\tau = 1.0$

Table 3.5: FR and FRtt parameters. The a_μ constant is expressed in MeV and the b_μ and R_μ in fm.

In Figs. 3.5, 3.6, 3.9, 3.7, 3.8 and 3.10 we show the behaviour of the FR and FRtt interactions for each channel, in both configuration and momentum spaces.

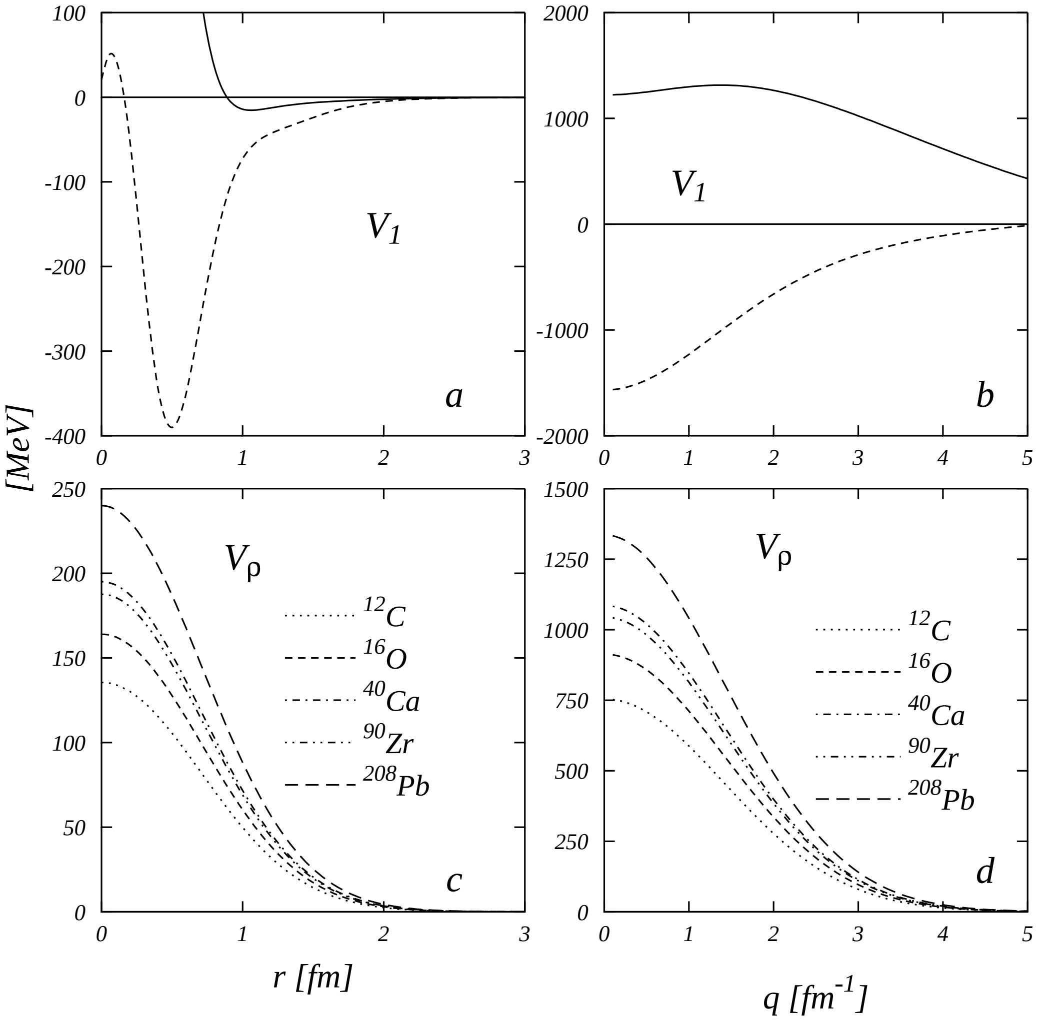

Figure 3.5: Scalar terms of the FR interaction in both r and q spaces. In the panels a and b the V_1 terms of our interaction, dashed lines, are compared with the analogous of the bare Argonne V18 potentials. In the lower panels the V_ρ terms for each nucleus are compared.

We remark that the density dependent terms are always repulsive. We summarize in Tab.3.6 the results obtained with the four interactions just described for the states we have used to adjust the interactions. For the ^{90}Zr nucleus the lowest state is, with FR and FRtt interaction the 2^+ excited state, but with the LM and LMtt interactions the 5^- excited state. For this reason we have set the interactions fitting these states.

		LM	LMtt	FR	FRtt	exp
^{12}C	E (MeV)	4.41	4.41	4.46	4.47	4.44
	B (e^2fm^6)	3.85	3.85	4.06	4.04	
$^{16}O(44)$	E (MeV)	6.14	6.14	6.14	6.13	6.13
	B (e^2fm^6)∗10^3	1.55	1.55	1.52	1.53	
$^{16}O(100)$	E (MeV)	6.13	6.13	6.13	6.14	6.13
	B (e^2fm^6)∗10^3	1.60	1.60	1.60	1.60	
^{40}Ca	E (MeV)	3.77	3.78	3.74	3.73	3.73
	B (e^2fm^6)∗10^4	1.36	1.33	1.35	1.36	
^{90}Zr	E (MeV)			2.18	2.19	2.18
	E (MeV)	2.25	2.29			2.32
	B (e^2fm^6)∗10^1			2.76	2.77	
	B (e^2fm^6)∗10^7	9.82	9.96			
^{208}Pb	E (MeV)	2.63	2.63	2.63	2.63	2.63
	B (e^2fm^6)∗10^5	6.62	6.62	5.61	5.66	6.12

Table 3.6: Energies and B-values obtained for excited states considered to fix our interactions.

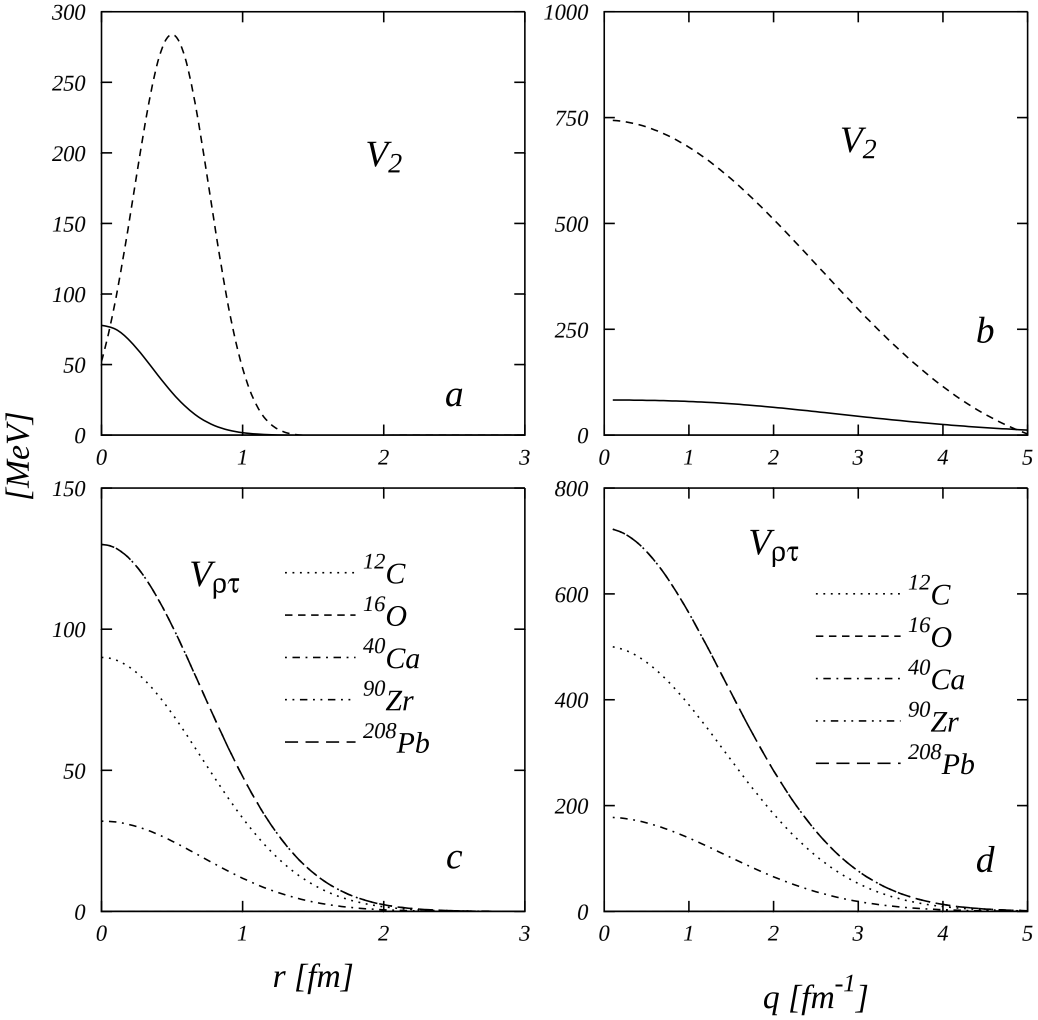

Figure 3.6: Same as Fig. 3.5 for the isospin channel.

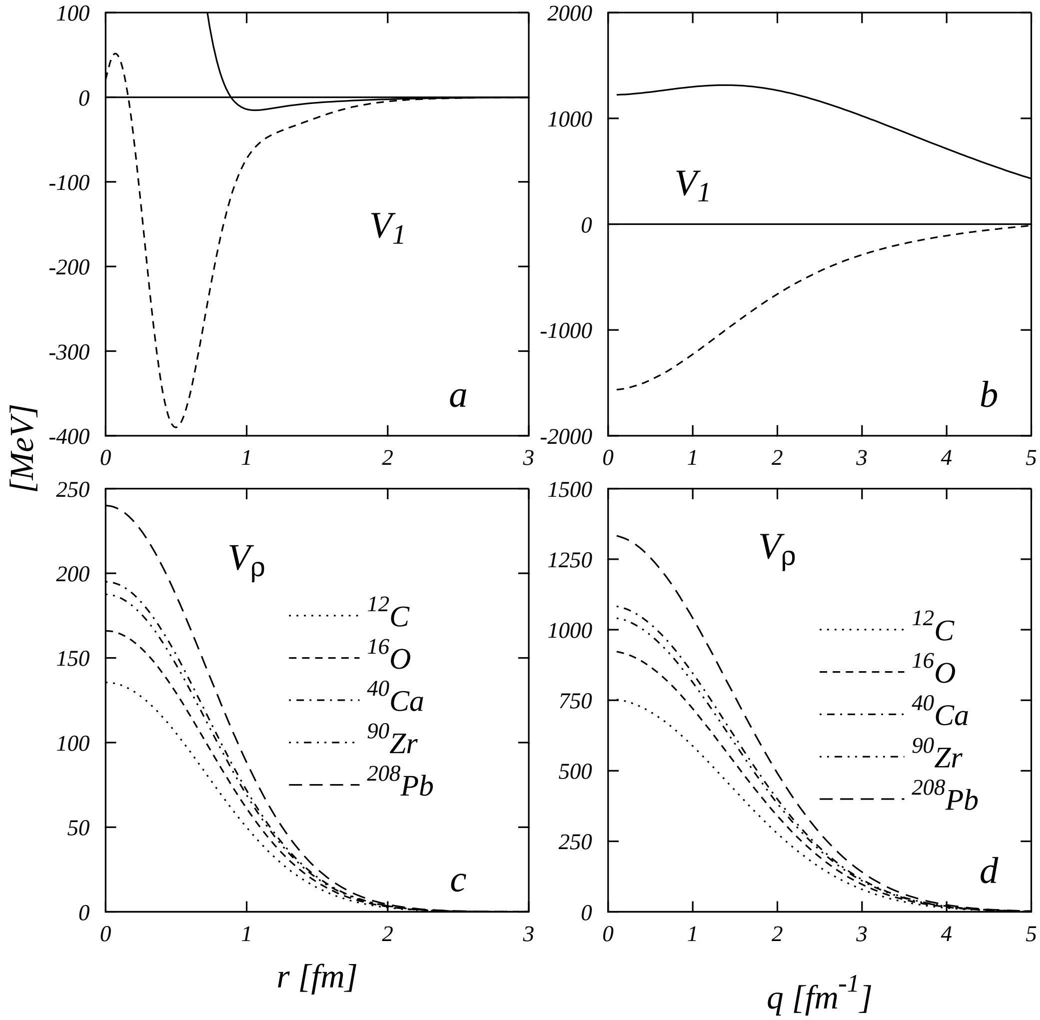

Figure 3.7: Scalar terms of the FRtt interaction in both r and q spaces. In the panels a and b the V_1 terms of our interaction, dashed lines, are compared with the analogous of the bare Argonne V18 potential. In the lower panels the V_ρ terms for each nucleus are compared.

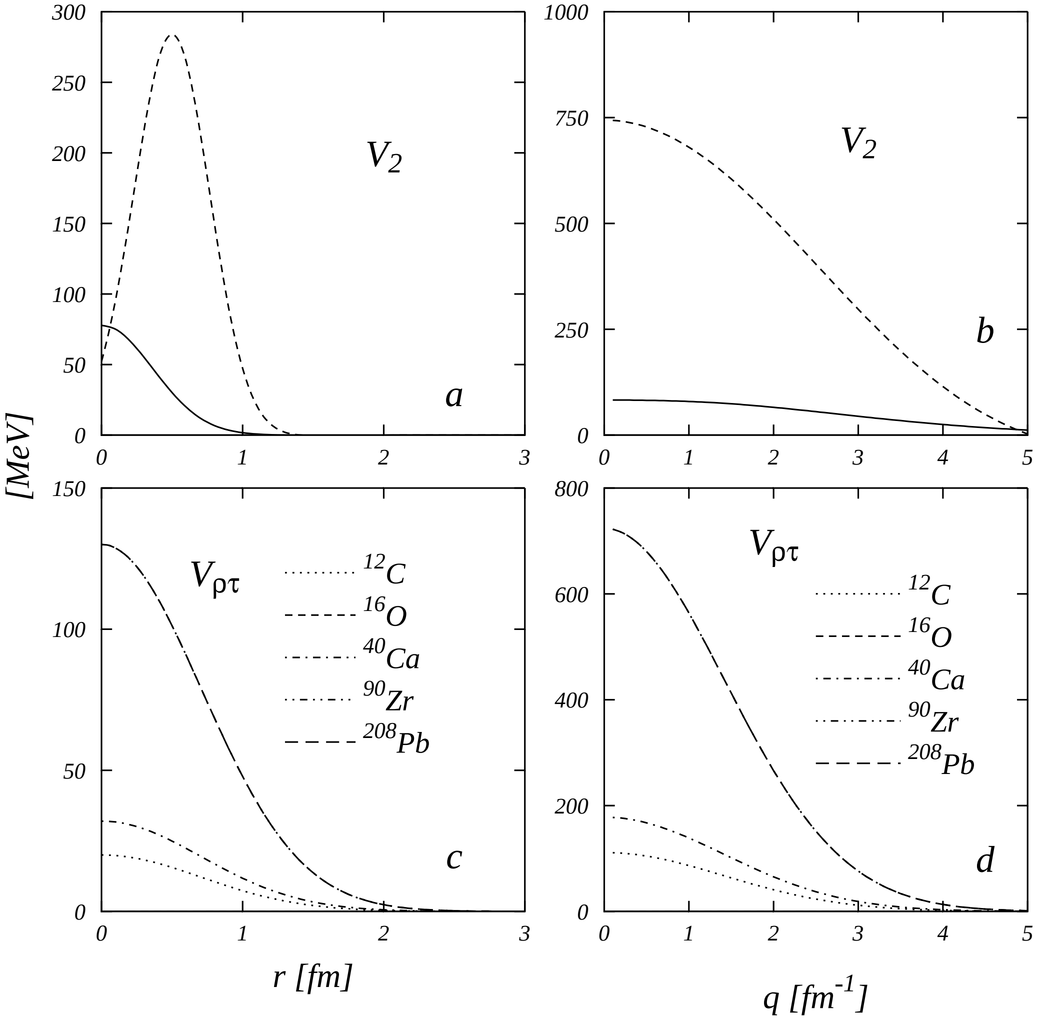

Figure 3.8: Same as Fig. 3.7 for the isospin channel.

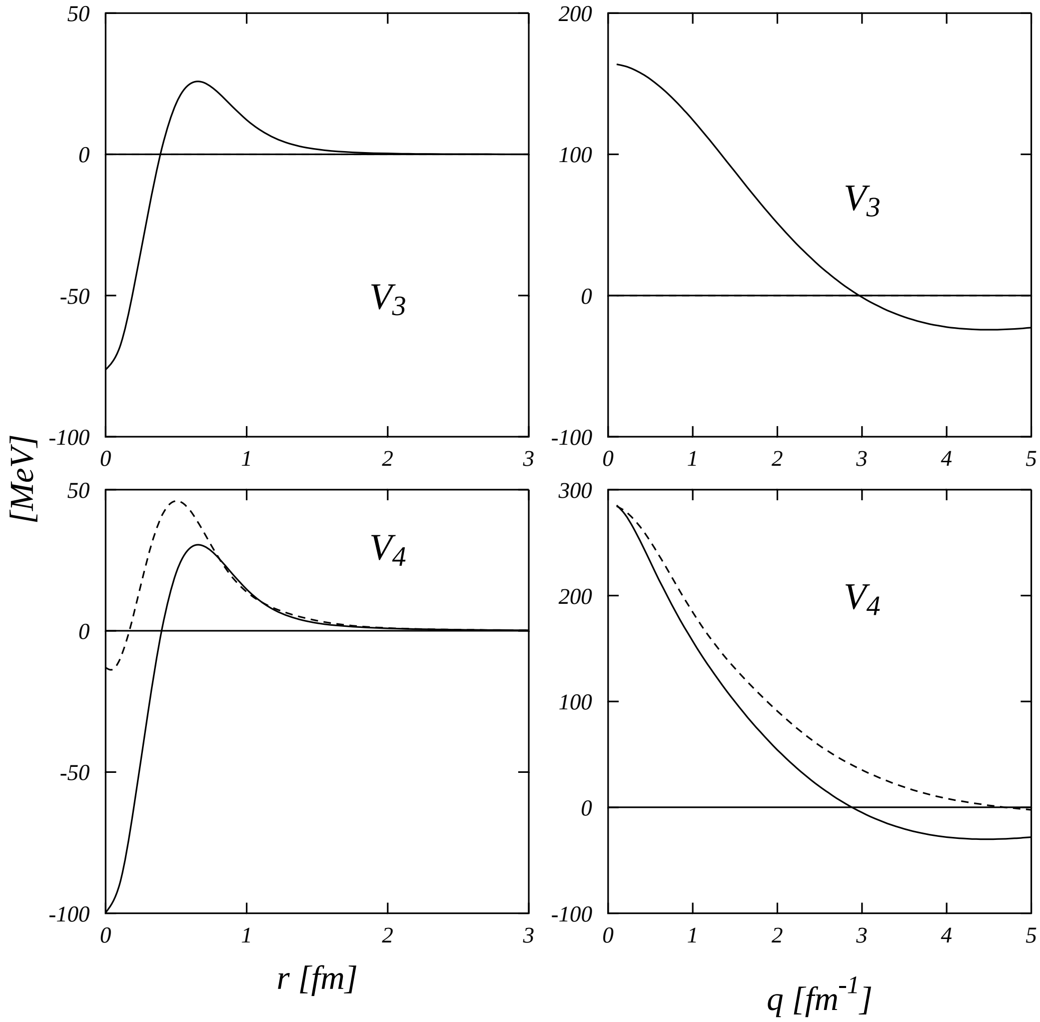

Figure 3.9: Spin, V_3, and spin isospin channels, V_4. The full lines indicate the bare V18 potential, the dashed lines the FR, FRtt potential.

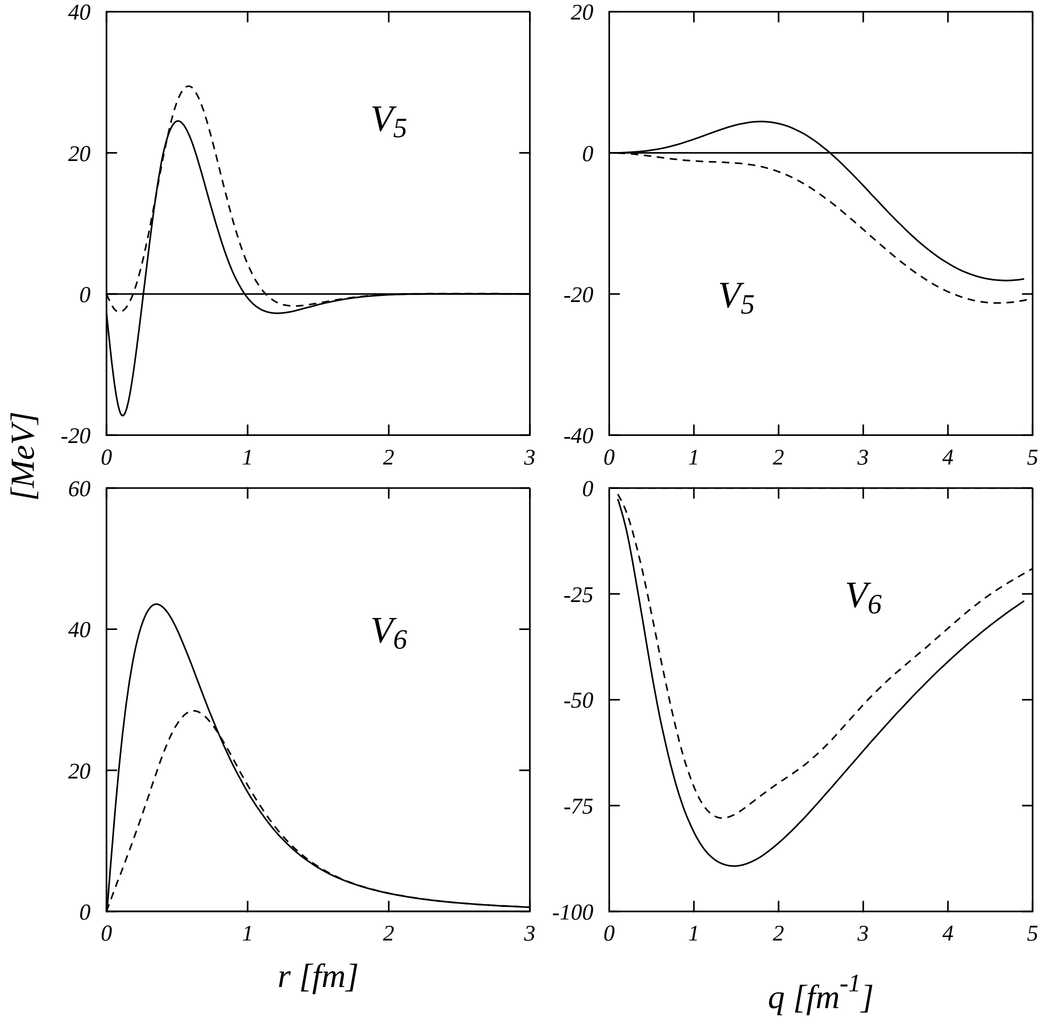

Figure 3.10: The same as Fig. 3.9 for the two tensor channels of FRtt.

3.3 Discrete RPA results

The discrete RPA calculations are rather straightforward. We did not use particular numerical techniques to diagonalize the RPA secular Eqs. (2.12-2.13). For a given value of the angular momentum and of the parity of the multipole excitation, all the compatible ph pairs in the chosen configuration space are selected. The number of RPA solutions is identical to the number of ph pairs. We have already discussed in sect. 3.1 the sensitivity to the truncation of the configuration space of the high energy spectrum.

In order to minimize this sensitivity in the following discussion we consider those low-lying states dominated by ph transitions where the particle state is bound. We present our results separately for each nucleus we have studied.

3.3.1 The ^{16}O nucleus

The spectrum of the ^{16}O nucleus we obtain is presented in Tab.3.7.

$^{16}O(44-states/100-states)$					
excitation	LM	LMtt	FR	FRtt	exp
3^-	6.14/6.13	6.14/6.13	6.14/6.13	6.13/6.14	6.13
2^-	11.80/11.80	11.80/11.80	11.51/11.51	11.51/11.51	8.87
0^-	12.33/12.33	11.19/ 11.15	12.15/12.15	11.84/11.84	10.96
0^-	—/—	12.39/12.29	13.13/13.10	12.23/12.23	12.80
4^-	18.15/18.15	18.15/18.15	17.75/17.75	17.73/17.73	17.79
4^-	21.41/21.11	20.59/20.34	19.88/19.80	19.45/19.40	18.98

Table 3.7: Low energy spectrum of the ^{16}O nucleus. All energies are expressed in MeV. We show results obtained by using two configuration spaces composed by 44 and 100 states. The experimental energies are taken from [40]

The first striking feature is the difference between the number of experimentally identified levels and those predicted by our calculations. This clearly shows that there are states that cannot be described by the RPA ansatz, Eq. (2.2). These states are mainly of natural parity type. The unnatural parity spectrum of negative parity is well reproduced as it is shown in Fig. 3.11.

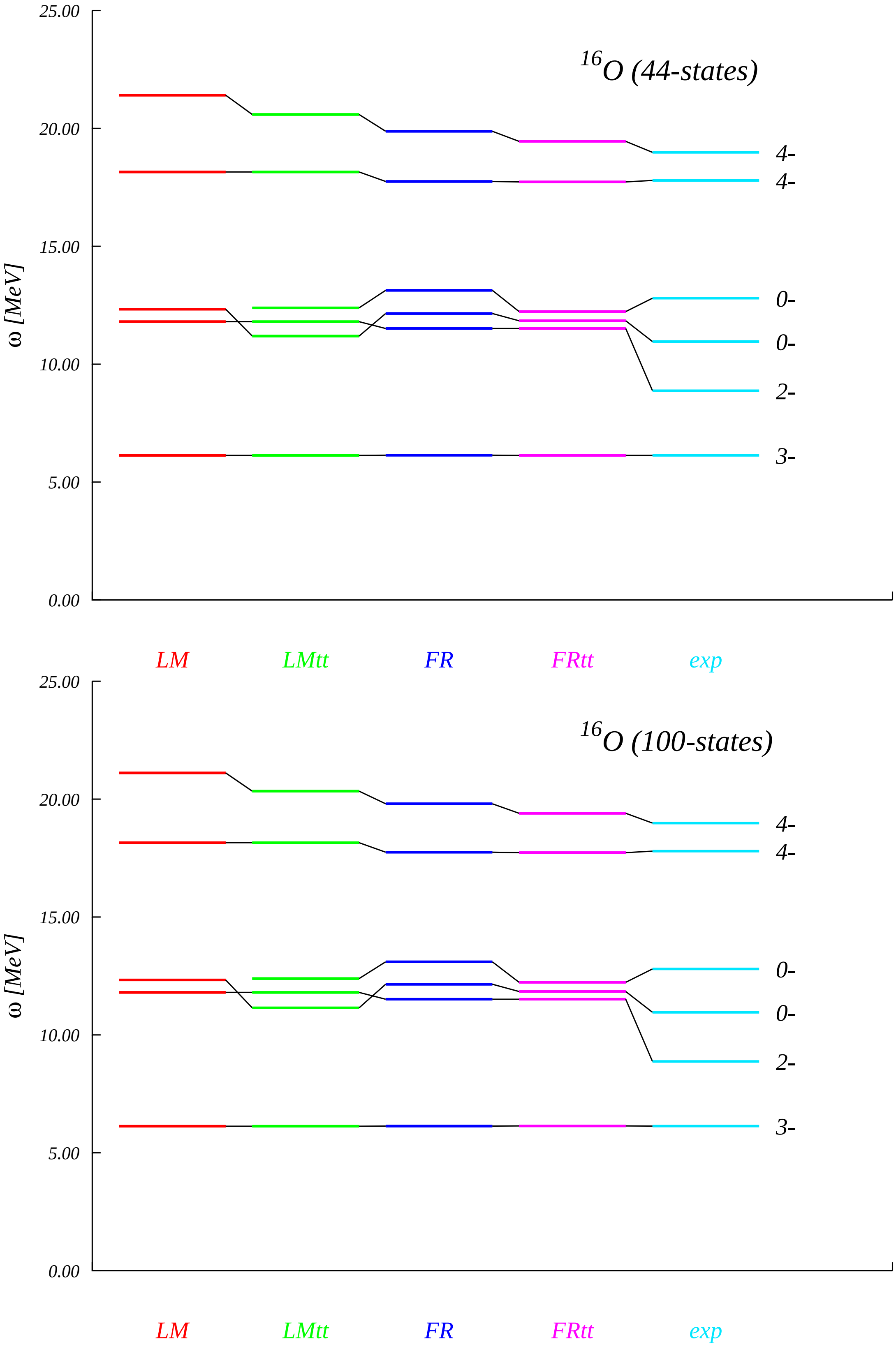

Figure 3.11: ^{16}O spectrum

Before discussing the details of the spectrum we want to study the stability of the RPA solutions with respect to the description of the excited states. In fact the study of sect 3.1 has been done by considering the energy spectrum only. As a test case we consider the electron scattering longitudinal response of the low lying 3^- state. The transition probability is calculated as indicated in Appendix E.

In a first calculation we tested the sensitivity of the results to changes in the value of r_{cut}.

We made calculations by using the same value of HO expansion coefficients, $N_{HO} = 50$, and we use a LM type of interaction where we changed V_ρ accordingly to the value of r_{cut} in order to reproduce the experimental energy. The values of the parameters used in these calculations are given in Tab. 3.8.

$r_{cut}[fm]$	$3^- E[MeV]$	$V_\rho[MeV fm^3]$
10	6.14	476.6
15	6.13	456.1
20	6.14	442.5
25	6.14	436.4

Table 3.8: Energies of the 3^- levels of ^{16}O obtained by varying r_{cut}. The results are obtained setting the V_ρ of the LM interaction in order to reproduce the experimental value.

The longitudinal responses calculated with different values of r_{cut} and the transition densities are shown in Fig. 3.12.

We have tested the stability of the solution with respect to the dimension of the configuration space. Longitudinal responses and transition densities calculated with 44 and 100 states are shown in Fig. 3.13.

We observe that the various interactions produce almost identical results. This indicates that the structure of this state is essentially dominated by the scalar term of the interaction which has been set to reproduce the excitation energy.

The responses obtained with the larger configuration space are slightly in better agreement with experimental data. The positions of the maxima of the transition density are located at a smaller r value than the experimental peak position. The value of the maxima of the transition density is underestimated in the calculation with 44 states and overestimated in the other case.

The main ph pairs that contribute to this excitation and their X and Y amplitudes are given in Tabs. 3.9 and 3.10

3^- (6.13 MeV)		LM		$LMtt$		FR		$FRtt$	
ω		6.14		6.14		6.14		6.13	
transition	ϵ_p -ϵ_h	X	Y	X	Y	X	Y	X	Y
$[(1d_{5/2})(1p_{3/2})^{-1}]_\pi$	17.84	-0.29	0.14	0.29	-0.14	0.28	-0.14	0.28	-0.14
$[(1d_{5/2})(1p_{1/2})^{-1}]_\pi$	11.51	-0.67	0.01	0.67	-0.21	0.68	-0.21	0.68	-0.21
$[(2d_{3/2})(1p_{3/2})^{-1}]_\pi$	21.31	0.22	-0.12	-0.22	0.12	-0.22	0.12	-0.22	0.12
$[(1d_{5/2})(1p_{3/2})^{-1}]_\nu$	17.67	0.28	-0.14	-0.28	0.14	-0.28	0.13	-0.28	0.13
$[(1d_{5/2})(1p_{1/2})^{-1}]_\nu$	11.51	0.66	-0.20	-0.66	0.20	-0.65	0.20	-0.65	0.20
$[(1d_{3/2})(1p_{3/2})^{-1}]_\nu$	21.47	-0.24	0.13	0.24	-0.13	0.23	-0.13	0.23	-0.13

Table 3.9: Main ph pairs for the lowest 3^- states and their X and Y amplitudes calculated with the four interactions with a configuration space of 44 states. We adopt the convention of indicating with π the proton ph pairs and with ν the neutron ones.

3^- (6.13 MeV)		LM		$LMtt$		FR		$FRtt$	
ω		6.14		6.14		6.14		6.13	
transition	ϵ_p -ϵ_h	X	Y	X	Y	X	Y	X	Y
$[(1d_{5/2})(1p_{3/2})^{-1}]_\pi$	17.84	-0.28	0.14	0.28	-0.14	0.28	-0.14	0.28	-0.14
$[(1d_{5/2})(1p_{1/2})^{-1}]_\pi$	11.51	-0.67	0.01	0.67	-0.21	0.68	-0.21	0.68	-0.21
$[(2d_{3/2})(1p_{3/2})^{-1}]_\pi$	21.31	0.22	-0.12	-0.22	0.12	-0.22	0.13	-0.22	0.13
$[(1d_{5/2})(1p_{3/2})^{-1}]_\nu$	17.67	0.28	-0.14	-0.28	0.14	-0.27	0.13	-0.27	0.13
$[(1d_{5/2})(1p_{1/2})^{-1}]_\nu$	11.51	0.65	-0.20	-0.65	0.20	-0.65	0.20	-0.65	0.20
$[(1d_{3/2})(1p_{3/2})^{-1}]_\nu$	21.47	-0.24	0.13	0.24	-0.13	0.23	-0.13	0.23	-0.13

Table 3.10: Main ph pairs for the lowest 3^- states and their X and Y amplitudes calculated with the four interactions with a configuration space of 100 states.

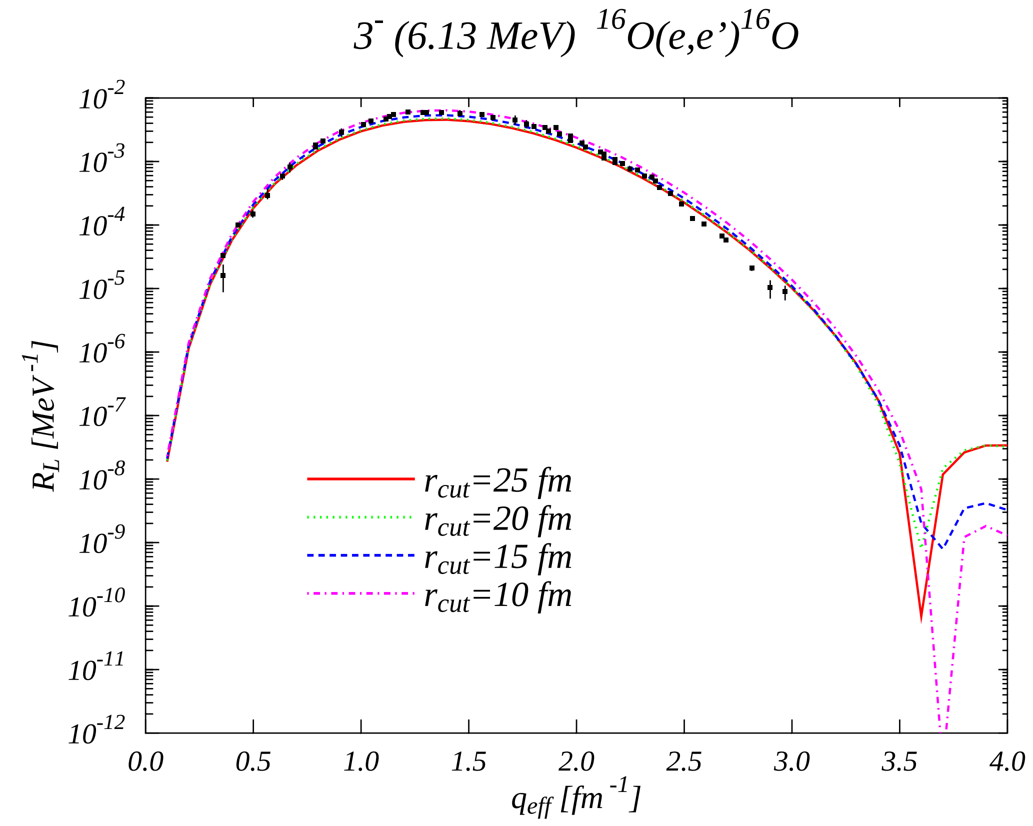

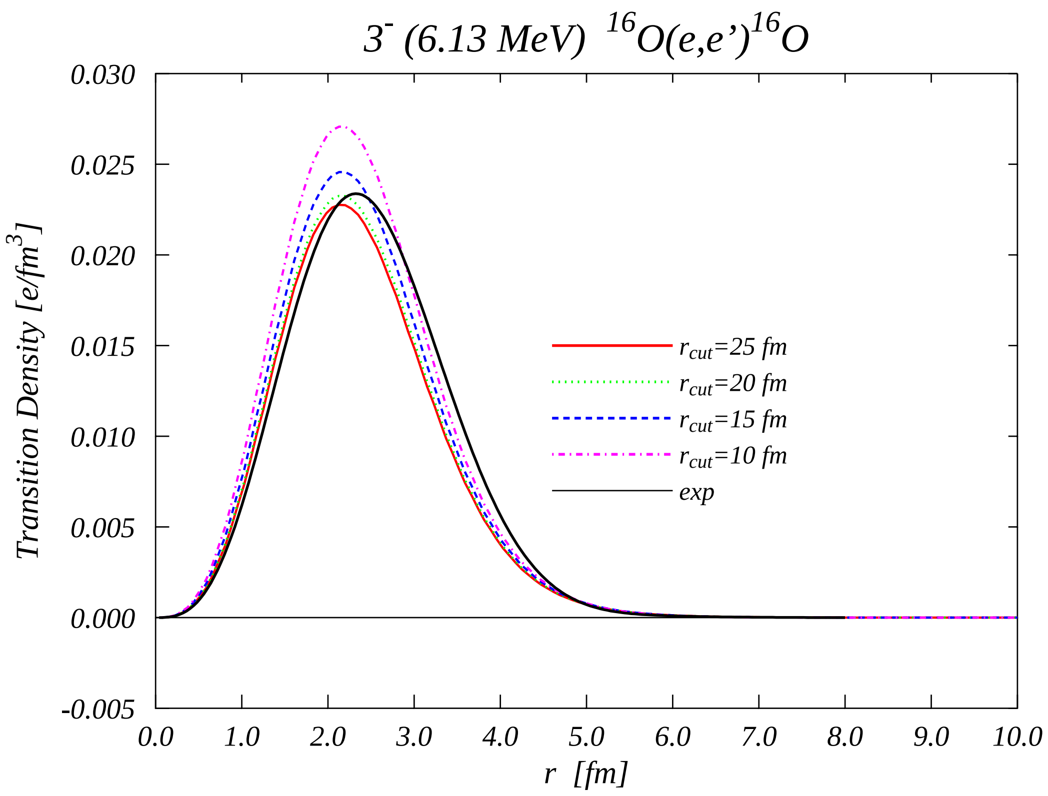

Figure 3.12: Longitudinal response and transition density for the low excited 3^- state of ^{16}O. Experimental data from [52].

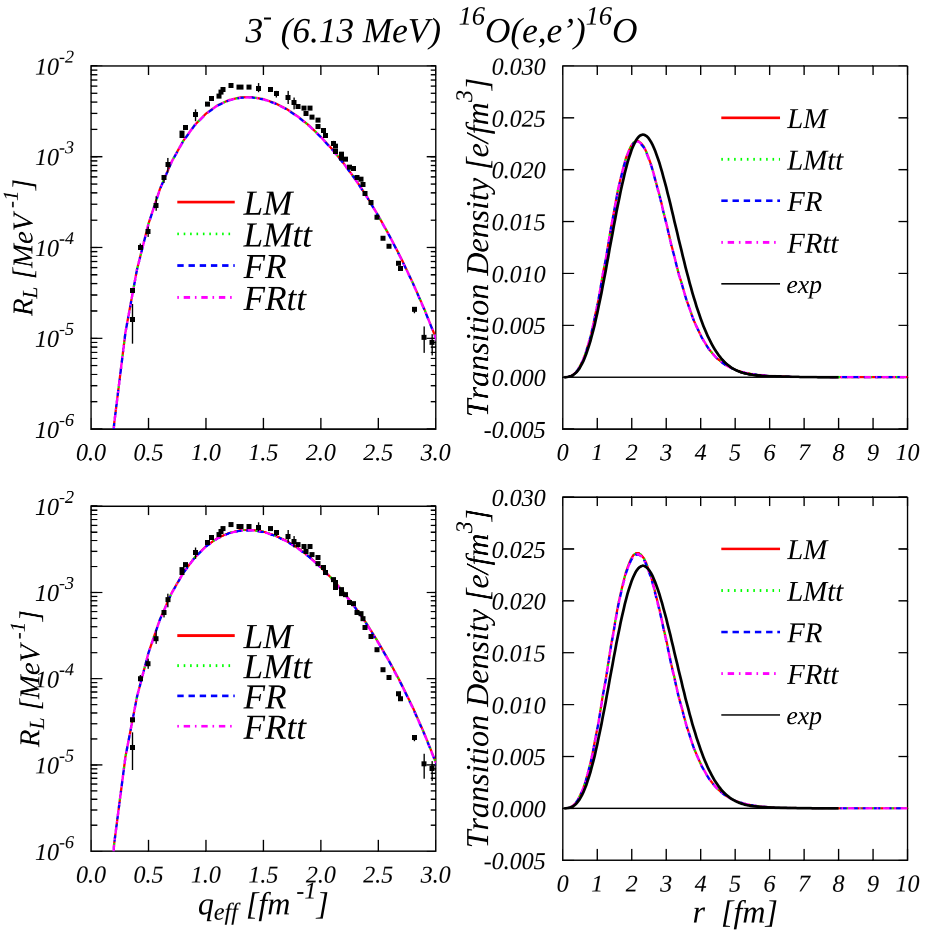

Figure 3.13: Longitudinal response and transition density for the low excited 3^- state of ^{16}O. In the upper panels we show the case of 44 states, in the lower the case of 100 states. Experimental data from [52].

We study now the spectrum related to the positive parity excitations. We show in Tab. 3.11 the energies of the first 0^+, 2^+ and 4^+ states calculated for different values of r_{cut} by using the LM interactions already used for the 3^- calculations of Tab. 3.8. The table shows that we obtain excitation energies above $10 MeV$. This is understandable in our computational scheme since particle and hole states must have the same parity, therefore the ph transition is done between HO major shells separated by $1\hbar\omega$, which have opposite parity. The table does not present any convergence of the results. This happens because the ph pairs dominating the transition are unbound.

To discuss this point further, we consider as an example the longitudinal response of the 0^+ state, and its transition densities, shown in Fig. 3.14. The various results presented in the figure have been obtained by using different values of r_{cut}. There is no indication of convergence in the two quantities shown in the figure. The main ph transitions are the $(2p_{1/2})(1p_{1/2})^{-1}$ for both protons and neutrons. We show in Fig. 3.15 the s.p. wave function of the $2p_{1/2}$ state for various values of r_{cut}. The different shape of this s.p. wave function clearly explains the instability of the result.

r_{cut}	0^+	2^+	4^+
10	17.99	17.31	18.58
15	15.15	15.08	17.39
20	14.05	14.04	15.38
25	13.68	13.67	14.65

Table 3.11: Energies in MeV of the 0^+, 2^+ and 4^+ levels of ^{16}O for different values of r_{cut}. The results have been obtained with the interaction used to obtain the results of Tab. 3.8.

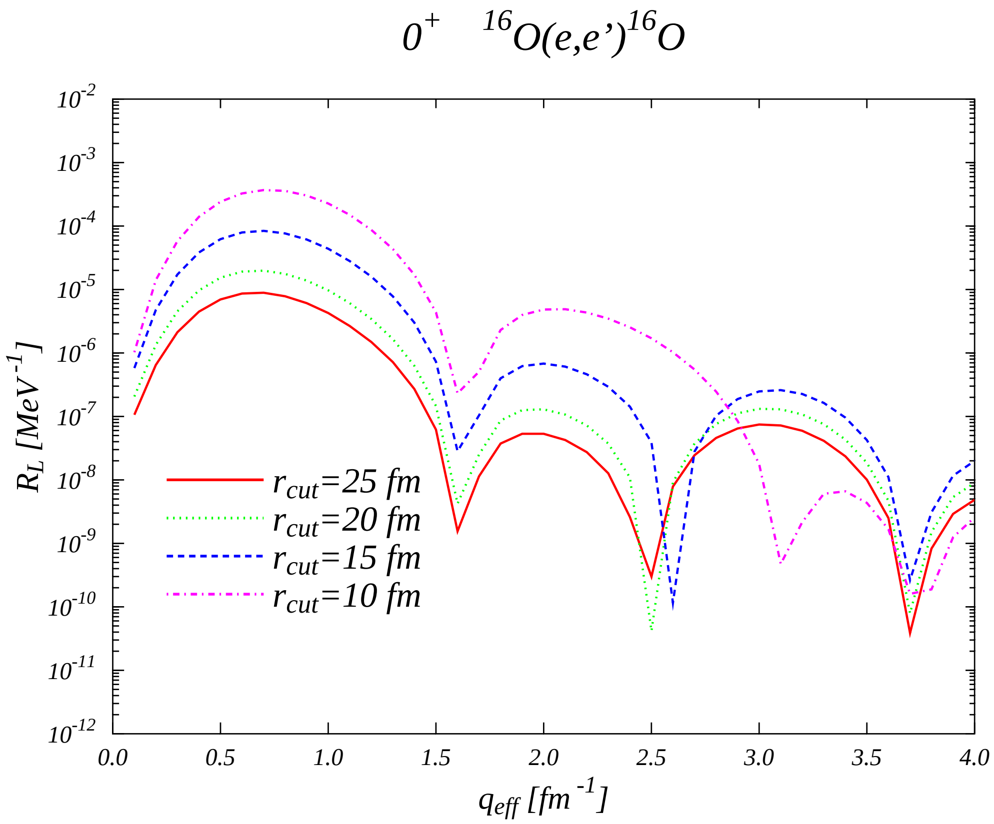

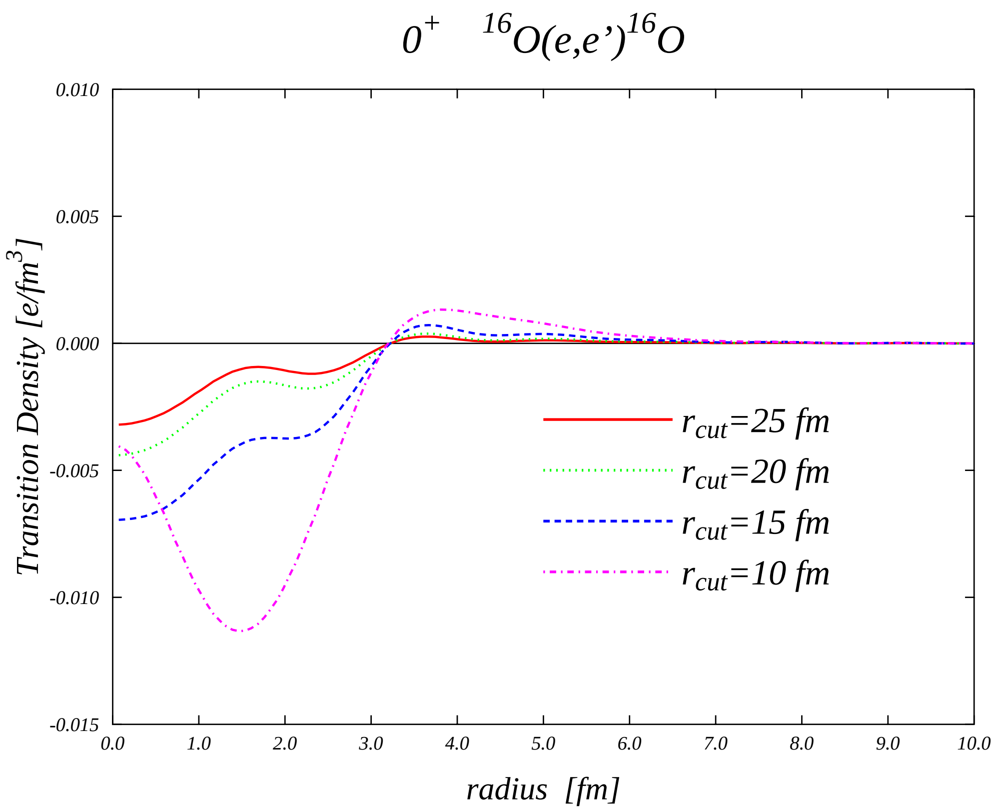

Figure 3.14: Longitudinal response and transition density for the excited state 0^+ of ^{16}O varying r_{cut}.

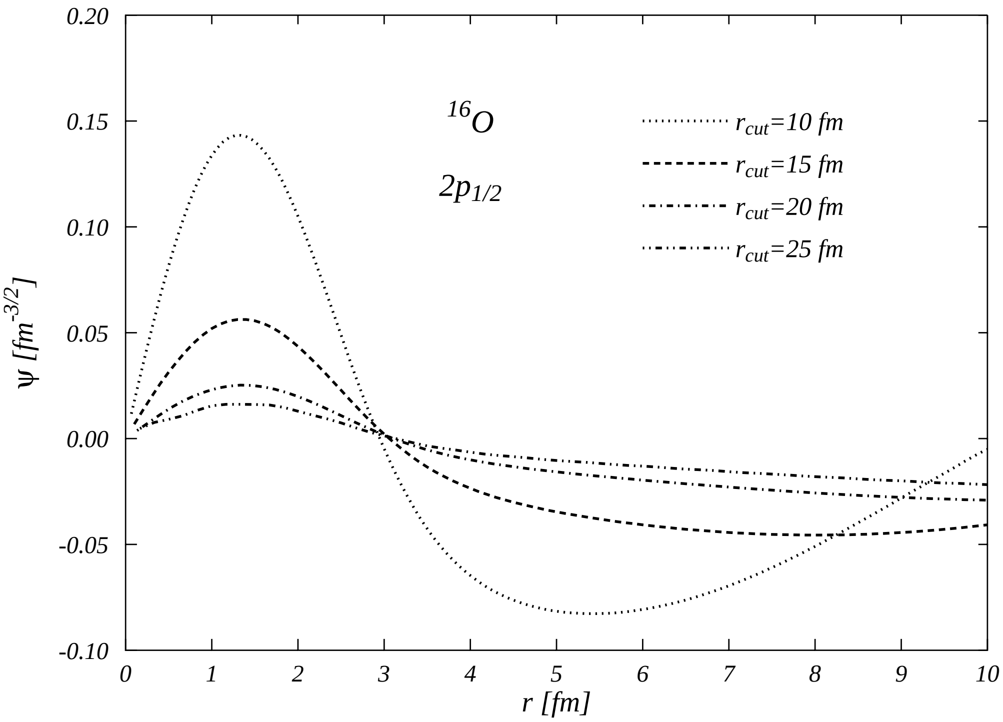

Figure 3.15: The $2p_{1/2}$ s.p. wave function obtained using different value of r_{cut} for ^{16}O.

The analysis done shows that only the excitation states where the particle is in a bound state can be described by these techniques. A state dominated by excitations in the continuum is greatly dependent on parameters as the configuration space, the number of expansion coefficients on harmonic oscillator and the radial distance r_{cut}.

We study now the negative parity states of the spectrum. In this case the change of parity allows ph excitations in the HO major shell just above the Fermi surface, where bound particle levels are present. In the following we consider states dominated by bound ph pairs. In the ^{16}O spectrum the first negative parity state, above the 3^-, is a 2^- excitation experimentally found at 8.87 MeV. We show in Tab.3.12 the main ph pairs and the X and Y amplitudes obtained for the four interactions under investigation.

2^- (8.87 MeV)		LM		$LMtt$		FR		$FRtt$	
ω		11.80		11.80		11.51		11.51	
transition	ϵ_p -ϵ_h	X	Y	X	Y	X	Y	X	Y
$[(1d_{5/2})(1p_{1/2})^{-1}]_\pi$	17.84	0.72	-0.01	0.72	-0.01	0.71	0.00	0.71	0.00
$[(1d_{5/2})(1p_{1/2})^{-1}]_\nu$	11.51	-0.69	0.01	-0.69	0.01	-0.70	0.00	-0.70	0.00

Table 3.12: Main ph pairs for the lowest 2^- states and their X and Y amplitudes calculated with the four interactions.

We observe that in all our calculations the excitation is dominated by the $(1d_{5/2})(1p_{1/2})^{-1}$ pair. We found excitation energies above $11 MeV$ rather close to the MF ph value. This indicates that in our calculations the residual interaction does not produce strong effects.

We show in Fig. 3.16 the transverse responses of this magnetic state and we compare them with the data of Ref. [53].

There is no agreement between the experimental response and the results of our calculations which are almost independent from the residual interaction.

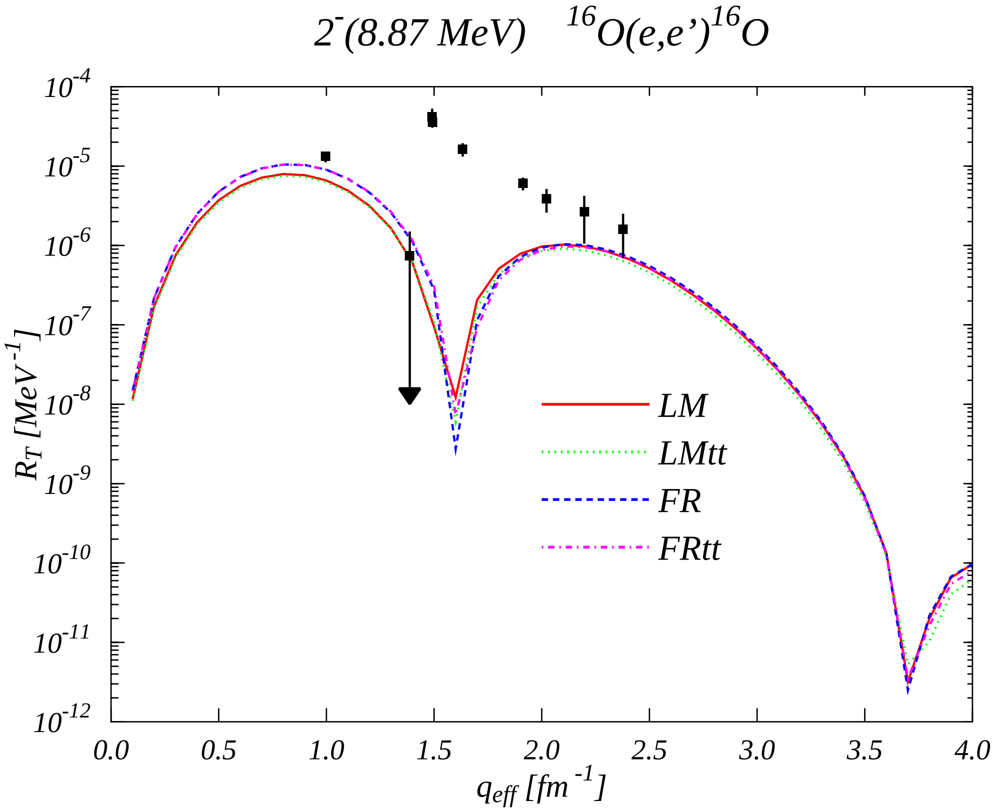

Figure 3.16: Transverse response for 2^- excited state in ^{16}O calculated with the different interactions used in our work. Experimental data from [53].

We repeated this type of investigation also for the two 4^- states at 17.79 and 18.98 MeV. We show in Tab.3.13 the main ph pairs and their X and Y amplitudes, and in Fig. 3.17 we compare the transverse responses with the data of Ref. [53].

The two states are dominated by the same ph pairs with analogous values of the X and Y amplitudes, the difference being in their relative phase: they belong to an isospin doublet, the lower energy state being of isoscalar nature and the higher energy state of isovector nature.

The agreement with experimental responses is much more satisfactory than that of the 2^- state. Also in this case we do not observe a remarkable sensitivity of the results to the details of the interaction.

4^- (17.79 MeV)		LM		$LMtt$		FR		$FRtt$	
ω		18.15		18.15		17.75		17.73	
transition	ϵ_p -ϵ_h	X	Y	X	Y	X	Y	X	Y
$[(1d_{5/2})(1p_{3/2})^{-1}]_\pi$	17.84	-0.70	-0.01	0.72	-0.01	0.71	0.00	0.71	0.00
$[(1d_{5/2})(1p_{3/2})^{-1}]_\nu$	17.67	0.71	0.01	-0.69	0.01	-0.70	0.00	-0.70	0.00
4^- (18.98 MeV)		LM		$LMtt$		FR		$FRtt$	
ω		21.41		20.59		19.88		19.45	
transition	ϵ_p -ϵ_h	X	Y	X	Y	X	Y	X	Y
$[(1d_{5/2})(1p_{3/2})^{-1}]_\pi$	17.84	-0.71	0.06	0.65	-0.05	0.72	0.04	0.74	-0.03
$[(1d_{5/2})(1p_{3/2})^{-1}]_\nu$	17.67	-0.70	0.07	0.63	-0.05	-0.68	0.04	0.68	-0.03

Table 3.13: Main ph pairs for the lowest 4^- states and their X and Y amplitudes calculated with the four interactions.

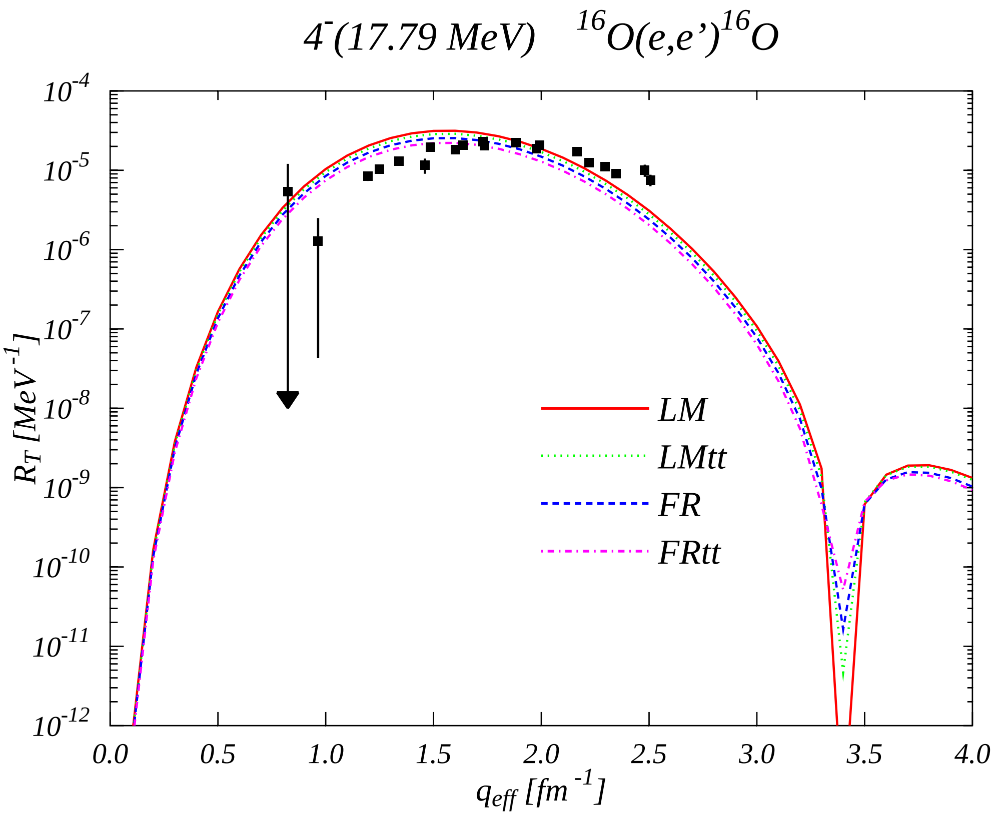

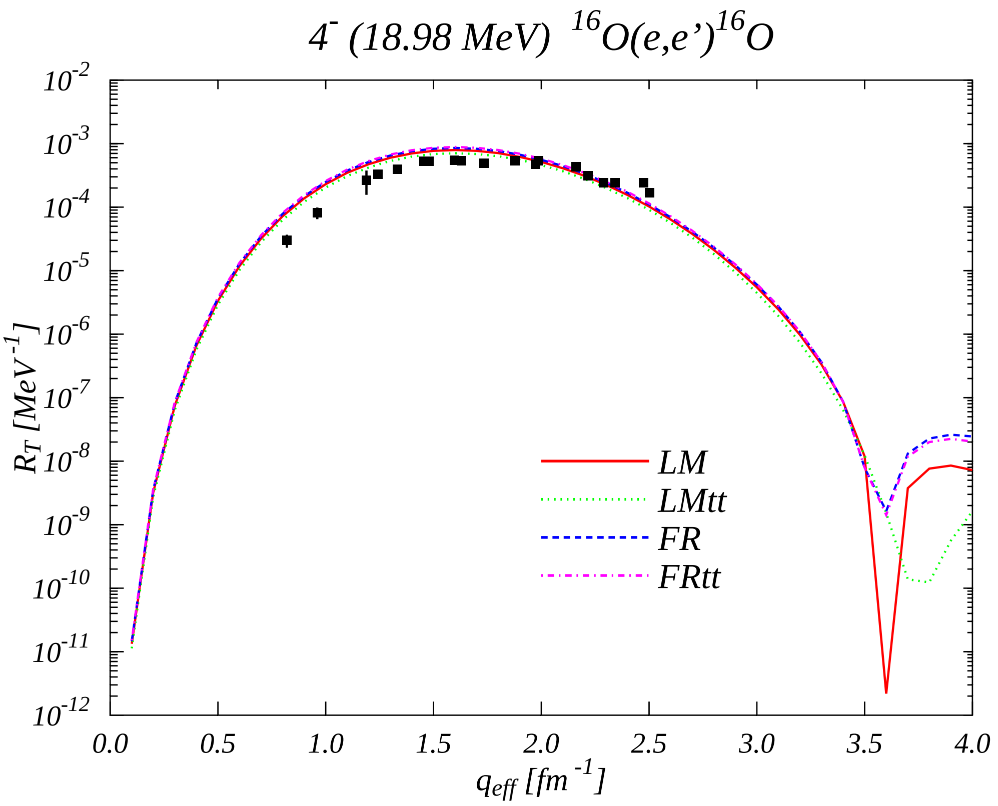

Figure 3.17: Transverse responses for the first two 4^- excited states in ^{16}O calculated with the different interactions used in our work. Experimental data from [53].

The situation changes for the 0^- states. We show in Tab. 3.14 the main ph pairs and the XY amplitudes. The table shows large sensitivity to the tensor term of 0^- excited state.

0^- (10.96 MeV)		LM		$LMtt$		FR		$FRtt$	
ω		12.33		11.19		12.15		11.84	
transition	ϵ_p -ϵ_h	X	Y	X	Y	X	Y	X	Y
$[(2s_{1/2})(1p_{1/2})^{-1}]_\pi$	12.01	-0.81	0.01	0.79	0.03	0.84	0.00	0.96	0.01
$[(2s_{1/2})(1p_{1/2})^{-1}]_\nu$	12.38	0.58	0.00	0.61	0.03	-0.54	0.00	0.27	0.01
0^- (12.80 MeV)		LM		$LMtt$		FR		$FRtt$	
ω				12.39		13.13		12.23	
transition	ϵ_p -ϵ_h	X	Y	X	Y	X	Y	X	Y
$[(2s_{1/2})(1p_{1/2})^{-1}]_\pi$	12.01			-0.61	0.01	0.51	-0.02	0.27	0.00
$[(2s_{1/2})(1p_{1/2})^{-1}]_\nu$	12.38			0.79	0.00	0.81	-0.02	-0.96	0.00

Table 3.14: Main ph pairs for the lowest 0^- states and their X and Y amplitudes calculated with the four interactions.

The second 0^- state isn't reproduced by LM interaction because in this case this excitation is dominated by excitation of a particle in continuum (Tab. 3.15).

0^- (12.80 MeV)		LM	
ω		13.47	
transition	ϵ_p -ϵ_h	X	Y
$[(2s_{1/2})(1p_{1/2})^{-1}]_\pi$	12.01	0.21	-0.01
$[(3s_{1/2})(1p_{1/2})^{-1}]_\pi$	13.54	-0.90	0.00
$[(2s_{1/2})(1p_{1/2})^{-1}]_\nu$	12.38	0.36	-0.01

Table 3.15: Main ph pairs for the second 0^- state and their X and Y amplitudes obtained with LM interaction.

The 0^- cannot be excited by electromagnetic probes, at least in the one-photon exchange picture. For this reason we calculated the neutral current (ν, ν') and ($\overline{\nu}$, $\overline{\nu}'$) cross sections [54, 55] which are shown in Fig. 3.18 as a function of the neutrino energy.

In this case the presence of the tensor term produces large differences in the results. The neutrino, and antineutrino, cross sections are enhanced in the excitation of the first 0^- state. The situation is reversed for the other state.

.

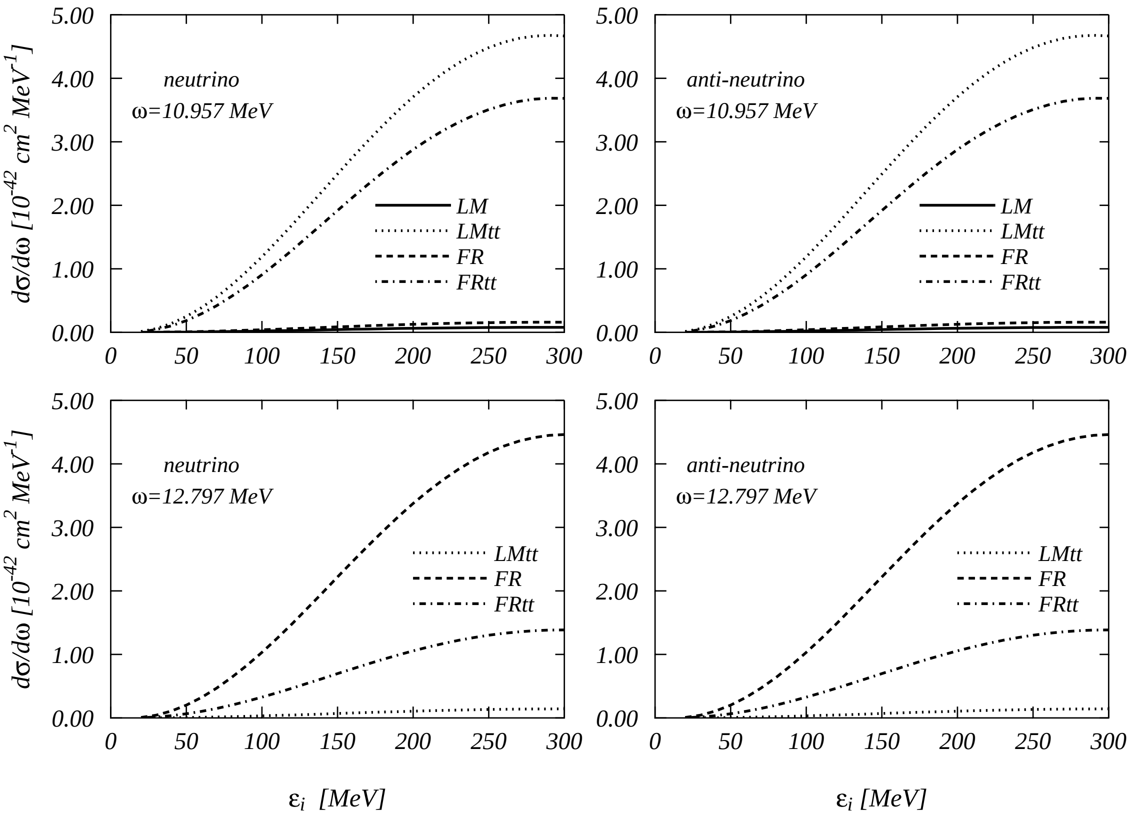

Figure 3.18: Cross sections of neutrino and anti-neutrino for the two 0^- states of ^{16}O as a function of the incoming lepton energy ε_i.

3.3.2 The ^{12}C nucleus

With the parameterizations described in the previous section, we obtain, for ^{12}C nucleus the spectrum presented in Tab. 3.16 and Fig. 3.19

^{12}C					
excitation	LM	LMtt	FR	FRtt	exp
2^+	4.41	4.41	4.46	4.47	4.44
3^-	11.51	11.51	11.83	11.83	9.64
1^-	15.00	15.00	15.54	15.55	10.84
2^-	16.26	16.20	16.07	16.03	11.83
1^+	14.41	14.41	13.89	13.87	12.71
2^-	—	17.26	17.23	17.14	13.35
1^+	18.13	17.97	18.17	18.05	15.11
4^-	18.21	18.21	17.78	17.75	18.27
4^-	21.70	20.80	19.92	19.49	19.50

Table 3.16: Low excited states in ^{12}C. The energies are expressed in MeV. The experimental values are taken from [40].

From the spectra of ^{12}C we observe that the experimental energies are always smaller than the theoretical ones. The presence of the tensor force does not change significatively the spectrum.

As electric states we consider the case of 2^+ and 3^- excitations. The main contribute to these excitations are given in Tabs. 3.17 and 3.18.

2^+ (4.44 MeV)		LM		$LMtt$		FR		$FRtt$	
ω		4.41		4.41		4.46		4.47	
transition	ϵ_p -ϵ_h	X	Y	X	Y	X	Y	X	Y
$[(1p_{1/2})(1p_{3/2})^{-1}]_\pi$	14.02	0.80	0.43	0.80	0.43	0.80	0.41	-0.80	-0.41
$[(1d_{5/2})(1s_{1/2})^{-1}]_\pi$	32.90	-0.25	-0.19	-0.25	-0.19	0.24	0.18	0.42	0.18
$[(2d_{3/2})(1s_{1/2})^{-1}]_\pi$	34.02	0.15	0.11	0.15	0.11	0.15	0.11	-0.15	-0.11
$[(1p_{1/2})(1p_{3/2})^{-1}]_\nu$	13.76	-0.80	-0.42	-0.80	-0.42	-0.79	-0.40	0.79	0.40
$[(1d_{5/2})(1s_{1/2})^{-1}]_\nu$	32.94	-0.25	-0.19	-0.25	-0.19	-0.24	-0.18	0.24	0.18
$[(2d_{3/2})(1s_{1/2})^{-1}]_\nu$	35.99	0.13	0.10	0.13	0.10	0.13	0.10	-0.13	-0.10

Table 3.17: Main ph pairs for the first 2^+ state and their X and Y amplitudes calculated with the four interactions.

In Fig. 3.20 we show the longitudinal and transverse responses for both the excitations. We observe that these states are insensitive to the differences between the interactions.

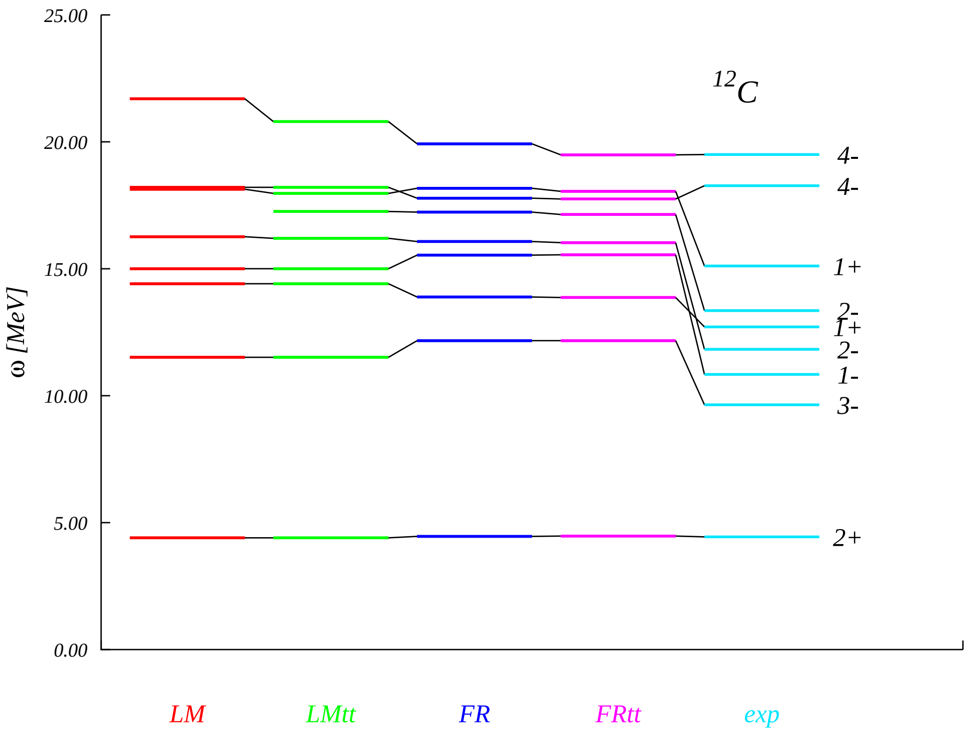

Figure 3.19: ^{12}C spectrum

3^- (9.64 MeV)		LM		$LMtt$		FR		$FRtt$	
ω		11.51		11.51		12.17		12.17	
transition	ϵ_p -ϵ_h	X	Y	X	Y	X	Y	X	Y
$[(1d_{5/2})(1p_{3/2})^{-1}]_\pi$	17.96	0.57	-0.12	-0.57	0.12	-0.57	0.11	0.57	-0.11
$[(2d_{3/2})(1p_{3/2})^{-1}]_\pi$	19.08	-0.45	0.11	0.45	-0.11	0.45	-0.10	-0.45	0.10
$[(1d_{5/2})(1p_{3/2})^{-1}]_\nu$	17.62	-0.59	0.12	0.59	-0.12	0.59	-0.11	-0.59	0.10
$[(1d_{3/2})(1p_{3/2})^{-1}]_\nu$	20.32	0.17	-0.05	-0.17	0.05	-0.17	0.04	0.17	-0.04
$[(2d_{3/2})(1p_{3/2})^{-1}]_\nu$	20.67	0.36	-0.10	-0.36	0.10	0.35	0.09	0.35	-0.09

Table 3.18: Main ph pairs for the first 3^- state and their X and Y amplitudes calculated with the four interactions.

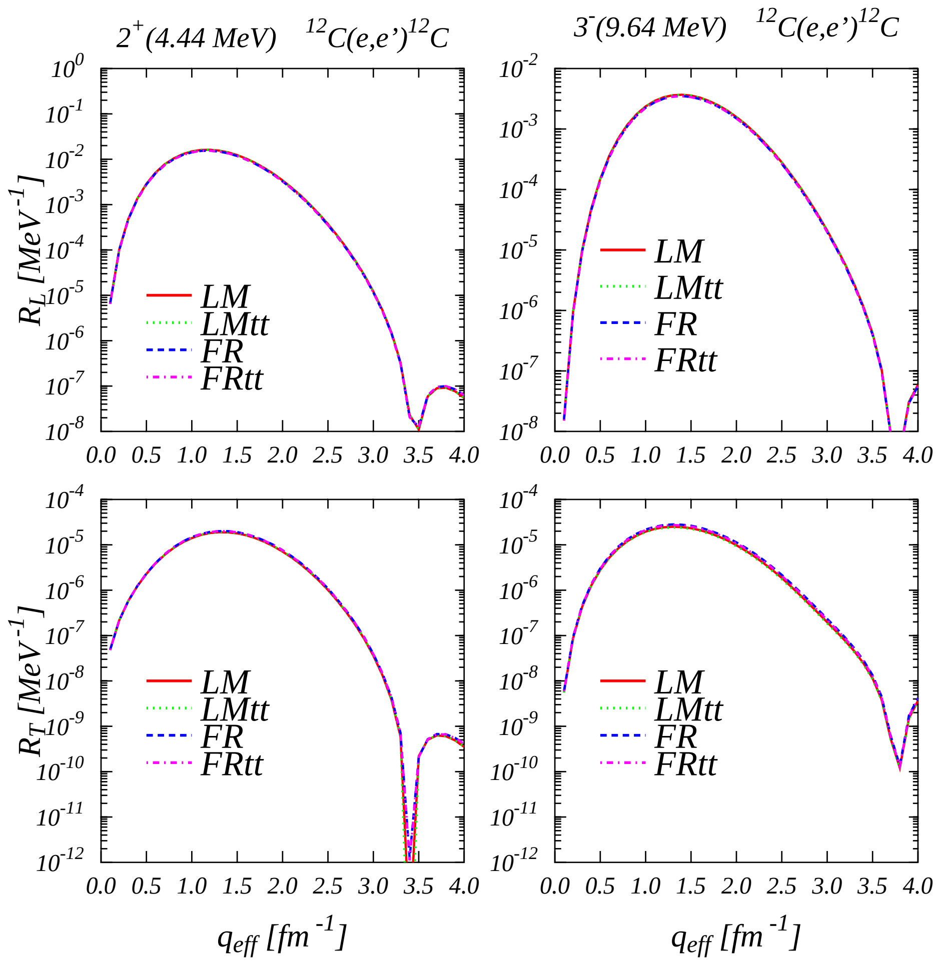

Figure 3.20: Longitudinal and transverse responses for the 2^+ and 3^- excited states in ^{12}C calculated with the different interactions used in our work.

We analyze in detail some unnatural parity states, whose properties have been measured. A first interesting case is given by the 4^- states. A strong peak is observed in electron scattering data at 19.5 MeV and several theoretical calculations predict a very strong isovector 4^- state in this energy region, dominated by $[(1d_{5/2})(1p_{3/2}){-1}]$ excitations [56].

Inelastic pion scattering measurements show a pair of isospin mixed states in the same region.

In our calculations we find two states, isoscalar and isovector, respectively, whose excitation energies are presented in table. 3.19 together with the values of X and Y amplitudes of the relevant ph pairs.

As in the case of the 4^- state in ^{16}O also these states form an isospin doublet. We compare in Fig. 3.21 our results with the experimental data [56].
The agreement with the measured points is remarkable. The results are rather insensitive to the residual interaction for the isovector state. The situation is slightly different for the isoscalar case where we show in Fig. 3.21 that the presence of the tensor term and of the finite range contributes to lower the value of the transverse response.

4^- (18.27 MeV)		LM		$LMtt$		FR		$FRtt$	
ω		18.21		18.21		17.78		17.75	
transition	ϵ_p -ϵ_h	X	Y	X	Y	X	Y	X	Y
$[(1d_{5/2})(1p_{3/2})^{-1}]_\pi$	17.96	0.68	0.00	0.67	0.00	0.66	0.00	0.64	0.00
$[(1d_{5/2})(1p_{3/2})^{-1}]_\nu$	17.62	-0.71	0.01	-0.74	0.01	-0.04	-0.00	-0.76	0.00
4^- (19.50 MeV)		LM		$LMtt$		FR		$FRtt$	
ω		21.70		20.80		19.92		19.49	
transition	ϵ_p -ϵ_h	X	Y	X	Y	X	Y	X	Y
$[(1d_{5/2})(1p_{3/2})^{-1}]_\pi$	17.96	-0.72	0.07	0.72	-0.05	-071	0.04	-0.76	0.03
$[(1d_{5/2})(1p_{3/2})^{-1}]_\nu$	17.62	-0.69	0.07	0.67	-0.05	-0.62	0.04	-0.64	0.03

Table 3.19: Main ph pairs for the lowest 4^- states and their X and Y amplitudes calculated with the four interactions.

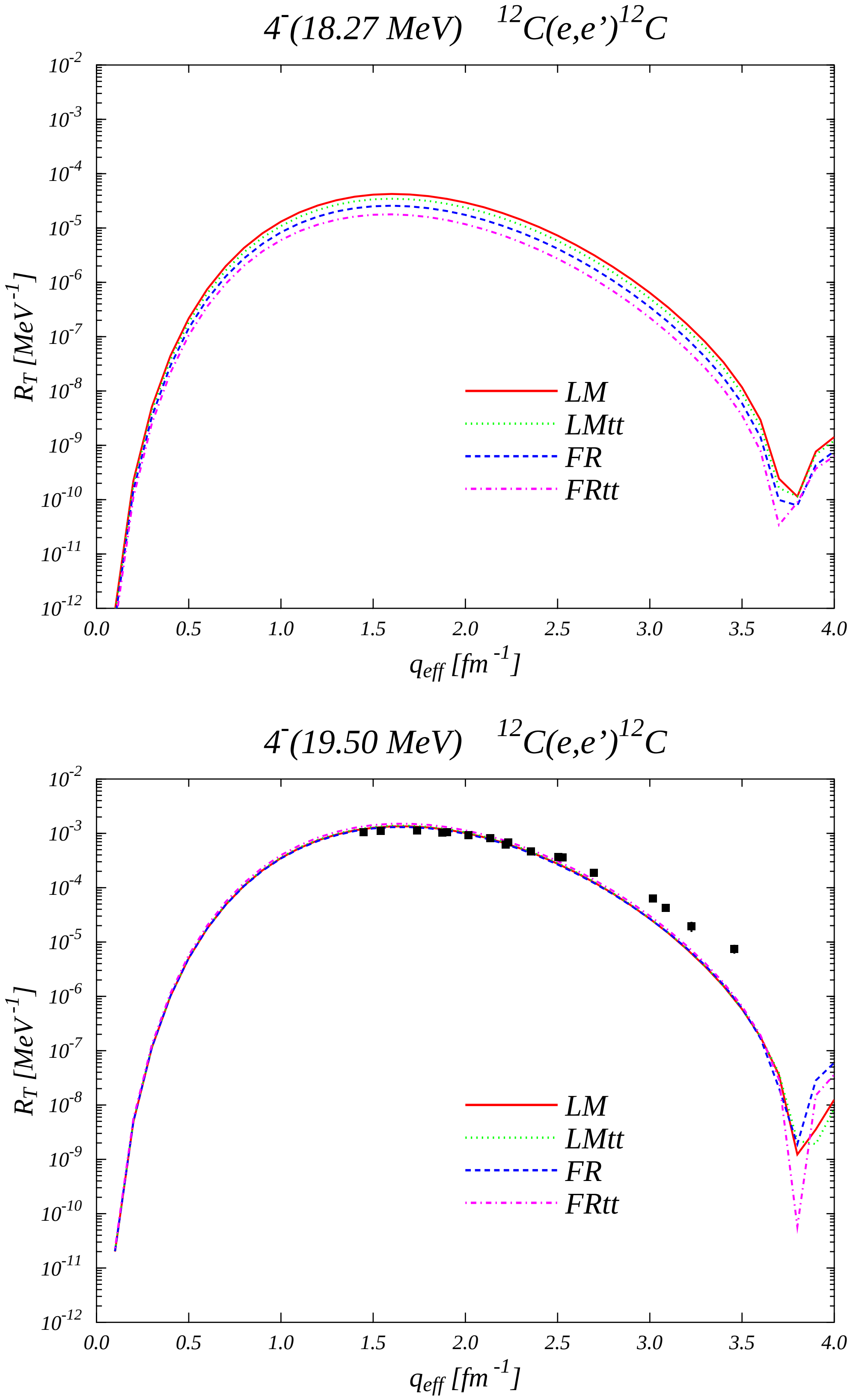

Figure 3.21: Transverse response for the two first 4^- excited state in ^{12}C calculated with the different interactions used in our work. Experimental data from [56].

The description of the 2^- states is less satisfactory. With all the residual interactions considered we find a first state, dominated by $[(2s_{1/2})(1p_{3/2})^{-1}]$ pairs, which we identify with the isoscalar state at 11.83 MeV. However, in all cases the curves we obtain for the transverse form-factor do not reproduce the experimental data, nor in magnitude neither as far as their q-dependence is concerned.

2^- (11.83 MeV)		LM		$LMtt$		FR		$FRtt$	
ω		16.26		16.20		16.07		16.03	
transition	ϵ_p -ϵ_h	X	Y	X	Y	X	Y	X	Y
$[(2s_{1/2})(1p_{3/2})^{-1}]_\pi$	15.85	-0.92	0.01	-0.95	0.01	0.95	0.00	0.96	0.00
$[(3s_{1/2})(1p_{3/2})^{-1}]_\pi$	17.36	-0.12	0.00	-0.10	0.00	-0.06	0.00	0.05	0.00
$[(2s_{1/2})(1p_{3/2})^{-1}]_\nu$	16.86	0.37	0.01	0.27	0.00	-0.29	0.00	-0.24	-0.01
2^- (13.35 MeV)		LM		$LMtt$		FR		$FRtt$	
ω				17.26		17.23		17.14	
transition	ϵ_p -ϵ_h	X	Y	X	Y	X	Y	X	Y
$[(1d_{5/2})(1p_{3/2})^{-1}]_\pi$	17.96			0.14	0.00	-0.03	0.00	-0.10	0.00
$[(2s_{1/2})(1p_{3/2})^{-1}]_\pi$	15.85			-0.11	0.00	0.18	-0.01	0.18	-0.01
$[(2d_{3/2})(1p_{3/2})^{-1}]_\pi$	19.08			-0.17	0.00	0.00	0.00	0.09	0.00
$[(3s_{1/2})(1p_{3/2})^{-1}]_\pi$	17.37			-0.52	0.00	0.67	0.00	0.37	0.00
$[(1d_{5/2})(1p_{3/2})^{-1}]_\nu$	17.62			0.25	0.00	-0.04	-0.00	-0.17	0.00
$[(2s_{1/2})(1p_{3/2})^{-1}]_\nu$	16.86			-0.76	0.01	0.71	-0.01	0.88	0.00

Table 3.20: Main ph pairs for the lowest 2^- states and their X and Y amplitudes calculated with LMtt, FR and FRtt interactions.

2^- (13.35 MeV)		LM	
ω		17.33	
transition	ϵ_p -ϵ_h	X	Y
$[(3s_{1/2})(1p_{3/2})^{-1}]_\pi$	17.37	0.90	0.00
$[(2s_{1/2})(1p_{1/2})^{-1}]_\nu$	16.86	0.43	0.00

Table 3.21: Main ph pairs for the second 2^- state and their X and Y amplitudes obtained with LM interaction.

For the LMtt, FR and FRtt interaction we find a second 2^- state at the energies reported in table 3.20; this is not reproduced by the LM interaction, for which the second excited state is dominated by the excitation of a particle in the continuum (Tab. 3.21). It is not clear whether this state should be identified with the 2^- state at 13.35 MeV, for which the $J^p = 2^-$ assignment is uncertain, or with the isovector 2^- state at 16.58 MeV.

We thus conclude that the present discrete RPA calculations do not provide a reliable description of the 2^- state.

Let us now turn our attention to the doublet of 1^+ states, observed at 12.71 MeV (T=0) and 15.11 (T=1), which are among the most studied and better experimentally estabilished states for ^{12}C.

In all our calculations we find a lowest state which is isoscalar, its main ph contributions come, as expected, from $[(1p_{1/2})(1p_{3/2})^{-1}]$ pairs. The corresponding values of the X, Y amplitudes are shown in table 3.22.

The values of the energy have already been reported in Table 3.22 and they all exceed the experimental value by 9-13%.

The corresponding transverse form factor is shown in Fig. 3.22, where we can see that both the values and the q-dependence of the experimental data are well reproduced, with the exception of the two experimental points at the center of the second peak. The form factor exhibits only a weak dependence on the choice of the residual interaction at small values of q, where the finite range and LM interactions give slightly different results, while there is practically no sensitivity to the inclusion of the tensor part.

1^+ (12.71 MeV)		LM		$LMtt$		FR		$FRtt$	
ω		14.41		14.41		13.89		13.87	
transition	ϵ_p -ϵ_h	X	Y	X	Y	X	Y	X	Y
$[(1p_{1/2})(1p_{3/2})^{-1}]_\pi$	14.02	-0.69	-0.01	-0.69	-0.01	0.69	0.00	-0.69	0.00
$[(1p_{1/2})(1p_{3/2})^{-1}]_\nu$	13.76	0.72	0.02	0.73	0.02	-0.72	0.00	0.72	0.00

Table 3.22: Main ph pairs for the lowest 1^+ states and their X and Y amplitudes calculated with the four interactions for ^{12}C nucleus.

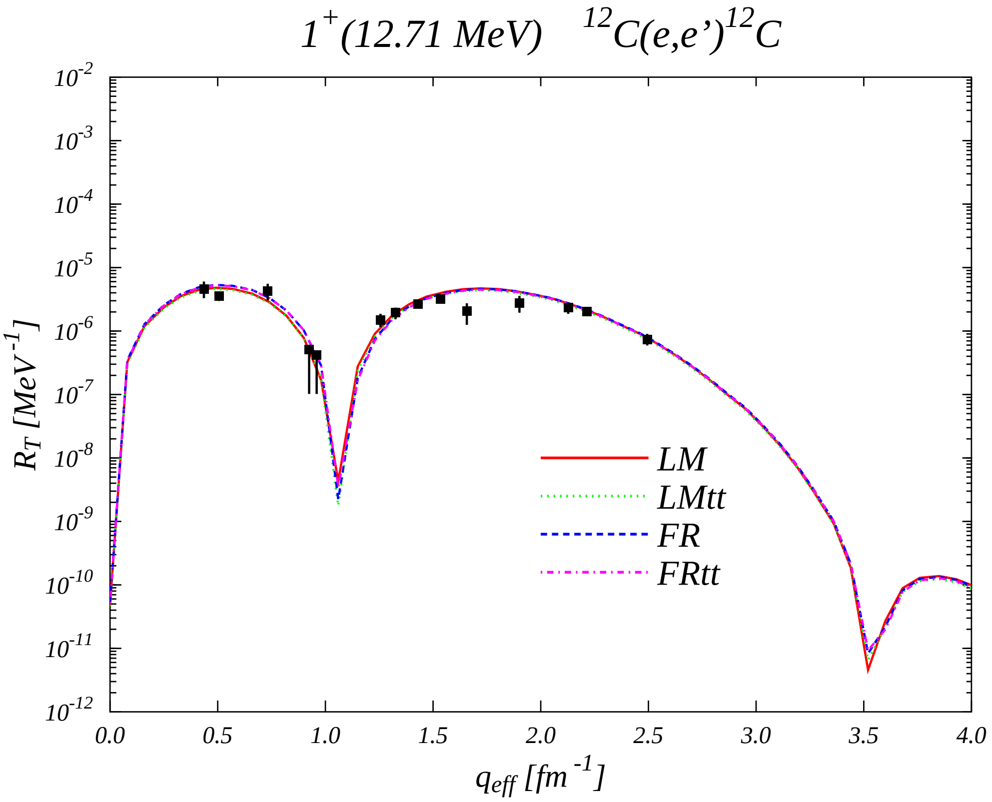

Figure 3.22: Transverse responses for the first 1^+ excited state in ^{12}C calculated with the different interactions used in our work. Experimental data from [53].

About the isovector state at 15.11 MeV for all interactions we don't find this state as the second state of the spectrum, but we first find some states dominated by ph pairs with the particle in the continuum. Although the state we identify as the T=1, 15.11 MeV state is clearly dominated by $[(1p_{1/2})(1p_{3/2})^{-1}]$ contributions, other ph pairs contribute with sizable values of the X amplitudes as reported in Tab. 3.23. The excitation energies we find exceed the experimental value by 18-20 %.

1^+ (15.11 MeV)		LM		$LMtt$		FR		$FRtt$	
ω		18.14		17.98		18.18		18.06	
transition	ϵ_p -ϵ_h	X	Y	X	Y	X	Y	X	Y
$[(1p_{1/2})(1p_{3/2})^{-1}]_\pi$	14.02	-0.66	-0.08	-0.65	-0.08	0.67	0.09	-0.66	-0.08
$[(2p_{3/2})(1p_{3/2})^{-1}]_\pi$	17.42	0.12	0.00	0.22	0.00	-0.12	0.00	0.16	0.00
$[(2p_{1/2})(1p_{3/2})^{-1}]_\pi$	17.43	0.14	0.00	0.15	0.00	-0.12	0.00	0.13	0.00
$[(3p_{3/2})(1p_{3/2})^{-1}]_\pi$	19.29	-0.22	0.01	-0.26	0.01	0.22	-0.01	-0.24	0.01
$[(3p_{1/2})(1p_{3/2})^{-1}]_\pi$	19.34	-0.23	0.01	-0.17	0.01	0.21	-0.01	-0.18	0.01
$[(1p_{1/2})(1p_{3/2})^{-1}]_\nu$	13.76	-0.63	-0.09	-0.61	-0.08	0.64	0.09	-0.63	-0.08
$[(2p_{3/2})(1p_{3/2})^{-1}]_\nu$	19.59	0.09	0.00	0.11	0.00	-0.09	0.00	0.10	0.00
$[(2p_{1/2})(1p_{3/2})^{-1}]_\nu$	19.60	-0.09	0.00	-0.07	0.00	0.08	0.00	-0.07	0.00
$[(3p_{3/2})(1p_{3/2})^{-1}]_\nu$	21.28	0.09	-0.01	0.13	-0.10	-0.09	0.01	0.11	-0.01
$[(3p_{1/2})(1p_{3/2})^{-1}]_\nu$	21.37	0.09	-0.01	0.07	-0.10	-0.09	0.01	0.08	-0.01

Table 3.23: Main ph pairs for the second 1^+ states and their X and Y amplitudes calculated with the four interactions for ^{12}C nucleus.

The transverse responses are shown in Fig. 3.23.

The q dependence of the transverse form factor is reproduced reasonably, all curves reproduce the second peak, but they overestimate the first one. The sensitivity to the choice of a zero-range or finite range interaction is rather small, on the other hand the form factor is sensitive to the inclusion of the tensor force, which has the effect of "pushing" the curves toward small q-values, improving the description of the region between the two peaks. The effects of the tensor force on the first peak go in the right direction, bringing the theoretical curves slightly closer to the data, but these changes are too small to get an agreement between theory and experiment.

3.3.3 The 1^+ isospin triplet for the $A = 12$ system

The isovector 1^+ state of ^{12}C at 15.11 is the member of a triplet which involves the 1^+ T=1 states of ^{12}B and ^{12}N, which are their ground states. We have calculated the first 1^+ states for ^{12}B and ^{12}N using the charge-changing discrete RPA formalism described in section 2.3.

The results are reported in Table 3.24

	LM	LMtt	FR	FRtt	exp
^{12}B	15.16	14.98	15.20	15.07	14.30
^{12}C	18.13	17.97	18.17	18.05	15.11
^{12}N	21.05	20.89	21.09	20.97	17.20

Table 3.24: First 1^+ states for ^{12}B and ^{12}N calculated with the four interactions.

As already observed for Carbon, also the energies of the Boron and Nitrogen states are overestimated. We observe however, that the correct sequence is obtained, with $E_B < E_C < E_N$, with a slightly larger splitting of the energy values than that observed experimentally.

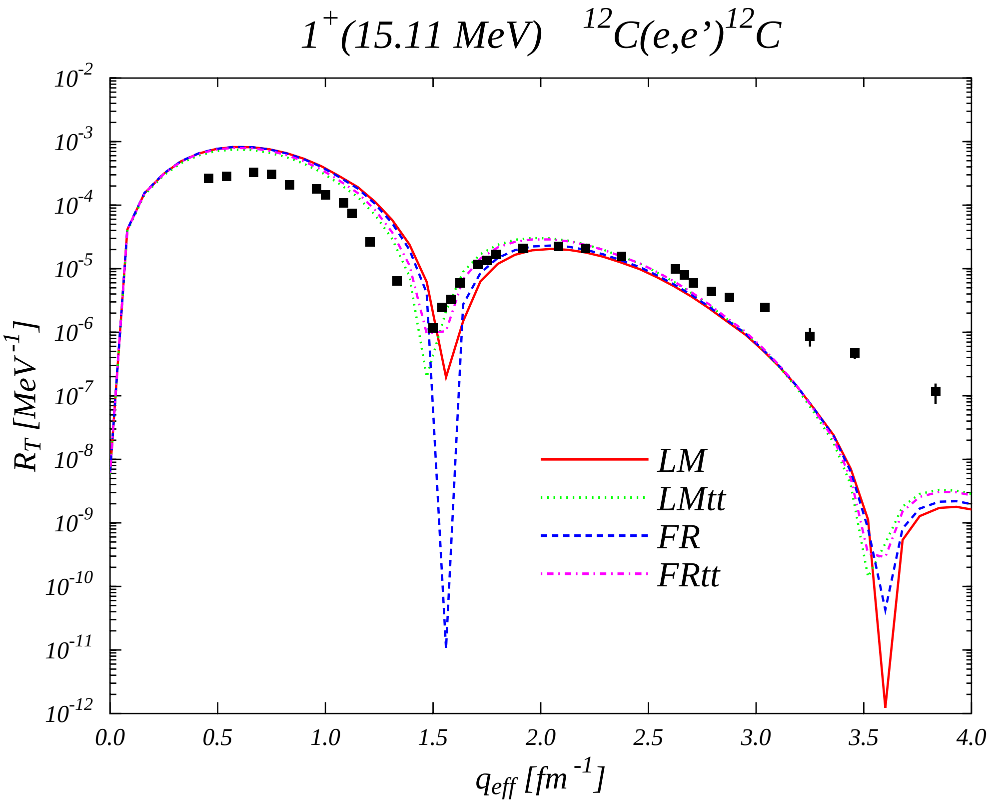

Figure 3.23: Transverse responses for the second 1^+ excited state in ^{12}C calculated with the different interactions used in our work. Experimental data from [53].

For ^{12}B we can clearly identify its 1^+ ground state, which is always the lowest energy state we find in our calculations. It is clearly dominated by a $[(1p_{1/2})_\nu(1p_{3/2})_\pi^{-1}]$ excitation, although non-negligible contributions come also from other ph pairs, as can be seen by the X,Y amplitude values of the most relevant contributions reported in table 3.25.

On the other hand, the description of the Nitrogen 1^+ state within our discrete RPA approach is less clear. For all the residual interactions considered the two lowest energy states we find are dominated by $[(2p_{3/2})_\pi(1p_{3/2})_\nu^{-1}]$ and $[(2p_{1/2})_\pi(1p_{3/2})_\nu^{-1}]$ pairs, having the particle state in the continuum. We identify as the "correct" 1^+ ^{12}N ground state the first state whose main ph contribution is the $[(1p_{1/2})(1p_{3/2})^{-1}]$. The values of the X,Y amplitudes contributing to this state are reported in table 3.26: we can see that there are sizable contributions also from $[(2p_{3/2})(1p_{1/2})]$ and $[(2p_{1/2})(1p_{3/2})]$ pairs. This is not unexpected, because analogous contributions for proton ph pairs are present also in the corresponding ^{12}C state, as we have shown in table 3.23.

1^+ (14.30 MeV)		*LM*		*LMtt*		*FR*		*FRtt*	
ω		15.16		14.98		15.20		15.07	
transition	ϵ_p -ϵ_h	X	Y	X	Y	X	Y	X	Y
$[(1p_{1/2})(1p_{3/2})^{-1}]_\pi$	11.00	0.98	0.15	-0.97	-0.15	0.98	0.16	-0.98	-0.15
$[(2p_{3/2})(1p_{3/2})^{-1}]_\pi$	16.83	-0.11	0.01	0.14	-0.01	-0.11	0.00	0.12	-0.01
$[(2p_{1/2})(1p_{3/2})^{-1}]_\pi$	16.84	0.11	-0.01	-0.09	0.00	0.10	0.00	-0.09	0.00
$[(3p_{3/2})(1p_{3/2})^{-1}]_\pi$	19.30	-0.13	0.01	0.18	-0.02	-0.13	0.01	0.15	0.01
$[(3p_{1/2})(1p_{3/2})^{-1}]_\pi$	19.34	-0.13	0.01	0.10	-0.01	-0.12	0.01	0.10	-0.01

Table 3.25: Main ph pairs for the lowest 1^+ states and their X and Y amplitudes calculated with the four interactions for ^{12}B nucleus.

1^+ (17.20 MeV)		*LM*		*LMtt*		*FR*		*FRtt*	
ω		21.05		20.89		21.09		20.97	
transition	ϵ_p -ϵ_h	X	Y	X	Y	X	Y	X	Y
$[(1p_{1/2})(1p_{3/2})^{-1}]_\pi$	16.78	-0.88	-0.01	0.83	0.09	-0.86	-0.10	-0.86	-0.01
$[(2p_{3/2})(1p_{3/2})^{-1}]_\pi$	20.18	0.14	0.00	-0.23	0.00	0.13	0.00	0.18	0.00
$[(2p_{1/2})(1p_{3/2})^{-1}]_\pi$	20.19	0.15	0.00	-0.16	0.00	0.14	0.00	0.15	0.00
$[(3p_{3/2})(1p_{3/2})^{-1}]_\pi$	22.06	-0.33	0.01	0.40	-0.01	-0.34	0.01	-0.38	0.01
$[(3p_{1/2})(1p_{3/2})^{-1}]_\pi$	22.10	-0.34	0.01	0.25	-0.01	-0.32	0.01	-0.28	0.01

Table 3.26: Main ph pairs for the considered 1^+ state and their X and Y amplitudes calculated with the four interactions for ^{12}N nucleus.

3.3.4 The ^{40}Ca nucleus

We show in Tab. 3.27 and Fig. 3.24 the spectrum of ^{40}Ca nucleus calculated with the four interactions

^{40}Ca					
excitation	LM	LMtt	FR	FRtt	exp
3^-	3.77	3.78	3.73	3.73	3.74
5^-	6.18	6.19	6.11	6.14	4.49
4^-	6.86	6.88	6.78	6.80	5.61
3^-	7.44	7.47	7.30	7.32	6.58
2^-	7.21	7.20	6.91	6.90	7.53
4^-	7.52	7.59	7.42	7.47	7.66
3^-	8.05	8.21	7.91	8.03	7.69
2^-	8.90	8.44	8.76	8.58	8.42
5^-	9.28	9.90	9.33	9.74	8.55

Table 3.27: Low excited states in ^{40}Ca. The energies are expressed in MeV. The experimental values are taken from [40]

We observe that the spectrum of ^{40}Ca is well reproduced by RPA calculations that however give value higher than experimental ones, except for 4^- states. The presence of tensor does not change significatively the excitation energy.

First we study the electric excitations 3^- and 5^-. The contribution to the first three 3^- excitations is given in Tabs. 3.28, 3.29 and 3.30.

3^- (3.74 MeV)		LM		$LMtt$		FR		$FRtt$	
ω		3.77		3.77		3.73		3.73	
transition	ϵ_p -ϵ_h	X	Y	X	Y	X	Y	X	Y
$[(1f_{7/2})(1d_{5/2})^{-1}]_\pi$	13.10	0.29	-0.17	0.29	-0.16	0.25	-0.14	0.25	-0.14
$[(1f_{7/2})(2s_{1/2})^{-1}]_\pi$	8.70	-0.53	0.22	-0.53	0.23	-0.54	0.22	-0.54	0.22
$[(1f_{7/2})(1d_{3/2})^{-1}]_\pi$	6.67	-0.46	0.15	-0.45	0.16	-0.40	0.12	-0.39	0.13
$[(2p_{3/2})(1d_{5/2})^{-1}]_\pi$	15.22	-0.13	0.08	-0.13	0.08	0.15	0.09	-0.16	0.09
$[(2p_{3/2})(1d_{3/2})^{-1}]_\pi$	8.79	0.31	-0.13	0.31	-0.13	0.40	-0.16	0.40	-0.16
$[(1f_{7/2})(1d_{5/2})^{-1}]_\nu$	13.24	-0.23	0.13	-0.24	0.13	-0.20	0.10	-0.20	0.11
$[(1f_{7/2})(2s_{1/2})^{-1}]_\nu$	9.84	0.39	-0.17	-0.40	-0.17	0.40	-0.17	0.40	-0.17
$[(1f_{7/2})(1d_{3/2})^{-1}]_\nu$	7.24	-0.35	0.10	-0.36	0.10	-0.30	0.08	-0.30	0.08
$[(1f_{5/2})(2s_{1/2})^{-1}]_\nu$	13.97	-0.18	0.11	-0.18	0.11	-0.18	0.11	-0.18	0.11
$[(1f_{3/2})(1d_{3/2})^{-1}]_\nu$	11.37	-0.19	0.10	-0.19	0.10	-0.15	0.08	-0.15	0.08
$[(2p_{3/2})(1d_{5/2})^{-1}]_\nu$	15.40	0.13	-0.08	0.13	-0.08	0.15	-0.09	0.15	-0.09
$[(2p_{3/2})(1d_{3/2})^{-1}]_\nu$	9.40	0.30	-0.12	0.30	-0.12	0.37	-0.15	0.38	-0.16

Table 3.28: Main ph pairs for the first 3^- states and their X and Y amplitudes calculated with the four interactions.

We show in Figs. 3.25 and 3.26 the longitudinal and transverse responses of the first two 3^- excited states of ^{40}Ca. We can see that also this excitation is dominated by discrete excitations. In Fig. 3.27 we show the RPA results for longitudinal and transverse responses for the third 3^- excited state compared to experimental data.

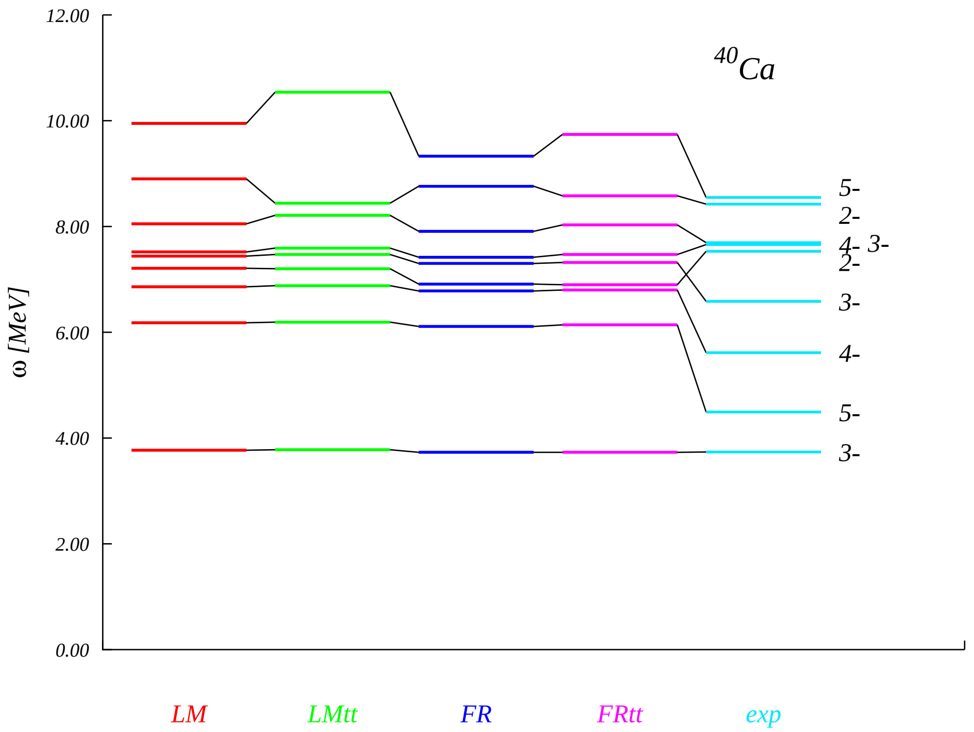

Figure 3.24: ^{40}Ca spectrum

We can observe that the transverse response is better described than the longitudinal one. The transverse response is close in shape and magnitude to the experimental data for all the interactions. The location of the maxima of the form factors for all the interactions occurs at the same q. The magnitude of the maxima is instead different. The longitudinal response shows a dependence to the finite range of the interaction but not to the presence of the tensor. The transverse form factors are very close to each other, only small differences can be observed in the LMtt result.

3^- (6.58 MeV)		LM		$LMtt$		FR		$FRtt$	
ω		7.44		7.47		7.30		7.32	
transition	ϵ_p -ϵ_h	X	Y	X	Y	X	Y	X	Y
$[(1f_{7/2})(1d_{5/2})^{-1}]_\pi$	13.10	-0.14	0.03	0.14	-0.32	0.13	-0.03	-0.13	0.03
$[(1f_{7/2})(2s_{1/2})^{-1}]_\pi$	8.70	0.49	-0.03	-0.50	0.02	-0.42	0.03	0.42	-0.03
$[(1d_{7/2})(1d_{3/2})^{-1}]_\pi$	6.67	-0.82	-0.01	0.78	0.01	0.84	0.02	-0.82	-0.02
$[(1f_{7/2})(2s_{1/2})^{-1}]_\nu$	9.84	-0.12	0.02	0.14	-0.03	0.10	-0.02	-0.12	0.02
$[(1f_{7/2})(1d_{3/2})^{-1}]_\nu$	7.24	-0.14	0.02	0.24	0.02	0.21	0.01	-0.28	0.02
$[(2p_{3/2})(1d_{3/2})^{-1}]_\nu$	9.40	-0.14	0.01	0.15	-0.01	0.13	-0.02	-0.14	0.01

Table 3.29: Main ph pairs for the second 3^- state and their X and Y amplitudes calculated with the four interactions.

3^- (7.69 MeV)		LM		$LMtt$		FR		$FRtt$	
ω		8.05		8.21		7.91		8.03	
transition	ϵ_p -ϵ_h	X	Y	X	Y	X	Y	X	Y
$[(1f_{7/2})(1d_{3/2})^{-1}]_\pi$	6.67	0.21	-0.02	0.26	-0.04	-0.25	0.02	0.29	0.03
$[(2p_{3/2})(1d_{3/2})^{-1}]_\pi$	8.79	-0.18	0.01	0.25	0.01	0.16	-0.01	0.20	0.00
$[(1f_{7/2})(2s_{1/2})^{-1}]_\pi$	8.70	-0.03	-0.02	-0.13	0.02	0.08	0.02	0.15	0.02
$[(1f_{7/2})(1d_{5/2})^{-1}]_\nu$	13.24	0.13	-0.02	0.13	-0.01	-0.11	0.02	-0.11	0.02
$[(1f_{7/2})(2s_{1/2})^{-1}]_\nu$	9.84	-0.32	0.01	-0.36	0.00	0.27	-0.01	0.29	0.00
$[(1f_{7/2})(1d_{3/2})^{-1}]_\nu$	7.24	-0.89	0.01	-0.83	0.02	0.90	0.00	0.86	0.00

Table 3.30: Main ph pairs for the third 3^- state and their X and Y amplitudes calculated with the four interactions.

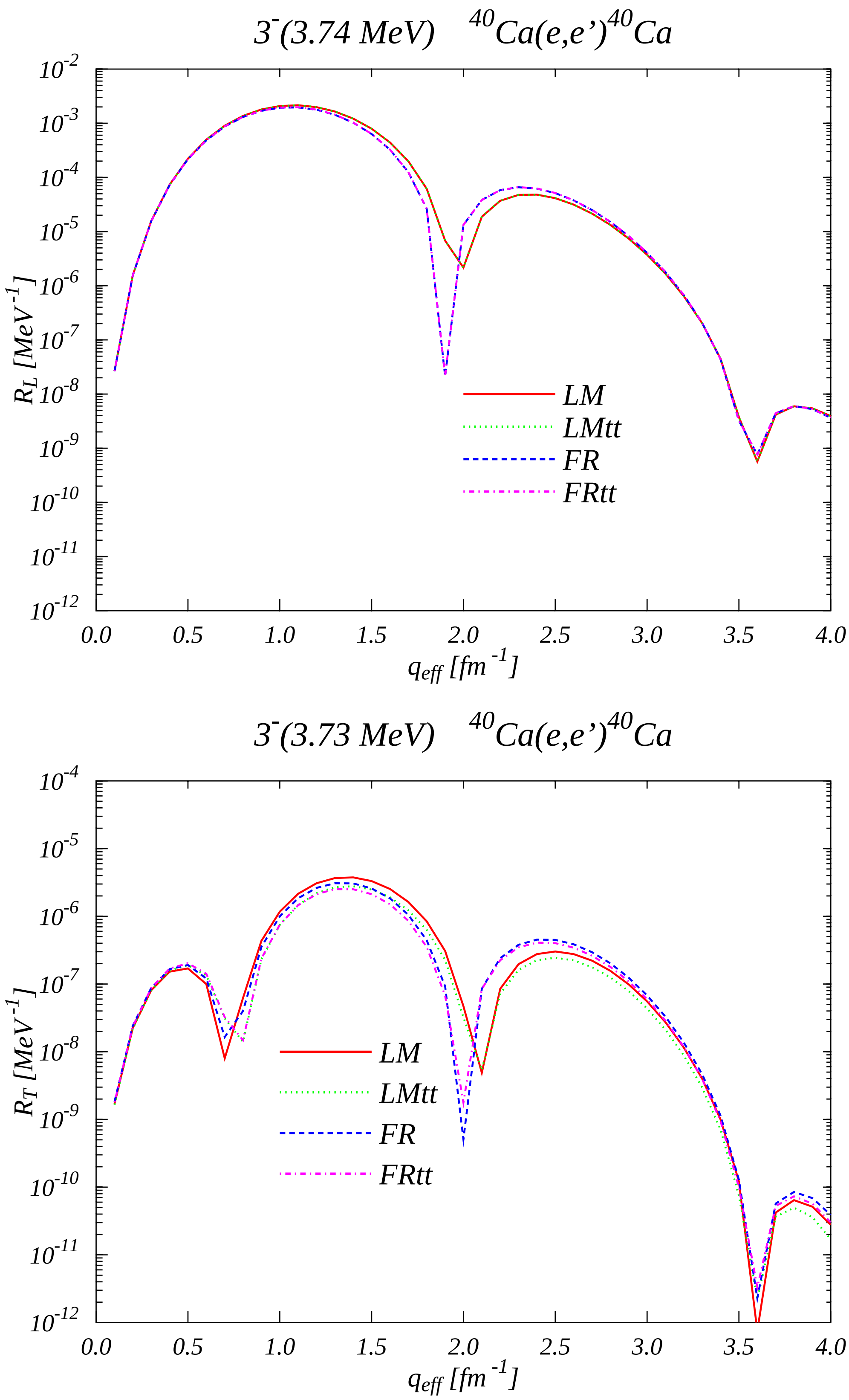

Figure 3.25: Longitudinal and transverse response for the first 3^- excited state in ^{40}Ca calculated with the different interactions used in our work.

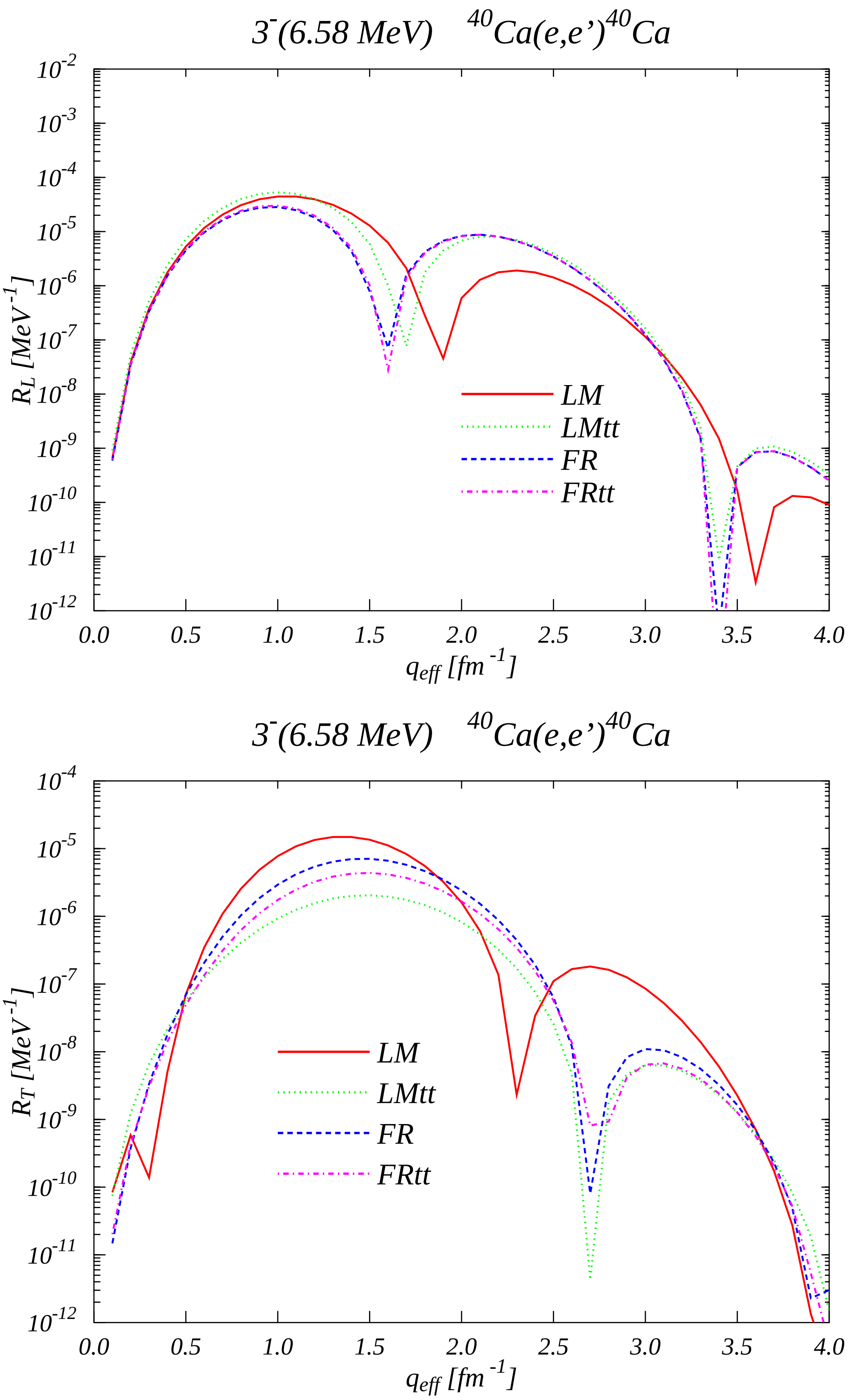

Figure 3.26: Longitudinal and transverse response for the second 3^- excited state in ^{40}Ca calculated with the different interactions used in our work.

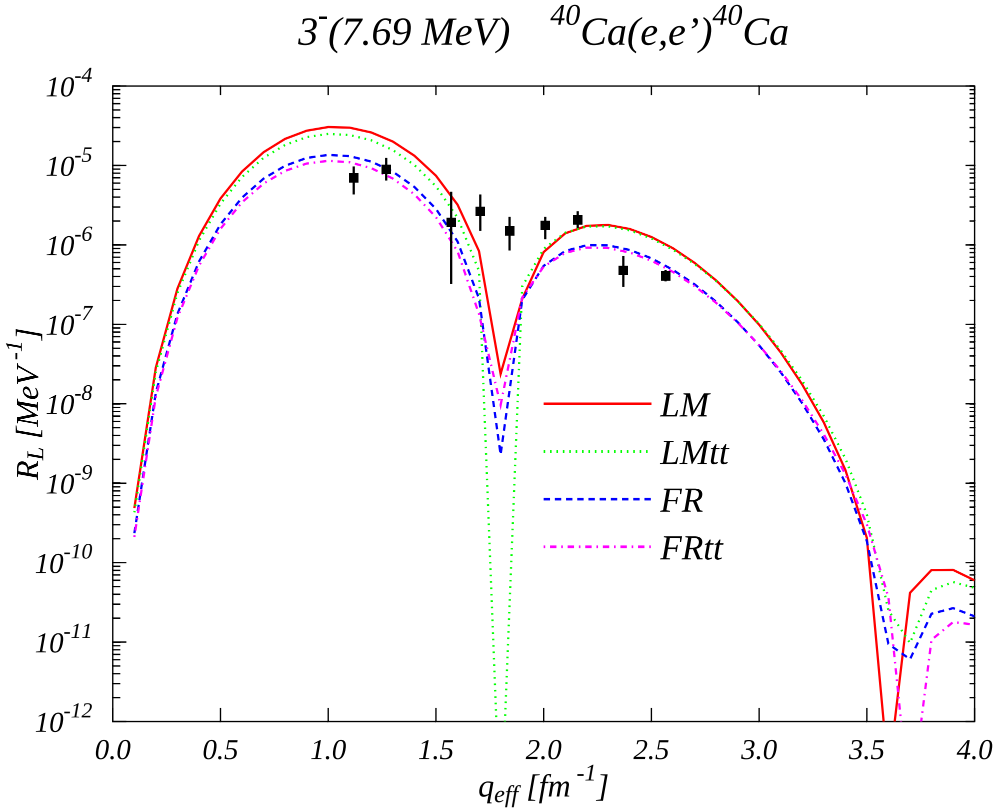

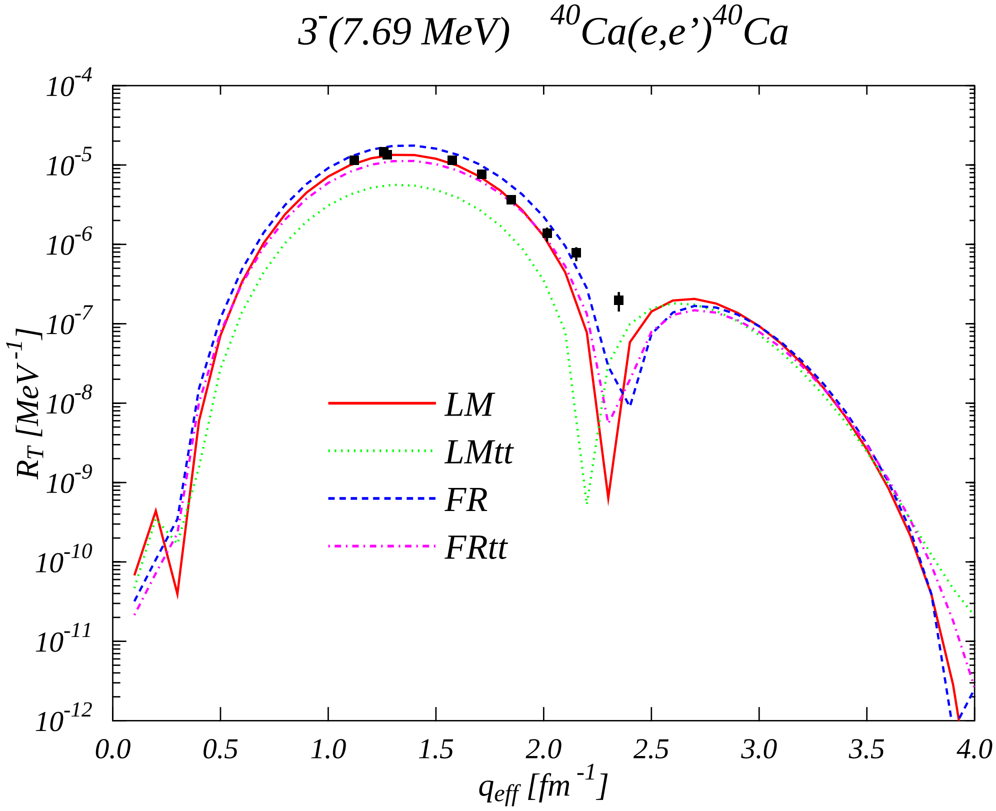

Figure 3.27: Longitudinal and transverse response for the third 3^- excited state in ^{40}Ca calculated with the different interactions used in our work. Experimental data from [57].

Now we consider the 5^- excited state. Also in this case the main ph excitations are dominated by bound ph pairs as we show in Tab. 3.31.

5^- (8.55 MeV)		LM		$LMtt$		FR		$FRtt$	
ω		9.95		10.54		9.33		9.74	
transition	ϵ_p -ϵ_h	X	Y	X	Y	X	Y	X	Y
$[(1f_{7/2})(1d_{5/2})^{-1}]_\pi$	13.10	-0.26	0.03	0.33	-0.02	2.11	-0.03	-0.24	0.03
$[(1f_{7/2})(1d_{3/2})^{-1}]_\pi$	6.67	-0.59	-0.02	0.58	0.00	0.59	0.04	-0.59	-0.03
$[(1f_{7/2})(1d_{5/2})^{-1}]_\nu$	13.24	-0.25	0.03	0.30	-0.02	0.20	-0.31	-0.23	0.02
$[(1f_{7/2})(1d_{3/2})^{-1}]_\nu$	7.24	0.72	0.02	0.68	0.00	-0.75	-0.04	0.73	0.02

Table 3.31: Main ph pairs for the second 5^- state and their X and Y amplitudes calculated with the four interactions.

The longitudinal and transverse responses are displayed in Fig. 3.28.

The level of agreement between the results of our calculations with the data is reasonably good. All the calculations overestimate the transverse response. Also in this case we can make analogous considerations about the role of finite range interaction. As we have seen for the 3^- state, also in this case the results obtained with zero range interactions are higher than those obtained with finite range interactions.
The presence of tensor terms in the interaction does not produce remarkable effects.

For the magnetic states we start by studying the 2^- excited states. Our calculations give the first 2^- states described in Tab. 3.32. These states are both dominated by transitions in the discrete. In Fig. 3.29 we show the transverse responses of these two states and we compare the responses of the state with higher energy to the experimental data of Ref [57]. We can observe that for the state at 8.9 MeV the tensor term modifies the shape of the transverse response. There is a lowering of the maxima and a shift of the position of the diffraction minima.

2^- (7.53 MeV)		LM		$LMtt$		FR		$FRtt$	
ω		7.21		7.20		6.91		6.90	
transition	ϵ_p -ϵ_h	X	Y	X	Y	X	Y	X	Y
$[(1f_{7/2})(1d_{3/2})^{-1}]_\pi$	6.67	0.81	-0.03	-0.83	0.32	-0.81	0.01	0.81	-0.01
$[(1f_{7/2})(1d_{3/2})^{-1}]_\nu$	7.24	0.58	0.00	-0.55	0.00	-0.59	-0.01	0.58	0.01
2^- (8.42 MeV)		LM		$LMtt$		FR		$FRtt$	
ω		8.90		8.44		8.76		8.58	
transition	ϵ_p -ϵ_h	X	Y	X	Y	X	Y	X	Y
$[(1f_{7/2})(1d_{5/2})^{-1}]_\pi$	13.10	0.17	0.03	-0.08	-0.02	-0.17	-0.03	0.13	0.03
$[(1f_{7/2})(1d_{3/2})^{-1}]_\pi$	6.67	-0.54	0.08	0.41	-0.05	0.55	-0.07	-0.49	0.06
$[(2p_{3/2})(1d_{3/2})^{-1}]_\pi$	8.79	0.17	0.00	0.49	0.01	0.08	0.00	-0.38	0.00
$[(1f_{7/2})(1d_{5/2})^{-1}]_\nu$	13.24	0.18	0.03	-0.09	-0.02	-0.17	-0.03	0.13	0.03
$[(1f_{7/2})(1d_{3/2})^{-1}]_\nu$	7.24	0.78	-0.08	-0.68	0.05	-0.77	0.07	0.71	-0.06

Table 3.32: Main ph pairs for the lowest 2^- states and their X and Y amplitudes calculated with the four interactions.

Another interesting case to investigate is the 4^- excitation. Our calculations give two low-lying 4^- states, one at 5.61 MeV and the other one at 7.66 MeV described in Tabs. 3.33 and 3.34. The relative transverse responses are shown in Fig. 3.30.

4^- (5.61 MeV)		*LM*		*LMtt*		*FR*		*FRtt*	
ω		6.86		6.88		6.78		6.80	
transition	ϵ_p -ϵ_h	X	Y	X	Y	X	Y	X	Y
$[(1f_{7/2})(1d_{3/2})^{-1}]_\pi$	6.67	0.95	-0.01	-0.94	0.01	0.96	0.00	0.96	0.01
$[(1f_{7/2})(1d_{3/2})^{-1}]_\nu$	7.24	0.27	0.01	-0.32	0.01	0.24	-0.01	0.28	0.01

Table 3.33: Main ph pairs for the first 4^- states and their X and Y amplitudes calculated with the four interactions.

4^- (7.66 MeV)		*LM*		*LMtt*		*FR*		*FRtt*	
ω		7.52		7.59		7.42		7.47	
transition	ϵ_p -ϵ_h	X	Y	X	Y	X	Y	X	Y
$[(1f_{7/2})(1d_{1/2})^{-1}]_\pi$	8.70	0.12	0.01	-0.11	0.00	-0.12	0.01	0.11	0.01
$[(1f_{7/2})(1d_{3/2})^{-1}]_\pi$	6.67	0.25	-0.01	-0.30	0.00	-0.23	0.01	0.27	-0.01
$[(1f_{7/2})(1d_{3/2})^{-1}]_\nu$	7.24	-0.95	0.02	0.93	-0.02	0.96	-0.01	-0.95	0.01

Table 3.34: Main ph pairs for the second 4^- states and their X and Y amplitudes calculated with the four interactions.

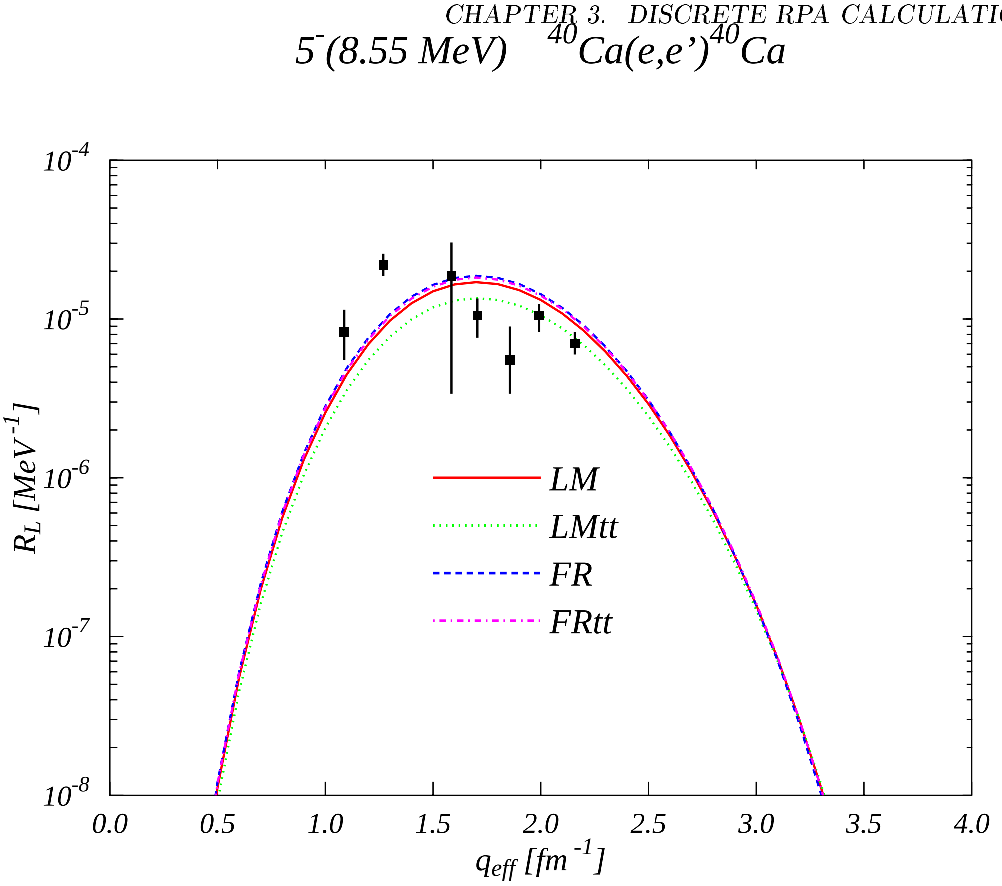

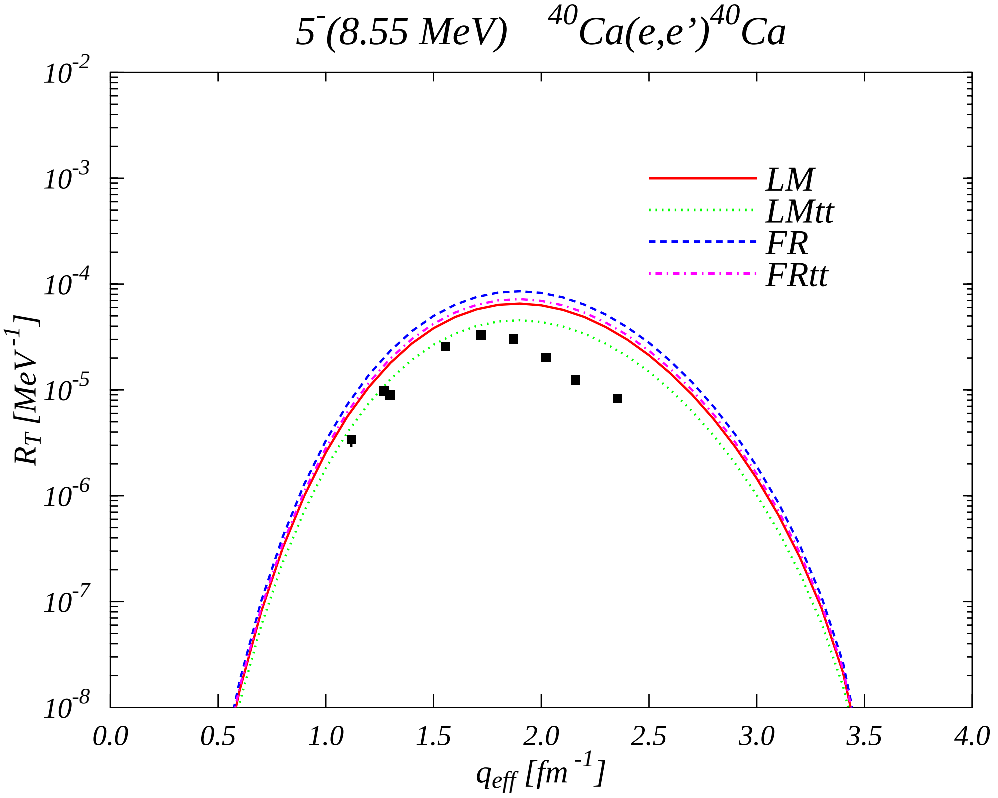

Figure 3.28: Longitudinal and transverse response for the second 5^- excited state in ^{40}Ca calculated with the different interactions used in our work. Experimental data from [57].

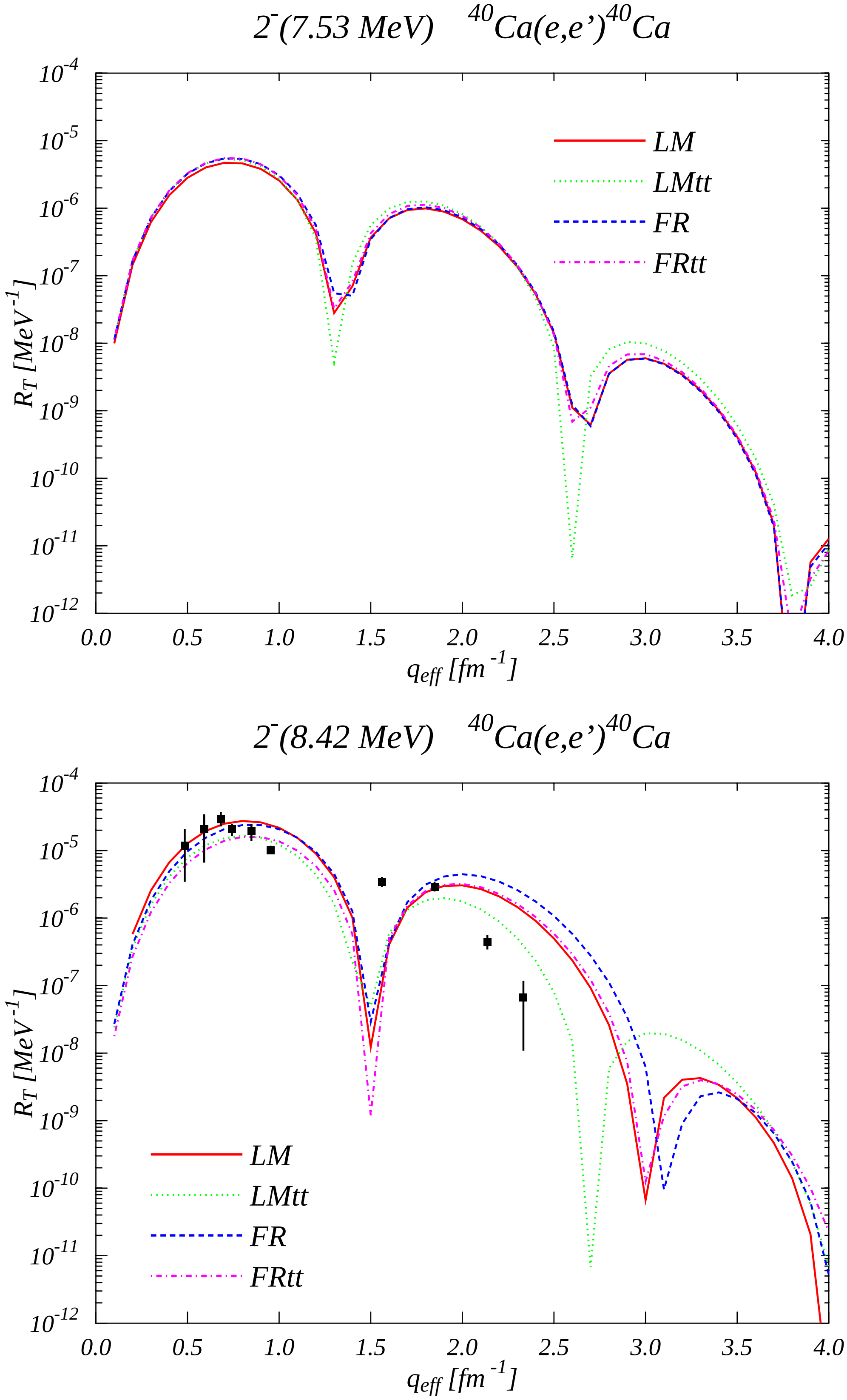

Figure 3.29: Transverse response for the lowest 2^- excited states in ^{40}Ca calculated with the different interactions used in our work. Experimental data from [57].

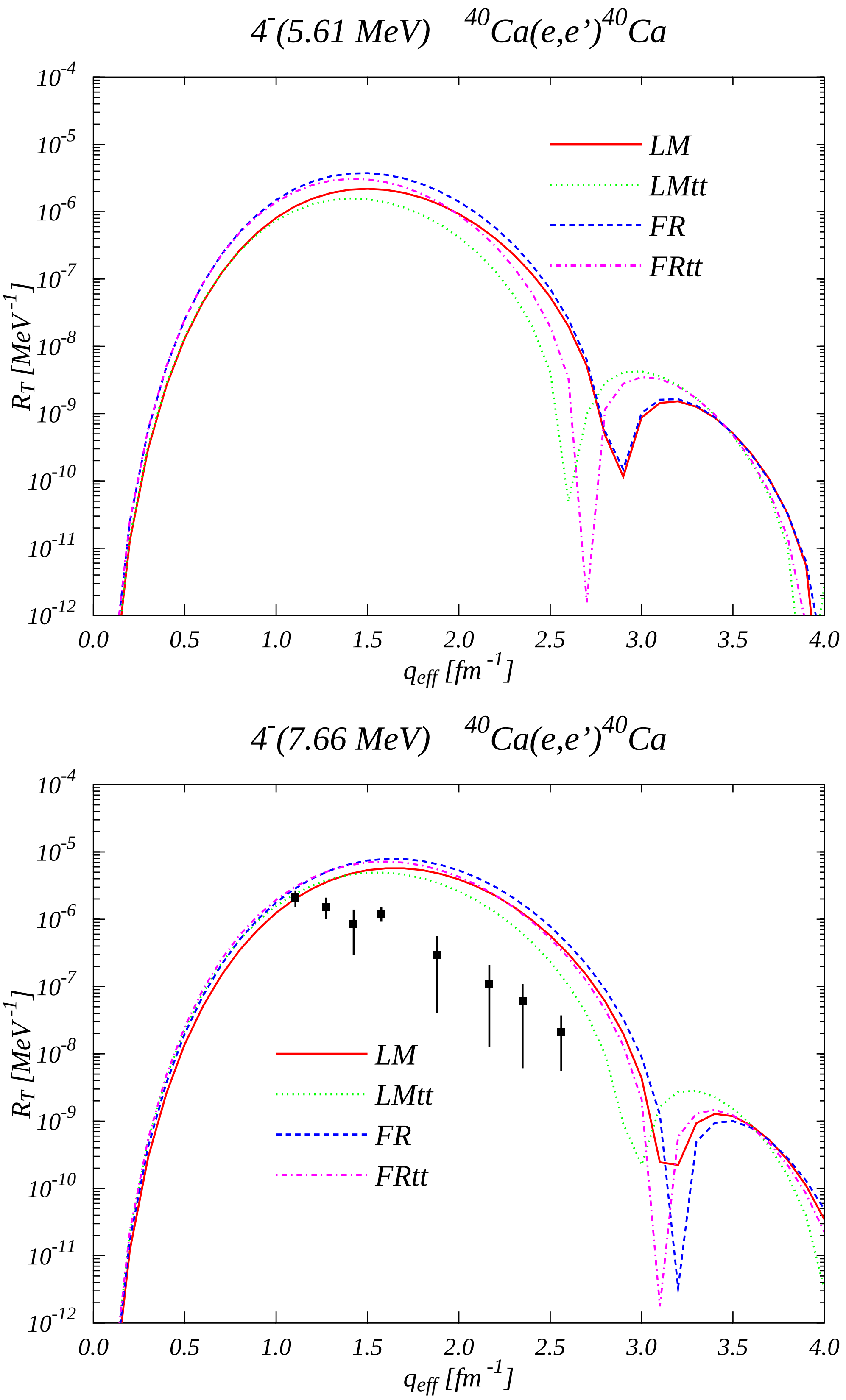

Figure 3.30: Transverse response for the two first 4^- excited states in ^{40}Ca calculated with the different interactions used in our work. Experimental data from [57].

3.3.5 The ^{48}Ca nucleus

^{48}Ca					
excitation	LM	LMtt	FR	FRtt	exp
2^+	4.80	4.92	4.55	4.61	3.83
4^+	4.82	4.83	4.78	4.78	4.50
3^-	4.31	4.34	4.51	4.52	4.51
3^+	5.03	4.99	4.96	4.94	4.61
5^+	5.26	5.16	5.04	4.98	5.15
4^-	6.44	6.41	6.36	6.35	6.10
2^-	7.53	7.06	7.30	7.10	6.89
6^-	11.29	11.31	11.01	10.99	8.56
1^+	9.65	9.38	9.68	9.50	10.23

Table 3.35: Lower excited states energies of ^{48}Ca expressed in MeV

The calculations for ^{48}Ca have been made with the same interactions used for ^{40}Ca. We show in Tab. 3.35 and in Fig. 3.31 the corresponding spectrum. The energies obtained are in good agreement with the experimental values. We observe that the tensor force increases the energies of electric states and decreases those of the magnetic states.

We start our analysis of magnetic states from the 3^+ excited state, which is dominated by a single discrete neutron excitation, as we can see from Tab. 3.36.

3^+ (4.61 MeV)		LM		$LMtt$		FR		$FRtt$	
ω		5.03		4.99		4.96		4.94	
transition	ϵ_p -ϵ_h	X	Y	X	Y	X	Y	X	Y
$[(2p_{3/2})(1f_{7/2})^{-1}]_\nu$	4.81	0.99	0.02	-0.99	-0.01	0.99	0.01	-0.99	0.013

Table 3.36: Main ph pairs for the first 3^+ state and their X and Y amplitudes calculated with the four interactions.

We notice that the transverse responses obtained with our calculations describe rather well the experimental data (Fig. 3.32).

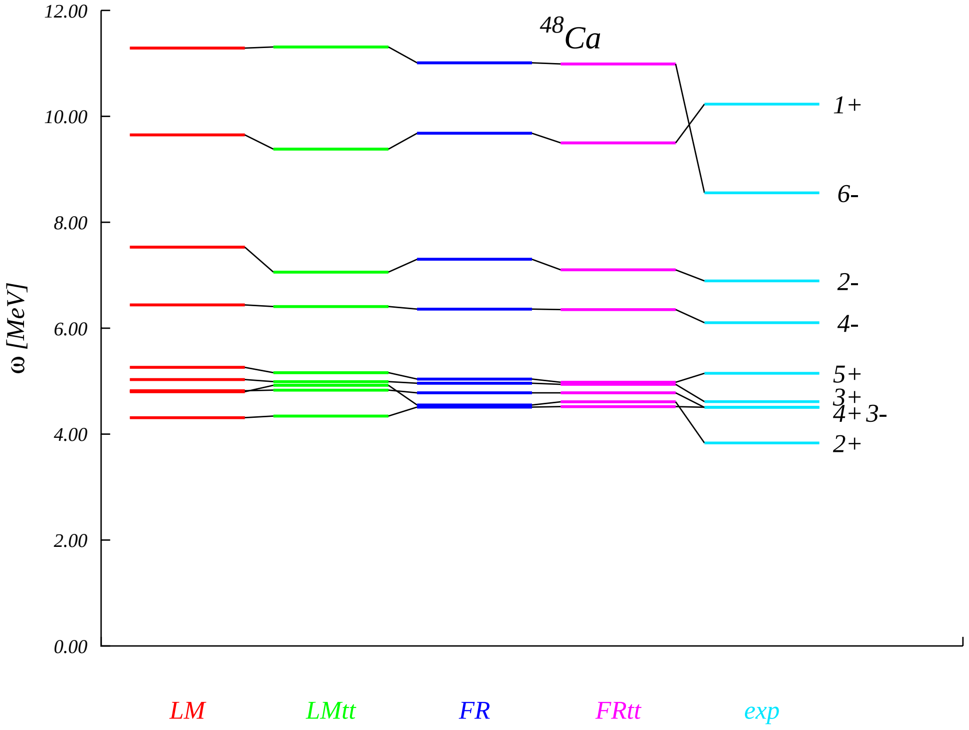

Figure 3.31: ^{48}Ca spectrum

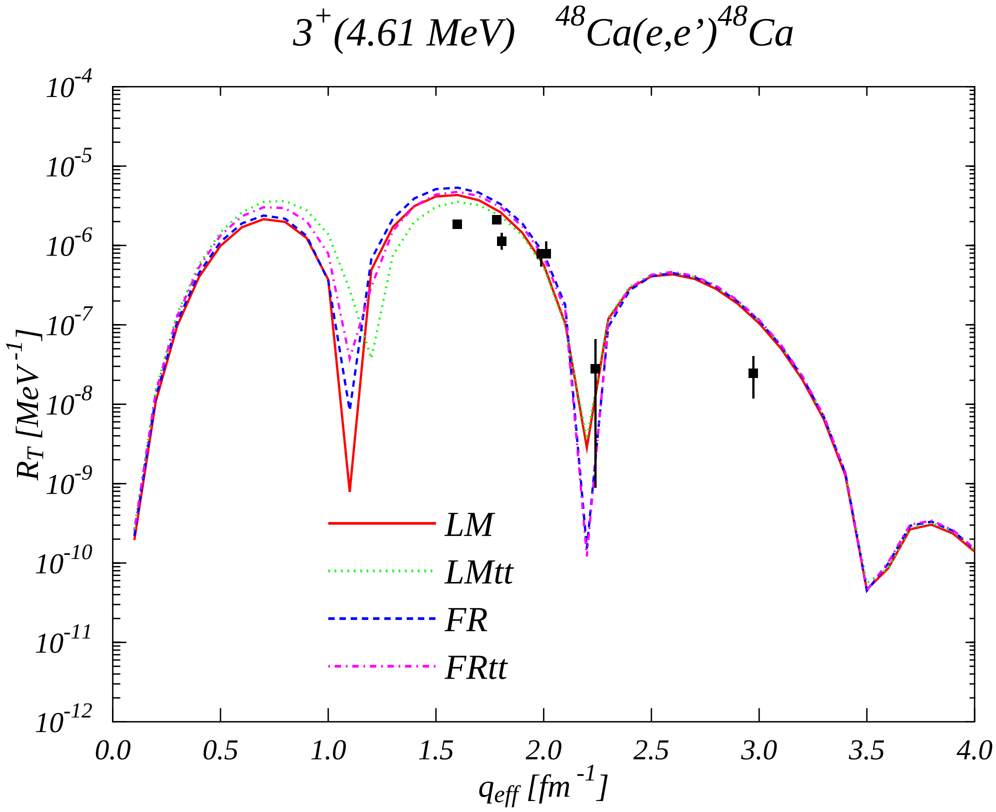

Figure 3.32: Transverse form factor for the excited state 3^+ for ^{48}Ca compared with experimental data [58].

Also the 5^+ excitation, entirely dominated by a single discrete excitation (Tab.3.37) describes well the transverse response as it is shown by Fig. 3.33.

5^+ (5.15 MeV)		LM		$LMtt$		FR		$FRtt$	
ω		5.26		5.16		5.04		4.98	
transition	ϵ_p -ϵ_h	X	Y	X	Y	X	Y	X	Y
$[(2p_{3/2})(1f_{7/2})^{-1}]_\nu$	4.81	0.99	0.04	-1.00	-0.03	1.00	0.02	1.00	0.02

Table 3.37: Main ph pairs for the first 5^+ state and their X and Y amplitudes calculated with the four interactions.

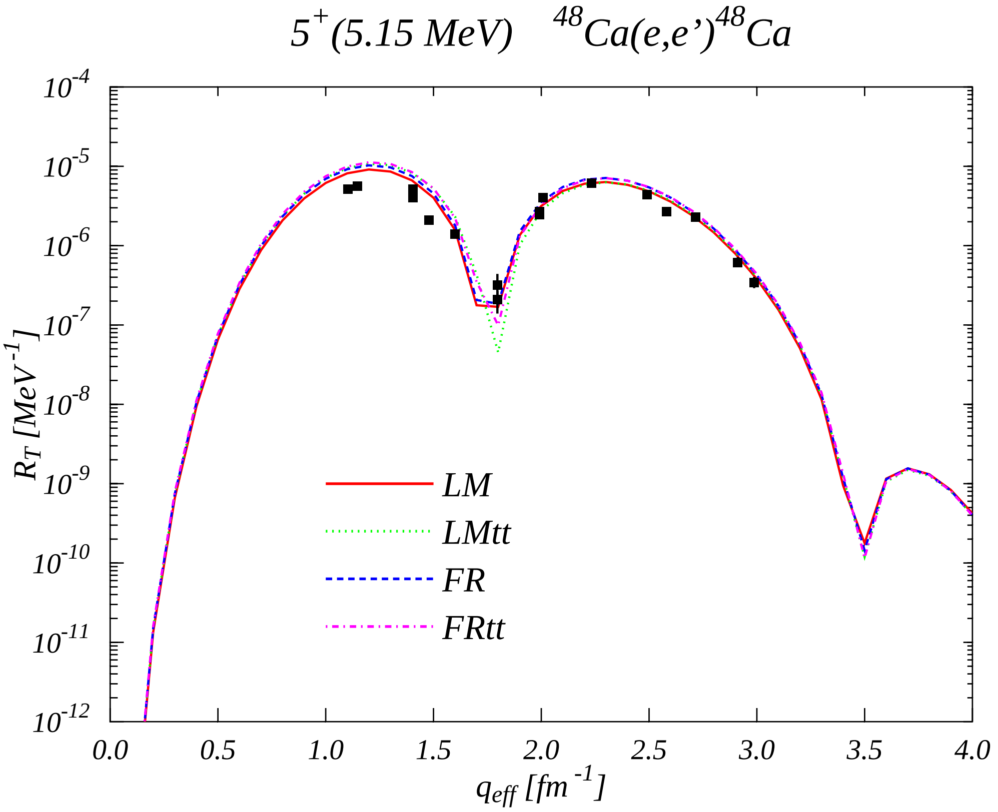

Figure 3.33: Transverse form factor for the excited state 5^+ for ^{48}Ca compared with experimental data [58].

Similar considerations can be made for the 4^- state. This state is described by two ph protons pairs, see Tab. 3.38. Our calculations describe reasonably well the transverse response, see Fig. 3.34. We observe in this case that finite range and tensor interactions enhance the response.

4^- (6.10 MeV)		LM		$LMtt$		FR		$FRtt$	
ω		6.44		6.41		6.36		6.35	
transition	ϵ_p -ϵ_h	X	Y	X	Y	X	Y	X	Y
$[(1f_{7/2})(2s_{1/2})^{-1}]_\pi$	6.18	0.85	-0.02	-0.90	0.02	0.90	-0.01	0.93	-0.01
$[(1f_{7/2})(1d_{3/2})^{-1}]_\pi$	6.54	0.52	0.00	-0.43	0.00	0.43	0.00	0.36	0.00

Table 3.38: Main ph pairs for the first 4^- state and their X and Y amplitudes calculated with the four interactions.

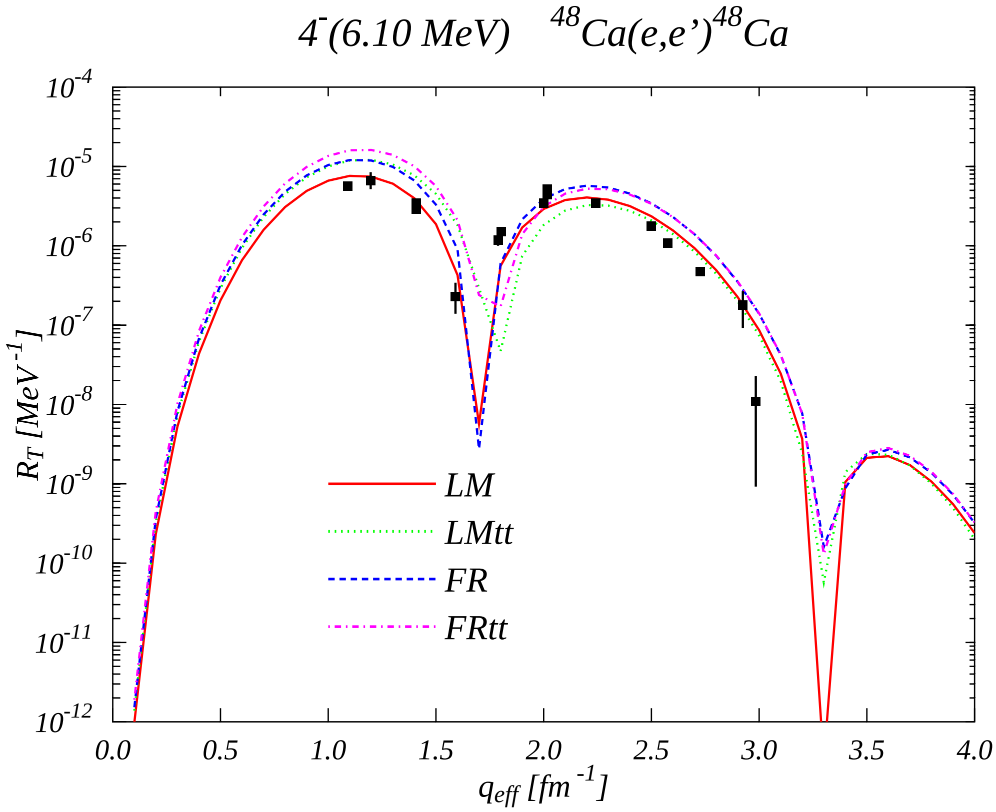

Figure 3.34: Transverse response for the excited state 4^- for ^{48}Ca. Experimental data from [58].

The 2^- excited state is described by the main discrete contributions shown in Tab. 3.39.

2^- (6.89 MeV)		LM		$LMtt$		FR		$FRtt$	
ω		7.53		7.06		7.30		7.10	
transition	ϵ_p -ϵ_h	X	Y	X	Y	X	Y	X	Y
$[(1f_{7/2})(1d_{3/2})^{-1}]_\pi$	6.54	-0.46	0.03	-0.70	0.03	-0.89	0.02	-0.78	0.02
$[(2p_{3/2})(2s_{1/2})^{-1}]_\pi$	9.27	-0.03	0.00	-0.11	0.01	-0.03	0.00	-0.07	0.01
$[(2p_{1/2})(1d_{3/2})^{-1}]_\pi$	10.06	0.03	0.00	0.13	0.02	0.00	0.00	0.07	0.01
$[(2p_{3/2})(2s_{1/2})^{-1}]_\pi$	7.41	-0.03	0.00	-0.36	0.00	-0.43	0.00	-0.48	-0.01
$[(2p_{3/2})(1d_{3/2})^{-1}]_\nu$	7.39	-0.87	0.01	0.55	0.012	0.07	0.00	0.35	0.01
$[(2p_{1/2})(1d_{3/2})^{-1}]_\nu$	9.83	-0.05	0.00	-0.13	0.02	0.00	0.00	-0.08	-0.01

Table 3.39: Main ph pairs for the first 2^- states and their X and Y amplitudes calculated with the four interactions.

In this case the transverse response appears to be sensitive to the finite range of the interaction. The FR responses are higher than those calculated with LM interactions in the two first maxima. The position of the third maximum is shifted at higher values of q. In general the behaviours of the responses at q values larger than $2.5 fm$ are very different.

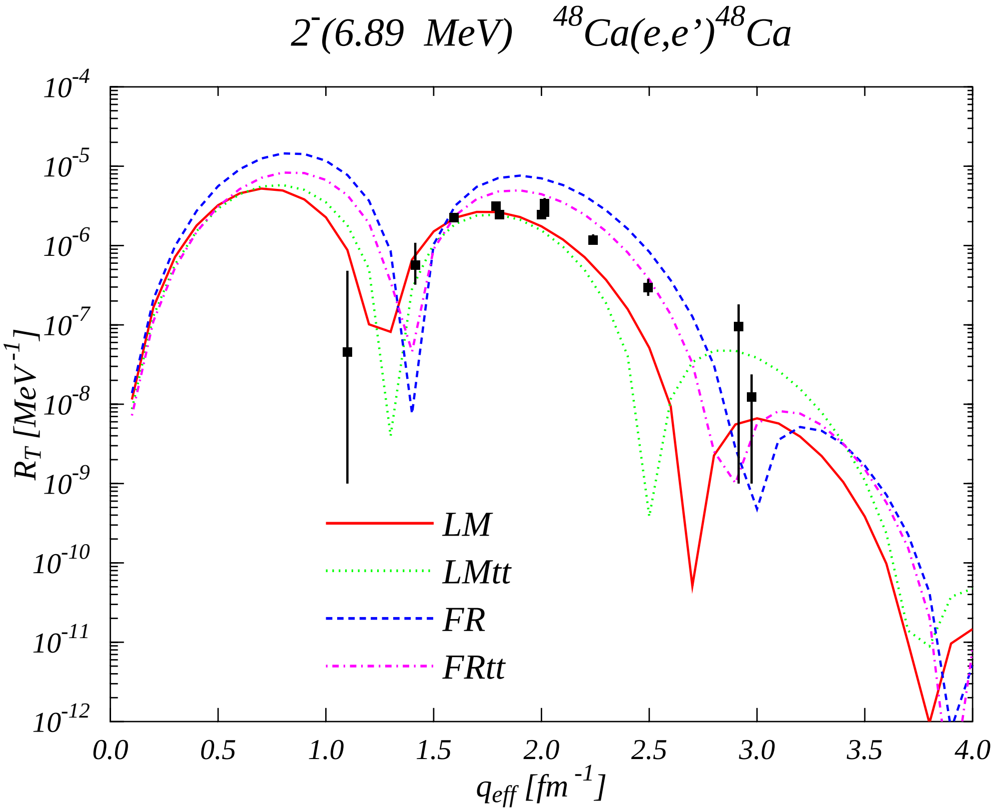

Figure 3.35: Transverse response for the 2^- excited state for ^{48}Ca compared with experimental data [58]

The main ph components of the 6^- state are shown in Tab. 3.40. We should remark that the neutron $1g_{9/2}$ s.p. wave function is unbound.

6^- (8.56 MeV)		*LM*		*LMtt*		*FR*		*FRtt*	
ω		11.29		11.31		11.01		10.99	
transition	ϵ_p -ϵ_h	X	Y	X	Y	X	Y	X	Y
$[(1f_{7/2})(1d_{5/2})^{-1}]_\pi$	10.71	-0.66	0.02	-0.65	0.02	0.54	0.00	0.81	-0.01
$[(1g_{9/2})(1f_{7/2})^{-1}]_\nu$	11.27	-0.74	0.00	-0.75	0.00	0.40	0.00	0.49	0.00

Table 3.40: Main ph pairs for the first 6^- state and their X and Y amplitudes calculated with the four interactions.

The transverse responses we have obtained are compared to the experimental ones [58] in Fig.3.36. While the two responses obtained with the LM zero range interactions almost coincide, the responses obtained with finite range forces are rather different. The finite range modifies the shape of the responses. The minimum is shifted to lower q values, and the width of the response is increased. The tensor force strongly enhances the response.

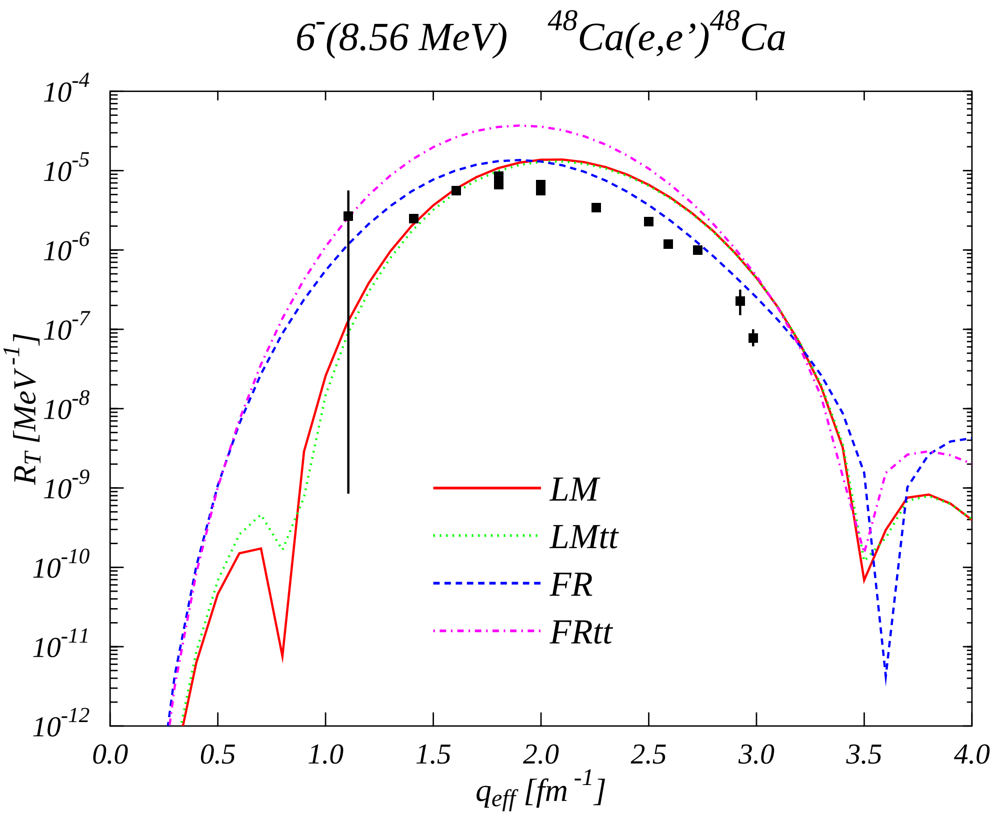

Figure 3.36: Transverse form factor for the excited state 6^- for ^{48}Ca compared with experimental data [58].

3.3.6 The ^{90}Zr nucleus

The spectrum of the ^{90}Zr nucleus is presented in Tab. 3.41 and in Fig. 3.37.

^{90}Zr					
excitation	LM	LMtt	FR	FRtt	exp
2^+	3.42	3.48	2.18	2.19	2.19
5^-	2.25	2.28	2.49	2.51	2.32
4^-	3.37	3.33	3.32	3.30	2.74
3^-	5.71	5.74	5.74	5.76	2.75
4^+	4.01	4.03	3.95	3.96	3.08
2^+	6.00	6.12	6.02	6.07	3.31
6^+	4.33	4.33	4.37	4.37	3.45
8^+	6.38	6.62	6.40	6.55	3.59
5^-	4.61	4.61	4.72	4.73	3.97
10^-	9.47	9.26	9.01	8.90	7.36

Table 3.41: Low excited states energies of ^{90}Zr in MeV

We can observe that in general the tensor interaction increases the energies of the electric states and reduces those of the magnetic states. For the electric states we study first the lowest 2^+ states. In Tab. 3.42 and Tab. 3.43 we report the contributions to the excitations of the most relevant ph pairs.

2^+ (2.19 MeV)		LM		$LMtt$		FR		$FRtt$	
ω		3.42		3.48		2.18		2.19	
transition	ϵ_p -ϵ_h	X	Y	X	Y	X	Y	X	Y
$[(2d_{5/2})(1g_{9/2})^{-1}]_\nu$	4.37	-0.96	-0.15	0.96	0.16	-0.97	-0.35	0.97	0.36

Table 3.42: Main ph pairs for the first 2^+ state and their X and Y amplitudes calculated with the four interactions.

2^+ (3.30 MeV)		LM		$LMtt$		FR		$FRtt$	
ω		6.00		6.12		6.02		6.07	
transition	ϵ_p -ϵ_h	X	Y	X	Y	X	Y	X	Y
$[(1g_{7/2})(1g_{9/2})^{-1}]_\nu$	5.70	0.98	0.04	-0.98	-0.05	0.98	0.03	-0.98	-0.03

Table 3.43: Main ph pairs for the second 2^+ state and their X and Y amplitudes calculated with the four interactions.

We observe that the first excited state is collective and there are significant contributions of unbound ph pairs excitations. The second state is instead dominated by discrete excitations.

We show in Fig. 3.38 the transition densities of these two states and we compare them with the empirical transition densities extracted from inelastic electron scattering data [59].

While in the case of the first 2^+ state the shape and order of magnitude of the empirical density are reproduced by our calculations, the behaviour we obtain for the transition densities for the second 2^+ state is wrong.

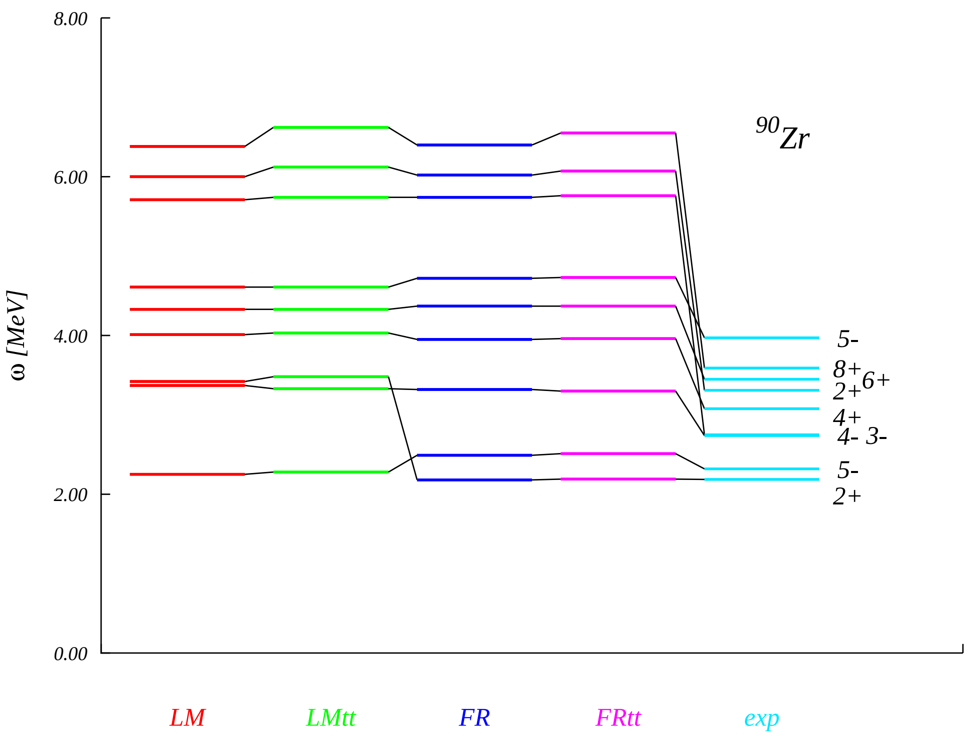

Figure 3.37: ^{90}Zr spectrum

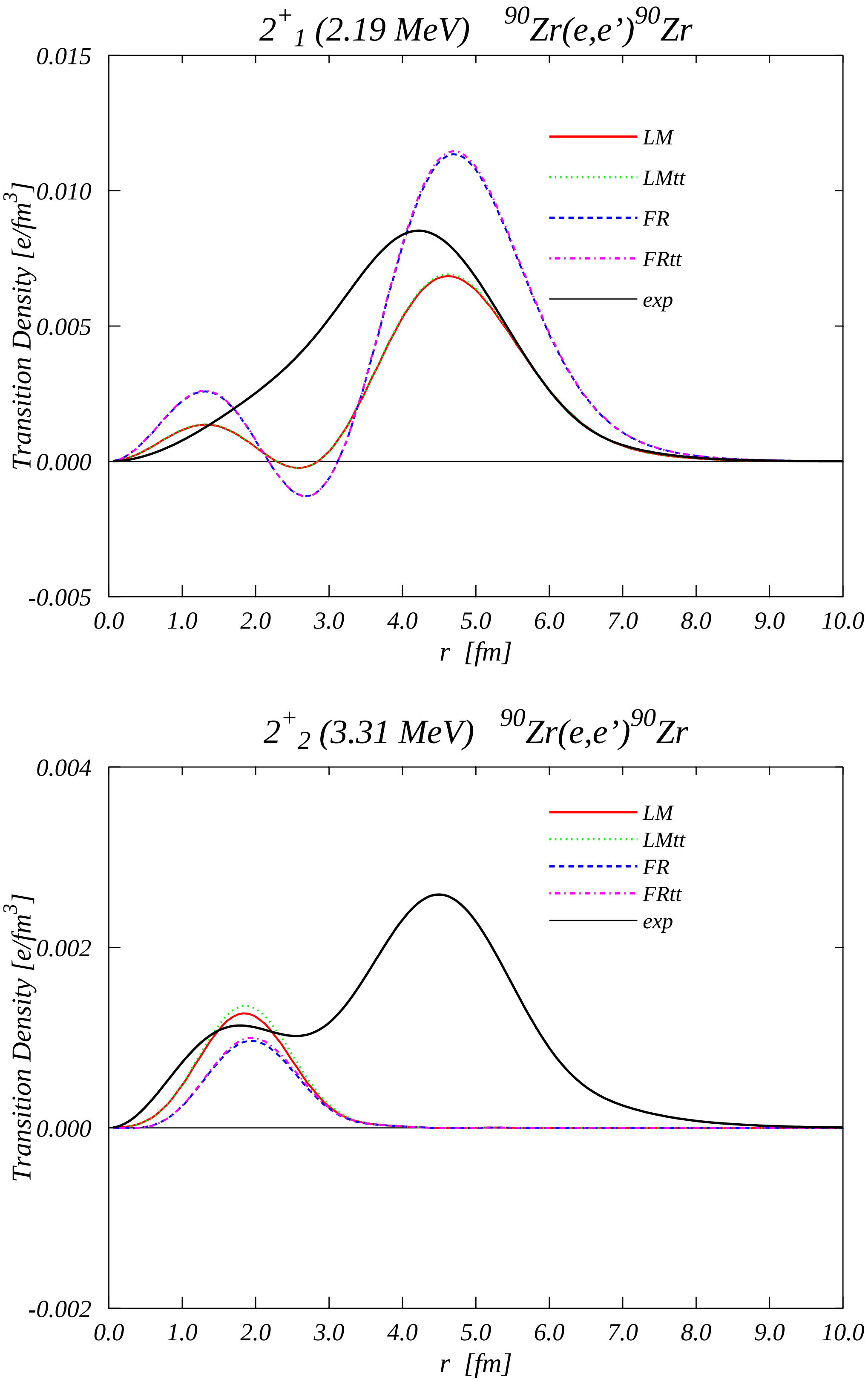

Figure 3.38: Transition density for the excited state 2^+ for ^{90}Zr compared with experimental data [59].

The large difference between the experimental and theoretical energy values is already an indicator of the fact that this 2^+ state cannot be properly described within the framework of the RPA theory.

Another electric state that we studied is the 4^+ excited state whose main ph pairs are indicated in Tab. 3.44.

4^+ (3.08 MeV)		LM		$LMtt$		FR		$FRtt$	
ω		4.01		4.03		3.95		3.96	
transition	ϵ_p -ϵ_h	X	Y	X	Y	X	Y	X	Y
$[(2d_{5/2})(1g_{9/2})^{-1}]_\nu$	4.37	-0.96	-0.05	0.96	0.05	-0.94	-0.05	0.95	0.05

Table 3.44: Main ph pairs for the first 4^+ state and their X and Y amplitudes calculated with the four interactions.

Also this state is dominated by discrete excitations, but the continuum contribution is not negligible.

In Fig. 3.39 we show the transition densities calculated with the various interactions, and we compare them with the empirical one [59]. While the order of magnitude of the experimental transition density is reasonably well reproduced, the theoretical transitions have an additional node at small values of r.

The tensor force does not produce effects, while there is a certain sensitivity to the finite range of the force.

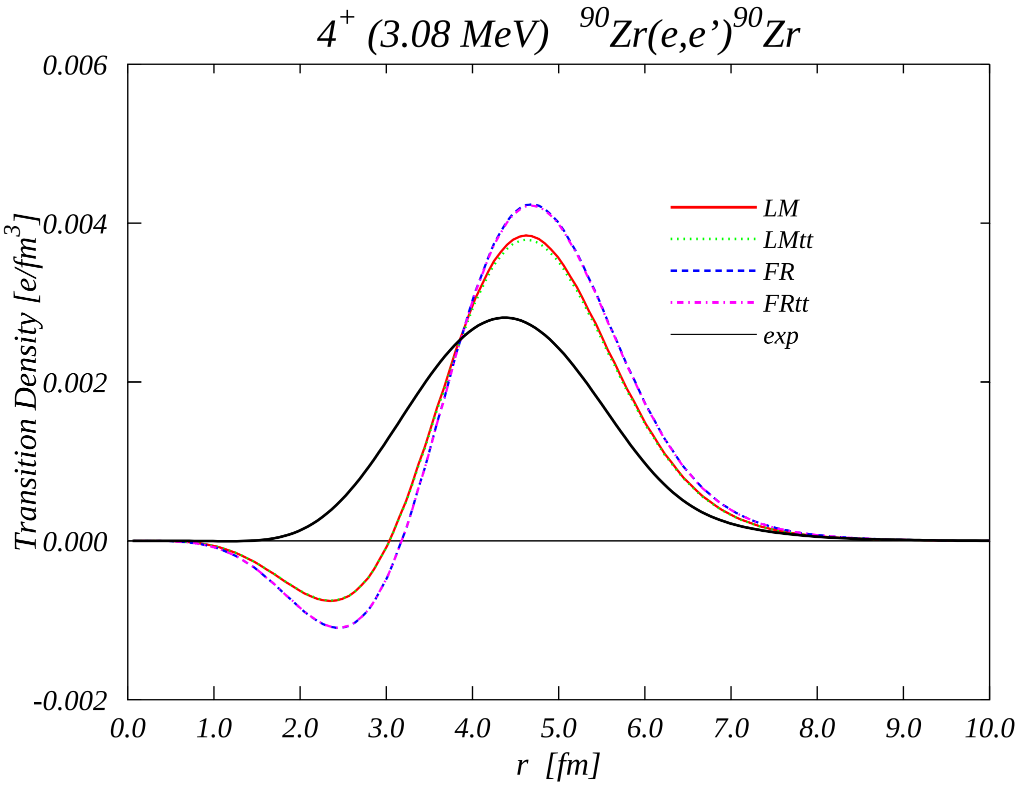

Figure 3.39: Transition density for the 4^+ excited state for ^{90}Zr compared to the experimental density [59].

As example of magnetic state we study the 10^- excitation. It is dominated by a single ph discrete excitation (Tab. 3.45) and its transverse response (Tab. 3.40) is in very good agreement with the experimental data [60].

10^- (7.36 MeV)		LM		$LMtt$		FR		$FRtt$	
ω		9.47		9.26		9.01		8.90	
transition	ϵ_p -ϵ_h	X	Y	X	Y	X	Y	X	Y
$[(1h_{11/2})(1g_{9/2})^{-1}]_\nu$	8.72	1.00	-0.04	-1.00	0.03	1.00	-0.02	-1.00	0.01

Table 3.45: Main ph pairs for the first 10^- states and their X and Y amplitudes calculated with the four interactions.

This is an almost pure ph excitation and the residual interaction does not play any role.

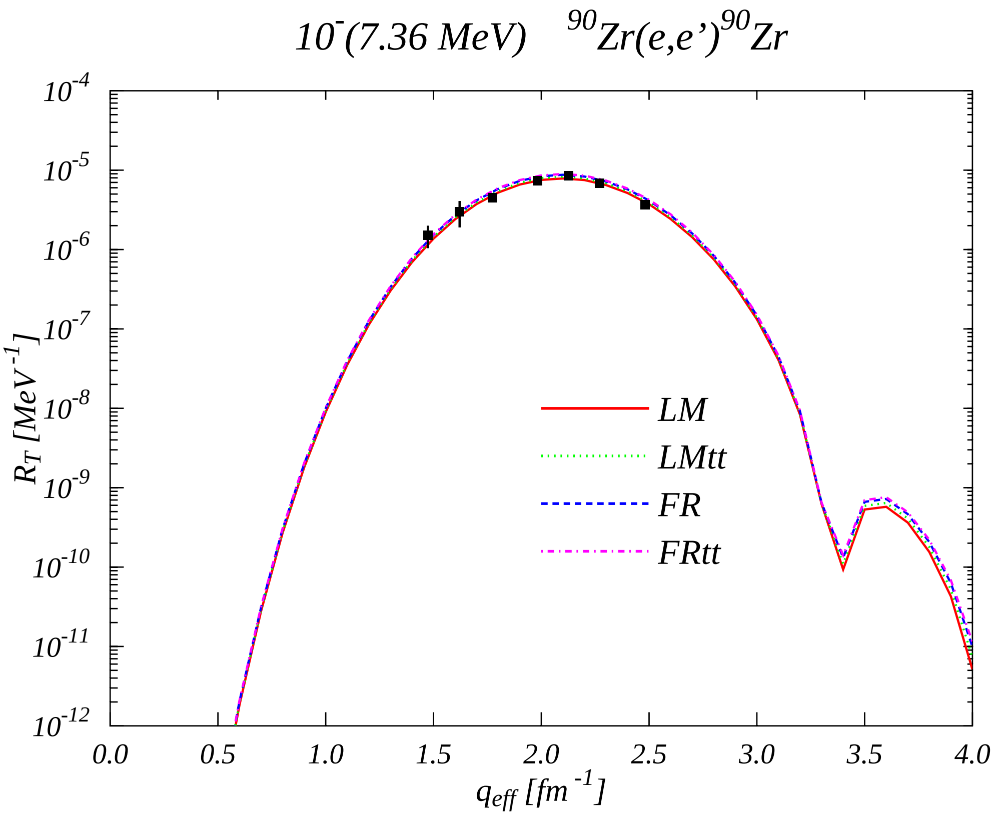

Figure 3.40: Transverse response of the 10^- state in ^{90}Zr compared with experimental data [60].

3.3.7 The ^{208}Pb nucleus

The spectrum of ^{208}Pb is presented in Tab. 3.46 and in Fig. 3.41.
The agreement with the experimental spectrum is quite satisfactory.

^{208}Pb					
excitation	LM	LMtt	FR	FRtt	exp
3^-	2.63	2.63	2.64	2.63	2.63
5^-	3.41	3.43	3.46	3.47	3.20
4^-	3.52	3.50	3.50	3.49	3.48
5^-	3.79	3.79	3.86	3.86	3.71
6^-	4.04	4.04	4.03	4.03	3.92
2^-	4.30	4.21	4.23	4.20	4.23
9^+	5.14	5.11	5.11	5.09	5.01
9^+	5.61	5.62	5.59	5.60	5.26
0^-	5.64	5.38	5.54	5.42	5.28
11^+	5.25	5.20	5.14	5.12	5.29
1^+	5.92	5.89	5.72	5.70	5.85
11^+	5.88	5.89	5.86	5.87	5.86
10^-	6.64	6.56	6.57	6.53	6.28
12^-	6.66	6.61	6.57	6.54	6.43
14^-	6.99	6.84	6.66	6.59	6.74
10^-	7.44	7.22	7.32	7.23	6.88
12^-	7.72	7.55	7.41	7.32	7.08
1^+	7.38	6.77	7.64	7.48	7.30

Table 3.46: Low excited states energies of ^{208}Pb in MeV

We start analysing the 3^- excited state described by Tab. 3.47 and Figs. 3.42 and 3.43.

3^- (2.63 MeV)		LM		$LMtt$		FR		$FRtt$	
ω		2.63		2.63		2.64		2.63	
transition	ϵ_p -ϵ_h	X	Y	X	Y	X	Y	X	Y
$[(1h_{9/2})(2d_{3/2})^{-1}]_\pi$	4.58	-0.37	0.10	0.37	-0.10	-0.30	0.08	-0.30	0.08
$[(2f_{7/2})(3s_{1/2})^{-1}]_\pi$	5.13	-0.28	0.09	0.28	-0.09	-0.30	0.01	-0.30	0.10
$[(2g_{9/2})(2f_{7/2})^{-1}]_\nu$	5.77	0.20	-0.07	-0.20	0.07	0.20	-0.08	0.20	-0.8
$[(2g_{9/2})(3p_{3/2})^{-1}]_\nu$	4.33	0.36	-0.09	-0.35	0.09	0.40	-0.01	0.39	-0.10
$[(1i_{11/2})(2f_{5/2})^{-1}]_\nu$	4.78	-0.49	0.15	0.49	-0.15	-0.48	0.14	-0.48	0.14
$[(1i_{15/2})(1i_{11/2})^{-1}]_\nu$	6.49	-0.32	0.13	0.32	-0.13	-0.24	0.10	-0.24	0.10

Table 3.47: Main ph pairs for the first 3^- state and their X and Y amplitudes calculated with the four interactions.

Our study of the magnetic excitations is related to the availability of electron scattering data. We start our study by considering the first two 9^+ states whose main ph transition pairs are presented in Tabs. 3.48 and Tab. 3.49. The RPA transverse responses are compared to the experimental data in Fig. 3.44.

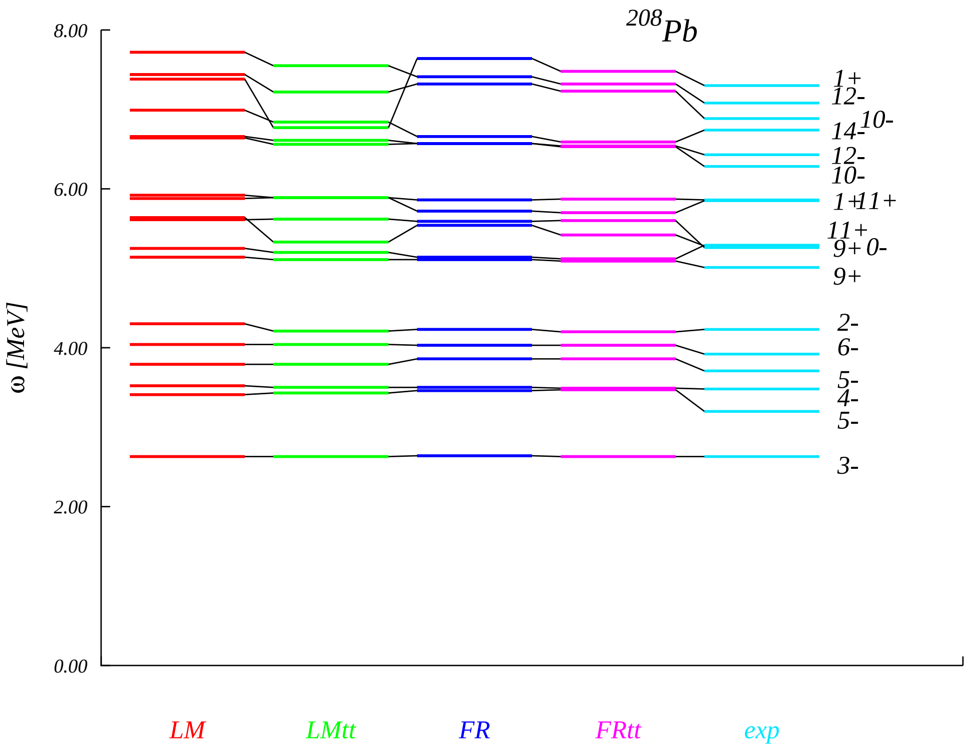

Figure 3.41: ^{208}Pb spectrum

The transverse responses of the lower state present three peaks in the region covered by the data, and this behaviour looks compatible with the distribution of the data. On the other hand the position of the experimental points of the other state is very different from the shape of the theoretical responses.

9^+ (5.01 MeV)		LM		$LMtt$		FR		$FRtt$	
ω		5.14		5.11		5.11		5.09	
transition	ϵ_p -ϵ_h	X	Y	X	Y	X	Y	X	Y
$[(2g_{9/2})(1i_{13/2})^{-1}]_\nu$	5.07	-0.98	0.01	0.99	0.00	-0.99	0.00	-0.99	0.00
$[(1j_{15/2})(3p_{3/2})^{-1}]_\nu$	5.75	-0.11	0.00	0.08	0.00	0.07	0.00	0.05	0.00

Table 3.48: Main ph pairs for the first 9^+ state and their X and Y amplitudes calculated with the four interactions.

9^+ (5.26 MeV)		LM		$LMtt$		FR		$FRtt$	
ω		5.61		5.62		5.59		5.60	
transition	ϵ_p -ϵ_h	X	Y	X	Y	X	Y	X	Y
$[(1h_{9/2})(1h_{11/2})^{-1}]_\pi$	5.57	-0.99	0.00	0.98	0.00	0.99	0.00	0.99	0.00

Table 3.49: Main ph pairs for the second 9^+ states and their X and Y amplitudes calculated with the four interactions.

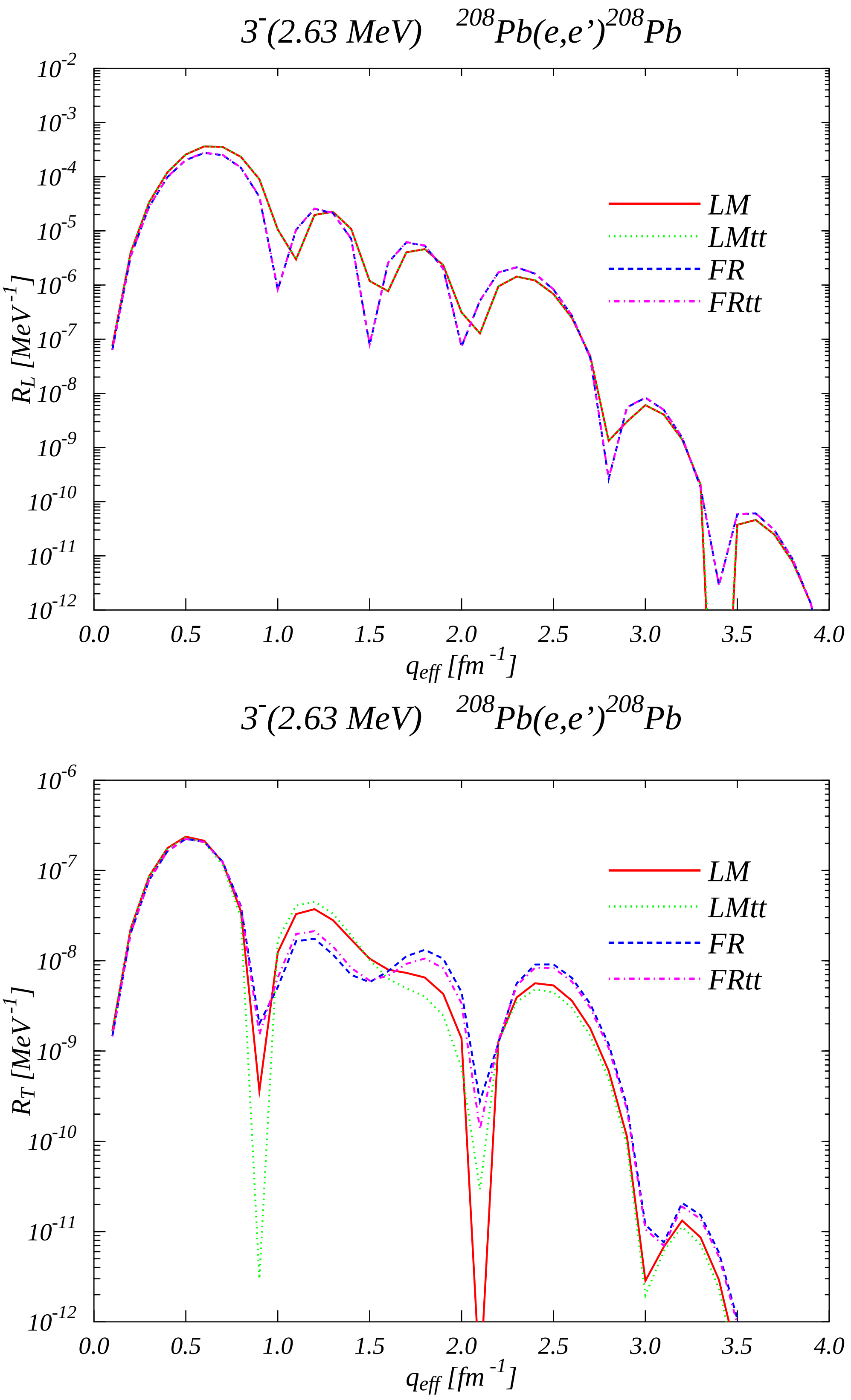

Figure 3.42: Longitudinal and transverse response of the first 3^- in ^{208}Pb.

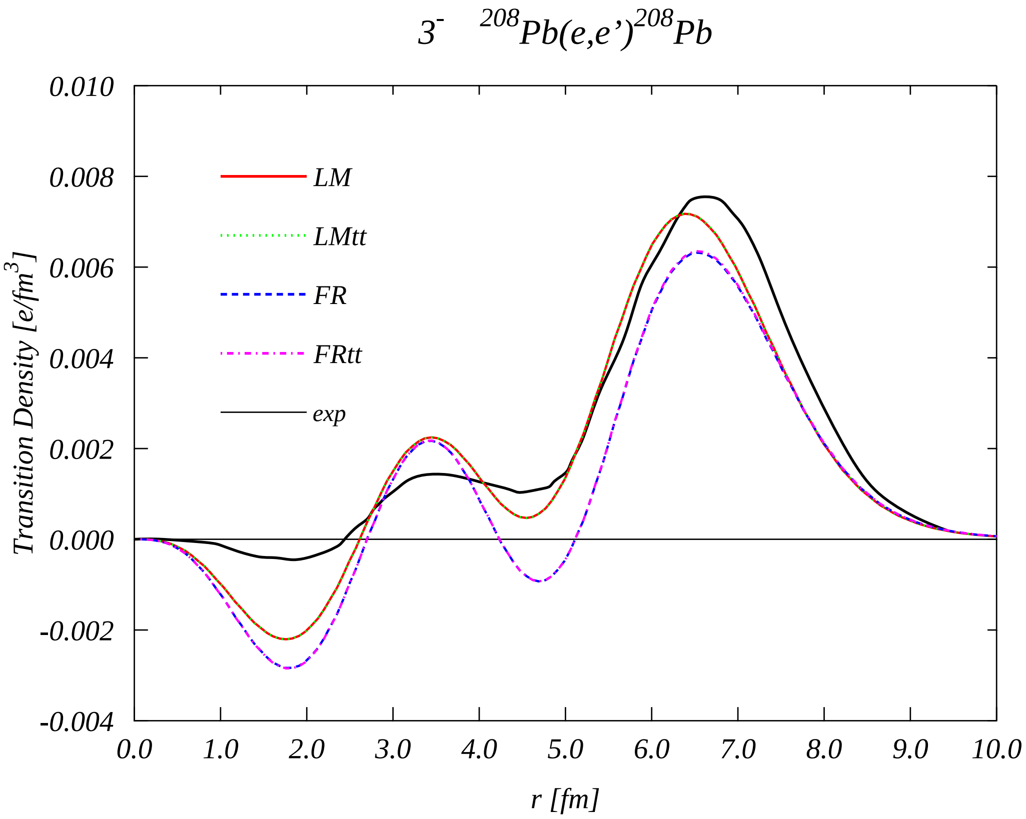

Figure 3.43: Transition density for the low excited 3^- state of ^{208}Pb. Experimental data from cite [61]

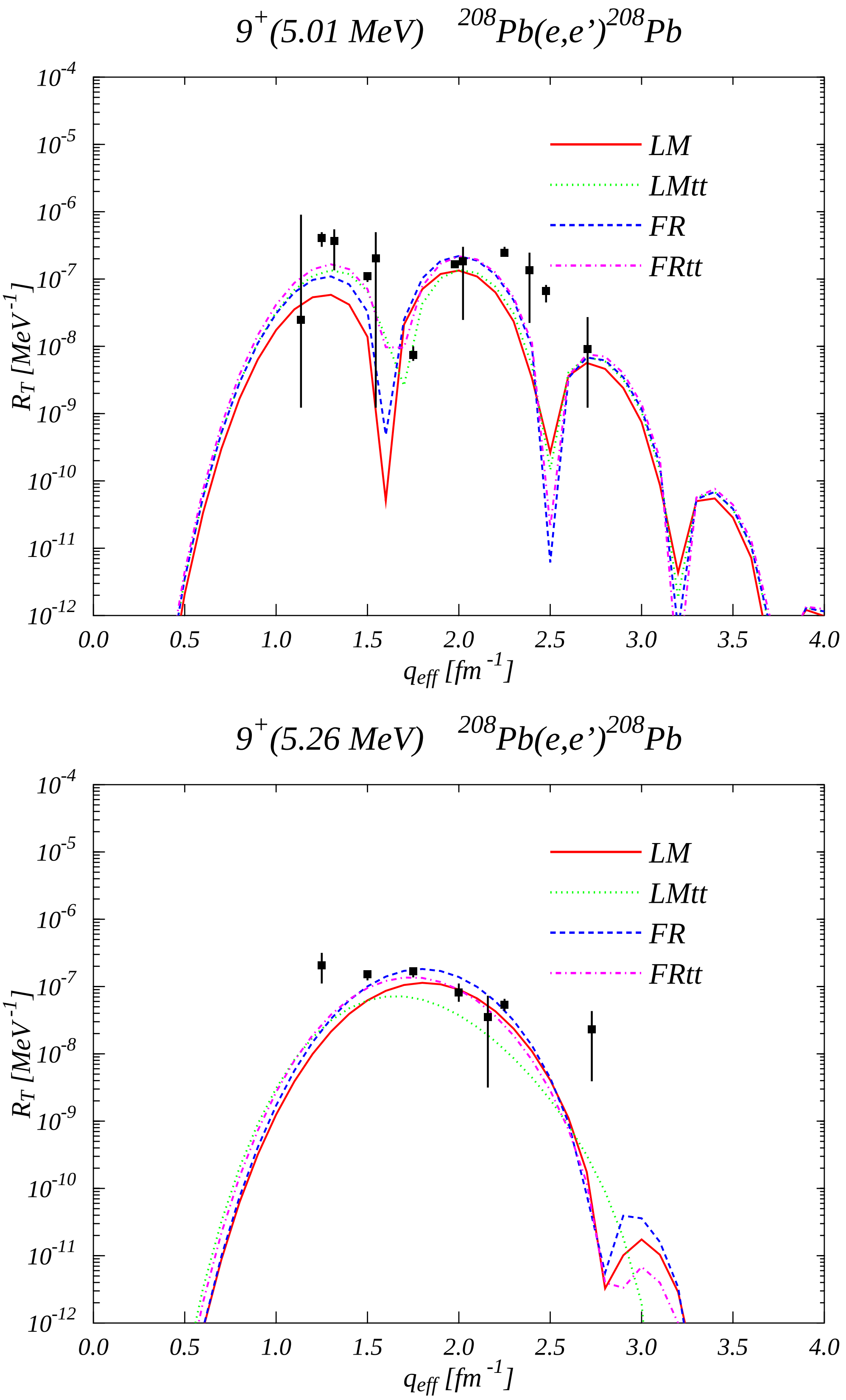

Figure 3.44: Transverse form factor of the first two 9^+ excited states for ^{208}Pb compared with the experimental data [62]

The information about the 11^+ states are given in Tabs. 3.50 and 3.51 and Fig. 3.45.

11^+ (5.29 MeV)		*LM*		*LMtt*		*FR*		*FRtt*	
ω		5.25		5.20		5.14		5.12	
transition	ϵ_p -ϵ_h	X	Y	X	Y	X	Y	X	Y
$[(2g_{9/2})(1i_{13/2})^{-1}]_\nu$	5.07	0.99	0.02	-0.99	-0.01	-1.00	0.01	-1.00	0.00

Table 3.50: Main ph pairs for the first 11^+ state and their X and Y amplitudes calculated with the four interactions.

11^+ (5.86 MeV)		*LM*		*LMtt*		*FR*		*FRtt*	
ω		5.88		5.89		5.86		5.87	
transition	ϵ_p -ϵ_h	X	Y	X	Y	X	Y	X	Y
$[(1i_{11/2})(1i_{13/2})^{-1}]_\nu$	5.84	-1.00	0.00	-1.00	0.00	-1.00	0.00	1.00	0.00

Table 3.51: Main ph pairs for the second 11^+ state and their X and Y amplitudes calculated with the four interactions.

Our calculations indicate for these states an almost pure 1p-1h structure. On the other hand the comparison with the transverse response data indicates a more complicated structure of the lower energy 11^+ state. The other state seem to be better described by our calculations, even though it seems that a shift of our responses toward higher values of q is required.

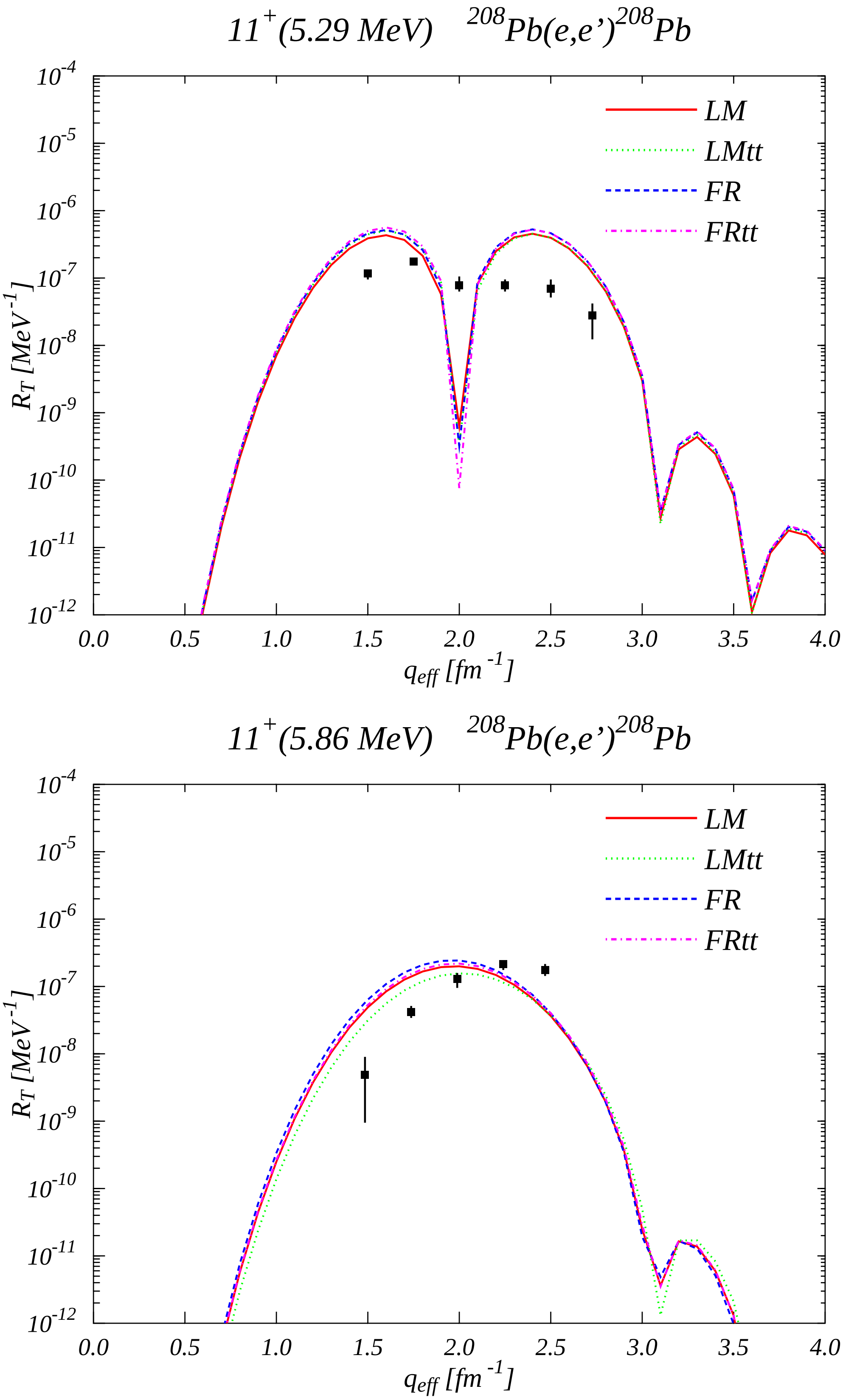

Figure 3.45: Transverse responses of 11^+ excited states in ^{208}Pb compared to experimental data [62].

The composition of the two first 1^+ states is presented in Tabs. 3.52, 3.53 and their responses are shown in Fig. 3.46 of ^{208}Pb.

1^+ (5.85 MeV)		LM		$LMtt$		FR		$FRtt$	
ω		5.92		5.89		5.72		5.70	
transition	ϵ_p -ϵ_h	X	Y	X	Y	X	Y	X	Y
$[(1h_{9/2})(1h_{11/2})^{-1}]_\pi$	5.57	-0.78	-0.02	-0.81	-0.02	-0.76	-0.01	-0.77	-0.01
$[(1i_{11/2})(1i_{13/2})^{-1}]_\nu$	5.84	-0.63	0.00	-0.58	0.00	-0.64	0.01	-0.64	0.01

Table 3.52: Main ph pairs for the first 1^+ state and their X and Y amplitudes calculated with the four interactions.

1^+ (7.30 MeV)		LM		$LMtt$		FR		$FRtt$	
ω		7.38		6.77		7.64		7.48	
transition	ϵ_p -ϵ_h	X	Y	X	Y	X	Y	X	Y
$[(1h_{9/2})(1h_{11/2})^{-1}]_\pi$	5.57	0.63	0.09	0.57	0.05	0.65	0.10	-0.64	-0.09
$[(1i_{11/2})(1i_{13/2})^{-1}]_\nu$	5.84	-0.78	-0.09	-0.80	-0.06	-0.77	-0.10	0.77	0.09

Table 3.53: Main ph pairs for the second 1^+ state and their X and Y amplitudes calculated with the four interactions.

In this case we can see that the responses obtained with LM, FR and FRtt are very similar. The inclusion of the tensor channel in the FR interaction does not change the response. There are instead large differences when we use the residual interaction LMtt, expecially at low momentum. In this case the response is rather different from that obtained without tensor channel. The same effect can be observed in the second 1^+ state, but here the differences show up at high transferred momenta.

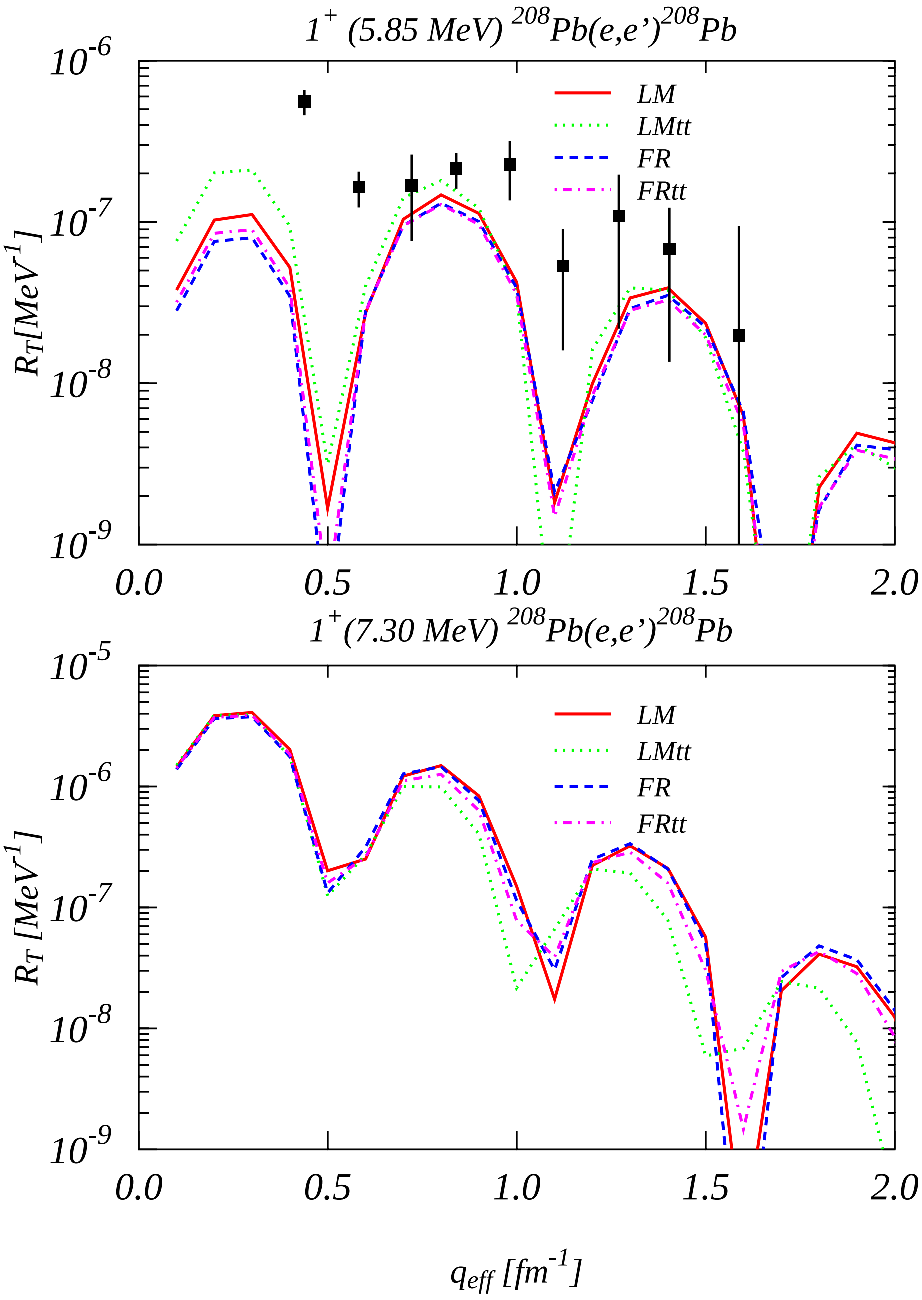

Figure 3.46: Transverse response of 1^+ excited states in ^{208}Pb compared to experimental data [63].

The information about the first two 10^- states is given in Tab. 3.54 and Tab. 3.55, and in Fig. 3.47 we show the transverse responses.

10^- (6.28 MeV)		LM		$LMtt$		FR		$FRtt$	
ω		6.64		6.56		6.57		6.53	
transition	ϵ_p -ϵ_h	X	Y	X	Y	X	Y	X	Y
$[(1i_{13/2})(1h_{11/2})^{-1}]_\pi$	7.18	0.20	0.00	0.05	0.00	-0.15	0.00	0.08	0.00
$[(1j_{15/2})(1i_{13/2})^{-1}]_\nu$	6.49	0.97	-0.01	0.99	0.00	-0.99	0.01	0.99	0.00

Table 3.54: Main ph pairs for the first 10^- state and their X and Y amplitudes calculated with the four interactions.

10^- (6.88 MeV)		LM		$LMtt$		FR		$FRtt$	
ω		7.44		7.22		7.32		7.23	
transition	ϵ_p -ϵ_h	X	Y	X	Y	X	Y	X	Y
$[(1i_{13/2})(1h_{11/2})^{-1}]_\pi$	7.18	-0.97	0.02	-0.93	0.00	0.99	-0.01	0.97	0.00

Table 3.55: Main ph pairs for the second 10^- state and their X and Y amplitudes calculated with the four interactions.

In general the transverse responses are reproduced in magnitude by RPA calculations (Fig. 3.47). This case is very interesting because, when we analyse the transverse response we can observe that only the presence of tensor channel can reproduce the second maximum in both states.

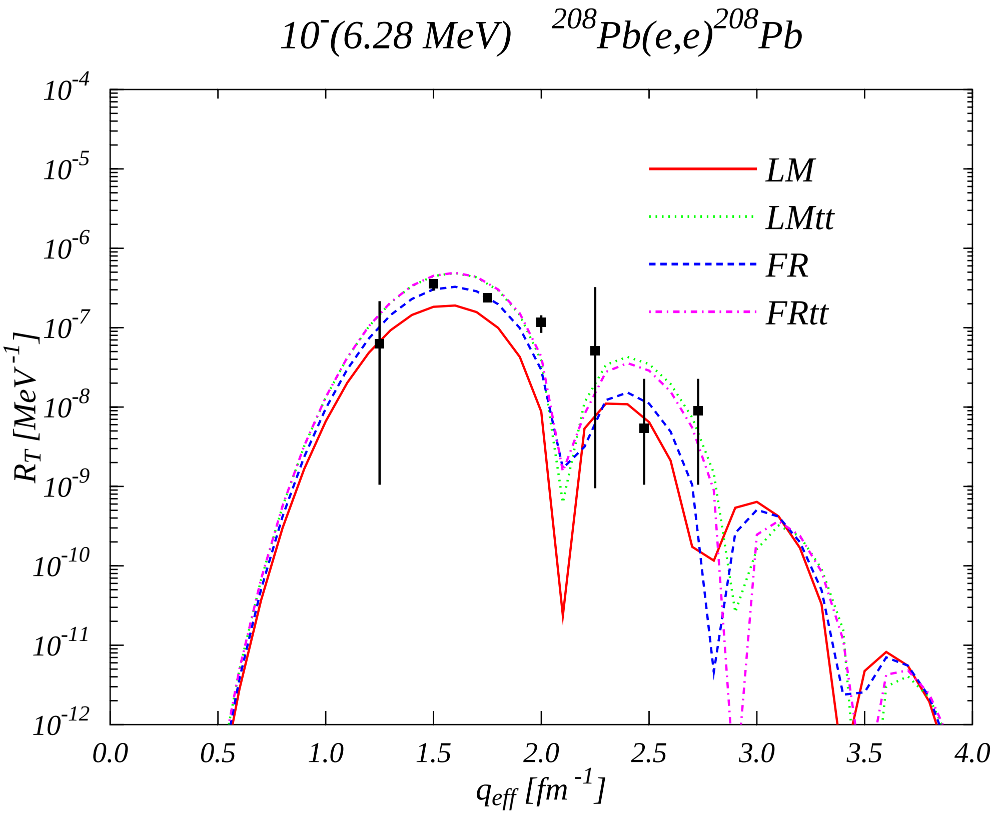

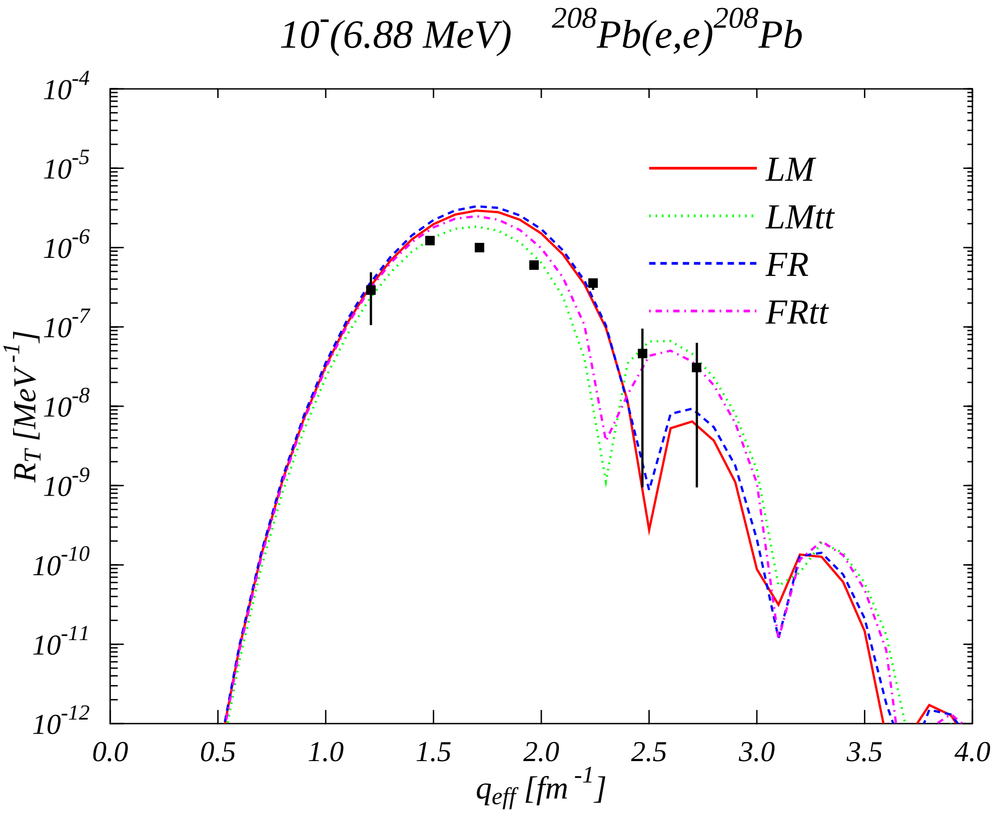

Figure 3.47: Transverse form factor of the 10^- states in ^{208}Pb compared with experimental data [62].

The 12^- and 14^- states have been widely studied because of their apparently simple structure. The ph description of the 12^- states is presented in Tabs. 3.56 and 3.57. Both states are mainly composed by two ph pairs, a proton and a neutron ph pair. The lowest energy state is neutron dominated, the other one is proton dominated.

12^- (6.43 MeV)		LM		$LMtt$		FR		$FRtt$	
ω		6.66		6.61		6.57		6.54	
transition	ϵ_p -ϵ_h	X	Y	X	Y	X	Y	X	Y
$[(1i_{13/2})(1h_{11/2})^{-1}]_\pi$	7.18	0.25	0.01	-0.16	0.00	-0.18	-0.01	0.11	0.00
$[(1j_{15/2})(1i_{13/2})^{-1}]_\nu$	6.49	0.96	-0.01	-0.99	0.01	-0.98	0.01	0.99	0.00

Table 3.56: Main ph pairs for the first 12^- state and their X and Y amplitudes calculated with the four interactions.

12^- (7.08 MeV)		LM		$LMtt$		FR		$FRtt$	
ω		7.72		7.55		7.41		7.32	
transition	ϵ_p -ϵ_h	X	Y	X	Y	X	Y	X	Y
$[(1i_{13/2})(1h_{11/2})^{-1}]_\pi$	7.18	-0.96	0.03	0.99	-0.02	0.98	0.01	0.99	-0.01
$[(1j_{15/2})(1i_{13/2})^{-1}]_\nu$	6.49	0.25	-0.02	-0.16	0.01	-0.18	0.01	-0.11	0.01

Table 3.57: Main ph pairs for the second 12^- state and their X and Y amplitudes calculated with the four interactions.

The transverse responses are compared to the experimental data in Fig. 3.48. The response of the proton state is reasonably well reproduced but for an possible quenching factor. In this case our RPA responses produce very similar results. The situation is remarkably different for the first 12^- state. In this case, finite range and tensor force strongly affect the response which changes in size by almost an order of magnitude.

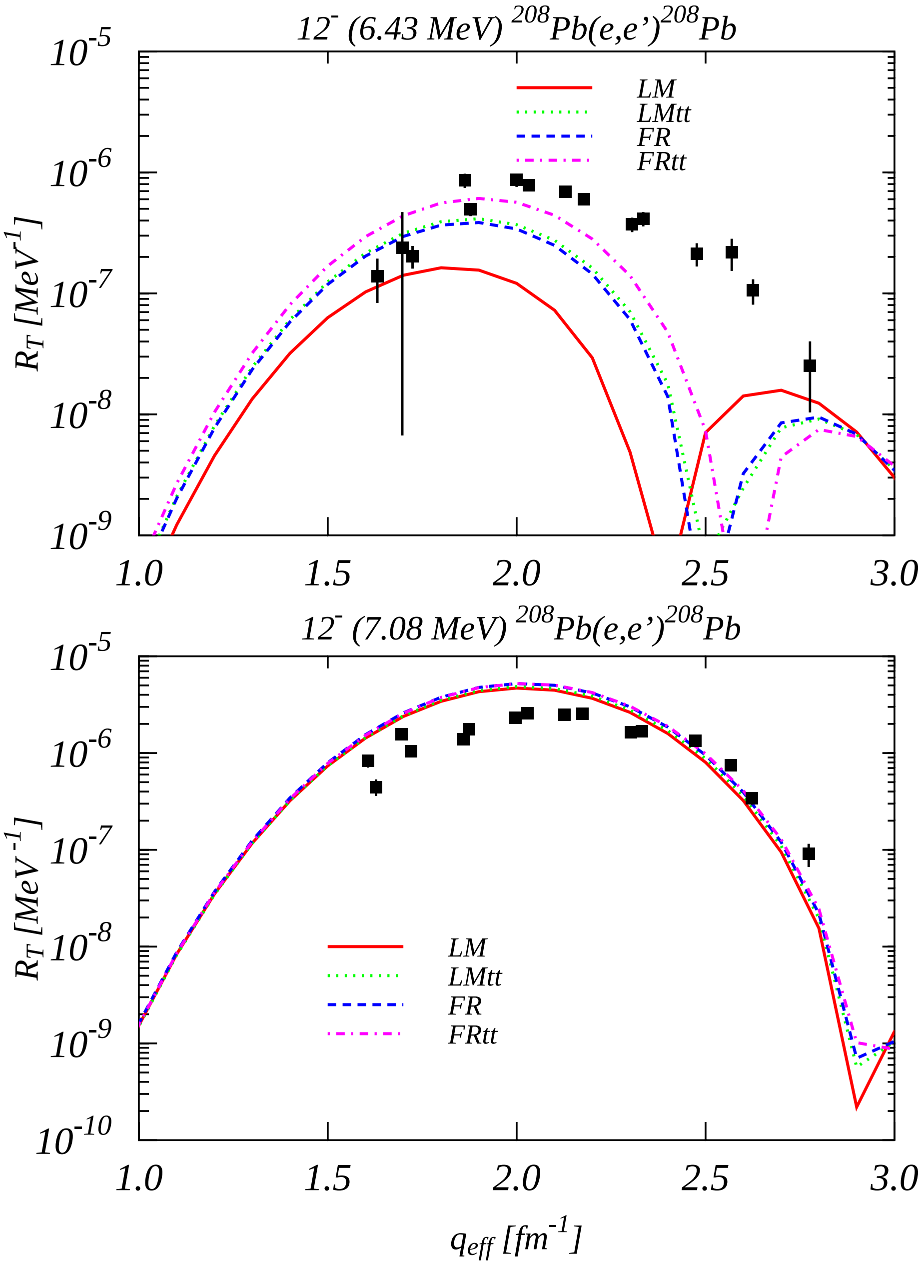

Figure 3.48: Transverse response for 12^- excited states in ^{208}Pb. Experimental data from [64]

The 14^- excited state is almost a pure single particle state as indicated in Tab. 3.58.

14^- (6.74 MeV)		*LM*		*LMtt*		*FR*		*FRtt*	
ω		6.99		6.84		6.66		6.59	
transition	ϵ_p -ϵ_h	X	Y	X	Y	X	Y	X	Y
$[(1j_{15/2})(1i_{13/2})^{-1}]_\nu$	6.49	-1.00	0.04	-1.00	0.03	-1.00	0.13	-1.00	0.01

Table 3.58: Main ph pairs for the first 14^- states and their X and Y amplitudes calculated with the four interactions.

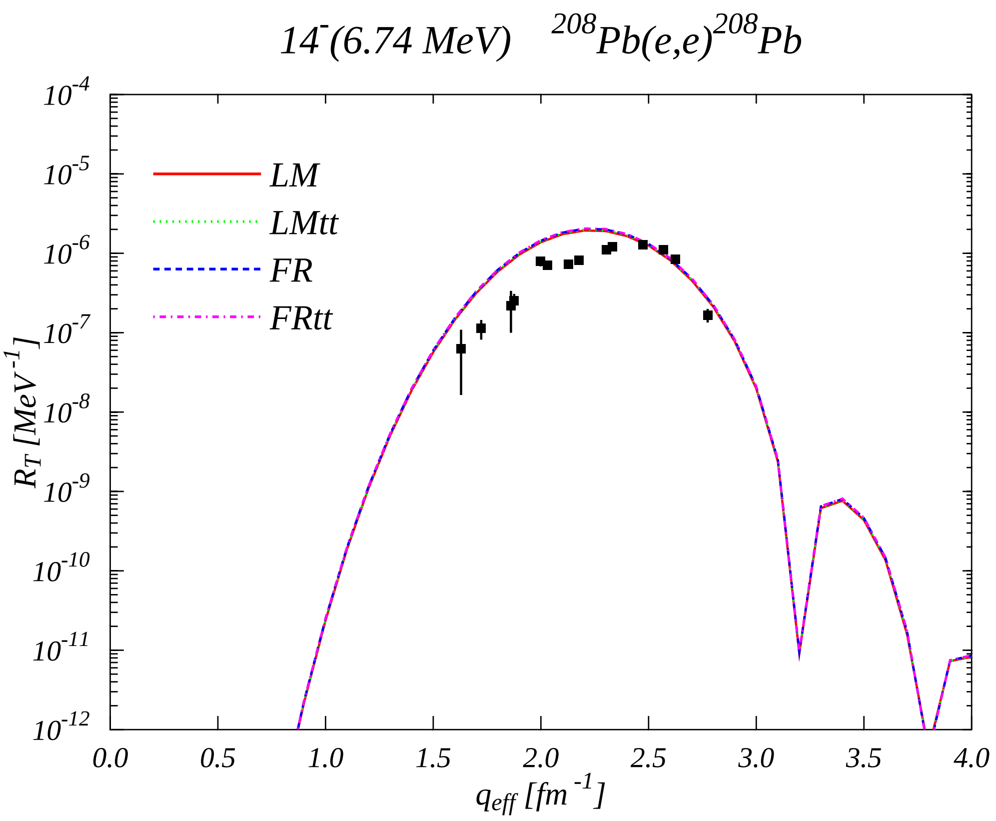

Figure 3.49: Transverse form factor of the 14^- state in ^{208}Pb. Data from [64]

The transverse responses are compared in Fig. 3.49 with the data. As in the protons 12^- case, the shape is reasonably well reproduced, even though a quenching factor is necessary. No sensitivity to the details of the residual interaction is shown.

3.4 Conclusions

We give now some closing remarks:

1. The use of the discrete RPA should be limited to the description of excited states dominated by bound ph pairs. For example we have seen that the 0^+, 2^+ and 4^+ excited states of ^{16}O can't be described with these techniques, on the contrary we obtain good descriptions of states dominated by the excitation of a bound particle. For example the 3^- and 4^- response of ^{16}O, the electric excitation 2^+ and 3^- of ^{12}C and the magnetic 4^- and 1^+ and so on.

2. Comparison with (e, e') data is necessary to have a better test of our solutions.

3. The finite range and tensor components produce seldom remarkable effects. We have seen strong sensitivity to the tensor component and finite range of the interaction in neutrino and antineutrino cross section of ^{16}O. The first 3^- excited state of ^{40}Ca seems to be influenced by the finite range of the interaction, especially the transverse response. The second 3^- state shows to be sensitive to the finite range of the interaction but also to the tensor channel. This is more evident in the transverse response. The same happens for the third 3^- and for the second 2^- and 4^-. For ^{48}Ca we observe remarkable sensitivity to the tensor and finite range interaction in the 2^- and 6^- excited states. Also the transition densities of 2^+ and 4^+ of ^{90}Zr show sensitivity to the finite range of the interaction but not to the tensor contribution. The same happens for the 3^- transition density of ^{208}Pb. Particularly interesting is the case of 10^- and 12^- of ^{208}Pb that show different responses with and without the tensor channel and using a zero range or a finite range interaction.

We have to remember that, because of their phenomenological input, the RPA results obtained within the LMFFS are the best one can expect in terms of comparison with experimental data. The prediction power of this approach is limited to the nuclei where s.p. energies, charge distributions, or at least *rms* charge radii, are known.

Chapter 4

RPA approach for hypernuclei

An interesting application of the RPA theory is the study of hypernuclei. The first experimental information about hypernuclei regarded their identification and the energy of the hyperon embedded in the nuclear medium. The improvement of the experimental techniques allows the measurement of high-quality excitation spectra. Hypernuclei excitations have been induced by (π^+,K^+) [65, 66, 67, 68], (K^-,π^-) [69, 70, 71] or $(e, e'K^+)$ [72, 73, 74] reactions. Another advance in the study of the excitation spectrum of hypernuclei is the γ-ray spectroscopy which will become a standard investigation tool in the future [75, 76].

A single Λ-hyperon hypernucleus, which we shall call hypernucleus henceforth, can be viewed as a many-body system of nucleons containing an impurity. In the mean-field (MF) approximation, the properties of the hypernucleus are determined only by those of the hyperon which moves in the average potential generated by the interaction with the nucleons. This model is quite successful in reproducing the binding energies of the hyperon in various medium-heavy nuclei [77].

While the energy of the hyperon in the nucleus is a single particle property, the excitation spectrum of the hypernucleus is a property related to the system as a whole.

We want to investigate, with RPA theory, the possible presence of collective phenomena in the spectrum of some hypernuclei. In our model, the hypernucleus is formed when a nucleon, from its state below the Fermi surface, a hole state, is transformed into a Λ which lies in one specific single particle state, named particle state. In the MF framework the hypernucleus spectrum is produced by single nucleon-Λ, i.e. particle-hole, excitation. In our model, the excited state of the hypernucleus is a combination of various particle-hole excitations. This combination is ruled by the residual Λ-nucleon interaction. The relevance of the residual interaction, and therefore the possible presence of collective phenomena, is investigated by comparing MF results with those obtained by our model.

In the next section we present some details of the model applied to hypernuclei. In Sect. 4.2 we indicate how the choice of the input of our calculations has been done. This input is composed, in addition to the set of single particle wave functions and energies, by the Λ-nucleon interactions. In this section we discuss briefly the role played in our model by the ground state correlations. A selected set of results concerning hypernuclei obtained from doubly-closed shell nuclei is discussed in Sect. 4.3. Finally, in Sect. 4.4 we summarize the basic findings of our study.

4.1 The formalism

In our model, the formation of a hypernucleus is described as a transition from the ground state of a nucleus to a state of a new baryonic system, where one nucleon has been transformed into a hyperon, which in our work is always a Λ. The strangeness contents of the nuclear system are changed, but we suppose they are compensated by the change of strangeness of the external probe which induces the transition. The operator describing the state of the hypernucleus satisfies the equations

$$Q^\dagger_\nu|\Psi_0>=|\Psi_\nu> \; ; \; Q_\nu|\Psi_0>=0 \; , \tag{4.1}$$

where the second equation defines the nuclear ground state. In our model, the operator $Q^\dagger_\nu$ is defined as

$$Q^\dagger_\nu = \sum_{\Lambda h} \left(W^\nu_{\Lambda h} a^\dagger_\Lambda a_h - Z^\nu_{\Lambda h} a^\dagger_h a_\Lambda \right) \ , \tag{4.2}$$

where we have indicated with $a^\dagger$ and a the creation and annihilation operators, respectively. The use of creation and annihilation operators implies the existence of a single particle wave functions basis. These wave functions describe the motion of each baryon in a mean field potential. All the baryons below the Fermi surface are nucleons, and we label them with a h, for hole. Above the Fermi surface we have hyperonic states labeled as Λ. We have indicated with W and Z the RPA amplitudes, which in our calculations are real numbers.

We write the hamiltonian describing the system as

$$H = \sum_{\alpha\alpha'} T_{\alpha\alpha'} a^\dagger_\alpha a_{\alpha'} + \frac{1}{4} \sum_{\alpha\alpha'\beta\beta'} \overline{V}_{\alpha\alpha'\beta\beta'} a^\dagger_\alpha a^\dagger_{\alpha'} a_{\beta'} a_\beta \ , \tag{4.3}$$

where the first term represents the kinetic energy, the bar over the interaction V indicates that both direct and exchange terms are considered, and the greek subindexes can assume the h or Λ labels.

We obtain RPA-like equations by applying the equation of motion method [39] together with the definitions (4.1,4.2) of the excitation operator and (4.3) of the hamiltonian:

$$W_{\Lambda h}(\epsilon_\Lambda - \epsilon_h) + \sum_{\Lambda' h'} \overline{V}_{\Lambda h' h \Lambda'} W_{\Lambda' h'} + \sum_{\Lambda' h'} \overline{V}_{\Lambda\Lambda' h h'} Z_{\Lambda' h'} = \omega W_{\Lambda' h'} \tag{4.4}$$

$$Z^*_{\Lambda h}(\epsilon_\Lambda - \epsilon_h) + \sum_{\Lambda' h'} \overline{V}_{\Lambda h' h \Lambda'} Z^*_{\Lambda' h'} + \sum_{\Lambda' h'} \overline{V}_{\Lambda\Lambda' h h'} W^*_{\Lambda' h'} = -\omega\nu Z^*_{\Lambda' h'} \ . \tag{4.5}$$

As it can be seen from the explicit expression of the operator $Q^\dagger_\nu$, Eq. (4.2), the Z amplitudes are related to ground state correlations. Particle-hole models analogous to the one we have just presented have been used in the past [78, 79] to describe hypernuclei, but the presence of the Z amplitudes was not considered. A discussion on the relevance of the ground state correlations introduced by the Z amplitudes is done in section 4.2. The angular momentum coupled amplitudes are defined in terms of the uncoupled ones as

$$W^J_{\Lambda h} = \sum_{m_\Lambda m_h} < j_\Lambda m_\Lambda j_h m_h | JM > W_{\Lambda h} \tag{4.6}$$

$$Z^J_{\Lambda h} = \sum_{m_\Lambda m_h} < j_\Lambda m_\Lambda j_h m_h | J - M > (-1)^{J-M} Z_{\Lambda h} \ . \tag{4.7}$$

In the above equations the j's indicate the total angular momentum characterizing the single particle wave function and the m's their z-axis components.

We define the matrix elements

$$H_{\Lambda h \Lambda' h'} = (\epsilon_\Lambda - \epsilon_h)\delta_{\Lambda\Lambda'}\delta_{hh'} + \overline{V}_{\Lambda h' h \Lambda'} \tag{4.8}$$

$$I_{\Lambda h \Lambda' h'} = \overline{V}_{\Lambda\Lambda' h h'} \ , \tag{4.9}$$

and we can express them as

$$H^J_{\Lambda h \Lambda' h'} = \epsilon_\Lambda - \epsilon_h + v^J_{\Lambda h \Lambda' h'} \tag{4.10}$$

$$I^J_{\Lambda h \Lambda' h'} = u^J_{\Lambda h \Lambda' h'} \ , \tag{4.11}$$

where we have defined

$$\begin{aligned} v^J_{\Lambda h \Lambda' h'} &= v^{Jdir}_{\Lambda h \Lambda' h'} - v^{Jexch}_{\Lambda h \Lambda' h'} \\ = &\sum_K (-1)^{j_h + j_{\Lambda'} + K} \hat{K} \left\{ \begin{array}{ccc} j_\Lambda & j_h & J \\ j_{\Lambda'} & j_{h'} & K \end{array} \right\} \\ &[< j_\Lambda j_{h'} K || V || j_h j_{\Lambda'} K > -(-1)^{j_h + j_{\Lambda'} - K} < j_\Lambda j_{h'} K || V || j_{\Lambda'} j_h K >] \ , \end{aligned} \tag{4.12}$$

and

$$u^J_{\Lambda h\Lambda' h'} = u^{Jdir}_{\Lambda h\Lambda' h'} - u^{Jexch}_{\Lambda h\Lambda' h'} = (-1)^{j_{h'}-j_{\Lambda'}-J} v^J_{\Lambda h h'\Lambda'} \ . \tag{4.13}$$

The calculation of the interaction matrix elements is done by using the Fourier transform of the interaction expressed in momentum space

$$v(|\mathbf{r}_1 - \mathbf{r}_2|) = \frac{1}{(2\pi)^3} \int d\mathbf{q} e^{i\mathbf{q}\cdot|\mathbf{r}_1-\mathbf{r}_2|} [F_\Lambda(q) + G_\Lambda(q)\boldsymbol{\sigma}(1)\cdot\boldsymbol{\sigma}(2) + H_\Lambda(q)S_{12}] \tag{4.14}$$

where we have used $q \equiv |\mathbf{q}|$. The explicit expressions of the matrix elements for the various terms of the interaction are given in the Appendix.

The solution of Eqs. (4.4), (4.5) provides the excitation energies ω and also the wave function of the excited state. The matrix element of the one-body operator inducing the transition from the nucleus ground state to the hypernucleus excited state is given by:

$$< J|T_J|0 >= \sum_{\Lambda h} \Big[W^J_{\Lambda h} < j_\Lambda||T_J||j_h > + (-1)^{J+j_\Lambda-j_h} Z^J_{\Lambda h} < j_h||T_J||j_\Lambda > \Big] \ . \tag{4.15}$$

For the natural parity states we calculate the transition matrix elements induced by the operator

$$T_J = j_J(qr)Y_{JM}(\Omega) \ , \tag{4.16}$$

therefore the matrix elements to be inserted in Eq. (4.15) are

$$< j_a||T_J||j_b >= \int drr^2 R^*_a(r)R_b(r)j_J(qr) < j_a||Y_J||j_b > \ , \tag{4.17}$$

For the unnatural parity states we use the operators

$$T_{L=J\pm1} = j_L(qr)\left[Y_L(\Omega)\otimes\boldsymbol{\sigma}(1)\right]^J_M \ , \tag{4.18}$$

therefore the matrix elements to be inserted in Eq. (4.15) are

$$< j_a||T_L||j_b >= \int drr^2 R^*_a(r)R_b(r)j_L(qr) < j_a||\left[Y_L(\Omega)\otimes\boldsymbol{\sigma}(1)\right]^J||j_b > \ , \tag{4.19}$$

We use standard techniques [39, 80], to obtain the expression of the transition matrix elements between two excited states of the hypernucleus

$$\begin{aligned} & < \Phi_\nu|(EM)|\Phi'_\nu > \\ = & \sum_{\Lambda h}\sum_{\Lambda' h'} \delta_{hh'} \left[W^\nu_{\Lambda h} W^{\nu'}_{\Lambda' h'} < \Lambda|(EM)|\Lambda' > - Z^\nu_{\Lambda h} Z^{\nu'}_{\Lambda' h'} < \Lambda'|(EM)|\Lambda > \right] \\ - & \sum_{\Lambda h}\sum_{\Lambda' h'} \delta_{\Lambda\Lambda'} \left[W^\nu_{\Lambda h} W^{\nu'}_{\Lambda' h'} < h'|(EM)|h > - Z^\nu_{\Lambda h} Z^{\nu'}_{\Lambda' h'} < h|(EM)|h' > \right] \ . \end{aligned} \tag{4.20}$$

where we have indicated with (EM) the one-body electromagnetic operator inducing natural or unnatural multipole transitions.

We calculate the electromagnetic transitions between two states of the hypernucleus by using the expression [81]

$$\mathcal{T}^L_{if} = \frac{4k}{\hbar c^2(2J_i+1)(2L+1)} |\langle J_f||(EM)_L||J_i\rangle|^2 \tag{4.21}$$

where the indexes i and f indicate, respectively, the initial and final state of the transition, k is the modulus of the emitted photon momentum, and $(EM)_L$ is the electromagnetic operator, of

	V_0^λ(MeV)	V_{ls}^λ(MeV)	a_0^λ(fm)	a_{ls}^λ(fm)	R_0^λ(fm)	R_{ls}^λ(fm)
$^{12}_\Lambda$C	29.00	2.00	0.60	0.60	2.50	2.50
$^{16}_\Lambda$O	29.00	2.00	0.60	0.60	2.50	2.73
$^{40}_\Lambda$Ca	29.00	2.00	0.60	0.60	2.50	4.00
$^{90}_\Lambda$Zr	29.00	2.00	0.60	0.60	2.50	5.60
$^{208}_\Lambda$Pb	29.00	2.00	0.60	0.60	2.50	7.60

Table 4.1: Values of the Woods-Saxon potential parameters used in our work for the nuclei we have studied

multipolarity L. In the above equation, as before, the double bar indicates that we have to evaluate the reduced matrix element of the angular dependent part.

We find that, in the angular momentum coupling scheme, the reduced transition matrix element between the two excited states *i.e.* Eq. (4.20), can be written as

$$
\begin{aligned}
&< J||(EM)_L||J' >= \hat{J}\hat{J}' \sum_{\Lambda h} \sum_{\Lambda' h'} \Bigg\{ \delta_{hh'} \left\{ \begin{array}{ccc} J' & L & J \\ j_\Lambda & j_h & j_{\Lambda'} \end{array} \right\} \\
&\Big[(-1)^{j_\Lambda + j_h + J' + L} W^J_{\Lambda h} W^{J'}_{\Lambda' h'} < j_\Lambda ||(EM)_L|| j_{\Lambda'} > \\
&-(-1)^{j_{\Lambda'} + j_{h'} + J'} Z^J_{\Lambda h} Z^{J'}_{\Lambda' h'} < j_{\Lambda'} ||(EM)_L|| j_\Lambda > \Big] \\
&-\delta_{\Lambda\Lambda'} \left\{ \begin{array}{ccc} L & J' & J \\ j_\Lambda & j_h & j_{h'} \end{array} \right\} \\
&\Big[(-1)^{j_{\Lambda'} + j_h + J} W^J_{\Lambda h} W^{J'}_{\Lambda' h'} < j_{h'} ||(EM)_L|| j_h > \\
&-(-1)^{j_\Lambda + j_{h'} + J' + L} Z^J_{\Lambda h} Z^{J'}_{\Lambda' h'} < j_h ||(EM)_L|| j_{h'} > \Big] \Bigg\} \, . \qquad (4.22)
\end{aligned}
$$

The expressions of the single particle matrix elements for natural parity (electric), and unnatural parity (magnetic) transitions, are given in E.

4.2 Details of the calculations

We have applied the formalism described in the previous section to calculate the excitation spectrum of single Λ hypernuclei formed by the excitation of nucleonic doubly closed shell nuclei. Specifically, we have investigated the $^{12}_\Lambda$C , $^{16}_\Lambda$O , $^{40}_\Lambda$Ca , $^{90}_\Lambda$Zr and $^{208}_\Lambda$Pb hypernuclei.

In analogy to what is done in the application of the LMFFS, the mean field is described by a phenomenological potential, in our case a spherical Woods-Saxon well, of the form

$$
\begin{aligned}
U^t(r) &= \frac{-V_0^t}{1 + \exp\left[\left(r - R_0^t\right)/a_0^t\right]} \\
&- \left[\frac{\hbar c}{m_\pi c^2}\right]^2 \left(\frac{V_{ls}^t}{a_{ls}^t\, r}\right) \frac{\exp\left[\left(r - R_{ls}^t\right)/a_{ls}^t\right]}{\left\{1 + \exp\left[\left(r - R_{ls}^t\right)/a_{ls}^t\right]\right\}^2} \, \mathbf{l} \cdot \boldsymbol{\sigma} - V_C^t(r) \, , \qquad (4.23)
\end{aligned}
$$

where m_π is the pion mass and the Coulomb term $V_C^t(r)$, active only for protons, is that produced by a homogeneous charge distribution.

For the nucleonic part we use the parameterizations given in sect. 1.1.

We use a spherical Woods-Saxon well also to describe the Λ mean field potentials with a set of parameters (Tab. 4.1) values very close to those given in [77].

We use V_0^Λ= 29.0 MeV, V_{ls}^Λ=2.0 MeV, and $a_0^\Lambda = a_{ls}^\Lambda$=0.6 fm for all the hypernuclei, and we change the radii in order to reproduce the ground state binding energies of the various hypernuclei. For ${}^{12}_{\Lambda}$C , ${}^{16}_{\Lambda}$O , ${}^{40}_{\Lambda}$Ca , ${}^{90}_{\Lambda}$Zr and ${}^{208}_{\Lambda}$Pb we use $R_0^\Lambda = R_{ls}^t$=2.50, 2.73, 4.00, 5.60, 7.60 fm, respectively.

The discretization of the continuum is obtained as explained in sect. 1.3. Since we are interested in the lowest excited states a proper description of the escape width is not necessary [44]. All the results discussed in sect. 4.3 have been obtained for excited states dominated by particle-hole transitions where the Λ is in a bound state.

Our calculations have been done with a configuration space which considers 54 single particle levels describing the Λ hyperon, up to the $5p_{1/2}$ level. This corresponds to consider 10 major harmonic oscillator shells. A comparison with results obtained with a smaller configuration space of only 22 states, up to the $3p_{1/2}$ level, shows differences in the eigenvalues of about 10, 20 keV.

As already indicated in Eq. (4.14), the residual interaction between Λ and the nucleons is considered to be a sum of scalar, spin and tensor terms

$$\begin{aligned} V_{\Lambda N} = V^c_{\Lambda N}(r) \quad &+ \quad V^\sigma_{\Lambda N}(r)\, \boldsymbol{\sigma}(\Lambda)\cdot\boldsymbol{\sigma}(N) \\ &+ \quad V^t_{\Lambda N}(r) \left[3\frac{(\boldsymbol{\sigma}(\Lambda)\cdot\mathbf{r})(\boldsymbol{\sigma}(N)\cdot\mathbf{r})}{\mathbf{r}^2} - \boldsymbol{\sigma}(\Lambda)\cdot\boldsymbol{\sigma}(N) \right] \ . \end{aligned} \tag{4.24}$$

In the above equations the symbol $\boldsymbol{\sigma}$ indicates the usual Pauli spin matrices and N the nucleon. With respect to the most commonly used expressions of the Λ-nucleon residual interaction [75], we do not consider the spin-orbit terms. The contribution of this term is rather small [82], and we consider it at the mean-field level by including a spin-orbit term in the Woods-Saxon potentials.

The sensitivity of our results to the Λ-nucleon interaction is tested by comparing the results obtained with three different parameterizations of the $V_{\Lambda N}^{c,\sigma,t}(r)$ functions. In a first parameterization, which we call LNδ, the three functions are considered of zero-range type

$$V_{\Lambda N}^{c,\sigma,t}(r) = U_{\Lambda N}^{c,\sigma,t}\,\delta(r) \ . \tag{4.25}$$

The values of the constants $U^{c,\sigma,t}$ are given in the first row of Tab. 4.2.

		c	σ	t
LNδ		20.0	70.0	-28.0
	w_1	-4.5	-1.26	15.0
LND	w_2	-104.0	-7.56	145.0
	w_3	590.0	182.0	1.0
	w_1	0.0	-1.0	8.0
LNDE	w_2	-92.0	-3.5	50.0
	w_3	518.0	90.0	100.0
	β_1	1.5	1.5	1.0
	β_2	0.9	0.9	0.6
	β_3	0.5	0.5	0.4

Table 4.2: Values of the parameters of the three Λ-nucleon interactions used in this work. The LNδ interaction is of zero range type, and, in the table, we indicate the values of the $U^{c,\sigma,t}$ parameters of Eq. (4.25) in MeV fm^3. The other two interactions have been constructed as indicated by Eqs. (4.26), and (4.27). The values of the w coefficients for the scalar (c) and spin (σ) channels are expressed in MeV, those of the tensor channel (t) in MeV fm^{-2}. The ranges of the gaussians β_i are the same for both LND and LNDE interactions and their values are expressed in fm.

For the other two interactions, in analogy to the YNG interaction [83, 84], we parametrize each radial term of the force (4.24) as a sum of three gaussians, specifically,

$$V_{\Lambda N}^{c,\sigma}(r) = \sum_{i=1,3} w_i^{c,\sigma} \exp[-(r/\beta_i^{c,\sigma})^2] \ , \tag{4.26}$$

for the scalar and spin terms, and

$$V^t_{\Lambda N}(r) = \sum_{i=1,3} w^t_i r^2 \exp[-(r/\beta^t_i)^2] \ , \tag{4.27}$$

for the tensor term.

The interaction LNδ and the finite range interaction we call LND in the following are used in calculations where only the direct terms of the interaction matrix elements, see Eq. (4.12), are considered, while we consider both direct and exchange terms when we use the finite range interaction we call LNDE. The values of the parameters of each interaction have been chosen to reproduce at best the energies of the first excited states of $^{16}_{\Lambda}$O . These parameters values are given in Tab. 4.2 and the momentum dependence of the three interactions is shown in Fig. 4.1. In Tab. 4.3, we compare the results of our calculations in $^{16}_{\Lambda}$O with the experimental values presented in Ref. [85]. In the table all the energies have been renormalized to the energy of the lowest state, which, in our calculations, is always the 0^-.

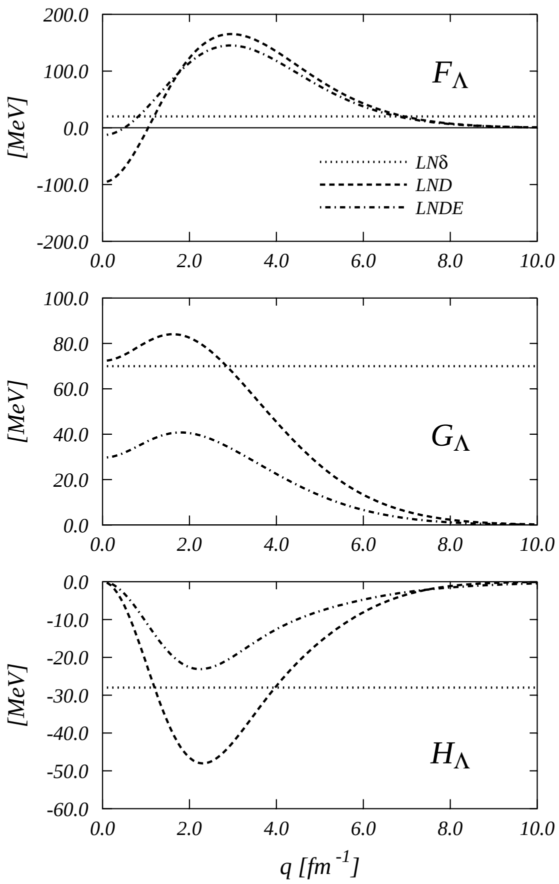

Figure 4.1: Momentum dependence of the Λ - nucleon interactions for each channel of Eq. (4.24). The $LN\delta$ zero-range interaction is constant in momentum space. The parameters of the other two interactions are given in Tab. 4.2.

In Tab. 4.3 we also show the results obtained in MF approximation. The MF spectrum shows a degeneracy between the 0^- and the first 1^-, which have the smallest energy. The energy of the second 1^- and the 2^- is already around 6 MeV. The residual interaction produces a relatively small shifts of an already reasonable mean-field spectrum.

		$^{16}_{\Lambda}$O				
J^π	p h	MF	LNδ	LND	LNDE	exp [85]
0^-	$(1s_{1/2})_\Lambda(1p_{1/2})_n^{-1}$	0.0	0.0	0.0	0.0	0.0
1_1^-	$(1s_{1/2})_\Lambda(1p_{1/2})_n^{-1}$	0.0	0.71	0.71	0.69	0.026
1_2^-	$(1s_{1/2})_\Lambda(1p_{3/2})_n^{-1}$	6.16	6.58	6.55	6.56	6.562
2^-	$(1s_{1/2})_\Lambda(1p_{3/2})_n^{-1}$	6.16	6.77	6.76	6.79	6.784
1^+	$(1p_{3/2})_\Lambda(1p_{1/2})_n^{-1}$	9.97	10.25	10.10	10.36	
2^+	$(1p_{3/2})_\Lambda(1p_{1/2})_n^{-1}$	9.97	10.33	10.39	10.43	
0^+	$(1p_{1/2})_\Lambda(1p_{1/2})_n^{-1}$	11.17	11.10	10.40	10.55	

Table 4.3: Energies in MeV of the $^{16}_{\Lambda}$O spectrum, obtained in MF approximation, and with the three interactions used in our work, compared to the experimental values given in Ref. [85]. The MF particle-hole components are also shown.

In the calculations with the LNδ and LND interactions the position of the 2^- is almost exclusively sensitive to the spin channel of the interaction. The 0^- state is sensitive also to the tensor channel and not to the scalar channel, since it is an unnatural parity multipole excitation. After setting the spin and the tensor parts of the interactions we adjusted the scalar part by considering the natural parity 1^- excitations. Clearly, in the case of the LNDE interaction, the fitting procedure is not so straightforward, since each channel of the force contributes to the other force channels through the exchange terms.

We have found parameterizations able to reproduce rather well the experimental values of the negative parity states of the spectrum, which generate a 0^+ state at a rather low energy. In some case this state becomes even the lowest energy state. There are no evidences of such a highly collective 0^+ state at low energy. On the contrary, there are indications of a 0^+ state around 10 MeV [86, 87]. The values given in Tab. 4.2, which are used in all the calculations presented in the next section, reproduce the low-lying negative spectrum of $^{16}_{\Lambda}$O and provide a 0^+ state around 11 MeV.

We have also calculated the spectrum of $^{16}_{\Lambda}$O with the YNG interaction of Ref. [83, 84]. This force reproduces the G-matrix interaction built on a Nijmegen Λ-nucleon potential [88]. The spectrum we have obtained with this interaction, is rather different from the experimental one. The lowest energy state is a 1^+ followed by a 1^- at 0.49 MeV, a 2^- at 13.34 MeV. The first 0^- excited state is at 17.94 MeV. These results indicate that the YNG interaction cannot be used in our calculations. This result is expected, since we work with an effective theory which uses an effective interaction already renormalized by many-body effects, not all of them included in the G-matrix calculations [89]. For this reason a straightforward comparison between our effective interactions with more microscopic interactions is not appropriate.

As we have already pointed out in the previous section, our model can be seen as the extension of the RPA theory to the description of the hypernucleus excitation. In this theory some ground state correlations are considered through the presence of the Z amplitudes. We studied the relevance of these correlations by comparing the results of our model with those obtained within the Tamm-Dancoff Approximation (TDA). The TDA calculations have been done by solving Eq. (4.4) without the term which multiplies the Z amplitude.

Since we work with a discrete configuration space, the number of eigenstates corresponding to positive energies obtained in RPA and TDA is the same. For this reason we can immediately identify the energy difference of each eigenstate. As example of the results we have obtained, we show in Fig. 4.2 these energy differences for the $^{16}_{\Lambda}$O and $^{208}_{\Lambda}$Pb hypernuclei as a function of the RPA energy. These results have been obtained by using the LNδ interaction. In the left panel of the figure we show 273 $^{16}_{\Lambda}$O energy differences corresponding to all the solutions we found for all the positive and negative parity multipole excitations up to $J = 4$. In the case of $^{208}_{\Lambda}$Pb we show

5024 energies differences corresponding to multipole excitations up to $J = 10$.

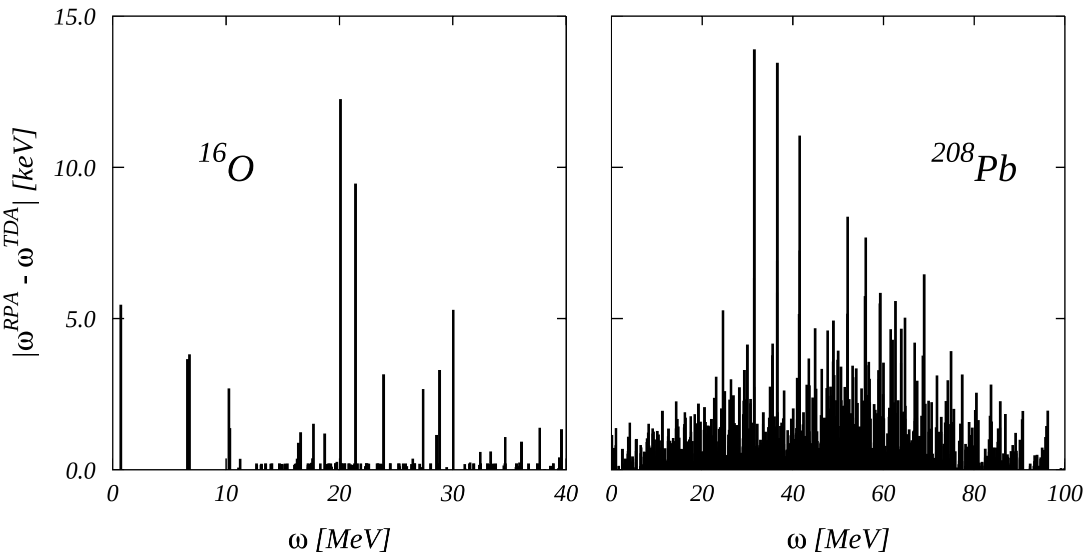

Figure 4.2: Differences between RPA and TDA energy eigenvalues of $^{16}_{\Lambda}$O and $^{208}_{\Lambda}$Pb hypernuclei calculated with the LNδ interaction.

We observe that only in few cases the energy differences are larger than 10 keV. Specifically, for the states of our interest, below 10 MeV for $^{16}_{\Lambda}$O and below 4 MeV for $^{208}_{\Lambda}$Pb , these differences are even smaller. We may conclude that in our calculations RPA and TDA approaches are quantitatively equivalent. In any case, all the results discussed in the next section have been obtained by solving the RPA-like equations.

4.3 Results

In this section we present a selection of our results. As pointed out in the introduction, the aim of our study is the search for collective effects. We investigate the spectra of the $^{12}_{\Lambda}$C , $^{16}_{\Lambda}$O , $^{40}_{\Lambda}$Ca , $^{90}_{\Lambda}$Zr and $^{208}_{\Lambda}$Pb hypernuclei, which are generated by transforming a neutron of a doubly closed shell nucleus into a Λ . We first present the results obtained for each hypernucleus, and then we discuss some global aspects of our results.

We start our presentation with the $^{16}_{\Lambda}$O , whose negative parity states of the spectrum, shown in Tab. 4.3, have been used to set the values of the force parameters. We also cared about the position of the 0^+ state around 11 MeV. The energies of the other positive parity states are a prediction of our model.

We observe that the RPA excitation energies are slightly larger, about 4% on average, than the MF energies, therefore the effects of the residual interaction are not relevant. The structure of the 0^+ state is somehow more collective than those of the other states of the spectrum. This feature becomes evident by observing the transition matrix elements from the ground state to the hypernuclear excited states. In Fig. 4.3 we show the transition form factors

$$F(q) = |< \Psi_0 | T(q) | \Psi_\nu >|^2 \ , \tag{4.28}$$

for the negative parity states of the spectrum and for the 0^+ and 2^+ states. The transition operators are defined in Eqs. (4.16) and (4.18) for natural and unnatural parity states respectively. For unnatural parity excitations, we use transition operators characterized by $L = J \pm 1$. In the case of 0^-, only the T_{J+1} is active, while for the 2^-, both operators are active. In this last case, however, we found that the T_{J+1} form factor is zero in mean-field approximation, and four orders of magnitudes lower than the T_{J-1} form factor when the residual interaction is active. For this reason we neglect it in our discussion. In Fig. 4.3 the transition form factors for the two 1^- states are labeled with the subindexes 1 and 2 to indicate the lower and higher energy states respectively, see Tab. 4.3. Finally, in the lower panels we show the transition form factors for the 2^+ and 0^+ states.

The behavior of these form factors as a function of q is rather interesting. Only the 0^+ transition shows a maximum at q values near zero. For this reason substitutional experiments such as (K^-, π^-) are better suited to investigate the 0^+ states than experiments which produce hypernuclei with a rather large value of the momentum transfer, such as $(e, e'K^+)$ [84].

In Fig. 4.3 the MF transition form factors are compared with those obtained by doing RPA calculations with the three interactions. For the cases we have investigated, we have found that the presence of the interaction does not modify sensitively the MF results, but for the 0^+ state. In this last case, while the LNδ result is similar to the MF one, the two finite-range interactions produce rather different form factors. In the MF model the particle-hole excitation generating the lowest 0^+ state is the $(1p_{1/2})_\Lambda (1p_{1/2})_n^{-1}$ transition. This is also the main transition (W=0.998) obtained in the calculation with the LNδ interaction. The situation changes slightly when the LND interaction is used, since a relevant contribution of the $(1p_{3/2})_\Lambda (1p_{3/2})_n^{-1}$ transition ($W = 0.121$) is associated to the still dominant $(1p_{1/2})_\Lambda (1p_{1/2})_n^{-1}$ transition (W=0.987). The calculation with the LNDE interaction produces a 0^+ state with a rather different structure. The main transition is now the $(1p_{3/2})_\Lambda (1p_{3/2})_n^{-1}$ (W=0.843) with a large contribution of the $(1p_{1/2})_\Lambda (1p_{1/2})_n^{-1}$ component (W=0.366) and also of the $(1s_{1/2})_\Lambda (1s_{1/2})_n^{-1}$ component (W=-0.327).

We obtain another indication of the relative collectivity of the 0^+ state by studying the electromagnetic transitions between the excited stated of $^{16}_{\Lambda}$O . The B-values of these transitions are shown in Tab. 4.4. Some of the transitions presented in Tab. 4.4 are zero in a MF calculation. The $(1^-_1 \rightarrow 0^-)$ and $(2^- \rightarrow 1^-_2)$ transitions do not occur since, in the MF model, initial and final states are degenerate. The $(0^+ \rightarrow 1^-_2)$ transition is zero for a different reason: expression (4.20) requires that $h = h'$ or that $p = p'$, but this does not occur in the case under discussion, as it is possible to observe from the MF single particle transitions presented in Tab. 4.3.

The transitions prohibited in MF calculations have relatively small values when the residual interaction is switched on. All the M1 transitions are modified on the second significant figure by the residual interaction. We use three digits to show the difference between the results obtained with the various interactions.

$^{16}_{\Lambda}$O					
	MF	LNδ	LND	LNDE	[90]
M1 ($1^-_1 \to 0^-$)	0.0	0.081	0.082	0.083	0.176
M1 ($1^-_2 \to 0^-$)	0.433	0.406	0.406	0.404	0.336
M1 ($1^-_2 \to 1^-_1$)	0.217	0.248	0.248	0.250	0.129
M1 ($2^- \to 1^-_1$)	0.650	0.680	0.680	0.683	
M1 ($2^- \to 1^-_2$)	0.0	0.050	0.049	0.048	
E1 ($0^+ \to 1^-_1$)	0.231	0.232	0.309	0.329	
E1 ($0^+ \to 1^-_2$)	0.0	0.012	0.002	0.006	

Table 4.4: Electromagnetic transitions between various states of $^{16}_{\Lambda}$O , in Weisskopf units, compared to the shell model results of Ref. [90].

The situation is rather different when the 0^+ state is present. The B-values of the $(0^+ \to 1^-_1)$ transition are quite different in the various calculations. The LNδ result is similar to that obtained in MF approximation, while the values obtained with the LND and LNDE interactions are 38% and 48% larger than the MF value. This result is again a consequence of the collective structure of the 0^+ state.

In Tab. 4.4 we compare some of our results with those obtained in shell model calculations [90]. The order of magnitude of the B-values is the same in the two calculations, but the differences are remarkable. Our results are roughly a factor two smaller for the $1^-_1 \to 0^-$ transition and a factor two larger for the $1^-_2 \to 1^-_1$ transition. The difference between the results of the other transition is 17%. It would be interesting to compare with experimental values. Unfortunately, while the experimental identification of the energies of the spectrum is quite accurate [91], the measure of the B-values of the transition requires higher statistics. The technological improvements are very promising and these measurements will become feasible in the near future.

Let us now discuss the $^{12}_{\Lambda}$C hypernucleus, whose energy spectrum is given in Tab. 4.5. Our results are compared with the energies measured in the E369 [68] and FINUDA [70] experiments. The uncertainty in the energy resolution of the E369 experiment is about 1.5 MeV, and that of the FINUDA experiment is 1.29 MeV. The angular momentum and parity assignment to the energies measured in the FINUDA experiment is our guess.

$^{12}_{\Lambda}$C							
J^π	p h	MF	LNδ	LND	LNDE	E369	FINUDA
1^-_1	$(1s_{1/2})_\Lambda(1p_{3/2})^{-1}_n$	0.0	0.0	0.0	0.0	0.0	0.0
2^-	$(1s_{1/2})_\Lambda(1p_{3/2})^{-1}_n$	0.0	0.26	0.24	0.27	-	-
1^-_2		-	-	-	-	2.63	2.54
1^-_3		-	-	-	-	6.09	5.04
0^+	$(1p_{3/2})_\Lambda(1p_{3/2})^{-1}_n$	10.03	9.61	8.39	8.28	8.12	7.14
2^+	$(1p_{3/2})_\Lambda(1p_{3/2})^{-1}_n$	10.03	9.38	9.33	9.79	-	9.34
1^+	$(1p_{3/2})_\Lambda(1p_{3/2})^{-1}_n$	10.03	9.69	9.58	9.94	11.00	11.21
3^+	$(1p_{3/2})_\Lambda(1p_{3/2})^{-1}_n$	10.03	9.87	9.80	9.95	-	-

Table 4.5: Energies in MeV of the $^{12}_{\Lambda}$C spectrum calculated in MF approximation and with the three interactions used in our work. The experimental values of E369 [68] are those reported in [75]. The values of the FINUDA experiment [70] have been rescaled with respect to the lowest energy value, and the angular momentum and parity assignment is our guess. The uncertainty in the energy resolution of the E369 experiment is 1.45 MeV, and that of the FINUDA experiment of 1.29 MeV. The MF particle-hole transitions are also shown.

The presence in the experimental spectrum of two 1^- states, that we have called $1^-_{2,3}$, is not predicted by our model. Shell model calculations [92, 93] indicate that these states are produced by neutron-Λ transitions where the neutron is in the $1p_{1/2}$ state, above the Fermi surface in the MF model. Our approach does not consider partial occupation probability of the single particle levels, therefore it is unable to predict these excitations. A description of ^{12}C as closed shell nucleus is reasonable in kinematic regions where the detailed shell structure is not relevant, such as giant resonances or the quasi-elastic region, but for the case we are treating it is inadequate.

Our model predicts the presence of excited states between 8 and 11 MeV. These states are all coming from the $(1p_{3/2})_\Lambda(1p_{3/2})_n^{-1}$ excitation, and in MF approximation are degenerate at 10.03 MeV. The residual interaction removes this degeneracy, and, in general, the excitation energy of each state is lowered with respect to the MF value. The 0^+ and 2^+ states are the lowest ones. The LND and LNDE interactions give the 0^+ around 8.5 MeV, where E369 finds a peak. The identification of this experimental peak with our 0^+ is however quite dubious, since the experiment produces hypernuclei by using a probe that transfers high momentum values to the system, while the 0^+ response has its maximum at small q values. This is shown in the lowest right panel of Fig. 4.4, where the transition form factor of this 0^+ state is shown.

In our search for collective effects we have studied the transition form factors of the various excitations, and, in Fig. 4.4, we show some of them. This figure is analogous to Fig. 4.3, but for $^{12}_{\Lambda}$C . We have selected the transition form factors of the positive states degenerate in MF, and the lowest 1^- state. For the 3^+ state we show only the T_{J-1} form factor, since the T_{J+1} is zero in the MF model.

The figure shows that the 2^+ and 3^+ transitions are essentially unaffected by the effective interaction, as it is the ground state 1^- transition. The 0^+ state, and, much more, the 1^+ state, are instead rather sensitive to the presence of the residual interaction. The structure of the 1^+ state is not collective. In our calculation this state is described by the combination of two particle-hole transitions, the $(1p_{3/2})_\Lambda(1p_{3/2})_n^{-1}$ transitions, which is the dominant one, and the $(1p_{1/2})_\Lambda(1p_{3/2})_n^{-1}$ transition. While in MF approximation this state is described only by the first transition, the relative weight of the two particle-hole components changes with the residual interaction. The values of the W amplitudes vary, respectively, from 0.99 and 0.10 for the LNDE interaction to 0.94 and 0.33 for LNδ. These different couplings between the two states are sufficient to produce the spreading of the form factors shown in Fig. 4.4.

Also the RPA structure of the 0^+ state is mostly described by the combination of the $(1p_{3/2})_\Lambda(1p_{3/2})_n^{-1}$ and $(1s_{1/2})_\Lambda(1s_{1/2})_n^{-1}$ transitions. These are the only two relevant transitions in the formation of the 0^+ state. The relative weights of these two transitions change by changing the residual interaction, and this produces the spreading of the form factors shown in Fig. 4.4.

The B-values of some of the γ transitions for the $^{12}_{\Lambda}$C hypernucleus are shown in Tab. 4.6, and are compared with the shell model results of Ref. [94]. The $2^- \to 1^-$ M1 transition is not present in the MF model, since the two states are degenerate. The RPA calculations remove this degeneracy and produce B-values which are almost insensitive to the different residual interactions.

$^{12}_{\Lambda}$C					
	MF	LNδ	LND	LNDE	[94]
M1 ($2^- \to 1^-_1$)	0.0	0.082	0.082	0.082	-
E1 ($0^+ \to 1^-_1$)	0.278	0.246	0.421	0.509	0.475
E1 ($2^+ \to 1^-_1$)	0.139	0.135	0.121	0.158	0.133
E1 ($2^+ \to 2^-$)	0.139	0.170	0.194	0.133	0.094

Table 4.6: Electromagnetic transitions between various states of $^{12}_{\Lambda}$C , in Weisskopf units, compared the shell model results of Ref. [94].

The B-values of the E1 transitions $2^+ \to 1^-_1$ and $2^+ \to 2^-$ obtained in the MF model are identical, since the wave functions of the initial and final states are the same, as it can be deduced from the MF transitions shown in Tab. 4.5. The B-values obtained in RPA calculations are rather similar to the MF values. The situation changes for the $0^+ \to 1^-_1$ E1 transition, where the RPA results modify the MF value by 10, 70 and 100% when the LNδ, LND and LNDE interactions are used, respectively. As for ${}^{16}_{\Lambda}$O , also in this case the structure of the 0^+ state is extremely sensitive to the residual interaction. In our model this state is described by a combination of the $(1p_{3/2})_\Lambda(1p_{3/2})_n^{-1}$ transition, the dominant one, and the $(1s_{1/2})_\Lambda(1s_{1/2})_n^{-1}$ transition. The coefficients of these two particle-hole transitions are changed by the residual interaction and this produce the changes in the B-values. The agreement between our results with those of the shell model [94] is much more satisfactory than in the case of the ${}^{16}_{\Lambda}$O hypernucleus.

In Tab. 4.7 we show the results relative to the spectrum of the ${}^{40}_{\Lambda}$Ca hypernucleus, for energies smaller than 10 MeV. The changes of the RPA energies, with respect to those of the MF calculations, are 3.5%, on average. The only exception is the 1^+_2 state which shows changes around 20 %. We have analyzed the transition form factors of this state, but we did not find any remarkable effect which distinguishes it from the MF result.

${}^{40}_{\Lambda}$Ca						
J^π	p h	MF	LNδ	LND	LNDE	[95]
1^+_1	$(1s_{1/2})_\Lambda(1d_{3/2})_n^{-1}$	0.0	0.0	0.0	0.0	0.22
2^+_1	$(1s_{1/2})_\Lambda(1d_{3/2})_n^{-1}$	0.0	0.16	0.21	0.19	0.0
0^+	$(1s_{1/2})_\Lambda(2s_{1/2})_n^{-1}$	2.60	2.50	2.74	2.42	2.92
1^+_2	$(1s_{1/2})_\Lambda(2s_{1/2})_n^{-1}$	2.60	3.07	3.13	2.93	3.44
2^+_2	$(1s_{1/2})_\Lambda(1d_{5/2})_n^{-1}$	6.00	6.04	6.08	6.09	6.19
3^+	$(1s_{1/2})_\Lambda(1d_{5/2})_n^{-1}$	6.00	6.10	6.10	6.11	6.01
2^-_1	$(1p_{3/2})_\Lambda(1d_{3/2})_n^{-1}$	7.81	7.72	7.69	7.77	7.98
0^-	$(1p_{3/2})_\Lambda(1d_{3/2})_n^{-1}$	7.81	7.77	8.02	7.07	9.54
1^-_1	$(1p_{3/2})_\Lambda(1d_{3/2})_n^{-1}$	7.81	7.95	7.91	8.05	8.78
3^-	$(1p_{3/2})_\Lambda(1d_{3/2})_n^{-1}$	7.81	8.04	8.24	7.99	8.55
2^-_2	$(1p_{1/2})_\Lambda(1d_{3/2})_n^{-1}$	8.58	8.61	8.59	8.59	9.53
1^-_2	$(1p_{1/2})_\Lambda(1d_{3/2})_n^{-1}$	8.58	8.74	8.51	8.36	9.27

Table 4.7: Energies in MeV of the ${}^{40}_{\Lambda}$Ca spectrum calculated in MF approximation and with the three interactions used in our work. Our results are compared with the shell model results of Ref. [95]. We have considered all the states with energy smaller than 10 MeV. The MF particle-hole transitions are shown.

We observe in Tab. 4.7 that, in our calculations, the ground state of the ${}^{40}_{\Lambda}$Ca system is produced by the $(1s_{1/2})_\Lambda(1d_{3/2})_n^{-1}$ transition which in MF approximation gives two degenerate states characterized by angular momenta and parity 1^+ and 2^+. All our RPA calculations remove the degeneracy by lowering the 1^+ state, while it is the opposite in the calculation of Ref. [95]. In general, the comparison between our results and those of Ref. [95] shows an agreement in terms of clustering of states around the MF single-particle transitions. However, within the set of states produced by the same MF transition, there are some inversions of the multipoles. This happens for the MF degenerate 2^+_2 and 3^+ states, as well as for the set of degenerate states produced by the $(1p_{3/2})_\Lambda(1d_{3/2})_n^{-1}$ transition and also for the $(1p_{1/2})_\Lambda(1d_{3/2})_n^{-1}$ transition. A measure of the experimental spectrum of ${}^{40}_{\Lambda}$Ca would clarify the situation.

In Tab. 4.8 we present the spectrum of the ${}^{90}_{\Lambda}$Zr hypernucleus for excitation energies below 6 MeV. Also in this case we observe that the changes with respect to the MF results are rather small, about 100 keV, less than 2% on average. We have studied the transition form factors for the various excitations, and, in some case, we have observed remarkable differences with respect to the MF results. However, in analogy to the discussion done for the ${}^{12}_{\Lambda}$C hypernucleus, these differences are not produced by really collective excitations of the system, but rather by a combination of two particle-hole transitions.

We show an example of that in Fig. 4.5 where the form factors for the 1^-_1 state of Tab. 4.8, calculated with various effective interactions, are shown. The MF wave function for this state is composed by the $(1s_{1/2})_\Lambda(2p_{1/2})_n^{-1}$ transition. The residual interaction couples a small amount, a W amplitude of about 0.1, of the $(1s_{1/2})_\Lambda(2p_{3/2})_n^{-1}$ transition. This produces the enhancement of

		${}^{90}_{\Lambda}$Zr			
J^π	p h	MF	LNδ	LND	LNDE
5^+	$(1s_{1/2})_\Lambda(1g_{9/2})_n^{-1}$	0.0	0.007	0.0	0.0
4^+	$(1s_{1/2})_\Lambda(1g_{9/2})_n^{-1}$	0.0	0.0	0.009	0.01
0^-	$(1s_{1/2})_\Lambda(2p_{1/2})_n^{-1}$	2.75	2.74	2.76	2.74
1^-_1	$(1s_{1/2})_\Lambda(2p_{1/2})_n^{-1}$	2.75	2.95	2.98	2.87
2^-_1	$(1s_{1/2})_\Lambda(2p_{3/2})_n^{-1}$	4.18	4.30	4.31	4.22
1^-_2	$(1s_{1/2})_\Lambda(2p_{3/2})_n^{-1}$	4.18	4.31	4.33	4.28
3^-_1	$(1s_{1/2})_\Lambda(1f_{5/2})_n^{-1}$	4.44	4.49	4.49	4.48
2^-_2	$(1s_{1/2})_\Lambda(1f_{5/2})_n^{-1}$	4.44	4.55	4.55	4.49
5^-_1	$(1p_{3/2})_\Lambda(1g_{9/2})_n^{-1}$	4.99	4.95	4.94	4.97
4^-_1	$(1p_{3/2})_\Lambda(1g_{9/2})_n^{-1}$	4.99	4.97	4.95	4.97
3^-_2	$(1p_{3/2})_\Lambda(1g_{9/2})_n^{-1}$	4.99	5.09	5.06	5.02
6^-	$(1p_{3/2})_\Lambda(1g_{9/2})_n^{-1}$	4.99	5.07	5.07	5.04
5^-_2	$(1p_{3/2})_\Lambda(1g_{9/2})_n^{-1}$	5.29	5.34	5.39	5.32
4^-_2	$(1p_{3/2})_\Lambda(1g_{9/2})_n^{-1}$	5.29	5.35	5.35	5.33

Table 4.8: Energies in MeV of the ${}^{90}_{\Lambda}$Zr spectrum calculated in MF approximation and with the three interactions used in our work. We have considered all the states with energy smaller than 6 MeV. The MF particle-hole transitions are shown.

the form factor around $q = 1.2\,\mathrm{fm}^{-1}$ and for $q > 2\,\mathrm{fm}^{-1}$. To illustrate better this two-components feature of the state under investigation, we have calculated the transition form factor by considering

$$|1^-_1 >= 0.990\,|(1s_{1/2})_\Lambda(2p_{1/2})_n^{-1} > +0.141\,|(1s_{1/2})_\Lambda(2p_{3/2})_n^{-1} > \quad . \tag{4.29}$$

In Fig. 4.5, the result obtained with this model is indicated by the black squares. We observe the excellent agreement with the RPA results around the main peak of the form factor. For q values larger than 3 fm^{-1}, the RPA form factors are larger than that obtained with the two-states model, indicating that the presence of other particle-hole components in the wave functions becomes evident in this momentum transfer region.

In Tab. 4.9 we show the energies of the excited states of ${}^{90}_{\Lambda}$Zr obtained by considering the transitions of the $1g_{9/2}$ neutron hole to the Λ single particle states. This MF picture has been used in the analysis of the (π^+, K^+) reaction on ${}^{89}_{\Lambda}$Y target [68]. In the same spirit, we have studied the excitation of this neutron hole into the s, p, d, f states of the Λ with $j_\Lambda = l_\Lambda + 1/2$. We have considered all the possible multipole excitations compatible with a specific neutron-Λ transition. Obviously, in the MF calculation all these states have the same excitation energy. The RPA calculations, however, give different energy values for each multipole excitation. In Tab. 4.9 we compare the MF energies for each transition with the RPA energies obtained by averaging the results of the various multipole excitations, and we also show their standard deviation. We observe that, within the statistical uncertainty, RPA and MF results coincide. Also the agreement with the experimental values is good, especially if we consider that the data are taken on a ${}^{89}_{\Lambda}$Y target, and they have an uncertainty of 1.65±0.10 MeV.

To conclude our analysis of the spectra of individual hypernuclei, we show in Tab. 4.10 the spectrum of ${}^{208}_{\Lambda}$Pb for energies below 3.5 MeV. Also in this case the differences between MF and RPA results are rather small. They are about 100 keV, more precisely, 2.6, 3.0 and 1.4% on average for LNδ, LND and LNDE calculations, respectively.

In Tab. 4.11 we show the energies of the excitations of the $1i_{13/2}$ neutron hole into the s, p, d, f, g states of the Λ with $j_\Lambda = l_\Lambda + 1/2$, in analogy to what we have done for the $1g_{9/2}$ state in ${}^{90}_{\Lambda}$Zr . The RPA energies are all compatible with the MF ones, within the statistical uncertainty. In the same table we compare our results with the energies given in Ref. [66] where the (π^+, K^+) scattering data on a ^{208}Pb target have been analyzed in terms of transitions of the $1i_{13/2}$ neutron hole. Since, in our calculations, the lowest energy of ${}^{208}_{\Lambda}$Pb is produced by the transition $(1s_{1/2})_\Lambda(3p_{1/2})_n^{-1}$, we have

			$^{90}_{\Lambda}$Zr		
p	MF	LNδ	LND	LNDE	exp [68]
$(1s_{1/2})_\Lambda$	0.0	0.003 ± 0.003	0.005 ± 0.009	0.007 ± 0.012	0.0
$(1p_{1/2})_\Lambda$	4.994	5.012 ± 0.061	5.010 ± 0.058	4.999 ± 0.031	4.9
$(1d_{5/2})_\Lambda$	10.749	10.783 ± 0.077	10.766 ± 0.060	10.743 ± 0.038	11.5
$(1f_{7/2})_\Lambda$	16.994	17.016 ± 0.035	17.013 ± 0.039	17.002 ± 0.029	19.0

Table 4.9: Energies, in MeV, of the various states coupled to the $1g_{9/2}$ neutron hole in $^{90}_{\Lambda}$Zr , calculated in MF and RPA approaches for the three Λ-nucleon interactions used in this work. The energies of the RPA results are the averages of the various excitation energies of each multipole excitation compatible with the indicated single particle transition. The experimental energies are those of the $^{89}_{\Lambda}$Y hypernucleus, and the uncertainty in the determination of the energy is roughly 1 MeV.

positioned the first experimental energy of Ref. [66] at 1.63 MeV, which is the difference between the $3p_{1/2}$ and $1i_{13/2}$ neutron single particle energies. The other energies have been consistently rescaled, and their values are shown in Tab. 4.11 by the column labeled exp1. The agreement is not satisfactory even if we consider that the experimental energy resolution is of 2.2 ± 0.1 MeV. We then set the position of the second experimental energy at 4.6 MeV, to match our second state, and we rescale the other energies. The corresponding values are shown in the column exp2. In this case the agreement with our results noticeably improves. The source of disagreement with our results is in the energy difference between the first two states.

Up to now, we have presented our results by considering individually each hypernucleus. To give a more general view, we show in Fig. 4.6 the density of states of the various hypernuclei as a function of the excitation energy. The different lines indicate the results obtained in MF and RPA approaches by using the various residual interactions. In our model, the number of excited states for a given multipolarity depends only on the configuration space, and not on the residual interaction. For this reason, differences between the lines of each panel of the figure indicate the relevance of the Λ-nucleon residual interaction which shifts the excitation energies with respect to the MF results. For each hypernucleus, we have taken into account all the possible multipole excitations which provide a solution below 20 MeV.

A first remark on the results shown in Fig. 4.6 is that the density of states in $^{208}_{\Lambda}$Pb is almost ten times larger than that of $^{12}_{\Lambda}$C or $^{16}_{\Lambda}$O . This is an indication of the energy resolution required to do γ spectroscopy in heavy hypernuclei. A second remark, more related to the aim of our investigation, is that the differences between the various lines seem to be more evident for light hypernuclei than for the heavier ones. This could indicate that the MF approach becomes more reliable the heavier is the hypernucleus, or in other words, that collective effects are more inhibited in heavy hypernuclei than in the light ones.

In order to investigate this issue, we calculate the normalized energy shift with respect to the MF energy,

$$\Delta E = \sum_{J}^{N_J} \left(\frac{1}{N_J} \sum_{i}^{S} \frac{\left|\omega_i^{J,\mathrm{RPA}} - \omega_i^{J,\mathrm{MF}}\right|}{\left|\omega_i^{J,\mathrm{RPA}} + \omega_i^{J,\mathrm{MF}}\right|} \right) \quad , \tag{4.30}$$

where we have indicated with N_J the number of multiple excitations we have considered, and the index i runs on all the S solutions having the same multipolarity. The above equation is meaningful since, as we have already mentioned, our model produces the same number of excited states in both MF and RPA calculations, therefore we can identify the energy shift of each MF solution. We show in Tab. 4.12 the ΔE values obtained for the various Λ-nucleon interactions. These results indicate that the deviations from the MF model are less important, the heavier is the nucleus.

We have compared the values of the hyperonic energy differences of Tab. 4.12 with analogous values calculated for excitations of ordinary nuclei. The RPA calculations for the doubly magic nuclei has been done with the zero-range Landau-Migdal interaction of Ref. [96]. This comparison indicates that collectivity in hypernuclei is much smaller than in ordinary nuclei. The ΔE values

		${}^{208}_{\Lambda}$Pb			
J^π	p h	MF	LNδ	LND	LNDE
0^-	$(1s_{1/2})_\Lambda(3p_{1/2})_n^{-1}$	0.0	0.0	0.0	0.0
1_1^-	$(1s_{1/2})_\Lambda(3p_{1/2})_n^{-1}$	0.0	0.09	0.12	0.06
2_1^-	$(1s_{1/2})_\Lambda(2f_{5/2})_n^{-1}$	0.57	0.59	0.60	0.59
3_1^-	$(1s_{1/2})_\Lambda(2f_{5/2})_n^{-1}$	0.57	0.62	0.64	0.60
1_2^-	$(1s_{1/2})_\Lambda(3p_{3/2})_n^{-1}$	0.90	0.96	0.98	0.93
2_2^-	$(1s_{1/2})_\Lambda(3p_{3/2})_n^{-1}$	0.90	1.00	1.01	0.96
6^+	$(1s_{1/2})_\Lambda(1i_{13/2})_n^{-1}$	1.63	1.63	1.63	1.62
7^+	$(1s_{1/2})_\Lambda(1i_{13/2})_n^{-1}$	1.63	1.63	1.63	1.63
3_2^-	$(1s_{1/2})_\Lambda(2f_{7/2})_n^{-1}$	2.34	2.38	2.40	2.36
4_1^-	$(1s_{1/2})_\Lambda(2f_{7/2})_n^{-1}$	2.34	2.39	2.40	2.37
1_1^+	$(1p_{3/2})_\Lambda(3p_{1/2})_n^{-1}$	2.99	3.00	3.00	2.99
2^+	$(1p_{3/2})_\Lambda(3p_{1/2})_n^{-1}$	2.99	3.01	3.03	3.01
0^+	$(1p_{1/2})_\Lambda(3p_{1/2})_n^{-1}$	3.09	3.08	3.07	3.07
1_2^+	$(1p_{1/2})_\Lambda(3p_{1/2})_n^{-1}$	3.09	3.11	3.11	3.10
4_1^-	$(1s_{1/2})_\Lambda(1g_{9/2})_n^{-1}$	3.41	3.41	3.41	3.40
5_1^-	$(1s_{1/2})_\Lambda(1g_{9/2})_n^{-1}$	3.41	3.42	3.42	3.41

Table 4.10: Energies in MeV of the ${}^{208}_{\Lambda}$Pb spectrum calculated in MF approximation and with the three interactions used in this work. We have considered all the states with energy smaller than 3.5 MeV. The MF particle-hole transitions are shown.

for ordinary nuclei are about five times larger than the analogous values obtained for hypernuclei.

			$^{208}_{\Lambda}$Pb			
p	MF	LNδ	LND	LNDE	exp1	exp2
$(1s_{1/2})_\Lambda$	1.633	1.630 $\pm$ 0.001	1.629 $\pm$ 0.002	1.623 $\pm$ 0.008	1.6	-3.0
$(1p_{1/2})_\Lambda$	4.621	4.629 $\pm$ 0.024	4.626 $\pm$ 0.025	4.616 $\pm$ 0.016	6.8	4.6
$(1d_{5/2})_\Lambda$	8.220	8.237 $\pm$ 0.036	8.230 $\pm$ 0.030	8.216 $\pm$ 0.017	12.84	8.24
$(1f_{7/2})_\Lambda$	12.344	12.354$\pm$ 0.020	12.345 $\pm$ 0.010	12.328 $\pm$ 0.014	18.29	13.69
$(1g_{9/2})_\Lambda$	16.926	16.948 $\pm$ 0.034	16.959 $\pm$ 0.040	16.926 $\pm$ 0.108	22.10	17.49

Table 4.11: Energies, in MeV, of the various states coupled to the $1i_{13/2}$ neutron hole in $^{208}_{\Lambda}$Pb , calculated in MF and RPA approaches for the three Λ-nucleon interactions used in our work. The energies of the RPA results are the averages of the various excitation energies of each multipole excitation compatible with the indicated single particle transition. The values shown in the columns exp1 and exp2 are the experimental energies of Ref. [66], rescaled in two different manners (see text).

	$J_{\rm max}$	LNδ	LND	LNDE
$^{12}_{\Lambda}$C	5	0.23 $\pm$ 0.07	0.26 $\pm$ 0.08	0.22 $\pm$ 0.06
$^{16}_{\Lambda}$O	4	0.33 $\pm$ 0.10	0.30 $\pm$ 0.09	0.11 $\pm$ 0.03
$^{40}_{\Lambda}$Ca	4	0.15 $\pm$ 0.04	0.12 $\pm$ 0.04	0.24 $\pm$ 0.07
$^{90}_{\Lambda}$Zr	6	0.10 $\pm$ 0.02	0.13 $\pm$ 0.03	0.09 $\pm$ 0.02
$^{208}_{\Lambda}$Pb	10	0.10 $\pm$ 0.02	0.13 $\pm$ 0.02	0.09 $\pm$ 0.01

Table 4.12: Renormalized energy differences Eq. (4.30). We have also indicated the maximum value of the angular momentum of the multipole excitation.

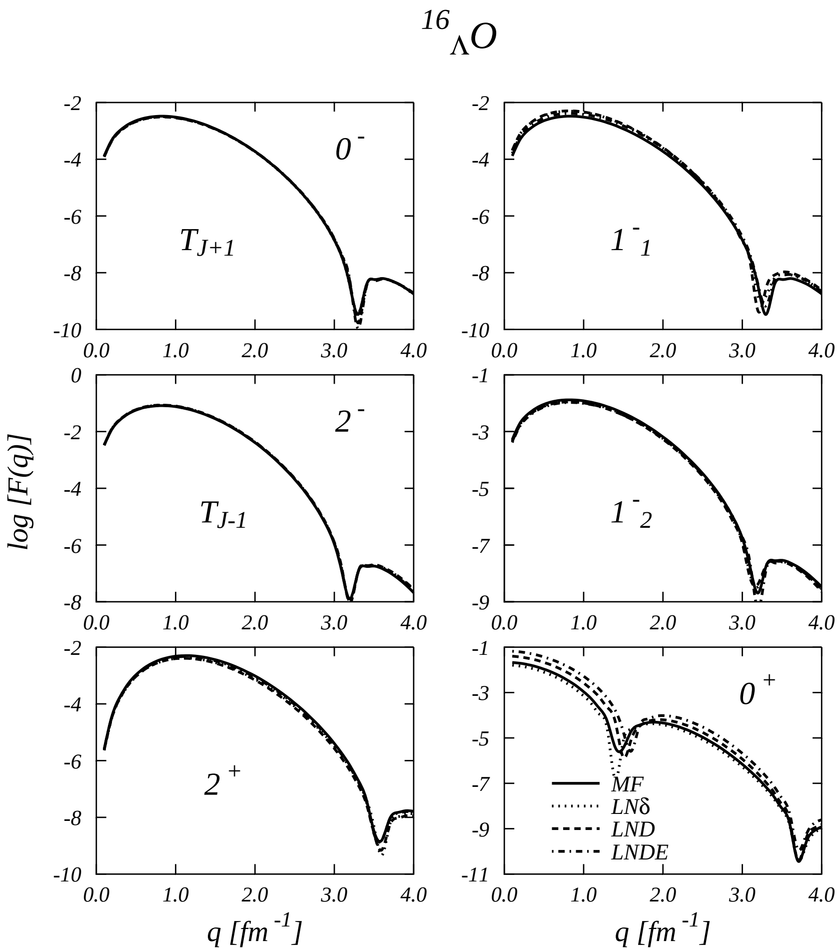

Figure 4.3: Transition form factors, Eq. (4.28), obtained in MF approximation and calculated with the three residual interactions used in this work, as a function of the momentum q of the operators (4.16) and (4.18). For the unnatural parity excitations 0^- and 2^-, the operator inducing the transition is indicated, see Eq. (4.18). The subindexes 1 and 2 of the 1^- states indicate the lower and higher energies states respectively, see Tab. 4.3.

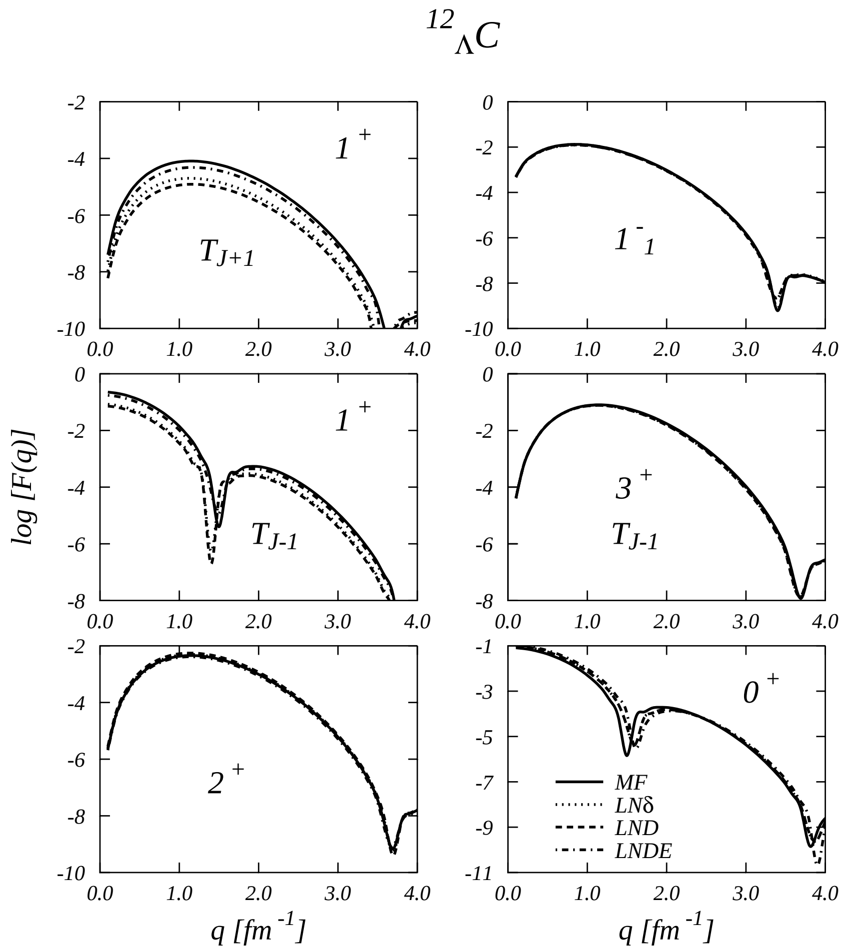

Figure 4.4: Transition form factors as in Fig. 4.3, but for $^{12}_{\Lambda}$C . The energies of the various excited states are given in Tab. 4.5.

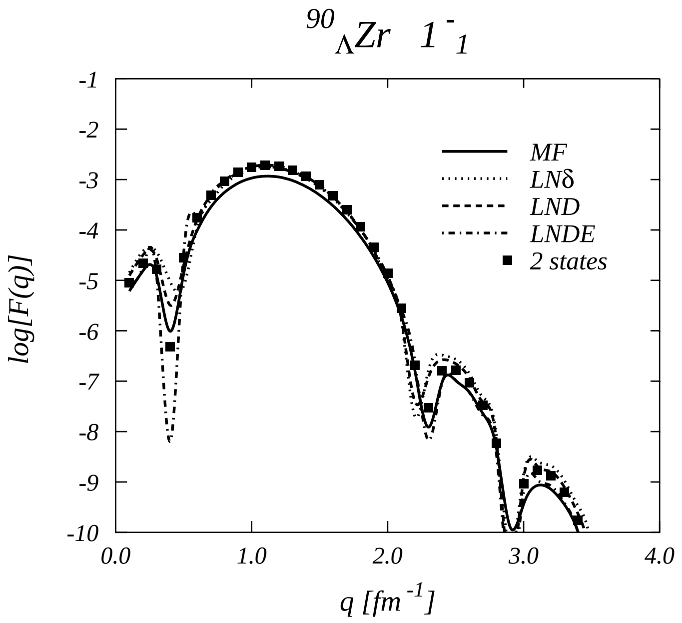

Figure 4.5: Transition form factors as in Fig. 4.3, for the 1_1^- state of ${}^{90}_{\Lambda}$Zr , see Tab. 4.8. The squares indicate the result obtained with the two-states model, Eq. (4.29).

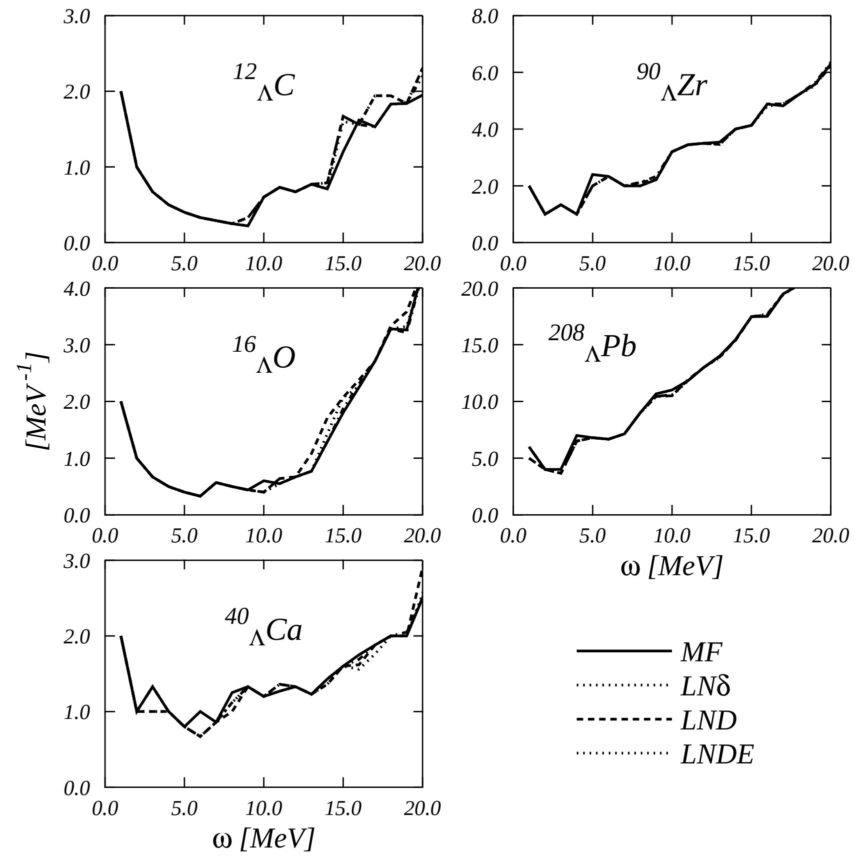

Figure 4.6: Density of states as a function of the excitation energy.

4.4 Conclusions

We have developed a particle-hole model where the formation of the hypernucleus is described as the excitation of a nucleon into a single particle state describing the Λ , and the hypernucleus state is a linear combination of elementary single particle excitations, the coefficients of the combinations being determined by the residual Λ -nucleon interaction.

Our model considers one-particle nucleon-Λ transitions, while shell model calculations are more elaborated. The limitations of our approach have been pointed out in the ${}^{12}_{\Lambda}$C case, where two states experimentally well identified are not predicted. These two states are related to the excitation of the neutrons lying on the $1p_{1/2}$ state which in our approach is empty. On the other hand, our model can handle larger configuration spaces than those manageable by shell model calculations. We can easily deal with hypernuclei as heavy as ${}^{208}_{\Lambda}$Pb .

Our approach is an effective theory, therefore it uses effective interactions, which cannot be straightforwardly related to the bare Λ -nucleon interactions.

As long as we had the possibility, we have compared our results with those obtained by other calculations, and with the experimental data.

The aim of our study was the search for some collective effects in the spectra of hypernuclei, for this reason we have studied the form factors of the transition producing the hypernucleus and we compared MF and RPA results. In few cases we have found remarkable differences, however, in all the cases but one, these differences could be explained by considering the excited state as combination of only two single particle transitions. This is not really what we would call a collective behavior of the system. The only situation standing out of this trend is that of the 0^+ excitation in ${}^{16}_{\Lambda}$O around 10 MeV, which has a more collective structure.

The energy shifts with respect to the MF results are indicators of effects coming from the Λ -nucleon interaction, and possibly of collective phenomena. Densities of states and average energy shifts do not show remarkable features beyond the MF approach. In our calculations the differences between MF and RPA results become smaller the heavier is the hypernucleus. This is an indication that perturbation effects produced by the Λ on the nuclear systems are better averaged in a heavy system.

The average energy shifts for hypernuclear excitations are, at their maximum, 20% of the shifts obtained for the excitation of a purely nucleonic system. This result is almost independent of the number of nucleons involved, and indicates that in hypernuclear excitation, effects beyond the MF are much less important than in the excitation of the ordinary nuclear system.

Chapter 5

RPA theory in continuum

We have studied in sect. 3.1 the sensitivity of the discrete RPA results to the choice of the s.p. configuration space. The description of the energy spectrum above the nucleon emission threshold requires a proper description of the continuum part of the s.p. configuration space.

The RPA equations (2.12) and (2.13)

$$(\epsilon_p - \epsilon_h - \omega)X^{\nu}_{ph} + \sum_{p'h'} \left(v_{ph,p'h'}X^{\nu}_{p'h'} + u_{ph,p'h'}Y^{\nu}_{p'h'}\right) = 0$$
$$(\epsilon_p - \epsilon_h + \omega)Y^{\nu}_{ph} + \sum_{p'h'} \left(v^*_{ph,p'h'}Y^{\nu}_{p'h'} + u^*_{ph,p'h'}X^{\nu}_{p'h'}\right) = 0$$

have been obtained discretizing the continuum space of the particles, that is considering for the operator of creation of ph pair the following expression:

$$Q^{\dagger}_{\nu} = \sum_{ph}\sum_{\epsilon_p > \epsilon_F} \left(X^{\nu}_{ph}a^{\dagger}_p a_h - Y^{\nu}_{ph}a^{\dagger}_h a_p\right) \tag{5.1}$$

The correct expression of $Q^{\dagger}_{\nu}$ in the RPA theory is given instead by (2.4)

$$\begin{aligned} Q^{\dagger}_{\nu} = \sum_{ph}\Bigg[&\sum_{\epsilon_p > \epsilon_F}^{0} \left(X^{\nu}_{ph}a^{\dagger}_p a_h - Y^{\nu}_{ph}a^{\dagger}_h a_p\right) + \\ &+ \int_0^{\infty} d\epsilon_p \left(X^{\nu}_{ph}(\epsilon_p)a^{\dagger}_p a_h - Y^{\nu}_{ph}(\epsilon_p)a^{\dagger}_h a_p\right)\Bigg] \end{aligned}$$

that considers a sum on the discrete energy state of bound particle and an integration on the continuum energy. In this way the RPA equations are rewritten as:

$$\begin{aligned} (\epsilon_p - \epsilon_h - \omega)X^{\nu}_{ph}(\epsilon_p) + \sum_{p'h'}^{discr} \left(v_{ph,p'h'}X^{\nu}_{p'h'} + u_{ph,p'h'}Y^{\nu}_{p'h'}\right) + \\ + \sum_{p'h'}^{cont} \int d\epsilon_{p'} \left(v_{ph,p'h'}X^{\nu}_{p'h'}(\epsilon_{p'}) + u_{ph,p'h'}Y^{\nu}_{p'h'}(\epsilon_{p'})\right) = 0 \end{aligned} \tag{5.2}$$

$$\begin{aligned} (\epsilon_p - \epsilon_h + \omega)Y^{\nu}_{ph} + \sum_{p'h'}^{discr} \left(v^*_{ph,p'h'}Y^{\nu}_{p'h'} + u^*_{ph,p'h'}X^{\nu}_{p'h'}\right) + \\ + \sum_{p'h'}^{cont} \int d\epsilon_{p'} \left(v^*_{ph,p'h'}Y^{\nu}_{p'h'}(\epsilon_{p'}) + u^*_{ph,p'h'}X^{\nu}_{p'h'}(\epsilon_{p'})\right) = 0 \end{aligned} \tag{5.3}$$

$$\tag{5.4}$$

In this formulation the X_{ph} and Y_{ph} of a particle in the continuum depend on ϵ_p. The integration on ϵ_p is made up to ∞ and this makes these equations numerically intractable. A solution is found reformulating the RPA equations using two new variables that allow us to rewrite Eqs. (5.2) and (5.3) in coordinate space representation. We define channel functions $f_{[p]h}(r)$ and $g_{[p]h}(r)$:

$$f_{[p]h}(r) = \sum_{\epsilon_p > \epsilon_F}^{0} X_{ph}(\epsilon_p) R_p(r, \epsilon_p) + \int_0^\infty d\epsilon_p X_{ph}(\epsilon_p) R_p(r, \epsilon_p) \tag{5.5}$$

$$g_{[p]h}(r) = \sum_{\epsilon_p > \epsilon_F}^{0} Y_{ph}(\epsilon_p) R_p(r, \epsilon_p) + \int_0^\infty d\epsilon_p Y_{ph}(\epsilon_p) R_p(r, \epsilon_p) \tag{5.6}$$

where $[p]$ indicates all the quantum numbers characterizing the s.p. state except the energy ϵ_p, that contain formally the integration on the s.p. energy of the particle in the continuum. With these two variables the RPA equations are transformed into a set of integro-differential equations. The radial wave functions are eigenfunctions of the one-body Schrödinger equation

$$h_p R_p(r, \epsilon_p) = \epsilon_p R_p(r, \epsilon_p) \tag{5.7}$$

and satisfy the closure relation

$$\sum_{\epsilon_\alpha < \epsilon_F} R^*_\alpha(r, \epsilon_\alpha) R_\alpha(r', \epsilon_\alpha) + \sum\!\!\!\!\!\!\int_{E_F}^{\infty} d\epsilon_\alpha R^*_\alpha(r, \epsilon_\alpha) R_\alpha(r', \epsilon_\alpha) = \delta(r - r'), \tag{5.8}$$

where we have indicated with the symbol $\sum\!\!\!\!\!\int_{E_F}^{\infty}$ a sum on the bound energies from ϵ_F to zero and an integral from zero to infinity.

Multiplying the first term of (5.2) on the left side for $R_p(r, \epsilon_p)$ and applying $\sum\!\!\!\!\!\int_{E_F}^{\infty} d\epsilon_p$ we obtain for the first term:

$$\begin{aligned} &\sum\!\!\!\!\!\!\int_{E_F}^{\infty} d\epsilon_p (\epsilon_p - \epsilon_h - \omega) X_{ph}(\epsilon_p) R_p(r, \epsilon_p) = \\ &(h_p - \epsilon_h - \omega) \sum\!\!\!\!\!\!\int_{E_F}^{\infty} d\epsilon_p X_{ph}(\epsilon_p) R_p(r, \epsilon_p) = \\ &\qquad = (h_p - \epsilon_h - \omega) f_{[p]h}(r) \end{aligned} \tag{5.9}$$

where we have substituted ϵ_p with the one-body Schrödinger hamiltonian. Getting together the direct and in the same way the exchange terms and remembering the closure relation (5.8), we obtain for the Eq. (5.2) the following formulation

$$\begin{aligned} (h_0 - \epsilon_h - \omega) f^{J,\omega}_{[p]h}(r) = - \sum_{[p']h'} \int dr' r'^2 \Big[& R^*_{h'}(r') R_h(r) f^{J\omega}_{[p']h'}(r') v^{dir}_{ph,p'h'}(r, r') + \\ & - R^*_{h'}(r') f^{J\omega}_{[p']h'}(r) R_h(r') v^{exch}_{ph,p'h'}(r, r') + \\ & + g^{*J\omega}_{[p']h'}(r') R_h(r) R_{h'}(r') u^{dir}_{ph,p'h'}(r, r') + \\ & - g^{*JE}_{[p']h'}(r') R_{h'}(r) R_h(r') u^{exch}_{ph,p'h'}(r, r') \Big] \\ & + BST, \end{aligned} \tag{5.10}$$

In an analogous way we obtain for Eq. (5.3) the following expression

$$(h_0 - \epsilon_h + \omega) g^{J,\omega}_{[p]h}(r) = - \sum_{[p']h'} \int dr' r'^2 \Big[R^*_{h'}(r') R_h(r) g^{J\omega}_{[p']h'}(r') v^{dir}_{ph,p'h'}(r,r') +$$
$$- R^*_{h'}(r') g^{J\omega}_{[p']h'}(r) R_h(r') v^{exch}_{ph,p'h'}(r,r') +$$
$$+ f^{*J\omega}_{[p']h'}(r') R_h(r) R_{h'}(r') u^{dir}_{ph,p'h'}(r,r') +$$
$$- f^{*J\omega}_{[p']h'}(r') R_{h'}(r) R_h(r') u^{exch}_{ph,p'h'}(r,r') \Big]$$
$$+ BST, \qquad (5.11)$$

where we have defined the Bound State term BST as:

$$BST = \sum_{[p']h'} \sum_{\epsilon_p < \epsilon_F} \int dr_1 r_1^2 \int dr_2 r_2^2 R_p(r) R^*_p(r_1)$$
$$\{ R^*_{h'}(r_2) \left[R_h(r_1) f_{[p']h'}(r_2) v^{dir}_{php'h'}(r_1,r_2) + \right.$$
$$\left. - R_h(r_2) f_{[p']h'}(r_1) v^{exch}_{php'h'}(r_1,r_2) \right] +$$
$$+ g^*_{[p']h'}(r_2) \left[R_h(r_1) R_{h'}(r_2) u^{dir}_{php'h'}(r_1,r_2) + \right.$$
$$\left. - R'_h(r_1) R_h(r_2) u^{exch}_{php'h'}(r_1,r_2) \right] \} . \qquad (5.12)$$

The presence of the BST term is due to first term of Eq. (5.8). This term is zero if there are no hole states with the same angular momenta l_p and j_p of the particle state.

To get unique solutions for $f_{[p]h}$ and $g_{[p]h}$ one has to specify the appropriate boundary conditions. We define *open channel* a ph pair where the particle is in the continuum. We solve Eqs. (5.10) and (5.11) a number of times equal to the number of open channels, each time by imposing that the particle is emitted in a specific open channel, characterized by the quantum numbers p_0, h_0, and called elastic channel. For this reason, for each value of the excitation energy, we have a number of RPA solutions equal to the number of open channels. The f and g functions have a ph pair index as indicated by their definitions (5.5), (5.6), and have in addition the $p_0 h_0$ index which indicates the elastic channel characterizing the RPA solution.

The outgoing asymptotic behaviour of the channel function $f^{[p_0]h_0}_{[p]h}$ must be identical to that of the free scattering solution R_{p_0} with $\epsilon_{p_0} = \epsilon_{h_0} + \omega$ and only the ingoing asymptotic form can change. The asymptotic behaviour for $f_{[p]h}$ in the elastic channel $[p_0]h_0$ is:

$$f^{[p_0]h_0}_{[p]h}(r \to \infty) \to R_{p_0}(r) \delta_{[p][p_0]} \delta_{hh_0} + \lambda H^-_p(\epsilon_h + \omega, r) \qquad (5.13)$$

where $H^-_p(\epsilon_h + \omega, r)$ is the ingoing Coulomb function (or Hankel function in case of a neutron channel) which corresponds to the quantum numbers $p^+ = (\epsilon_h + \omega, [p])$. We indicate with R_{p_0} the wave function in the continuum with energy $\epsilon_p > 0$. The channel function $g^{[p_0]h_0}_{[p]h}$ behaves asymptotically like a bound state with the energy $\epsilon_h - \omega$.

$$g^{[p_0]h_0}_{[p]h}(r \to \infty) \to \chi \frac{1}{r} exp \left[-r \left(\frac{2m|\epsilon_h - \omega|}{\hbar^2} \right)^{\frac{1}{2}} \right] . \qquad (5.14)$$

A possible way of solving the continuum RPA equations is to discretize the r space on a given mesh and to use finite difference numerical methods [22]. This method is applicable when zero range interactions are used. Since we want to use finite range interactions and deal with the exchange matrix elements, we use a technique consisting in expanding the channel functions on a complete basis [25], [24]. We choose a set of functions which already obey the correct boundary conditions.

For $\epsilon_p > 0$ the wave functions of interest for the present purpose are Sturm Bessel functions [26, 27, 28, 29, 30] for $\epsilon_p > 0$, which are defined as eigenstates of the following differential equation:

$$[h_0 - V_{WS}(r) - \epsilon_p] \Phi^\mu_p(r) = - \frac{\hbar^2}{2m} \overline{U}^\mu_p(r) \Phi^\mu_p(r). \qquad (5.15)$$

In the above equation V_{WS} is the mean-field Woods-Saxon potential, ϵ_p is the energy of the particle in MeV and $\overline{U}_p^\mu(r)$ is a complex potential of the form:

$$\overline{U}_p^\mu(r) = \begin{cases} \frac{2m}{\hbar^2}\left(\overline{V}_p^\mu + i\overline{W}_p^\mu\right) & \text{if } r \le a \\ 0 & \text{if } r > a \end{cases}$$

where $\overline{V}_p^\mu$ and $\overline{W}_p^\mu$ are real constants determined by the boundary condition on the SB functions at $r = a$; ϵ_p is the center of mass energy in MeV. Expressing h_0 in radial coordinate we have:

$$\left[-\frac{\hbar^2}{2m}\frac{d^2}{dr^2} - \frac{\hbar^2}{m}\frac{1}{r}\frac{d}{dr} + \frac{\hbar^2}{2m}\frac{l(l+1)}{r^2} - \epsilon_p\right]\Phi_p^\mu(r) = -\frac{\hbar^2}{2m}\overline{U}_p^\mu(r)\Phi_p^\mu(r) \tag{5.16}$$

where m is the particle mass, and l refers to the orbital angular momentum and assumes only integer values.
The SB functions Φ_p^μ are defined so that the following orthogonality relation holds:

$$(\overline{V}_p^\mu + i\overline{W}_p^\mu)\int_0^a r^2 dr \Phi_p^\mu(r)\Phi_p^\nu(r) = \delta_{\mu\nu} \tag{5.17}$$

For $\epsilon_p < 0$ we expand the channel functions on a set of real Sturm functions, which are defined as eigenstates of the following real differential equation:

$$(h_0 - \epsilon_p)\Phi_p^\mu(r) = -\alpha_p^\mu V(r)\Phi_p^\mu(r) \tag{5.18}$$

with α a real eigenvalue. The auxiliary real potential V is chosen equal to the potential part V_{WS} in the mean field hamiltonian h_0 (Eq. (1.5)).

For the Sturm function Φ_p^μ the following orthogonality relation holds:

$$\int_0^\infty dr r^2 \Phi_p^\mu(r)V(r)\Phi_p^\nu(r) = \frac{\delta_{\mu\nu}}{\alpha_p^\mu} \tag{5.19}$$

Since the sturmian functions, with this term we indicate both the SB functions and bound Sturm functions, are not in general orthogonal to the occupied states, we define the orthogonalized sturmian functions as:

$$\widetilde{\Phi}_p^\mu(r) = \Phi_p^\mu(r) - \sum_{\substack{\epsilon_i < \epsilon_F \\ i = p}} R_i(r)\int dr' r'^2 R_i(r')\Phi_p^\mu(r') \tag{5.20}$$

The real constants $\overline{V}_p^\mu$, $\overline{W}_p^\mu$ and α_p^μ are determined by imposing the appropriate boundary conditions to the sturmian functions that are:

$$\Phi_p^\mu(r \to \infty) \to \lambda\frac{H_p^-(\epsilon_p, r)}{r} \tag{5.21}$$

if $\epsilon_p > 0$, and:

$$\Phi_p^\mu(r \to \infty) \to \chi\frac{1}{r}exp\left[-r\left(\frac{2m|\epsilon_p|}{\hbar^2}\right)^{\frac{1}{2}}\right] \tag{5.22}$$

if $\epsilon_p < 0$.

As an example in Fig. 5.1 we show in the upper panel the real and imaginary part of a set of SB functions for protons of positive energy of $30MeV$ in ^{16}O with angular orbital momentum $l = 1$ and total angular momentum $j = 3/2$. In the lower panel we show the Sturm function for protons of negative energy of $-30MeV$ with angular orbital momentum and $l = 0$ and total angular momentum $j = 1/2$ and $l = 1$ and $j = 3/2$.

The figure clarifies the meaning of the index μ, analogous to that of the principal quantum number in the radial solution of the one-particle Schródinger equation. The number of nodes of the sturmian functions is linked to the index μ. We observe that when the index increases by one unity an additional node appears in the wave function. The sturmian functions are constructed to have the same asymptotic behaviour independently of the number of nodes: the SB function, outside the range where the potential is different form zero, behave like the Hankel function, the bound Sturm functions like a decreasing exponential.

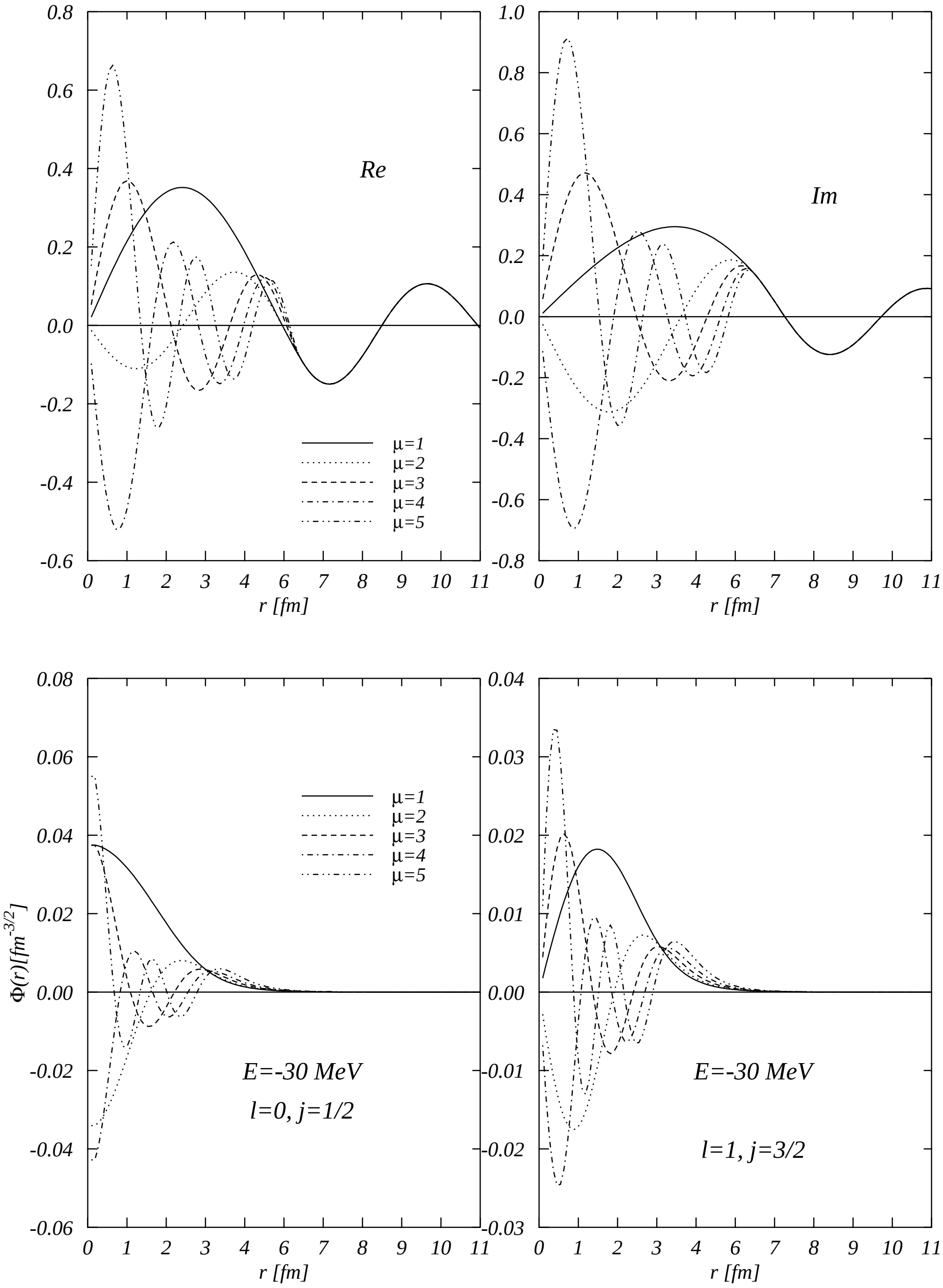

Figure 5.1: SB functions relative to an energy of $30MeV$ (upper panel) and Sturm bound functions for $-30MeV$ (lower panel). These sturmian functions have been calculated for a proton with $l = 1$ and $j = 3/2$ in ^{16}O in the upper panel and for for a proton with $l = 0$ and $j = 1/2$ and $l = 1$ and $j = 3/2$ in the lower panel.

We expand the channel functions $f_{[p]h}^{[p_0]h_0}$ and $g_{[p]h}^{[p_0]h_0}$ on the basis of the orthogonalized sturmian functions according to

$$\begin{aligned} f_{[p]h}^{[p_0]h_0}(r) &= R_{p_0}(r)\delta_{[p][p_0]}\delta_{hh_0} + \sum_{\mu} c_{ph}^{+\mu}\widetilde{\Phi}_p^{+\mu}(r) \\ g_{[p]h}^{[p_0]h_0}(r) &= \sum_{\mu} c_{ph}^{-\mu}\widetilde{\Phi}_p^{-\mu}(r) \end{aligned} \tag{5.23}$$

where the symbols + and − indicate that the sturmian functions are evaluated for $\epsilon_p = \epsilon_h + \omega$ or $\epsilon_p = \epsilon_h - \omega$ respectively. By inserting Eqs. (5.23) in the RPA secular equations (5.10) and (5.11) we obtain a system of linear equations whose unknowns are the expansion coefficients (see Appendix G):

$$\sum_{\mu}\sum_{[p']h'}\Bigg\{\Big[\delta_{[p][p']}\delta_{hh'}\Big(\delta_{\mu\nu} - \langle P_p^{+\nu}|V_{WS}|P_p^{+\mu}\rangle + \sum_{\substack{\epsilon_i<\epsilon_F \\ i=p}}(\epsilon_p-\epsilon_h-\omega)\langle P_p^{+\nu}|p\rangle\langle p|P_p^{+\mu}\rangle\Big) + \\ -\langle \widetilde{P}_p^{+\nu}h'|V|h\widetilde{P}_{p'}^{+\mu}\rangle\Big]c_{p'h'}^{+\mu} - (-)^{j_{p'}-j_{h'}+J}\langle \widetilde{P}_p^{+\nu}\widetilde{P}_{p'}^{-\mu *}|V|hh'\rangle c_{p'h'}^{-\mu *}\Bigg\} = \langle \widetilde{P}_p^{+\nu}h_0|V|hp_0\rangle \tag{5.24}$$

and:

$$\sum_{\mu}\sum_{[p']h'}\Bigg\{\Big[\delta_{[p][p']}\delta_{hh'}\Big(\delta_{\mu\nu} + \sum_{\substack{E_i<E_f \\ i=p}}(\epsilon_p-\epsilon_h+\omega)\langle P_p^{-\nu}|p\rangle\langle p|P_p^{-\mu}\rangle\Big) + \\ -\langle \widetilde{P}_p^{-\nu}h'|V|h\widetilde{P}_{p'}^{-\mu}\rangle\Big]c_{p'h'}^{-\mu} - (-)^{j_{p'}-j_{h'}+J}\langle \widetilde{P}_p^{-\nu}\widetilde{P}_{p'}^{+\mu *}|V|hh'\rangle c_{p'h'}^{+\mu *}\Bigg\} = (-)^{j_{p_0}-j_{h_0}+J}\langle \widetilde{P}_p^{-\nu}p_0|V|hh_0\rangle \tag{5.25}$$

With the symbol $|P_p^{+\mu}\rangle$ we indicate a s.p. wave function whose radial part is the sturmian function $\Phi_p^{+\mu}$ and whose angular part has the quantum numbers of the particle $|p\rangle$

$$\begin{aligned} |P_p^{+\mu}\rangle = \Phi_p^{+\mu}(r,\epsilon_p=\epsilon_h+\omega)|l_p\frac{1}{2}j_p\rangle = \\ = \Phi_p^{+\mu}(r,\epsilon_p=\epsilon_h+\omega)\mathcal{Y}_{l_pj_p}(\Omega) \end{aligned} \tag{5.26}$$

where $\mathcal{Y}_{l_pj_p}$ is the spin spherical-harmonics. The term

$$\langle P_p^{+\nu}|V_{WS}|P_p^{+\mu}\rangle = \int dr r^2\Phi_p^{+\nu}(r)V_{WS}(r)\Phi_p^{+\mu}(r) \tag{5.27}$$

in Eq. (5.24) is zero if $E_h+\omega<0$, and the explicit expression of $\langle P_p^{+\nu}|p\rangle$ is

$$\langle P_p^{+\nu}|p\rangle = \int dr r^2\Phi_p^{+\nu}(r)R_p(r). \tag{5.28}$$

In Eqs. (5.24), (5.25) we use the following expression of $\langle ab|V|cd\rangle$

$$\langle ab|V|cd\rangle = \int\int dr_1dr_2r_1^2r_2^2\left[\langle v_{abcd}^{dir}\rangle R_a^*(r_1)R_b^*(r_2)V(r_1,r_2)R_c(r_1)R_d(r_2)+ \\ -\langle v_{abcd}^{exch}\rangle R_a^*(r_1)R_b^*(r_2)V(r_1,r_2)R_d(r_1)R_c(r_2)\right] \tag{5.29}$$

5.1 Continuum RPA calculation for the ^{16}O nucleus

In this section we present some results obtained by solving the CRPA equations with the method described in the previous section. We have done calculations for ^{16}O, and we have used the interactions described in sect 3.2.

We have calculated the total photoabsorption cross section for a multipole excitation of angular momentum J, by using Eq. (2.44). For electric multipole excitations, natural parity, we have calculated the quantity

$$S_J(\omega) = \int_0^\omega dE \Big(\frac{\hbar c}{E}\Big)^{2J-2} \sigma_J(E) \tag{5.30}$$

and we have compared its behaviour with the theoretically expected value

$$S_J = \frac{1}{2J+1}\left(\frac{1}{\hbar c}\right)\frac{(\hbar c)^2}{mc^2}\pi^2 \frac{J+1}{[(2J-1)!!]^2}\sum_a < i|r_a^{2J-2}|i > e_a^2. \tag{5.31}$$

We have calculated the proton, neutron, isoscalar and isovector responses, by using the following equation

$$B_J(\omega) = |\langle J^\pi, \omega | T_J | 0\rangle|^2. \tag{5.32}$$

For proton and neutron responses we use

$$T_J = \sum_i t_J(r_i) \mathcal{Y}_{J,0}(\Omega_i) \tag{5.33}$$

where the sum runs only on protons or on neutrons, respectively.

The isoscalar response has been obtained by using the operator of equation (5.33) with the sum running on all the nucleons, and the isovector response has been defined as

$$T_J = \frac{Z}{A}\sum_i^{neutrons} t_J(r_i)\mathcal{Y}_{J,0}(\Omega_i) - \frac{N}{A}\sum_i^{protons} t_J(r_i)\mathcal{Y}_{J,0}(\Omega_i) \tag{5.34}$$

For the isoscalar response we have used $t_J(r) = r^J$, except for the monopole case where we have used $t_J(r) = r^2$. For the isovector dipole we have taken $t_J(r) = r$, whereas for the isoscalar dipole we adopt the scattering operator $t_J(r) = r^3 - 5/3\langle r^2\rangle r$ to eliminate the contribution of spurious states mixing [97].

The energy moments can be calculated by

$$m_k = \int_0^\infty \omega^k B_J(\omega) d\omega \tag{5.35}$$

Then the centroid, constrained and scaling energies of the giant resonance are computed as

$$E_{cen} = \frac{m_1}{m_0} \tag{5.36}$$

$$E_{con} = \sqrt{\frac{m_1}{m_{-1}}} \tag{5.37}$$

$$E_S = \sqrt{\frac{m_3}{m_1}} \tag{5.38}$$

In Fig. 5.2 we show the comparison between the CRPA calculation and the discrete calculation for the B-value of the 1^- excitation. We observe that we have a general good agreement.

We start our discussion of the results by pointing out the relevance of our approach which has the possibility of treating the exchange diagram terms. This is a new feature with respect to the Fourier-Bessel CRPA of Refs. [21, 23, 55].

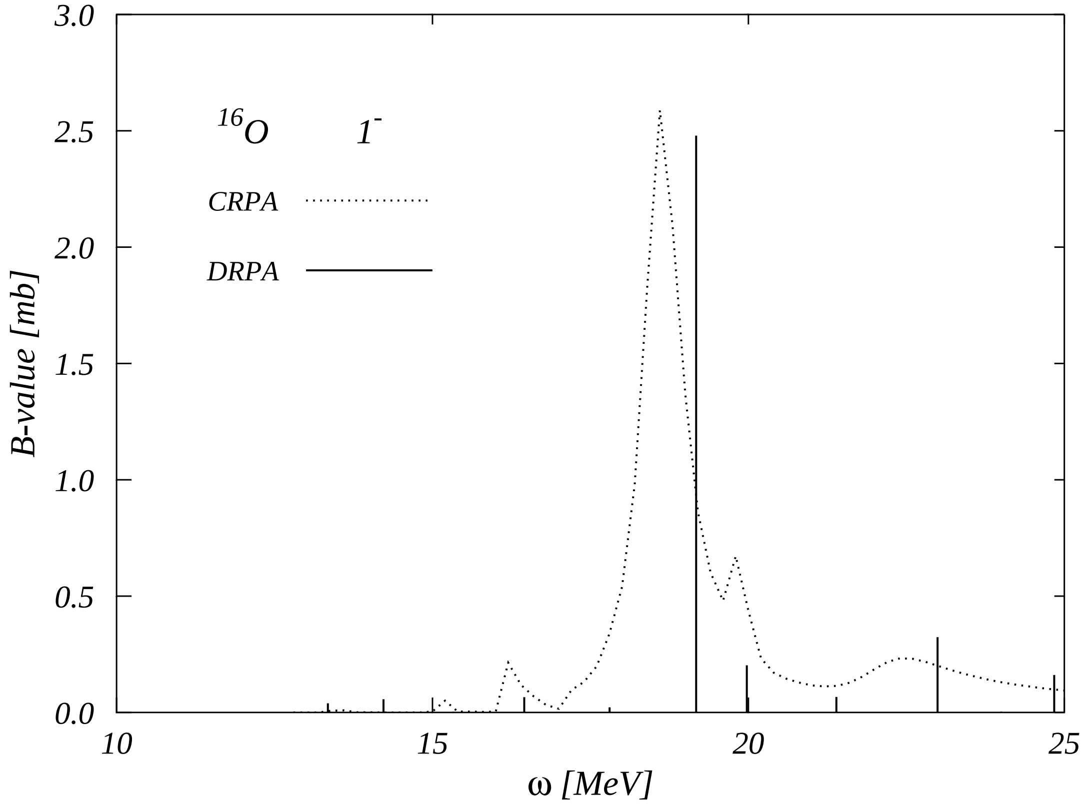

Figure 5.2: B-values of the 1^- excitation for ^{16}O calculated with our CRPA and discrete RPA.

We have tested our CRPA comparing our calculations with the Fourier-Bessel RPA with a zero range interaction with no density dependence. The results for the 1^- of ^{16}O are shown in Fig. 5.3. Also in this case the B-value have the same behaviour showing the same positions for the pecks and almost the same magnitude.

As an example of these calculations we show in Fig. 5.4 the photoabsorption cross section for the 1^- excited state of ^{16}O calculated by using the FRtt interaction introduced in section 3.2 considering only the direct terms and the direct+exchange terms.

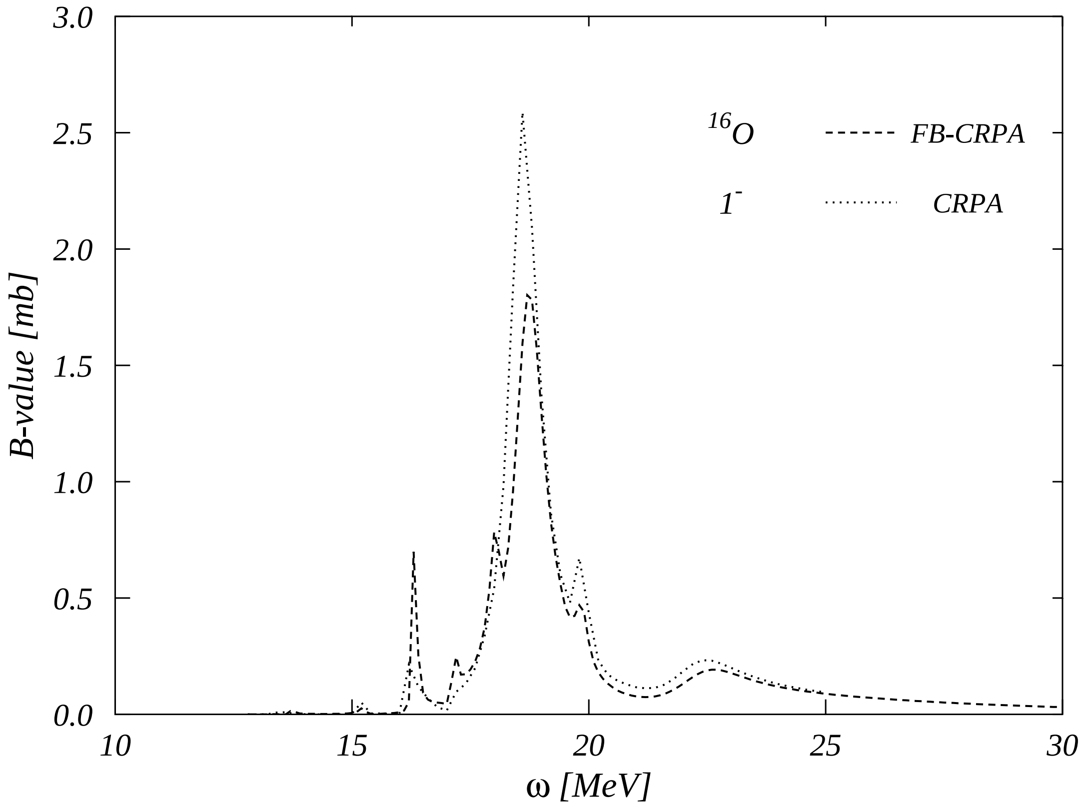

Figure 5.3: B-values of the 1^- excitation for ^{16}O calculated with our CRPA and Fourier-Bessel continuum RPA (label FB-CRPA).

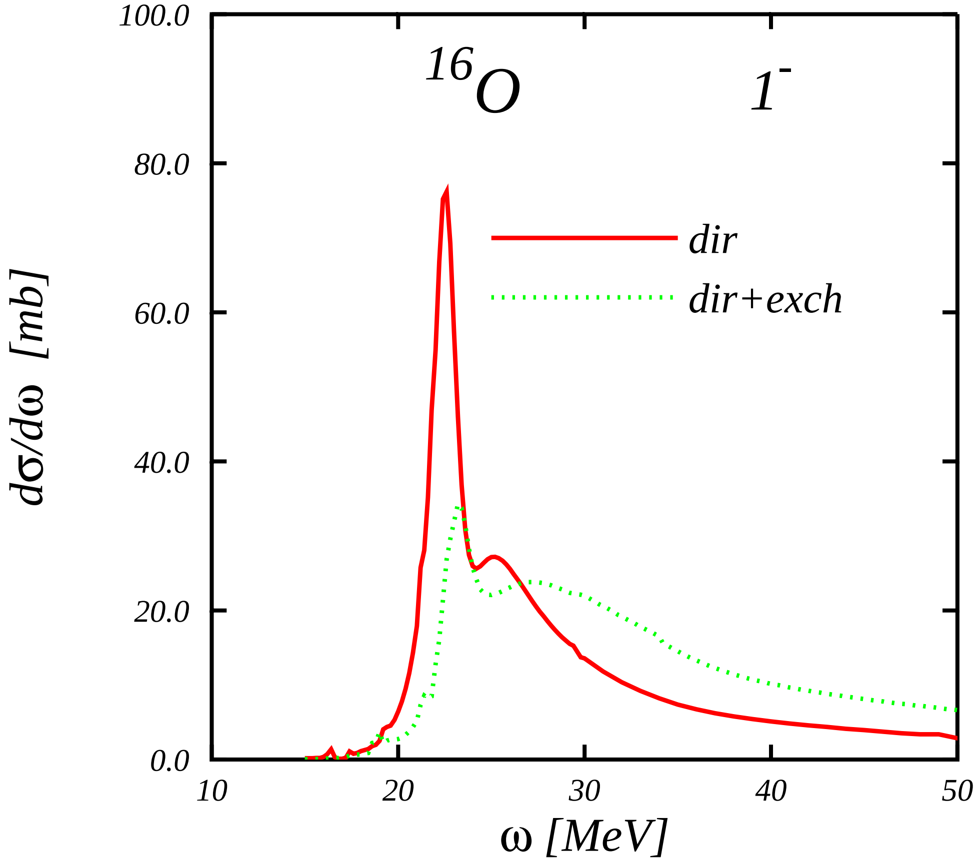

Figure 5.4: Photo absorption cross section of ^{16}O for 1^- excitation with the FRtt interaction considering only the direct and direct+exchange interaction matrix elements.

The role of the exchange diagrams is not negligible. The interaction used in this calculation has been adjusted to take into account in an effective manner the contribution of the exchange terms diagrams. For this reason, the results without exchange would describe the data better. However, the point we want to make here is that in a fully consistent calculation, where one uses the same interaction to describe the ground state, to generate the set of s.p. wave functions and energies, and to perform the RPA calculations, the exchange diagrams cannot be neglected.

The results we present in the following have been obtained within our CRPA approach with the interactions defined in Sect. 3.2. We start our discussion of the ^{16}O excitation by considering the excitation of the 1^- multipole. We controlled that the spurious isoscalar excitation related to the center of mass motion, is not present in the excitation spectrum. In Fig. 5.5 we compare the results obtained with the four interactions considered with the total photoabsorption cross section data of Ref. [98]. In Fig. 5.6 we show the sum rule exhaustion, Eq. 5.30, calculated for the 1- cross sections, and also a band obtained by integrating the experimental points.

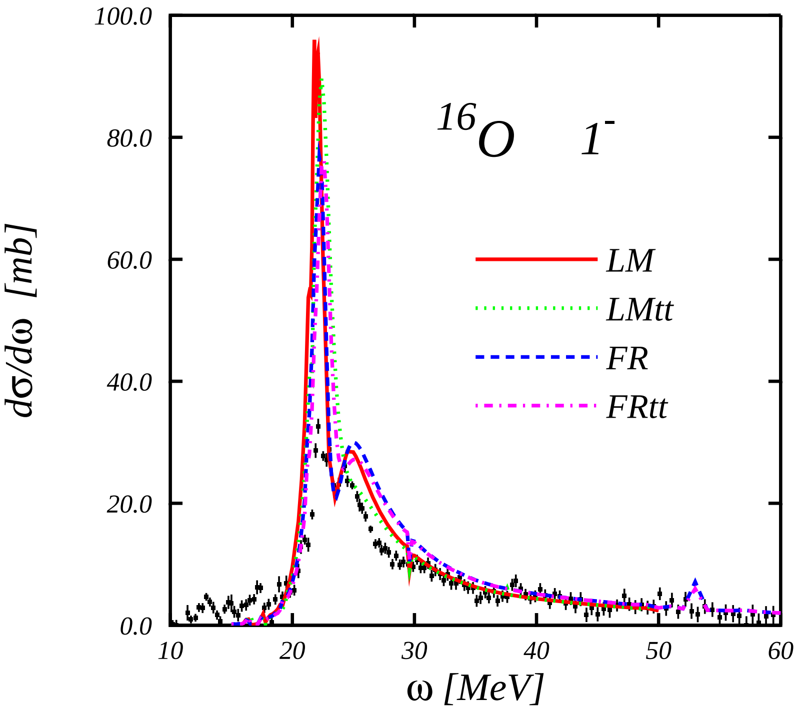

Figure 5.5: CRPA results for the 1^- excitation compared with the total photoabsorption data of Ref. [98].

We first remark that the four responses are rather similar. The number and the position of the maxima are essentially the same for the four calculations. The similarity of the theoretical results is shown also in Fig. 5.6. We show in Tabs. 5.1 and 5.2 the values of the momenta and of the energies for the various responses. These results are also indicating that the various interactions produce very similar results. As a general trend we observe that the zero range interactions produce values slightly smaller than those obtained with finite range interactions.

The comparison with the data shows that the position of the peak is well reproduced. We should remember that the parameters of the interaction have been adjusted to reproduce properties of

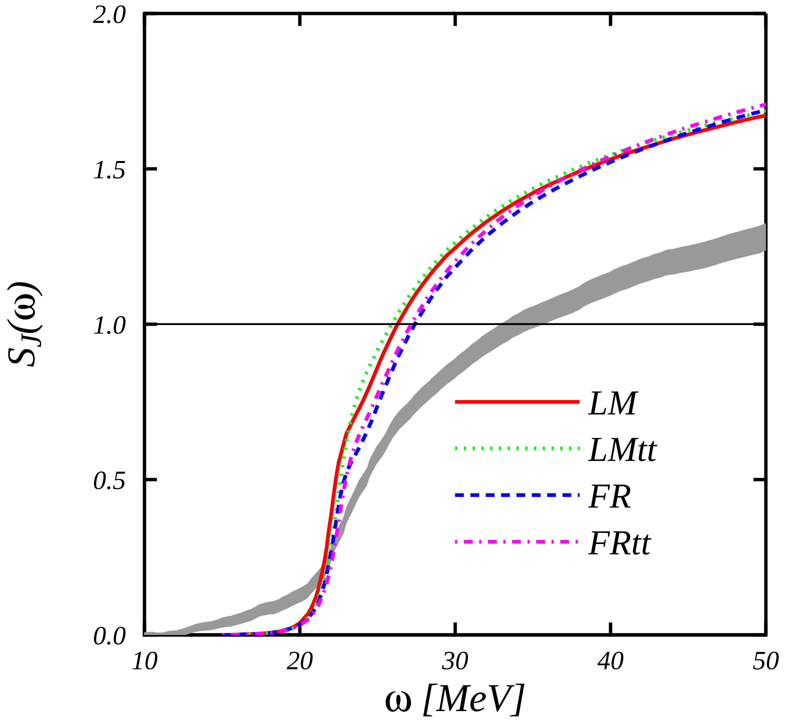

Figure 5.6: Sum rule exhaustion (Eq. (5.30)) for the 1^- excitation. The gray band indicates the experimental result.

the low-lying spectrum, by using a discrete, and limited, s.p. configuration space. The position of the peak of the resonance is a genuine prediction of our calculations. Clearly the magnitude of the cross section is too high and the width is narrower than the experimental one. These are well known features of the CRPA calculations [21, 99, 22, 55]. The inclusion of excitations more complex than the 1p-1h considered by the RPA is probably curing these problems [100].

From Fig. 5.6 of the sum rule exhaustion, we can infer further information about our results. The first remark is about the fact that the theoretical responses and experimental ones show exhaustion to values above the expected one. This value has been obtained by assuming that the hamiltonian commutes with the excitation operator. The results of Fig. 5.6 clearly indicate the poor quality of this assumption in the case of the 1^- excitation. We should remark that the terms of the hamiltonian which do not commute with the excitation operator are those which depend on the isospin. The 1^- excitation is mainly of isovector nature, therefore dominated by the isospin dependent terms of the interaction. The fact that the theoretical strengths are much higher than the experimental one should be further studied.

k	interaction	PROTONS	NEUTRONS	ISOVECTOR	ISOSCALAR
-1	LM	1.69412E-01	1.57613E-01	1.55095E-01	8.41802E-03
	LMtt	1.68544E-01	1.59385E-01	1.55909E-01	8.00706E-03
	FR	1.62989E-01	1.50926E-01	1.49549E-01	7.40922E-03
	FRtt	1.64421E-01	1.52714E-01	1.50956E-01	7.61131E-03
0	LM	4.16805E+00	3.95970E+00	3.84187E+00	2.22002E-01
	LMtt	4.16575E+00	4.00962E+00	3.87241E+00	2.12889E-01
	FR	4.20336E+00	3.97255E+00	3.89004E+00	1.97920E-01
	FRtt	4.23533E+00	4.01390E+00	3.92276E+00	2.01853E-01
1	LM	1.07075E+02	1.03914E+02	9.92948E+01	6.19987E+00
	LMtt	1.07367E+02	1.05182E+02	1.00193E+02	5.96521E+00
	FR	1.15476E+02	1.11176E+02	1.07620E+02	5.70617E+00
	FRtt	1.16049E+02	1.12005E+02	1.08241E+02	5.78555E+00
3	LM	8.41329E+04	8.50392E+04	7.88320E+04	5.75409E+03
	LMtt	8.47004E+04	8.56551E+04	7.94314E+04	5.46918E+03
	FR	1.13959E+05	1.12302E+05	1.06861E+05	6.26968E+03
	FRtt	1.13495E+05	1.12094E+05	1.06480E+05	6.31382E+03

Table 5.1: The values of m_{-1}, m_0, m_1 and m_3 in fm^4MeV^{-1} for the 1^- excitation of ^{16}O obtained with the four interactions used in our work.

	interaction	PROTONS	NEUTRONS	ISOVECTOR	ISOSCALAR
E_{cen}	LM	2.56894E+01	2.62430E+01	2.58454E+01	2.79271E+01
	LMtt	2.57737E+01	2.62324E+01	2.58735E+01	2.80202E+01
	FR	2.74724E+01	2.79860E+01	2.76655E+01	2.88307E+01
	FRtt	2.74002E+01	2.79042E+01	2.75931E+01	2.86622E+01
E_{con}	LM	2.51403E+01	2.56768E+01	2.53026E+01	2.71385E+01
	LMtt	2.52393E+01	2.56889E+01	2.53503E+01	2.72946E+01
	FR	2.66174E+01	2.71408E+01	2.68259E+01	2.77515E+01
	FRtt	2.65670E+01	2.70819E+01	2.67775E+01	2.75704E+01
E_S	LM	2.80310E+01	2.86070E+01	2.81766E+01	3.04647E+01
	LMtt	2.80872E+01	2.85369E+01	2.81565E+01	3.02795E+01
	FR	3.14143E+01	3.17825E+01	3.15111E+01	3.31475E+01
	FRtt	3.12729E+01	3.16353E+01	3.13645E+01	3.30350E+01

Table 5.2: The constrained (E_{con}), scaling (E_S) and the centroid energies (E_{cen}) in MeV for the 1^- excitation of ^{16}O obtained with the four interactions used in our work.

The contribution of the 2^+ excitation to the total photoabsorption cross section is shown in Fig. 5.7. Also in this case the various RPA results are very similar, as it is indicated by the momenta and the weighted energies values shown in Tabs. 5.3 and 5.4. Especially the weighted energies are very similar.

k	interaction	PROTONS	NEUTRONS	ISOVECTOR	ISOSCALAR
-1	LM	3.14268E+00	2.78445E+00	2.20501E+00	1.00357E+00
	LMtt	3.11887E+00	2.66091E+00	2.19332E+00	8.03453E-01
	FR	4.09658E+00	2.44565E+00	2.36877E+00	9.36750E-01
	FRtt	2.68631E+00	2.36950E+00	2.16009E+00	4.92091E-01
0	LM	9.77744E+01	9.61225E+01	7.65350E+01	3.49821E+01
	LMtt	9.73198E+01	8.81972E+01	7.56845E+01	2.25258E+01
	FR	1.14226E+02	8.35460E+01	7.93084E+01	2.17393E+01
	FRtt	8.84721E+01	8.21069E+01	7.54440E+01	1.52512E+01
1	LM	3.43857E+03	3.78563E+03	2.93814E+03	1.57474E+03
	LMtt	3.42449E+03	3.26181E+03	2.87589E+03	7.65088E+02
	FR	3.73578E+03	3.18161E+03	2.98222E+03	6.21603E+02
	FRtt	3.26229E+03	3.15286E+03	2.90830E+03	5.74659E+02
3	LM	6.57621E+06	8.97065E+06	6.21642E+06	5.48901E+06
	LMtt	6.51368E+06	6.65620E+06	5.92143E+06	1.92136E+06
	FR	6.74511E+06	6.73949E+06	6.15264E+06	1.46984E+06
	FRtt	6.58040E+06	6.72842E+06	6.12325E+06	1.65405E+06

Table 5.3: The values of m_{-1}, m_0, m_1 and m_3 in fm^4MeV^{-1} for the 2^+ excitation of ^{16}O obtained with the four interactions used in our work.

	interaction	PROTONS	NEUTRONS	ISOVECTOR	ISOSCALAR
E_{cen}	LM	3.51684E+01	3.93834E+01	3.83895E+01	4.50156E+01
	LMtt	3.51880E+01	3.69831E+01	3.79984E+01	3.39650E+01
	FR	3.27051E+01	3.80821E+01	3.76029E+01	2.85936E+01
	FRtt	3.68736E+01	3.83995E+01	3.85492E+01	3.76796E+01
E_{con}	LM	3.30780E+01	3.68722E+01	3.65032E+01	3.96124E+01
	LMtt	3.31359E+01	3.50118E+01	3.62105E+01	3.08585E+01
	FR	3.01981E+01	3.60684E+01	3.54820E+01	2.57599E+01
	FRtt	3.48484E+01	3.64775E+01	3.66930E+01	3.41730E+01
E_S	LM	4.37320E+01	4.86792E+01	4.59975E+01	5.90395E+01
	LMtt	4.36129E+01	4.51736E+01	4.53761E+01	5.01128E+01
	FR	4.24917E+01	4.60246E+01	4.54214E+01	4.86271E+01
	FRtt	4.49123E+01	4.61959E+01	4.58851E+01	5.36499E+01

Table 5.4: The constrained (E_{con}), scaling (E_S) and the centroid energies (E_{cen}) in MeV for the 2^+ excitation of ^{16}O obtained with the four interactions used in our work.

In the panel showing the sum rule exhaustion, we notice that all the calculations saturate at values smaller than that theoretically expected by Eq. (H.25). This may be due to the main isoscalar character of this type of excitation.

Two facts should be pointed out in the comparison with the 1^- results. The first one indicates that the 2^+ cross sections are two orders of magnitude smaller than the 1^- cross sections. This is due to the fact that we are studying the photo excitation, therefore the momentum transfer value is the smallest one compatible with the excitation energy. The excitation of the same multipoles with other probes, electrons for example, allows one to transfer larger momentum values. This enhances the contribution of the 2^+ with respect that of the 1^- multipole [99]. The second fact to be pointed out is that the maximum of the resonance is at about 33 MeV, against the 23 MeV of the dipole resonance.

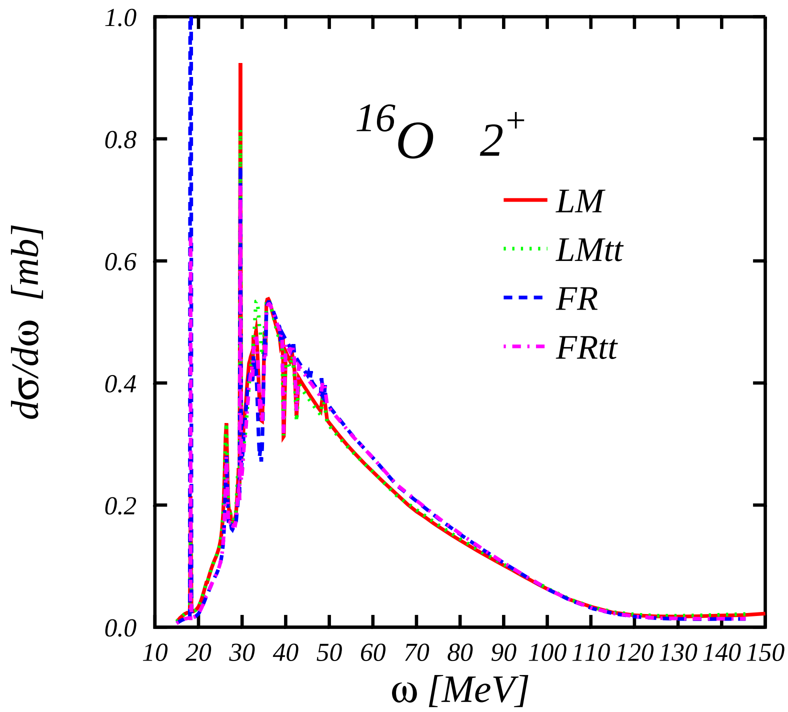

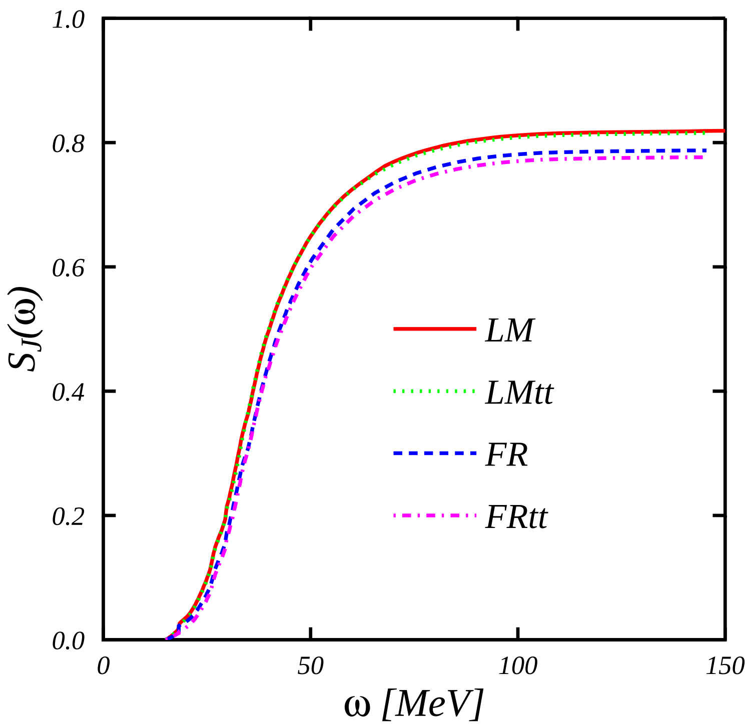

Figure 5.7: The same as Figs. 5.5 and 5.6 for the 2^+ excitation.

The results regarding the excitation of the 3^- resonance are shown in Fig. 5.8 and in Tabs. 5.5, 5.6. In this case there is a non-negligible difference between the results obtained with zero and finite range forces. The peaks of the resonances are around 90 MeV. Those of the zero-range forces are slightly larger, and in general the cross section seems to be shifted of about 10 MeV. The contribution of 3^- excitation to the total photoabsorptionn cross section is two oders of magnitude smaller than that of the 2^+.

k	interaction	PROTONS	NEUTRONS	ISOVECTOR	ISOSCALAR
-1	LM	9.55801E+01	8.11708E+01	5.26482E+01	1.42909E+02
	LMtt	8.73077E+01	7.17801E+01	4.37782E+01	1.43063E+02
	FR	8.47990E+01	7.03662E+01	4.25493E+01	1.40133E+02
	FRtt	8.96582E+01	7.65618E+01	4.83640E+01	1.38984E+02
0	LM	3.09972E+03	2.71640E+03	1.76186E+03	4.58477E+03
	LMtt	2.96049E+03	2.55859E+03	1.61287E+03	4.58669E+03
	FR	2.89906E+03	2.52181E+03	1.59945E+03	4.44392E+03
	FRtt	2.97419E+03	2.61750E+03	1.69032E+03	4.42210E+03
1	LM	1.17558E+05	1.07020E+05	7.28874E+04	1.57606E+05
	LMtt	1.15156E+05	1.04290E+05	7.03191E+04	1.57616E+05
	FR	1.12870E+05	1.02610E+05	7.01032E+04	1.50547E+05
	FRtt	1.13981E+05	1.04019E+05	7.14709E+04	1.50117E+05
3	LM	2.86545E+08	2.79632E+08	2.20326E+08	2.51050E+08
	LMtt	2.85665E+08	2.78595E+08	2.19378E+08	2.51008E+08
	FR	2.72444E+08	2.65050E+08	2.13395E+08	2.21408E+08
	FRtt	2.72559E+08	2.65175E+08	2.13557E+08	2.21238E+08

Table 5.5: The values of m_{-1}, m_0, m_1 and m_3 in $fm^4 MeV^{-1}$ for the 3^- excitation of ^{16}O obtained with the four interactions used in our work.

	interaction	PROTONS	NEUTRONS	ISOVECTOR	ISOSCALAR
E_{cen}	LM	3.79255E+01	3.93976E+01	4.13695E+01	3.43760E+01
	LMtt	3.88976E+01	4.07608E+01	4.35989E+01	3.43637E+01
	FR	3.89333E+01	4.06891E+01	4.38294E+01	3.38772E+01
	FRtt	3.83235E+01	3.97399E+01	4.22825E+01	3.39471E+01
E_{con}	LM	3.50706E+01	3.63105E+01	3.72078E+01	3.32091E+01
	LMtt	3.63176E+01	3.81170E+01	4.00782E+01	3.31923E+01
	FR	3.64832E+01	3.81868E+01	4.05903E+01	3.27768E+01
	FRtt	3.56551E+01	3.68596E+01	3.84418E+01	3.28650E+01
E_S	LM	4.93707E+01	5.11166E+01	5.49802E+01	3.99111E+01
	LMtt	4.98064E+01	5.16851E+01	5.58547E+01	3.99065E+01
	FR	4.91303E+01	5.08240E+01	5.51726E+01	3.83495E+01
	FRtt	4.89005E+01	5.04905E+01	5.46629E+01	3.83897E+01

Table 5.6: The constrained (E_{con}), scaling (E_S) and the centroid energies (E_{cen}) in MeV for the 3^- excitation of ^{16}O obtained with the four interactions used in our work.

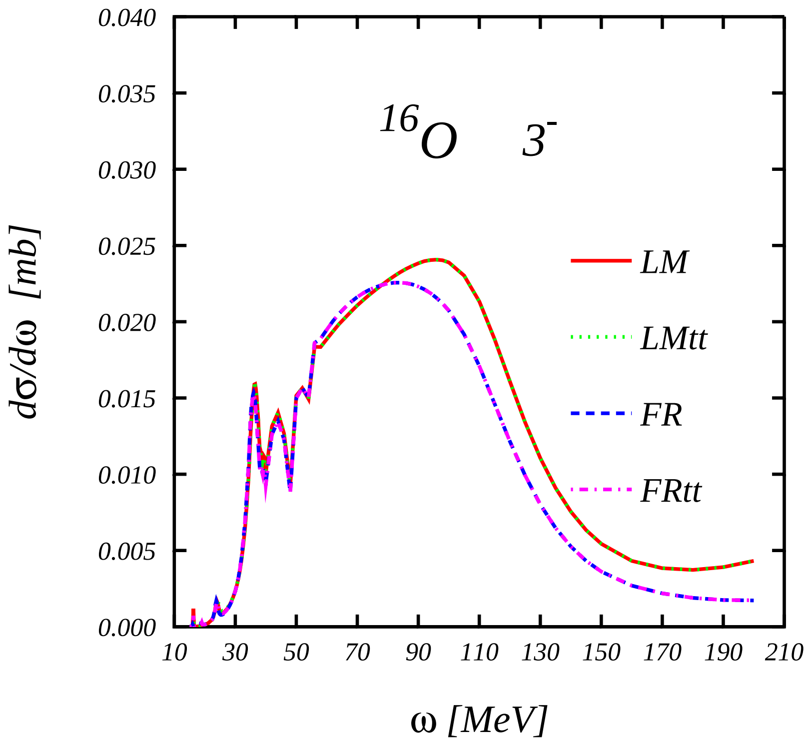

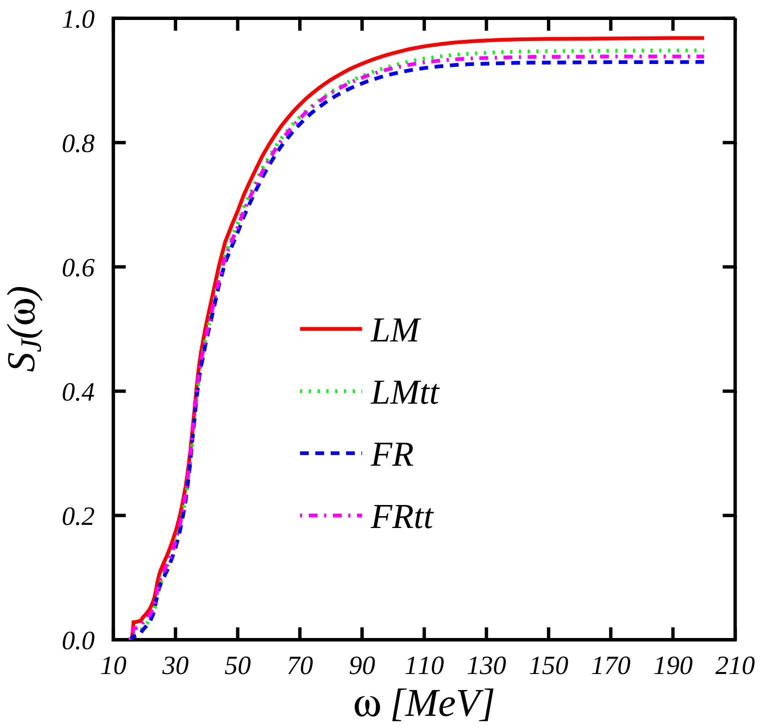

Figure 5.8: The same as Figs. 5.5 and 5.6 for the 3^- excitation.

We conclude this section by showing in Fig. 5.9 the contribution to the total photoabsorption cross section of two magnetic, unnatural parity, multipole excitations. In the upper panel we show the 1^+, and in the lower panel the 2^-. Clearly, the magnitude of these contributions is much smaller than that of the 1^-. We should however consider that these resonances can be relevant in hadron and neutrino scattering processes [55]. Our interaction produce results for the 1^+ excitation which almost overlap. The situation is quite different for the 2^- excitation which shows a remarkable sensitivity to the finite range of the force, and also to the presence of the tensor channel.

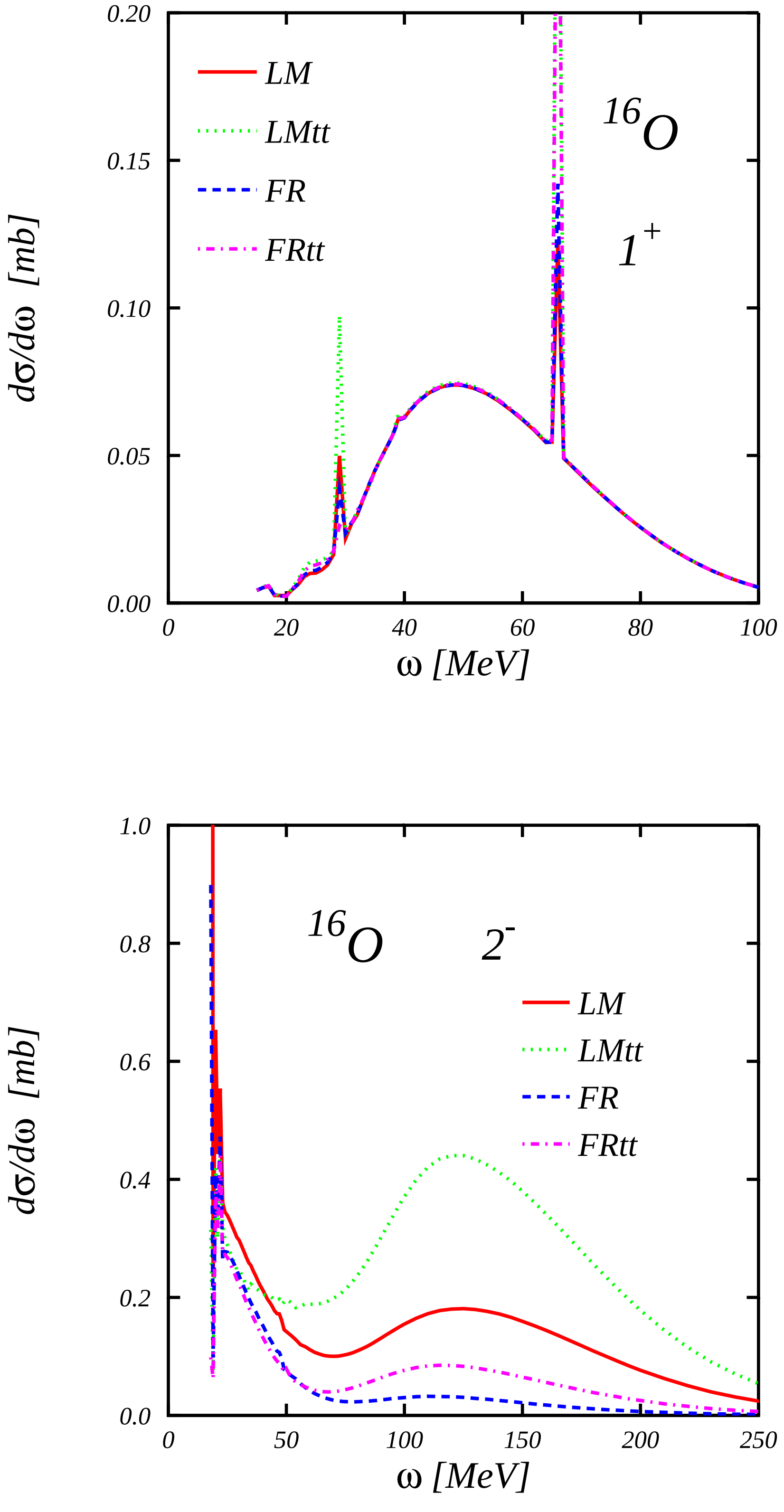

Figure 5.9: Photo absorption cross section of ^{16}O for 1^+ and 2^- excitations.

5.2 Conclusions

Even if the results we have shown are limited to the ^{16}O nucleus and to the contribution to the total photoabsorption cross section, we think that the potentiality of our approach is demonstrated. The proper treatment of the continuum is necessary to obtain accurate descriptions of the giant resonances. The use of finite range forces which consider also the tensor channel is important to describe the excitation of magnetic resonances. Furthermore the treatment of the exchange matrix elements is necessary if is one is aiming to make self-consistent calculations, as those we shall present in the next chapter.

Chapter 6

Selfconsistent RPA calculations

6.1 Numerical solution of Hartree-Fock equations

In this chapter we use as s.p. basis the wave functions that are derived from Hartree-Fock equations [101, 102] solved with an iterative method.

6.2 S.p. basis

In this section we show the neutron and proton distribution obtained in HF theory and we compare them with those obtained with the Woods-Saxon potential. Then we will show the energy spectra obtained by the two way and compare with experiment.

We show in the next figure the proton and neutron distribution for nuclei of ^{12}C, ^{40}Ca, ^{48}Ca, ^{16}O, ^{90}Zr obtained with HF theory.

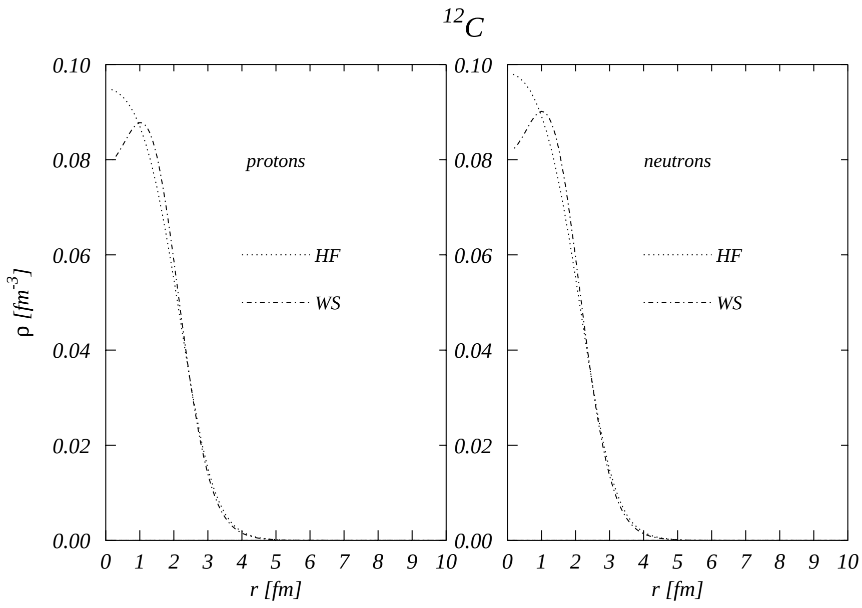

Figure 6.1: Proton and neutron distribution for ^{12}C.

The distributions of ^{12}C and ^{16}O show differences for small r, but for the first nucleus the HF calculations are higher than that of WS, while for the second the contrary happens.

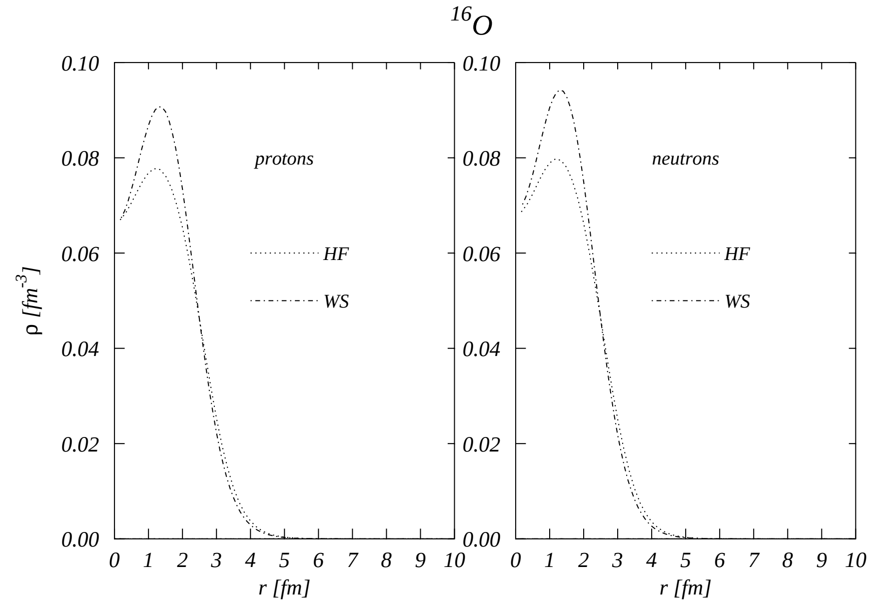

Figure 6.2: Proton and neutron distribution for ^{16}O.

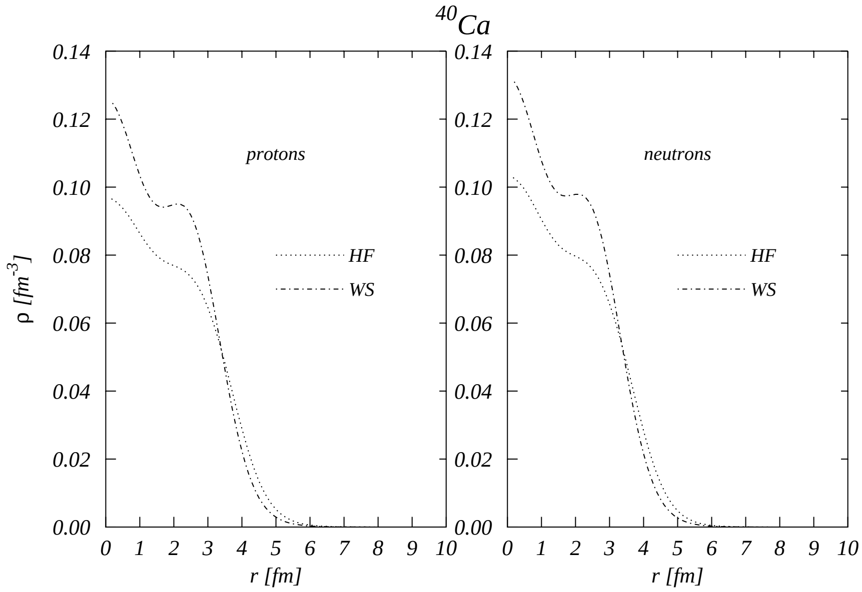

Figure 6.3: Proton and neutron distribution for ^{40}Ca.

The calculations for ^{40}Ca and ^{48}Ca give HF distributions always smaller than WS ones.

The proton distribution for ^{90}Zr is very similar to that of the WS potential. Instead the HF neutron distribution is much larger than the WS one.

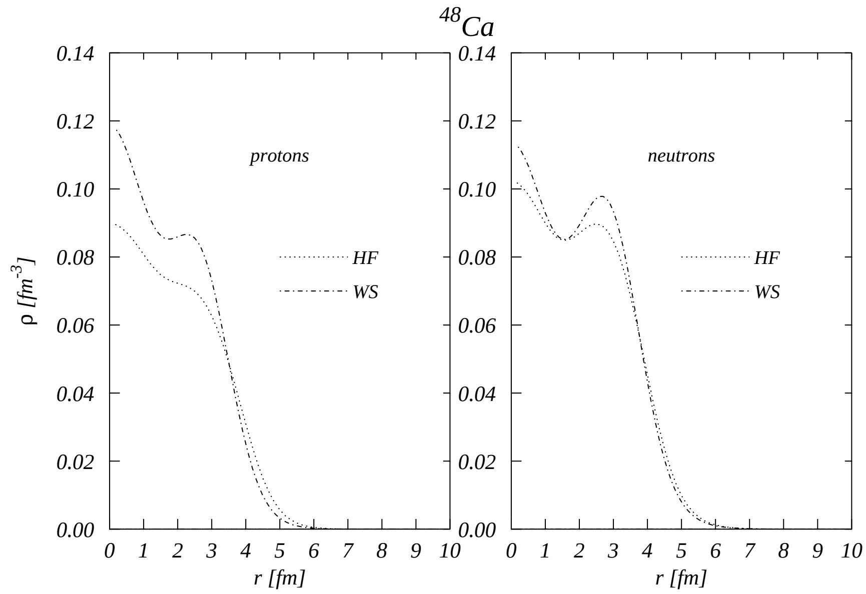

Figure 6.4: Proton and neutron distribution for ^{48}Ca.

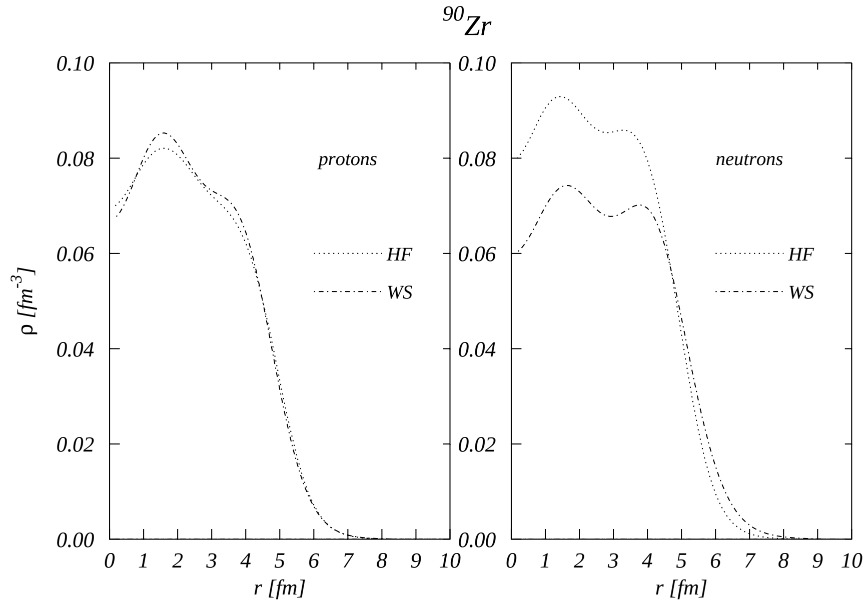

Figure 6.5: Proton and neutron distribution for ^{90}Zr.

In Tabs. 6.1 - 6.5 we show the s.p. spectra (limited to the bound states) for the six nuclei under study. We compare these energies with the experimental ones, and with that obtained with the WS potential. The line in the tables indicates the Fermi level, which separates the occupied states (hole states), from the empty ones (particle states).

^{12}C	j	l	n	E [MeV] HF	WS	Exp
Protons	1/2	0	1	-34.72	-30.90	-30.90
	3/2	1	1	-14.34	-15.75	-15.96
	1/2	1	1	-7.28	-12.95	-1.94
	5/2	2	1	1.52	-0.78	
Neutrons	1/2	0	1	-37.82	-34.04	-34.04
	3/2	1	1	-16.88	-18.92	-18.72
	1/2	1	1	-10.12	-15.06	-4.96
	5/2	2	1	-0.90	-3.88	-1.10
	1/2	0	2	-0.45	-1.96	-1.86

Table 6.1: S.p. energies in MeV calculated with the Woods-Saxon potential for ^{12}C. The experimental values are taken from [40].

The spectrum of ^{16}O is in quite good agreement with the experimental and WS ones for levels below the Fermi level. For the particle states the differences are higher, moreover there is an inversion of the $2s_{1/2}$ and $1d_{5/2}$ neutrons states, but we have to notice also that on HF theory gives the $1d_{5/2}$ proton state unbound in agreement with the experimental evidence.

^{16}O	j	l	n	E [MeV] HF	WS	Exp
Protons	1/2	0	1	-36.17	-29.92	-29.81
	3/2	1	1	-18.44	-16.93	-18.44
	1/2	1	1	-12.69	-12.75	-12.11
	5/2	2	1	1.85	-3.77	-0.60
	1/2	0	2	0.65	-0.90	-0.10
Neutrons	1/2	0	1	-39.47	-33.98	-34.03
	3/2	1	1	-21.72	-20.52	-21.81
	1/2	1	1	-15.84	-16.63	-15.65
	5/2	2	1	-5.84	-6.84	-4.14
	1/2	0	2	-2.19	-3.90	-3.27
	3/2	2	1	0.88	-0.29	

Table 6.2: The same as Tab. 6.1 for ^{16}O. Experimental values from [40]

In Tab. 6.2 we show the s.p. spectrum of ^{16}O. The larger differences are for the most bound proton and neutron states. The HF theory gives the proton states above Fermi level all unbound unlike the experimental data. This happens also for the $1d_{3/2}$ neutron state.

For ^{40}Ca we observe a good agreement for the states below the Fermi level, except for the most bound states. In the particle energies there is an inversion of the neutron $2p_{1/2}$ and $1f_{5/2}$ levels. Similar considerations can be done for the ^{48}Ca nucleus, Tab. 6.4. Here the inversion is on the same proton states.

In Fig. 6.5 we show the ^{90}Zr spectrum.

^{40}Ca	j	l	n	E [MeV] HF	WS	Exp
Protons	1/2	0	1	-44.83	-36.00	-36.18
	3/2	1	1	-30.19	-26.51	-26.62
	1/2	1	1	-26.52	-23.02	-23.14
	5/2	2	1	-15.63	-16.19	-14.73
	1/2	0	2	-10.14	-10.30	-10.33
	3/2	2	1	-9.29	-8.71	-8.30
	7/2	3	1	-1.68	-5.31	-1.63
Neutrons	1/2	0	1	-52.16	-42.57	-42.57
	3/2	1	1	-37.33	-32.42	-32.42
	1/2	1	1	-33.58	-29.80	-29.80
	5/2	2	1	-22.65	-21.37	-21.60
	1/2	0	2	-17.25	-16.42	-18.20
	3/2	2	1	-16.15	-15.70	-15.60
	7/2	3	1	-8.69	-9.76	-8.36
	3/2	1	2	-3.63	-4.85	-6.20
	1/2	1	2	-1.67	-2.30	-1.96
	5/2	3	1	-0.62	-0.82	-4.23

Table 6.3: The same as Tab. 6.1 for ^{40}Ca. Experimental values from [40].

^{48}Ca	j	l	n	E [MeV] HF	WS	Exp
Protons	1/2	0	1	-51.12	-39.70	-39.70
	3/2	1	1	-37.45	-30.56	-30.56
	1/2	1	1	-34.19	-28.36	-28.36
	5/2	2	1	-23.16	-20.34	-20.34
	3/2	2	1	-17.03	-15.47	-16.17
	1/2	0	2	-16.70	-15.24	-15.81
	7/2	3	1	-8.91	-9.37	-9.63
	3/2	1	2	-2.14	-3.66	-6.54
	5/2	3	1	-0.56	-1.31	-5.82
	1/2	1	2	-0.16	-1.08	-6.11
Neutrons	1/2	0	1	-53.09	-39.19	-39.19
	3/2	1	1	-38.00	-30.11	-30.11
	1/2	1	1	-35.74	-28.06	-28.06
	5/2	2	1	-23.08	-20.11	-20.11
	1/2	0	2	-18.06	-15.66	-12.55
	3/2	2	1	-18.07	-15.59	-12.53
	7/2	3	1	-9.13	-9.51	-9.95
	3/2	1	2	-4.37	-4.88	-5.24
	1/2	1	2	-2.56	-2.70	-2.70
	5/2	3	1	-1.55	-2.17	-2.17

Table 6.4: The same as Tab. 6.1 for ^{48}Ca. Experimental values from [40].

^{90}Zr	j	l	n	E HF	WS	Exp
Protons	1/2	0	1	-50.46	-35.13	-63.96
	3/2	1	1	-40.12	-29.22	
	1/2	1	1	-38.15	-28.15	
	5/2	2	1	-28.66	-22.27	
	3/2	2	1	-24.71	-19.95	
	1/2	0	2	-22.88	-18.62	-21.80
	7/2	3	1	-16.68	-14.49	-17.00
	5/2	3	1	-10.51	-10.59	-10.80
	3/2	1	2	-9.48	-9.77	-10.40
	1/2	1	2	-7.50	-8.36	-8.36
	9/2	4	1	-4.52	-6.08	-5.17
	5/2	2	2	2.78	-1.04	
	7/2	4	1	3.55	-0.39	
Neutrons	1/2	0	1	-59.33	-41.03	
	3/2	1	1	-47.89	-34.81	
	1/2	1	1	-46.52	-33.77	
	5/2	2	1	-35.52	-27.72	
	3/2	2	1	-32.52	-25.41	
	1/2	0	2	-31.04	-24.54	
	7/2	3	1	-23.12	-19.92	
	5/2	3	1	-17.92	-16.01	
	3/2	1	2	-17.58	-15.75	
	1/2	1	2	-15.94	-14.32	
	9/2	4	1	-11.07	-11.58	-11.57
	5/2	2	2	-5.41	-7.13	-7.20
	7/2	4	1	-3.65	-5.88	-5.87
	1/2	0	3	-3.36	-5.40	
	3/2	2	2	-2.77	-4.70	-2.90
	11/2	5	1	0.39	-2.84	

Table 6.5: The same as Tab. 6.1 for ^{90}Zr. Experimental values from [40]

6.3 Continuum with HF

In Fig. 6.6 we compare the first three $s_{1/2}$ s.p. states obtained by HF calculation, with those obtained by using WS potential.

We observe that the wave functions of the first sp state are very similar. This is a bound state.

The second state (that is unbound for HF calculations in agreement with experimental data but it is bound with the WS potential) shows differences in magnitude (the HF wave function is always smaller than the other).

Larger differences can be noticed in the third state where besides the considerations about the magnitude done in the second state, we observe that the maxima are shifted.

6.4 Gogny interaction

The residual interaction used to do our selfconsistent RPA calculations is the Gogny interaction. It has the following expression

$$\begin{aligned} V(1,2) = \sum_{i=1}^{2} e^{-(\boldsymbol{r_1}-\boldsymbol{r_2})^2/\mu_i^2}(W_i + B_i\hat{P}_\sigma - H_i\hat{P}_\tau - M_i\hat{P}_\sigma\hat{P}_\tau) + \\ +W_{LS}(\boldsymbol{\sigma_1}+\boldsymbol{\sigma_2})\boldsymbol{k}\times\delta(\boldsymbol{r_1}-\boldsymbol{r_2})\boldsymbol{k} + \\ +t_0(1+x_0\hat{P}_\sigma)\delta(\boldsymbol{r_1}-\boldsymbol{r_2})\rho^\alpha\Big(\frac{1}{2}(\boldsymbol{r_1}+\boldsymbol{r_2})\Big) \end{aligned} \tag{6.1}$$

It is easy to find the correspondence between the Gogny term and our interaction term (2.23). The expression in parenthesis of the first line of (6.1) can be rewritten as:

$$\begin{aligned} W + B\frac{1}{2}(1+\boldsymbol{\sigma_1}\cdot\boldsymbol{\sigma_2}) - H\frac{1}{2}(1+\boldsymbol{\tau_1}\cdot\boldsymbol{\tau_2}) - M\frac{1}{4}(1+\boldsymbol{\sigma_1}\cdot\boldsymbol{\sigma_2})(1+\boldsymbol{\tau_1}\cdot\boldsymbol{\tau_2}) = \\ = W + \frac{B}{2} + \frac{B}{2}\boldsymbol{\sigma_1}\cdot\boldsymbol{\sigma_2} - \frac{H}{2} - \frac{H}{2}\boldsymbol{\tau_1}\cdot\boldsymbol{\tau_2} - \frac{M}{4} - \frac{M}{4}\boldsymbol{\sigma_1}\cdot\boldsymbol{\sigma_2} - \frac{M}{4}\boldsymbol{\tau_1}\cdot\boldsymbol{\tau_2} - \frac{M}{4}\boldsymbol{\sigma_1}\cdot\boldsymbol{\sigma_2}\boldsymbol{\tau_1}\cdot\boldsymbol{\tau_2} = \\ = (W + \frac{B}{2} - \frac{H}{2} - \frac{M}{4}) + (\frac{B}{2} - \frac{M}{4})\boldsymbol{\sigma_1}\cdot\boldsymbol{\sigma_2} + (-\frac{H}{2} - \frac{M}{4})\boldsymbol{\tau_1}\cdot\boldsymbol{\tau_2} - \frac{M}{4}\boldsymbol{\sigma_1}\cdot\boldsymbol{\sigma_2}\boldsymbol{\tau_1}\cdot\boldsymbol{\tau_2} \end{aligned} \tag{6.2}$$

in this way we can immediately identify the V_c, V_σ, V_τ and $V_{\sigma\tau}$ terms.

The density dependent term of (6.1) can be rewritten as:

$$t_0(1+x_0P_\sigma)\rho^\alpha = t_0\Big[1 - \frac{x_0}{2}(1+\boldsymbol{\tau_1}\cdot\boldsymbol{\tau_2})\Big]\rho^\alpha = \Big[t_0(1-\frac{x_0}{2}) - \frac{t_0x_0}{2}\boldsymbol{\tau_1}\cdot\boldsymbol{\tau_2}\Big]\rho^\alpha \tag{6.3}$$

From the parameters fixed for the D1 interaction [31, 32] we derive the correspondent values for our interactions. These values are shown in Tab.6.6

i	b=$\frac{1}{\mu_i^2}[fm^-2]$	$V_c[MeV]$	$V_\sigma[MeV]$	$V_\tau[MeV]$	$V_{\sigma\tau}$
1	2.05	-198.41	-44.11	253.99	5.89
2	0.69	-29.58	11.35	-1.43	17.20

Table 6.6: Values of the parameters of the D1 interaction.

The index i refers to each of the two gaussians. The other values are: $V_\rho = 675MeV$, $V_{\rho\tau} = -675MeV$, $W_{LS} = 115MeV$, $t_0 = 1350MeVfm^4$, $\alpha = 1/3$ and $x_0 = 1.0$.

6.5 Self-consistent discrete RPA results

6.5.1 The ^{16}O nucleus

The spectrum of ^{16}O nucleus obtained with the D1 interaction is presented in Tab.6.7.

^{16}O			
excitation	D1	FRtt	exp
3^-	7.44	6.14	6.13
2^-	10.61	11.51	8.87
0^-	15.34	11.84	10.96
0^-	13.34	12.23	12.80
4^-	19.43	17.73	17.79
4^-	15.50	19.45	18.98

Table 6.7: Low energy spectrum of the ^{16}O nucleus. All the energies are expressed in MeV. The experimental energies are taken from [40]

We observe that the D1 calculations give energy states always higher than the experimental data. The only exception is for the second 4^- excitation energy state. We have also to observe the inversion of the isoscalar and isovector 4^- states.

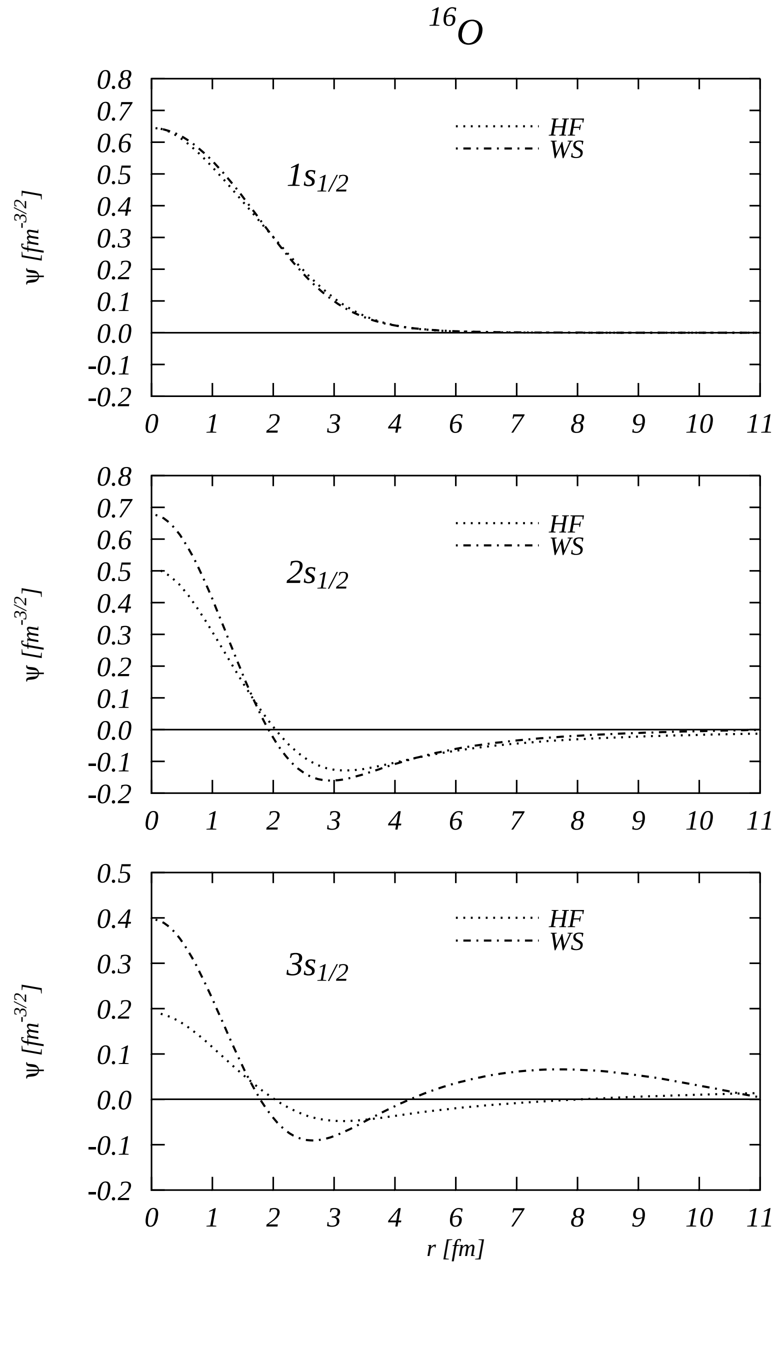

Figure 6.6: S.p. wave functions for $s_{1/2}$ states obtained with HF and WS methods.

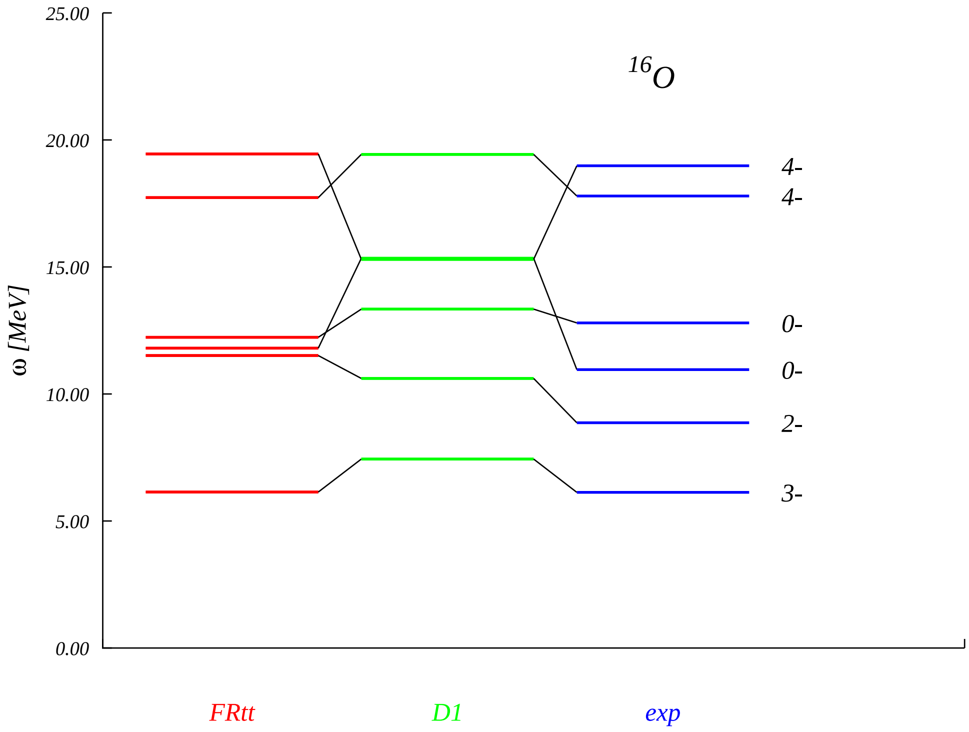

Figure 6.7: ^{16}O spectrum

We start the analysis of the details of the spectrum by studying the longitudinal response and the transition density of the 3^- excited state. We make a comparison with the RPA results obtained with the FRtt interaction in LMFFS framework.

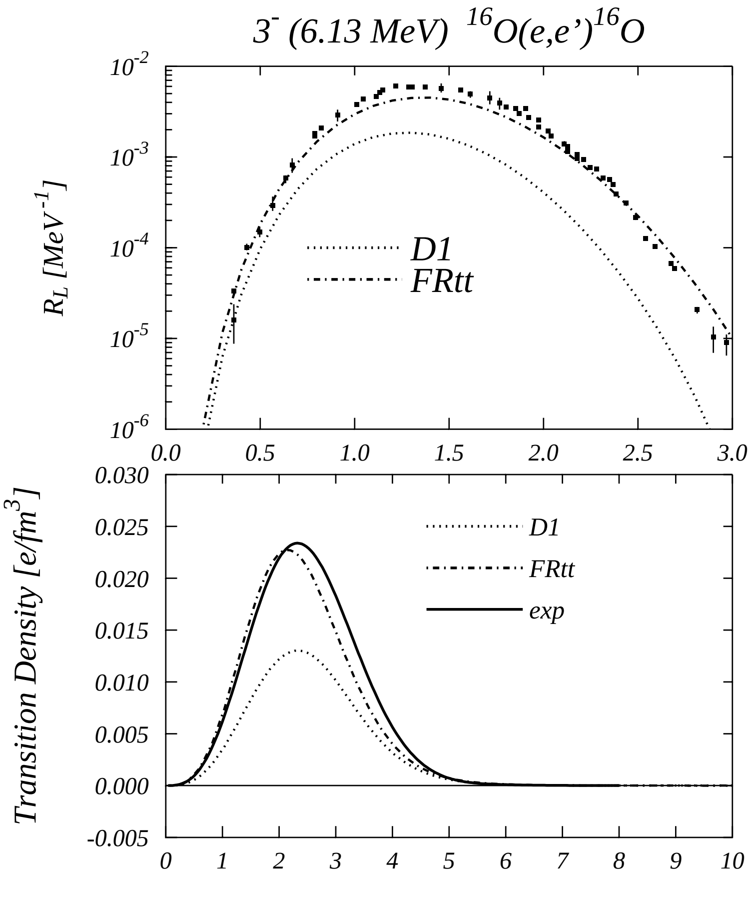

Figure 6.8: Longitudinal response and transition density for the lowest 3^- excited state of ^{16}O. Experimental data from [52]

.

We present in Tab. 6.8 the main ph pairs and their RPA amplitudes for the lowest 3^- state. This state is less collective than those obtained in the LMFFS approach, as it comes out from the comparison with the results shown in Tab. 3.9, and from Fig. 6.8. In this figure the D1 self-consistent results for the longitudinal response and transition density are compared with those obtained in LMFFS with the FRtt interaction. The D1 response and transition density are smaller than the FRtt ones, due to lack of collectivity. For this reason the comparison with the experimental response and transition density is not satisfying.

3^- (6.13 MeV)		$D1$	
ω		7.44	
transition	ϵ_p -ϵ_h	X	Y
$[(1d_{5/2})(1p_{3/2})^{-1}]_\pi$	15.99	-0.20	0.07
$[(1d_{5/2})(1p_{1/2})^{-1}]_\pi$	10.25	-0.67	0.01
$[(1d_{5/2})(1p_{3/2})^{-1}]_\nu$	15.88	0.20	-0.07
$[(1d_{5/2})(1p_{1/2})^{-1}]_\nu$	10.04	0.70	-0.10

Table 6.8: Main ph pairs for the lowest 3^- state and their X and Y amplitudes calculated with the D1 interaction.

We show in Tab. 6.9 and Fig. 6.9 the results obtained for the first 2^- state. The main ph pairs characterizing the transition are the same as the ones obtained in the LMFFS calculations, (see Tab. 3.12). In the D1 calculation the neutron ph excitation dominates, while in the results of Tab. 3.12 proton and neutron excitations have similar amplitudes. This difference produces the remarkable difference in the response shown in Fig. 6.9.

2^- (8.87 MeV)		$D1$	
ω		10.61	
transition	ϵ_p -ϵ_h	X	Y
$[(1d_{5/2})(1p_{1/2})^{-1}]_\pi$	10.25	- 0.66	0.01
$[(1d_{5/2})(1p_{1/2})^{-1}]_\nu$	10.04	0.75	-0.01

Table 6.9: Main ph pairs for the lowest 2^- state and their X and Y amplitudes calculated with the D1 interaction.

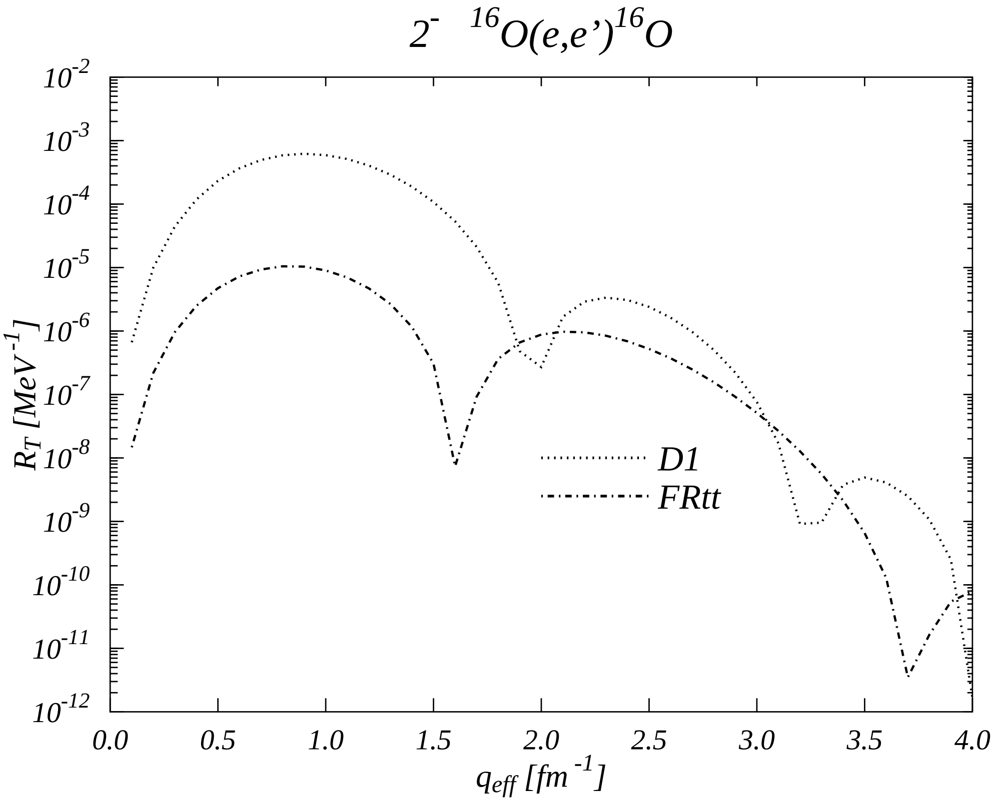

Figure 6.9: Transverse response for the 2^- excited state in ^{16}O calculated with the D1 interaction.

As we have already pointed out in sect. 3.3.1, the 4^- excited states form an isospin doublet, see Tab. 3.13 and Fig. 3.17. The lower energy state ($\omega = 17.79 MeV$) is isoscalar, the higher energy state ($\omega = 18.98 MeV$) is isovector. The D1 calculations invert the position of the two states. This is clearly shown in Fig. 6.10 where the D1 responses are compared with the FRtt responses of Chap. 3. and with the data.
The D1 response obtained for $15.5 MeV$ compares well with the isovector responses. The D1 response for $19.43 MeV$ compares well with the isoscalar responses.

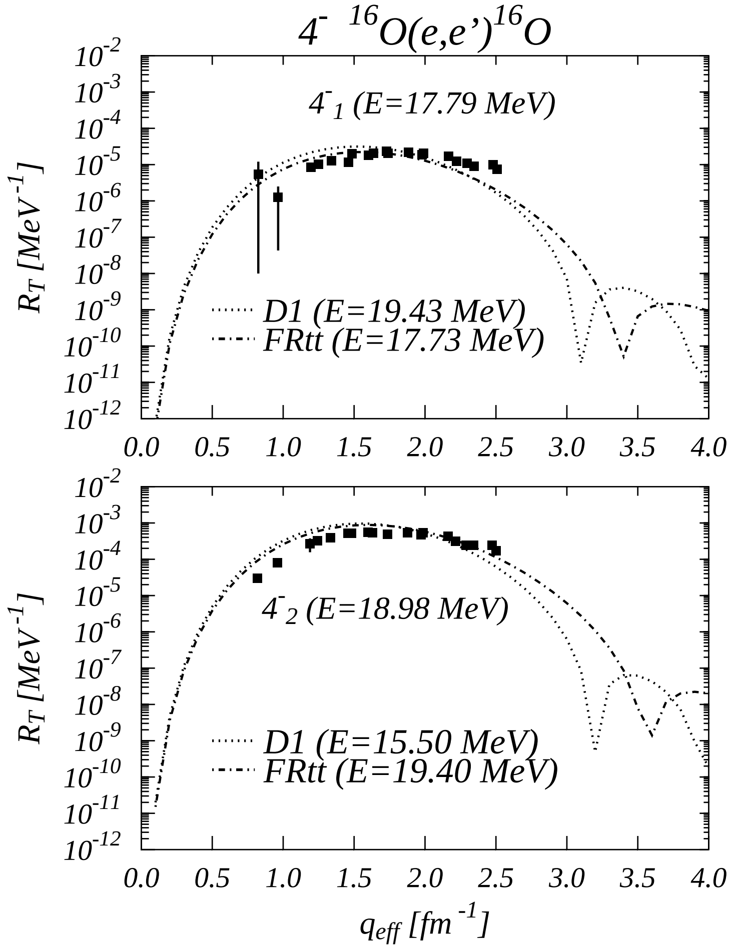

Figure 6.10: Transverse responses for the first two 4^- excited states in ^{16}O calculated with the D1 and FRtt interactions. Experimental data from [53]

4^- (17.79 MeV)		$D1$	
ω		19.43	
transition	ϵ_p -ϵ_h	X	Y
$[(1d_{5/2})(1p_{3/2})^{-1}]_\pi$	16.00	0.71	-0.06
$[(1d_{5/2})(1p_{3/2})^{-1}]_\nu$	15.88	0.70	-0.06
4^- (18.98 MeV)		$D1$	
ω		15.50	
transition	ϵ_p -ϵ_h	X	Y
$[(1d_{5/2})(1p_{3/2})^{-1}]_\pi$	16.00	-0.70	-0.01
$[(1d_{5/2})(1p_{3/2})^{-1}]_\nu$	15.88	0.71	0.01

Table 6.10: Main ph pairs for the lowest 4^- states and their X and Y amplitudes calculated with the D1 interaction.

6.5.2 The ^{12}C nucleus

We show in Tab. 6.11 and Fig. 6.11 the D1 spectrum and we compare it with the experimental one and with that obtained with the FRtt force. The agreement with the experimental spectrum is rather poor. There are many inversions in the levels position.

^{12}C			
excitation	D1	FRtt	exp
2^+	2.64	4.47	4.44
3^-	14.81	11.83	9.64
1^-	10.91	15.55	10.84
2^-	17.05	16.03	11.83
1^+	11.17	13.87	12.71
2^-	16.75	17.14	13.35
1^+	7.73	18.05	15.11
4^-	19.16	17.75	18.27
4^-	15.63	19.49	19.50

Table 6.11: Low excited states in ^{12}C. The energies are expressed in MeV. The experimental values are taken from [40]

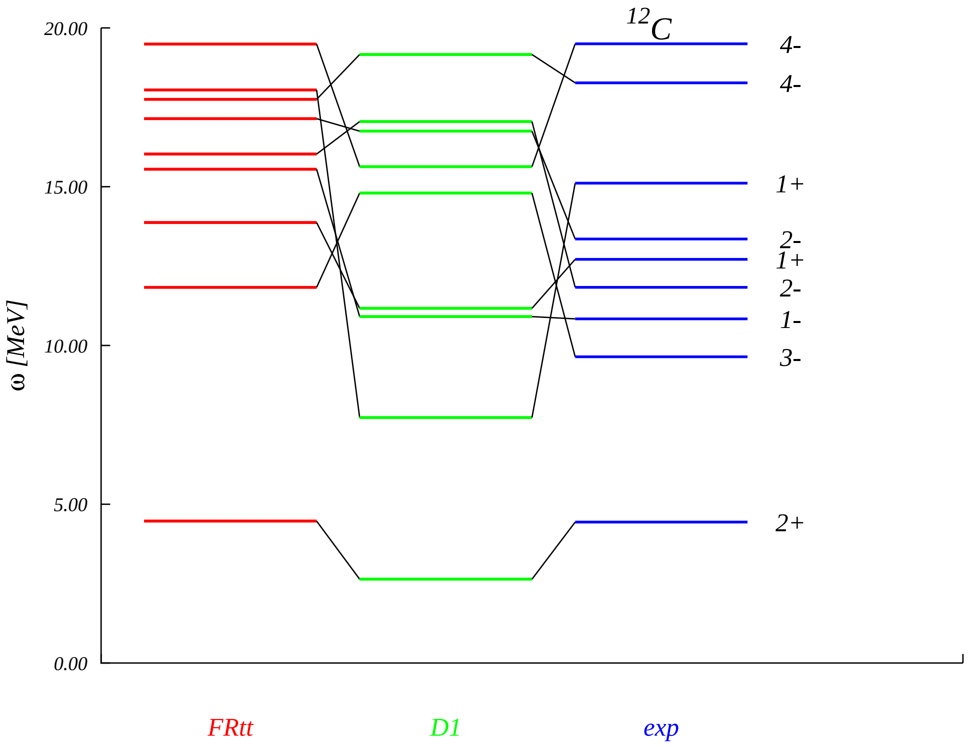

Figure 6.11: ^{12}C spectrum

We have studied the excitation of the first 2^+ and 3^- states. We present in Tabs. 6.12 and 6.13 their main ph components and in Fig. 6.12 the longitudinal and transverse electron scattering responses,and we compare them with the FRtt responses.

2^+ (4.44 MeV)		$D1$	
ω		2.64	
transition	ϵ_p -ϵ_h	X	Y
$[(1p_{1/2})(1p_{3/2})^{-1}]_\pi$	7.06	-0.76	-0.32
$[(1p_{1/2})(1p_{3/2})^{-1}]_\nu$	6.76	0.79	0.33

Table 6.12: Main ph pairs for the first 2^+ state and their X and Y amplitudes calculated with the D1 interaction.

3^- (9.64 MeV)		$D1$	
ω		14.81	
transition	ϵ_p -ϵ_h	X	Y
$[(1d_{5/2})(1p_{3/2})^{-1}]_\pi$	15.87	-0.56	0.02
$[(2d_{5/2})(1p_{3/2})^{-1}]_\pi$	16.08	-0.44	0.02
$[(1d_{5/2})(1p_{3/2})^{-1}]_\nu$	15.98	0.70	-0.03

Table 6.13: Main ph pairs for the first 3^- state and their X and Y amplitudes calculated with the D1 interaction.

For both states the behaviour of the longitudinal responses is quite clean. The shapes of the responses are similar for both the calculations, and the D1 results are smaller than those obtained with the FRtt calculations.

The situation for the transverse responses is quite different. For the 2^+ state the D1 response is higher than the FRtt one. For the 3^- state the two responses have the same magnitude, however, the D1 response has a minimum at small momenta that there is not present in FRtt calculations.

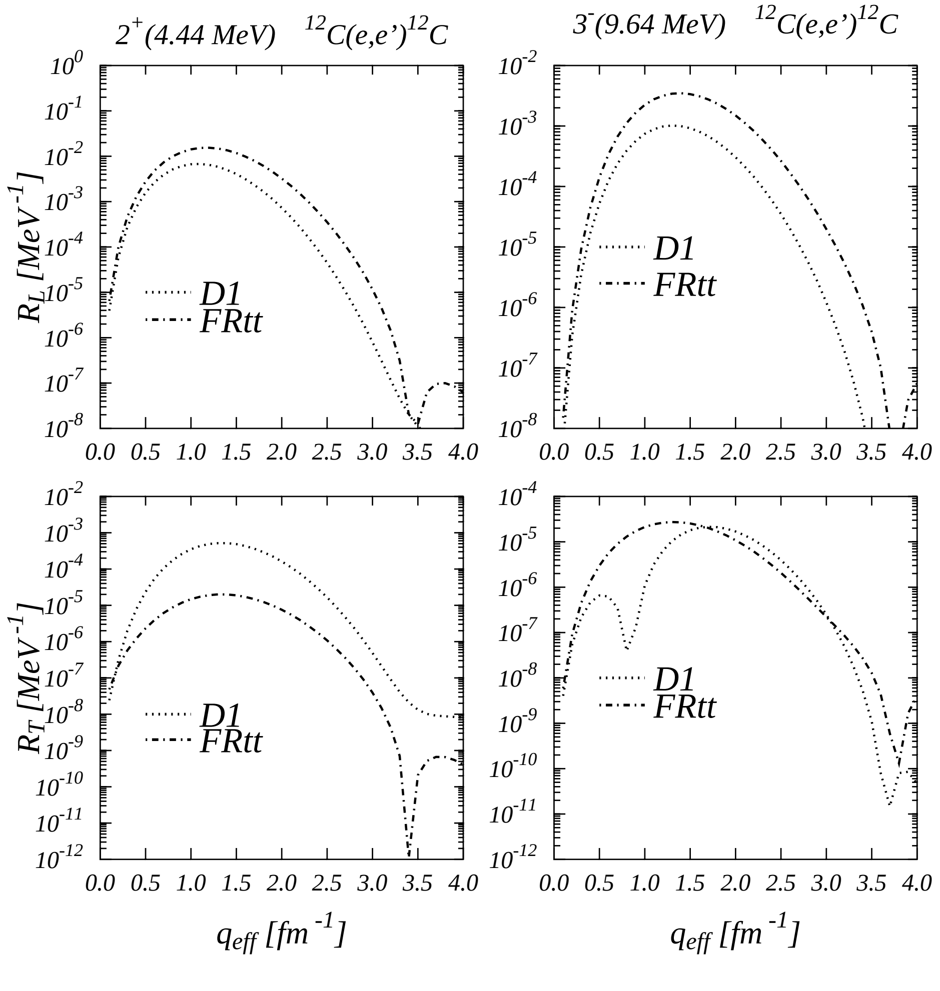

Figure 6.12: Longitudinal and transverse responses for the 2^+ and 3^- excited states in ^{12}C calculated with the D1 and FRtt interactions.

Also in the case of ^{12}C the 4^- states form an isospin doublet, and also in this case the D1 interaction inverts their position in the spectrum, producing an isovector state lower in energy than the isoscalar one. This is shown in Tabs. 6.14, 6.15 and in Fig. 6.13.

4^- (18.27 MeV)		$D1$	
ω		19.16	
transition	ϵ_p -ϵ_h	X	Y
$[(1d_{5/2})(1p_{3/2})^{-1}]_\pi$	15.87	0.49	-0.04
$[(2d_{5/2})(1p_{3/2})^{-1}]_\pi$	16.08	0.48	-0.04
$[(1d_{5/2})(1p_{3/2})^{-1}]_\nu$	15.98	0.71	-0.05

Table 6.14: Main ph pairs for the isoscalar 4^- state and their X and Y amplitudes calculated with the D1 interactions.

4^- (19.50 MeV)		$D1$	
ω		15.63	
transition	ϵ_p -ϵ_h	X	Y
$[(1d_{5/2})(1p_{3/2})^{-1}]_\pi$	15.87	0.66	0.00
$[(2d_{5/2})(1p_{3/2})^{-1}]_\pi$	16.08	0.33	0.00
$[(1d_{5/2})(1p_{3/2})^{-1}]_\nu$	15.98	-0.67	-0.01

Table 6.15: Main ph pairs for the isovector 4^- state and their X and Y amplitudes calculated with the D1 interaction.

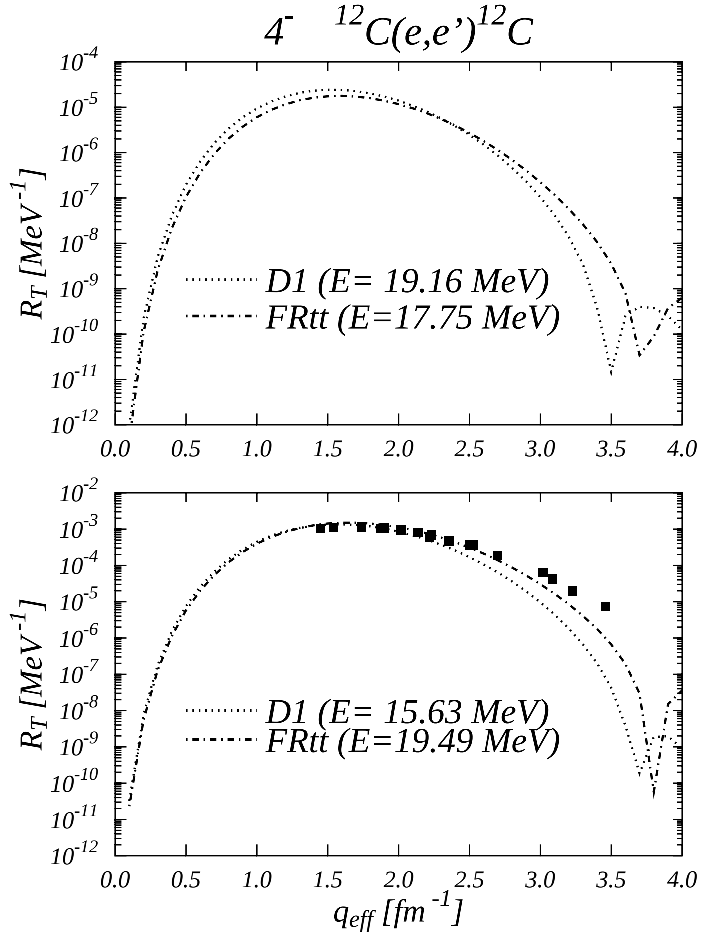

Figure 6.13: Transverse response for the first two 4^- excited state in ^{12}C calculated with the D1 and FRtt interactions. Experimental data for the isovector state at $19.50 MeV$ from [56].

The isoscalar and isovector 2^- excited states are not well identified as like in the LMFFS calculations. The main contribution of the ph pairs for the first states that we find are given in Tab. 6.16.

2^- (11.83 MeV)		$D1$	
ω		17.05	
transition	ϵ_p -ϵ_h	X	Y
$[(1d_{5/2})(1p_{3/2})^{-1}]_\pi$	15.87	0.26	0.00
$[(2s_{1/2})(1p_{3/2})^{-1}]_\pi$	15.35	-0.10	0.00
$[(2d_{5/2})(1p_{3/2})^{-1}]_\pi$	16.08	0.29	0.00
$[(3s_{1/2})(1p_{3/2})^{-1}]_\pi$	16.01	-0.31	0.00
$[(1d_{5/2})(1p_{3/2})^{-1}]_\nu$	15.98	0.21	0.00
$[(2s_{1/2})(1p_{3/2})^{-1}]_\nu$	16.43	-0.75	0.00
$[(3s_{1/2})(1p_{3/2})^{-1}]_\nu$	17.57	0.36	0.00
2^- (13.35 MeV)		$D1$	
ω		16.75	
transition	ϵ_p -ϵ_h	X	Y
$[(1d_{5/2})(1p_{3/2})^{-1}]_\pi$	15.87	-0.41	0.00
$[(2s_{1/2})(1p_{3/2})^{-1}]_\pi$	15.35	-0.10	0.00
$[(2d_{5/2})(1p_{3/2})^{-1}]_\pi$	16.08	-0.49	0.01
$[(3s_{1/2})(1p_{3/2})^{-1}]_\pi$	16.01	-0.37	0.00
$[(1d_{5/2})(1p_{3/2})^{-1}]_\nu$	15.98	0.66	-0.01

Table 6.16: Main ph pairs for the lowest 2^- states and their X and Y amplitudes calculated with the D1 interaction.

Let us now turn our attention to the doublet of 1^+ states whose main component are shown in Tab. 6.17 (first state) and Tab. 6.18 (second).

The corresponding transverse form factors are shown in Figs. 6.14, 6.15.

1^+ (12.71 MeV)		$D1$	
ω		11.17	
transition	ϵ_p -ϵ_h	X	Y
$[(1p_{1/2})(1p_{3/2})^{-1}]_\pi$	7.06	-0.73	-0.09
$[(1p_{1/2})(1p_{3/2})^{-1}]_\nu$	6.76	-0.69	-0.09

Table 6.17: Main ph pairs for the lowest 1^+ state and their X and Y amplitudes calculated with the D1 and FRtt interaction.

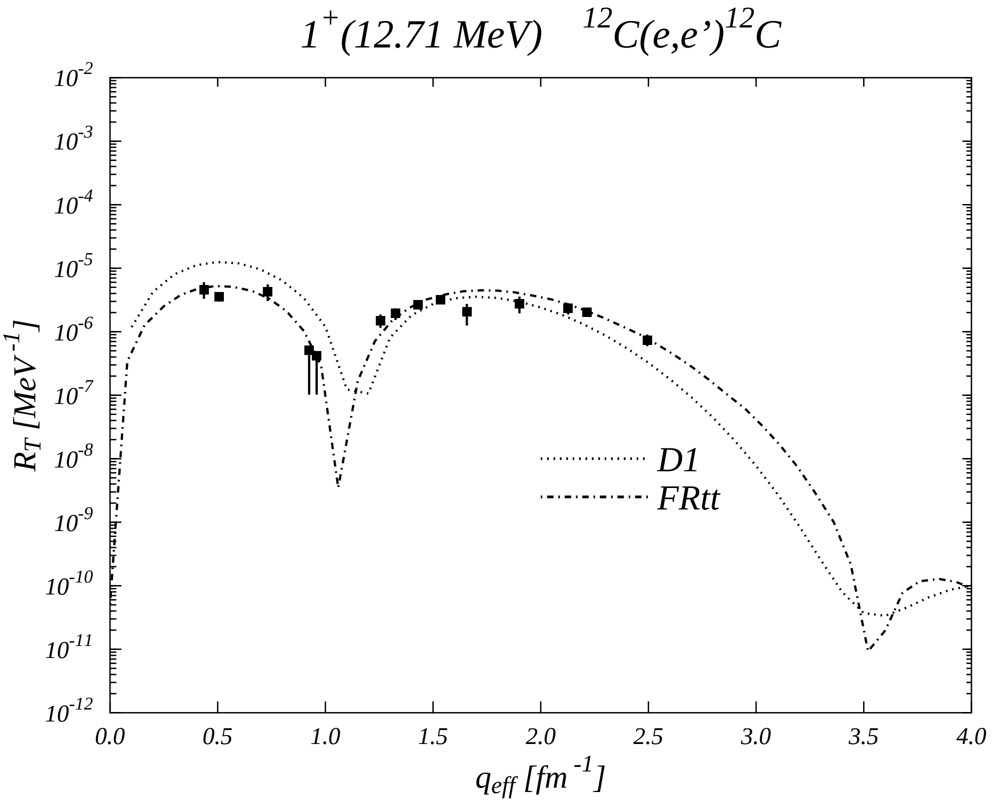

Figure 6.14: Transverse responses for the first 1^+ excited state in ^{12}C calculated with the D1 interaction. Experimental data from [53].

1^+ (15.11 MeV)		$D1$	
ω		7.73	
transition	ϵ_p -ϵ_h	X	Y
$[(1p_{1/2})(1p_{3/2})^{-1}]_\pi$	7.06	-0.68	-0.03
$[(1p_{1/2})(1p_{3/2})^{-1}]_\nu$	6.76	0.73	0.048

Table 6.18: Main ph pairs for the second 1^+ state and their X and Y amplitudes calculated with the D1 interaction.

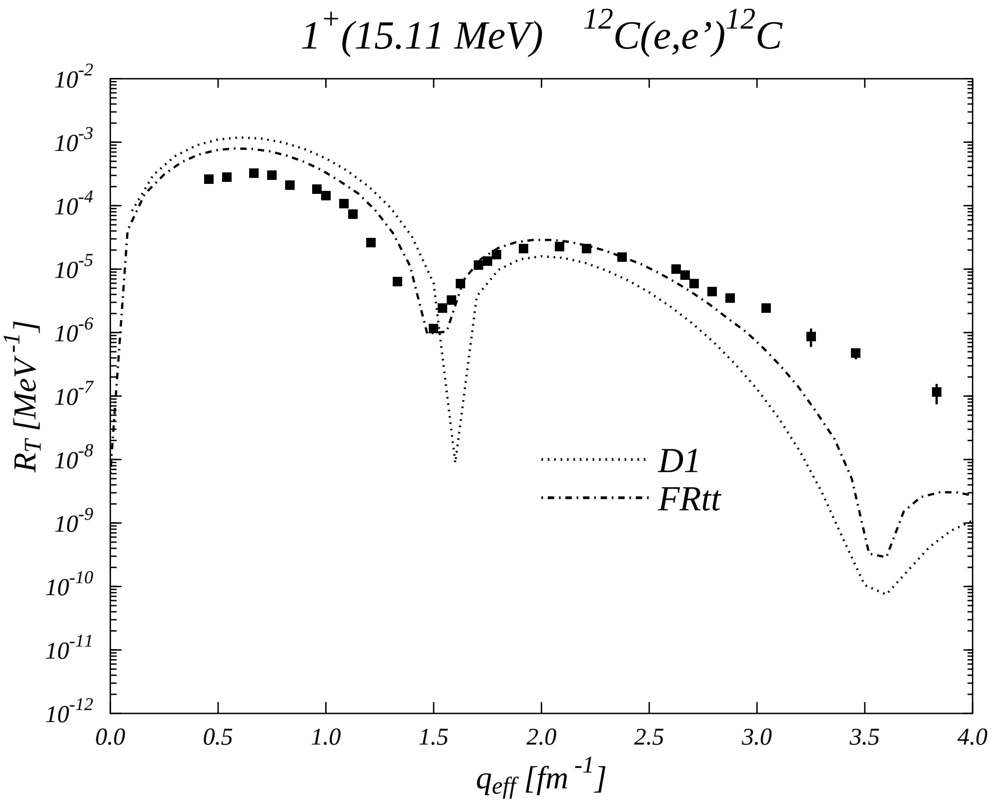

Figure 6.15: Transverse responses for the second 1^+ excited state in ^{12}C calculated with the D1 and FRtt interactions. Experimental data from [53].

6.5.3 The ^{40}Ca nucleus

We show in Tab. 6.19 and Fig. 6.16 the spectrum of ^{40}Ca nucleus compared with the FRtt spectrum and with the experimental one.

^{40}Ca			
excitation	D1	FRtt	exp
3^-	6.15	3.73	3.74
5^-	4.92	6.14	4.49
4^-	7.85	6.80	5.61
3^-	7.94	7.32	6.58
2^-	9.54	6.90	7.53
4^-	7.57	7.47	7.66
3^-	8.25	8.03	7.69
2^-	7.96	8.58	8.42
5^-	9.38	9.74	8.55

Table 6.19: Low excited states in ^{40}Ca. The energies are expressed in MeV. The experimental values are taken from [40].

There is a reasonable agreement with the experimental energies. We have to notice the inversion, in the D1 calculations, of the first two 3^- and 5^- states and of the isoscalar and isovector 4^- excited states.

We study the structure of the 3^- excitations, as we have done in sect 3.3.4. The ph pairs compositions of the three states are shown in Tabs. 6.20, 6.21 and 6.22 and in Fig. 6.17 we show longitudinal and transverse responses. In all the three cases there is a reasonable agreement between D1 and FRtt results for the longitudinal responses, while the transverse responses are rather different.

For the highest of these three states we have also a comparison with the data. The D1 longitudinal response shows a slightly better agreement with the data than the FRtt response. However, the D1 transverse response is one order of magnitude off with respect to the experimental points which, on the other hand, are well described by the FRtt response.

3^- (3.74 MeV)		$D1$	
ω		6.15	
transition	ϵ_p -ϵ_h	X	Y
$[(1f_{7/2})(1d_{5/2})^{-1}]_\pi$	13.95	-0.19	0.08
$[(1f_{7/2})(2s_{1/2})^{-1}]_\pi$	8.46	-0.32	0.06
$[(1f_{7/2})(1d_{3/2})^{-1}]_\pi$	7.61	-0.59	0.06
$[(1f_{7/2})(1d_{5/2})^{-1}]_\nu$	13.96	0.19	-0.07
$[(1f_{7/2})(2s_{1/2})^{-1}]_\nu$	8.56	0.33	-0.06
$[(1f_{7/2})(1d_{3/2})^{-1}]_\nu$	7.46	0.61	-0.06

Table 6.20: Main ph pairs for the first 3^- state and their X and Y amplitudes calculated with the D1 interaction.

The longitudinal responses are quite similar to that obtained in non-self-consistent calculations. Larger differences are found in the transverse responses, in particular the D1 calculations give the first maximum of the longitudinal response for the first state higher than that obtained with the

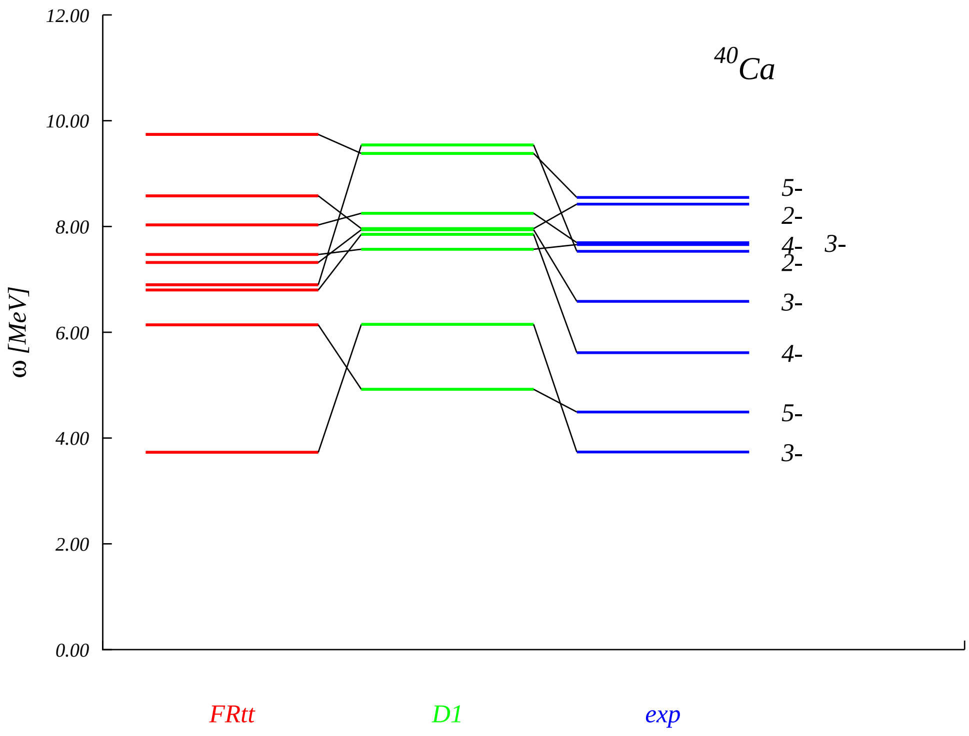

Figure 6.16: ^{40}Ca spectrum

FRtt interaction and that of the third state smaller. Moreover we observe differences in the number of peaks.

3^- (6.58 MeV)		$D1$	
ω		7.94	
transition	ϵ_p -ϵ_h	X	Y
$[(1f_{7/2})(1d_{3/2})^{-1}]_\pi$	7.61	-0.32	-0.02
$[(1f_{7/2})(2s_{1/2})^{-1}]_\pi$	8.46	0.64	-0.03
$[(1f_{7/2})(1d_{3/2})^{-1}]_\nu$	7.46	0.36	0.01
$[(1f_{7/2})(2s_{1/2})^{-1}]_\nu$	8.56	-0.58	0.03

Table 6.21: Main ph pairs for the second 3^- state and their X and Y amplitudes calculated with the D1 interaction.

3^- (7.69 MeV)		$D1$	
ω		8.25	
transition	ϵ_p -ϵ_h	X	Y
$[(1f_{7/2})(1d_{3/2})^{-1}]_\pi$	7.61	0.48	0.00
$[(1f_{7/2})(2s_{1/2})^{-1}]_\pi$	8.46	-0.51	-0.01
$[(1f_{7/2})(1d_{3/2})^{-1}]_\nu$	7.46	0.48	0.00
$[(1f_{7/2})(2s_{1/2})^{-1}]_\nu$	8.56	-0.52	-0.01

Table 6.22: Main ph pairs for the third 3^- state and their X and Y amplitudes calculated with D1 interaction.

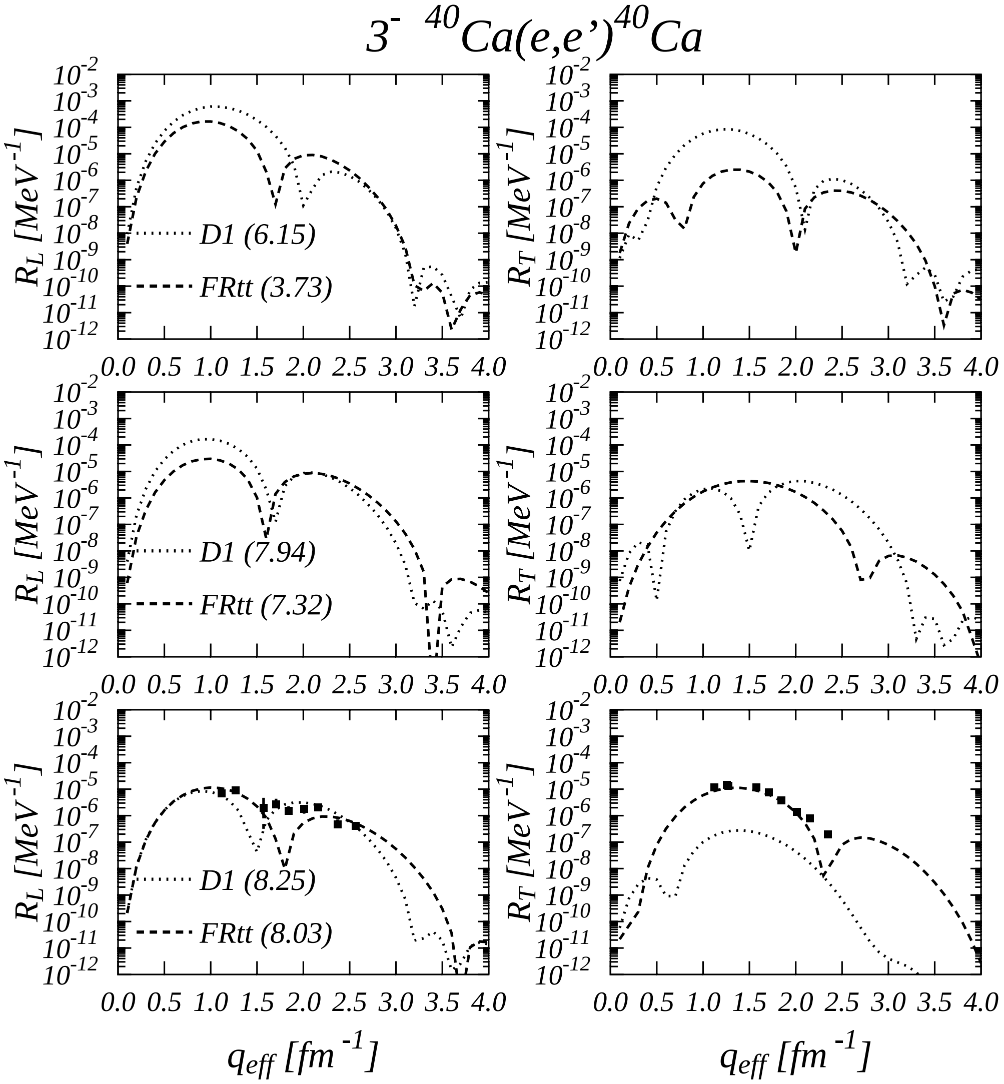

Figure 6.17: Longitudinal and transverse response for the first three 3^- excited state in ^{40}Ca calculated with the D1 and FRtt interactions. In parenthesis we have indicated the energy obtained in MeV. Experimental data from [57].

We show in Tab. 6.23 and in Fig. 6.18 the ph pair composition of the first 5^- excited state, and the electron scattering responses. In this case there are large difference with the FRtt results. The D1 longitudinal response is much larger than that of the FRtt calculation, and the situation is reversed in the transverse response. The FRtt responses are much closer to the data with respect to the D1 responses.

5^- (8.55 MeV)		$D1$	
ω		9.38	
transition	ϵ_p -ϵ_h	X	Y
$[(1f_{7/2})(1d_{3/2})^{-1}]_\pi$	7.61	-0.71	0.01
$[(1f_{7/2})(1d_{3/2})^{-1}]_\nu$	7.46	-0.70	0.01

Table 6.23: Main ph pairs for the second 5^- state and their X and Y amplitudes calculated with the D1 interaction.

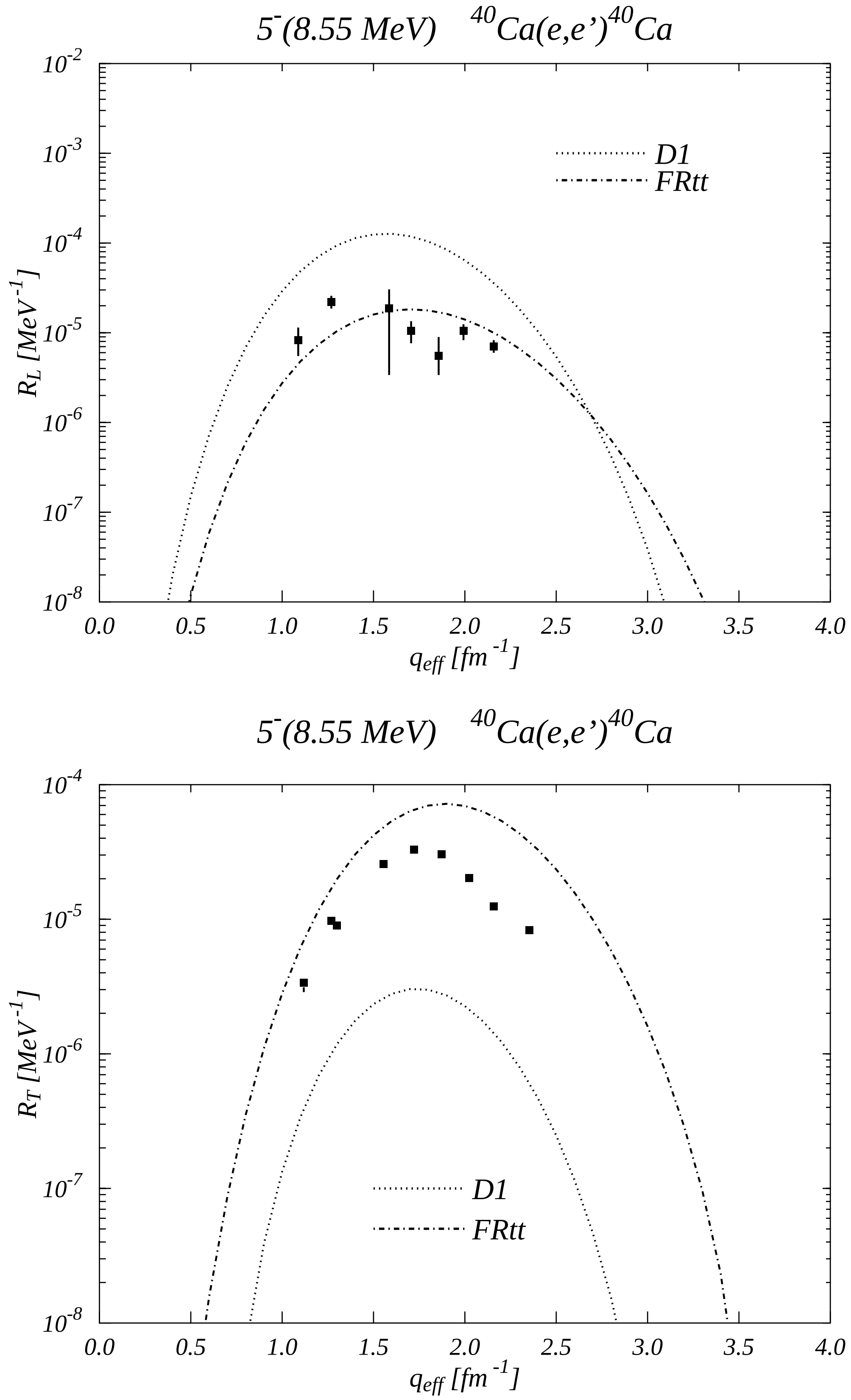

Figure 6.18: Longitudinal and transverse response for the second 5^- excited state in ^{40}Ca calculated with the D1 and FRtt interactions. Experimental data from [57].

We start our study of the magnetic excitations by studying the 2^- states forming an isospin doublet. The ph pair compositions of the two states are given in Tabs. 6.24 and 6.25 and in Fig. 6.19 the responses are shown. We notice the inversion of the two states produced by the D1 interaction.
The shape of the isoscalar D1 response is remarkably different from the FRtt response. There are large differences also in the transverse isovector response. In the comparison with the data the FRtt result is able to reproduce the experimental points at low q, while the D1 response reproduces the data at the second maximum.

2^- (7.53 MeV)		$D1$	
ω		9.54	
transition	ϵ_p -ϵ_h	X	Y
$[(1f_{7/2})(1d_{5/2})^{-1}]_\pi$	13.95	-0.24	-0.03
$[(1f_{7/2})(1d_{3/2})^{-1}]_\pi$	7.61	-0.68	0.03
$[(1f_{7/2})(1d_{5/2})^{-1}]_\nu$	13.97	-0.24	-0.03
$[(1f_{7/2})(1d_{3/2})^{-1}]_\nu$	7.46	-0.64	0.03

Table 6.24: Main ph pairs for the isoscalar 2^- state and their X and Y amplitudes calculated with the D1 interaction.

2^- (8.42 MeV)		$D1$	
ω		7.96	
transition	ϵ_p -ϵ_h	X	Y
$[(1f_{7/2})(1d_{3/2})^{-1}]_\pi$	7.61	0.68	-0.01
$[(1f_{7/2})(1d_{3/2})^{-1}]_\nu$	7.46	-0.72	0.01

Table 6.25: Main ph pairs for the lowest 2^- state and their X and Y amplitudes calculated with the D1 interaction.

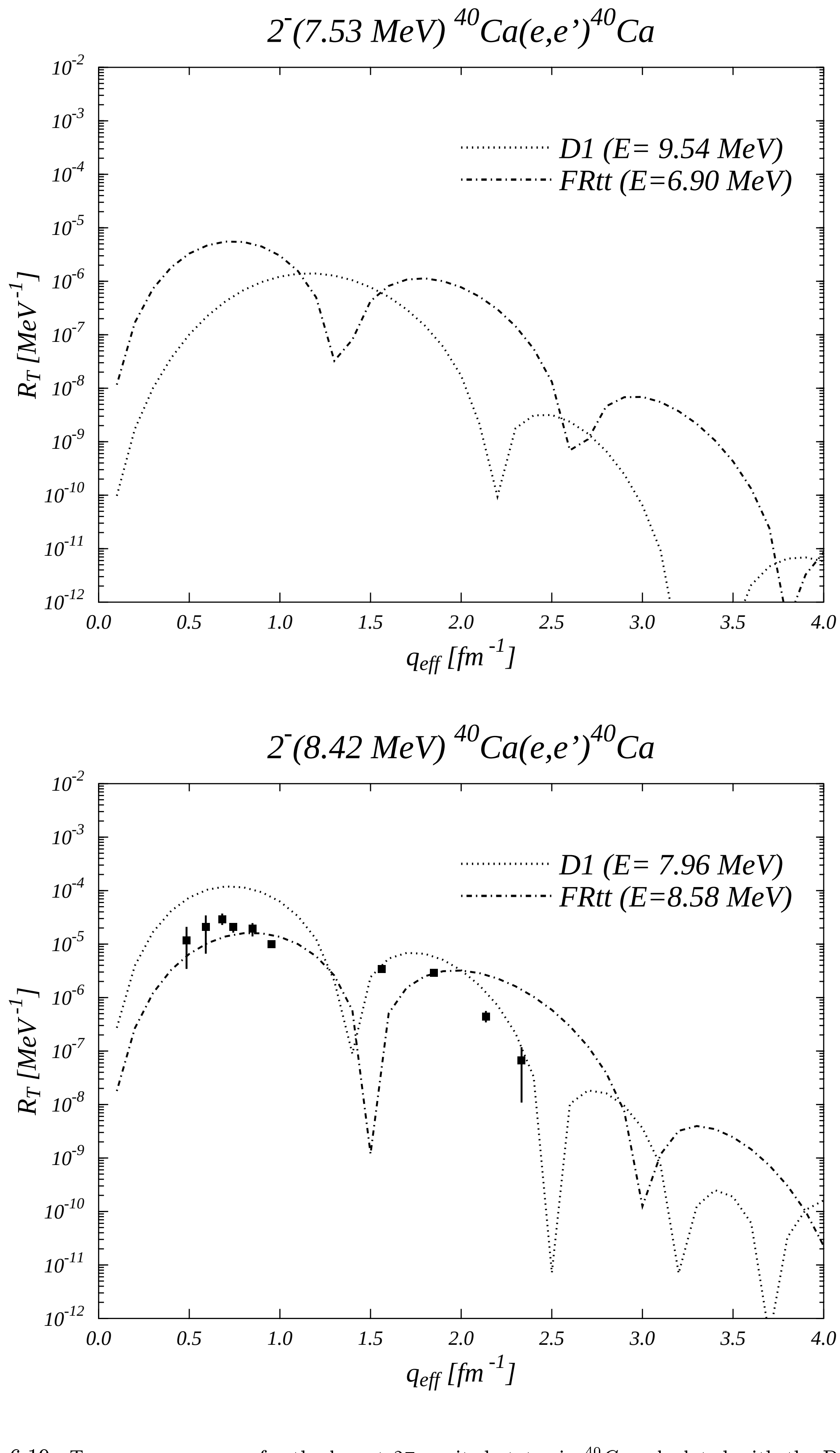

Figure 6.19: Transverse response for the lowest 2^- excited states in ^{40}Ca calculated with the D1 and FRtt interactions. Experimental data from [57].

Another interesting case to investigate is the 4^- excitation. Also in this case our calculations give two low-lying 4^- states, one at 7.57 MeV and the other one at 7.85 MeV described in Tabs. 6.26 and 6.27. Also in this case the isoscalar and isovector energy are inverted. The relative transverse responses are shown in Fig. 6.20.

4^- (5.61 MeV)		$D1$	
ω		7.57	
transition	ϵ_p -ϵ_h	X	Y
$[(1f_{7/2})(1d_{3/2})^{-1}]_\pi$	7.61	0.52	0.00
$[(1f_{7/2})(1d_{3/2})^{-1}]_\nu$	7.46	-0.85	0.00

Table 6.26: Main ph pairs for the first 4^- state and their X and Y amplitudes calculated with the D1 interaction.

4^- (7.66 MeV)		$D1$	
ω		7.85	
transition	ϵ_p -ϵ_h	X	Y
$[(1f_{7/2})(1d_{3/2})^{-1}]_\pi$	7.61	-0.83	0.00
$[(1f_{7/2})(2s_{1/2})^{-1}]_\pi$	8.46	-0.17	0.01
$[(1f_{7/2})(1d_{3/2})^{-1}]_\nu$	7.46	-0.50	0.00
$[(1f_{7/2})(2s_{1/2})^{-1}]_\nu$	8.56	-0.13	-0.01

Table 6.27: Main ph pairs for the second 4^- state and their X and Y amplitudes calculated with the D1 interaction.

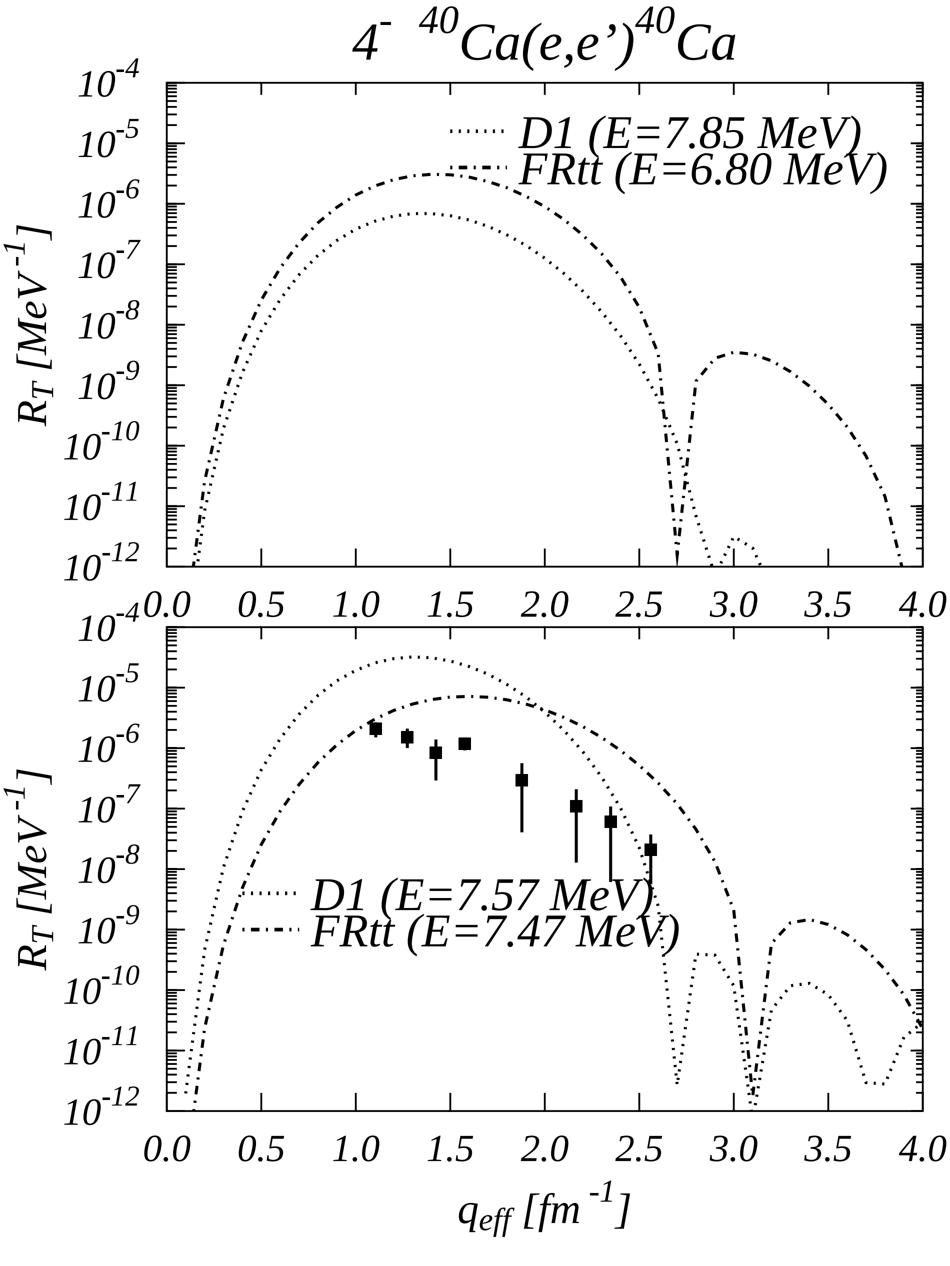

Figure 6.20: Transverse response for the 4^- excited state in ^{40}Ca calculated with the D1 and FRtt interactions. Experimental data from [57].

6.5.4 The ^{48}Ca nucleus

^{48}Ca			
excitation	D1	FRtt	exp
2^+	4.42	4.61	3.83
4^+	4.69	4.78	4.50
3^-	7.00	4.52	4.51
3^+	5.00	4.94	4.61
5^+	5.29	4.98	5.15
4^-	8.51	6.35	6.10
2^-	9.35	7.10	6.89
6^-	15.36	10.99	8.56
1^+	9.66	9.50	10.23

Table 6.28: Lower excited states energies of ^{48}Ca expressed in MeV

We show in Tab. 6.28 and in Fig. 6.21 the spectrum of the ^{48}Ca nucleus.

We consider first the excitation of the 3^+ and 5^+ states whose ph pair components and transverse responses are shown in Tabs. 6.29 and 6.30 and in Fig. 6.22. These states are described by a single ph pair, which is the same in both cases.

3^+ (4.61 MeV)		$D1$	
ω		5.00	
transition	ϵ_p -ϵ_h	X	Y
$[(2p_{3/2})(1f_{7/2})^{-1}]_\nu$	4.76	-0.98	-0.01

Table 6.29: Main ph pairs for the first 3^+ states and their X and Y amplitudes calculated with the D1 interaction.

5^+ (5.15 MeV)		$D1$	
ω		5.29	
transition	ϵ_p -ϵ_h	X	Y
$[(2p_{3/2})(1f_{7/2})^{-1}]_\nu$	4.76	-1.00	-0.02

Table 6.30: Main ph pairs for the first 5^+ states and their X and Y amplitudes calculated with the D1 interaction.

The agreement with the FRtt results, and also with the data is quite good in both cases. In these excitations the role of the residual interaction is irrelevant, and the differences between the two calculations are only due to the differences in the s.p. wave functions, which are shown in Fig. 6.23.

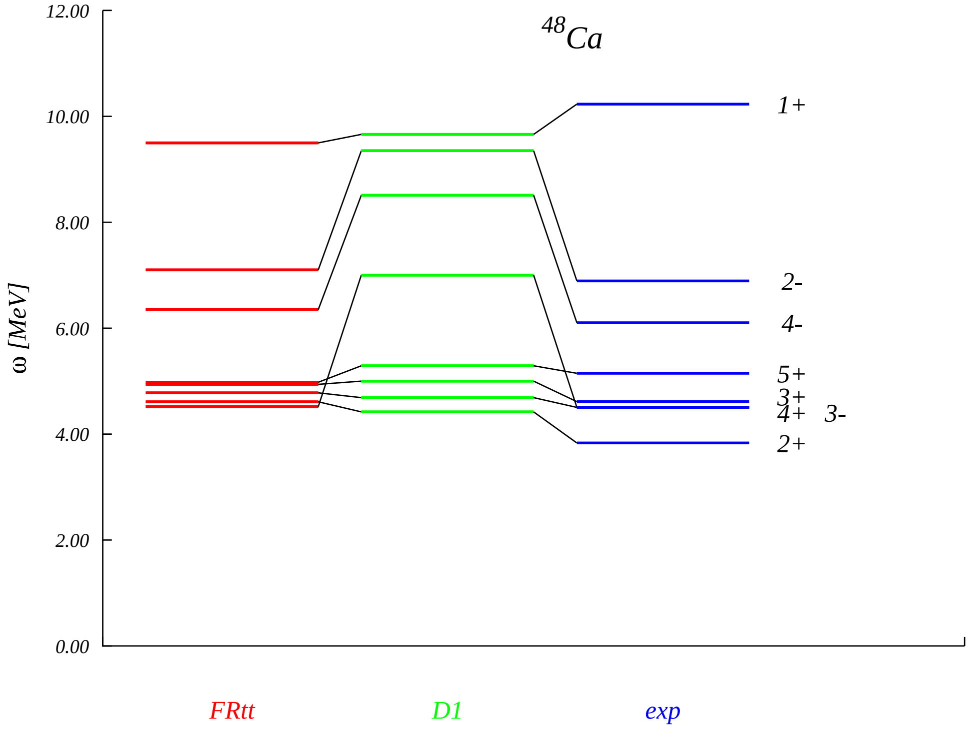

Figure 6.21: ^{48}Ca spectrum

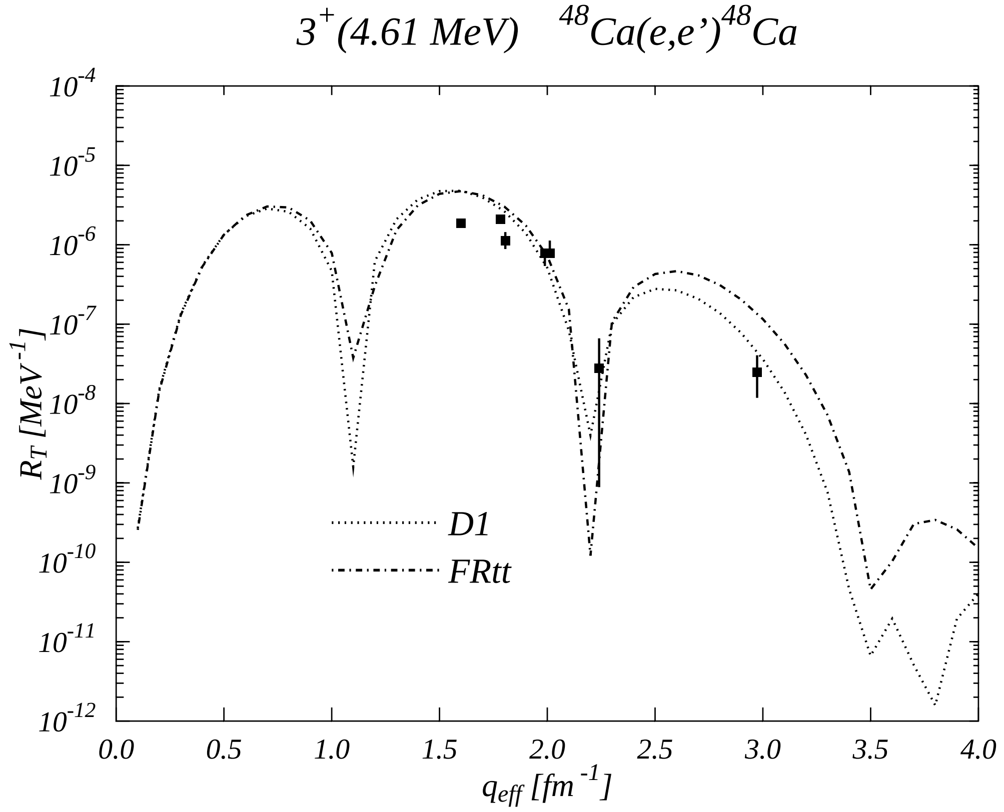

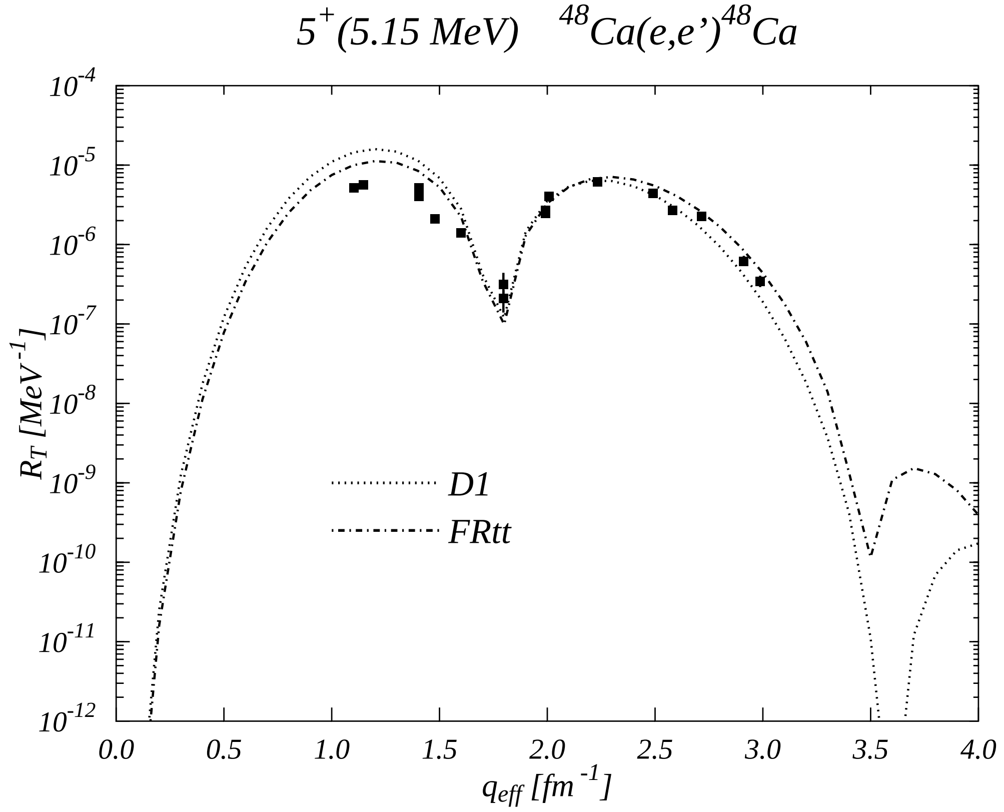

Figure 6.22: Transverse form factor for the excited states 3^+ and 5^+ for ${}^{48}Ca$ with the D1 and FRtt interactions compared with experimental data [58].

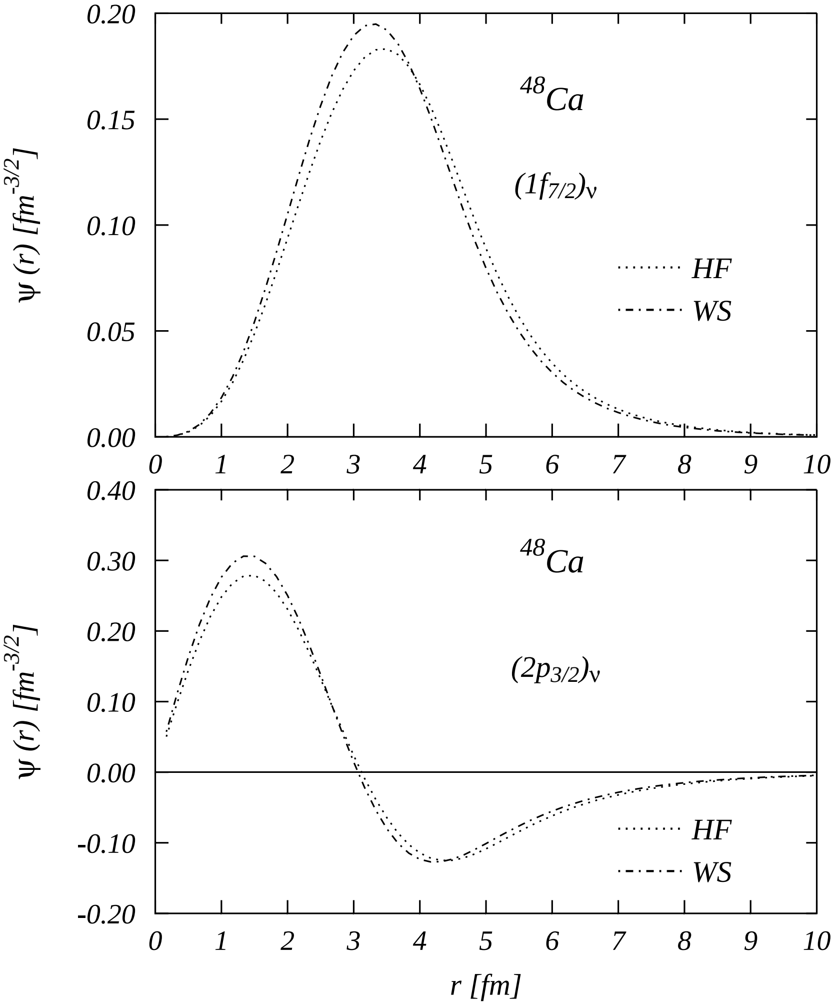

Figure 6.23: S.p. wave functions for the particle and hole states of Tabs. 6.29 and 6.30.

Another excited state which is an almost pure single ph excitation is the 6^- whose configuration is presented in Tab. 6.31, and whose response is shown in Fig. 6.24 together with the FRtt response, and the experimental data [58]. In this case, the differences between the results of the two calculations are larger than in the 3^+ and 5^+ cases. This is explained by a larger difference between the s.p. wave functions involved in the calculation as it is shown in Fig. 6.25.

6^- (8.56 MeV)		$D1$	
ω		15.36	
transition	ϵ_p -ϵ_h	X	Y
$[(1f_{7/2})(1d_{5/2})^{-1}]_\pi$	14.24	0.96	-0.04

Table 6.31: Main ph pairs for the first 6^- state and their X and Y amplitudes calculated with the D1 interaction.

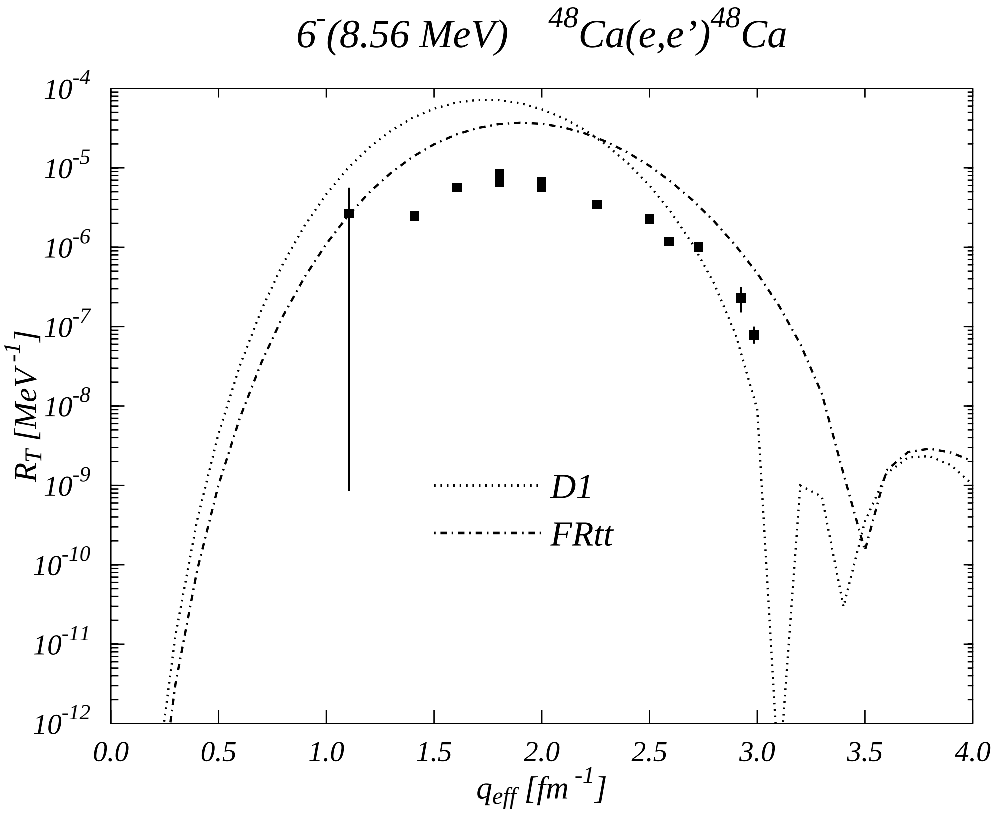

Figure 6.24: Transverse form factor for the excited state 6^- for ^{48}Ca compared with experimental data [58].

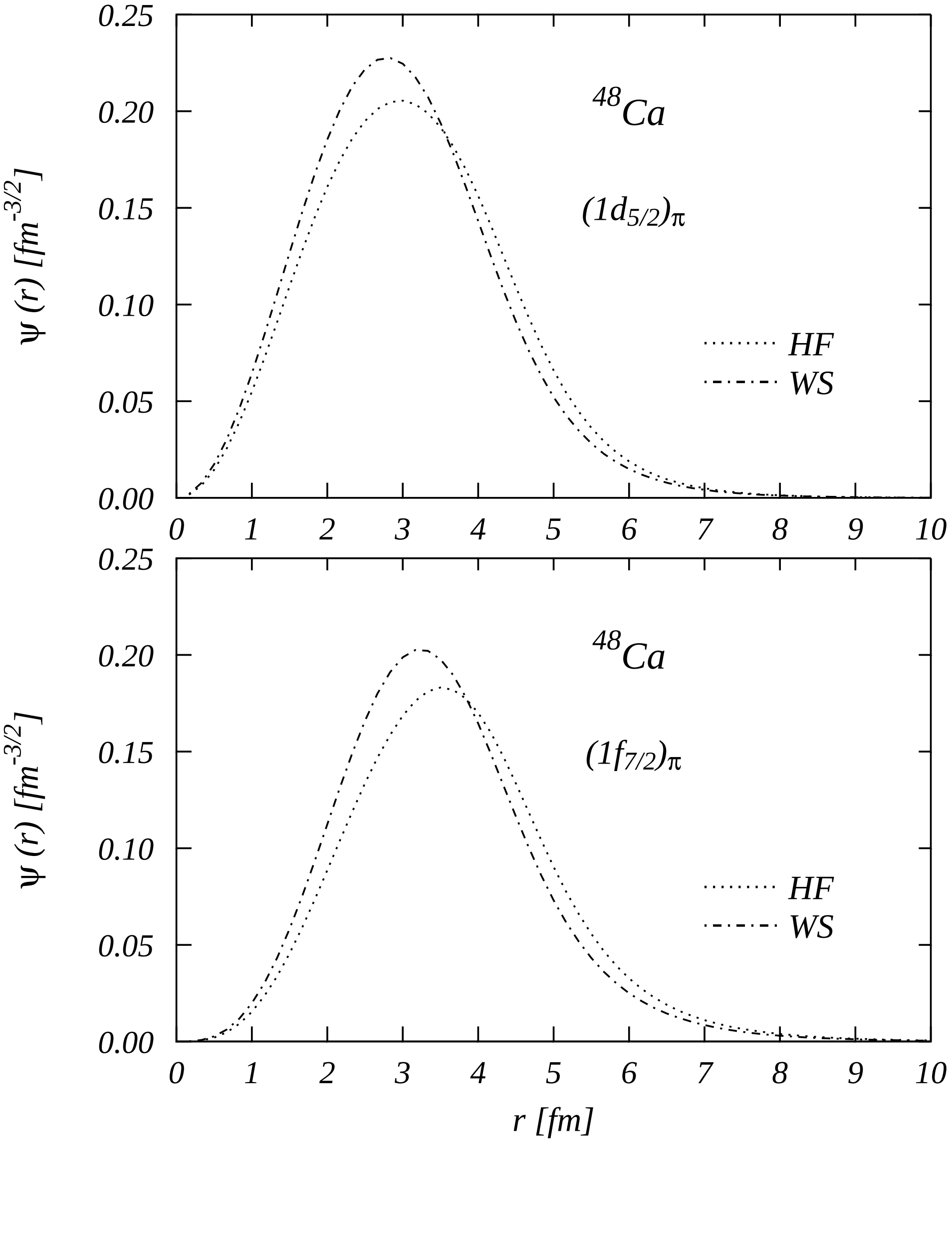

Figure 6.25: S.p. wave functions for the particle and hole states of Tab. 6.31.

Also in the 4^- case the D1 interaction inverts the order of the first two states. This is evident in Fig. 6.26 where the D1 responses are compared with those obtained with the FRtt interaction. Experimental data are available only for the first state.

4^- (6.10 MeV)		$D1$	
ω		8.51	
transition	ϵ_p -ϵ_h	X	Y
$[(1f_{7/2})(2s_{1/2})^{-1}]_\pi$	7.78	0.72	-0.01
$[(1f_{7/2})(1d_{3/2})^{-1}]_\pi$	8.12	-0.68	0.02

Table 6.32: Main ph pairs for the second 4^- states and their X and Y amplitudes calculated with the D1 interaction.

4^- (7.40 MeV)		$D1$	
ω		8.11	
transition	ϵ_p -ϵ_h	X	Y
$[(1f_{7/2})(2s_{1/2})^{-1}]_\pi$	7.78	0.73	0.00
$[(1f_{7/2})(1d_{3/2})^{-1}]_\pi$	8.12	0.68	0.01

Table 6.33: Main ph pairs for the first 4^- state and their X and Y amplitudes calculated with the D1 interaction.

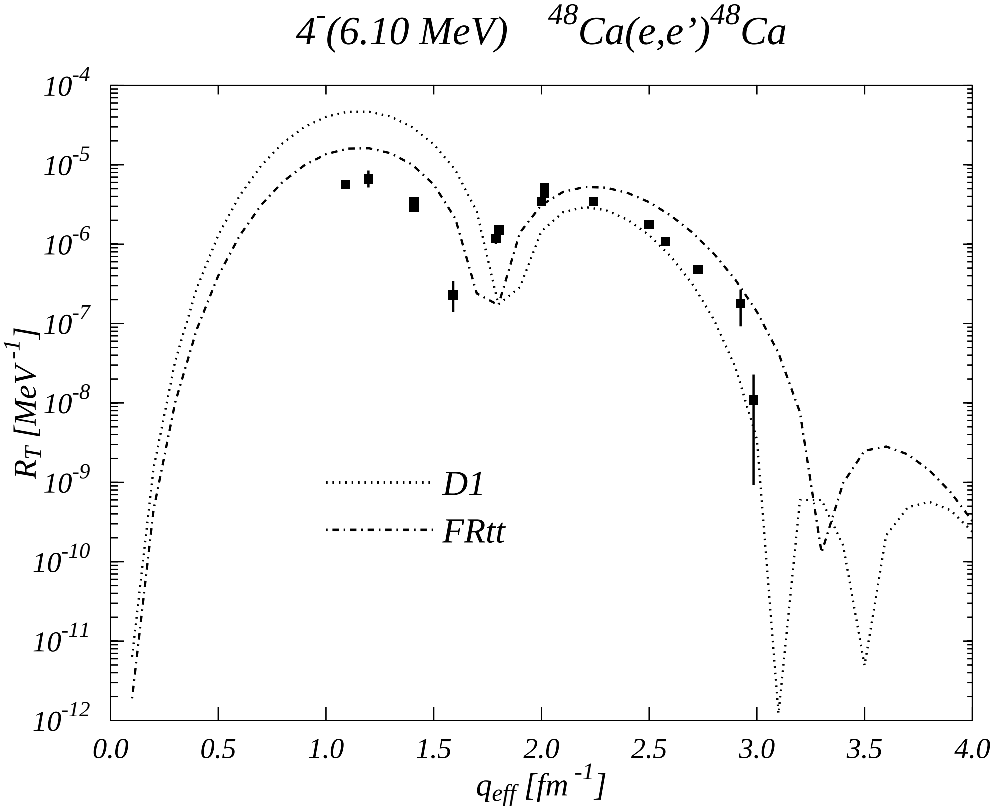

Figure 6.26: Transverse response for the excited state 4^- for ^{48}Ca. Experimental data from [58].

We conclude the discussion of the ^{48}Ca nucleus by showing results for the 2^- excitation in Tab. 3.39 and Fig. 6.27. In this case the differences with the FRtt results are remarkable.

2^- (6.89 MeV)		$D1$	
ω		9.35	
transition	ϵ_p -ϵ_h	X	Y
$[(1f_{7/2})(1d_{3/2})^{-1}]_\pi$	8.12	-0.96	0.03
$[(1f_{7/2})(1d_{5/2})^{-1}]_\pi$	14.24	-0.18	-0.03

Table 6.34: Main ph pairs for the first 2^- states and their X and Y amplitudes calculated with the D1 interaction.

The identification of this state is ambiguous. The comparison between experimental and theoretical responses is given in Fig. 6.27.

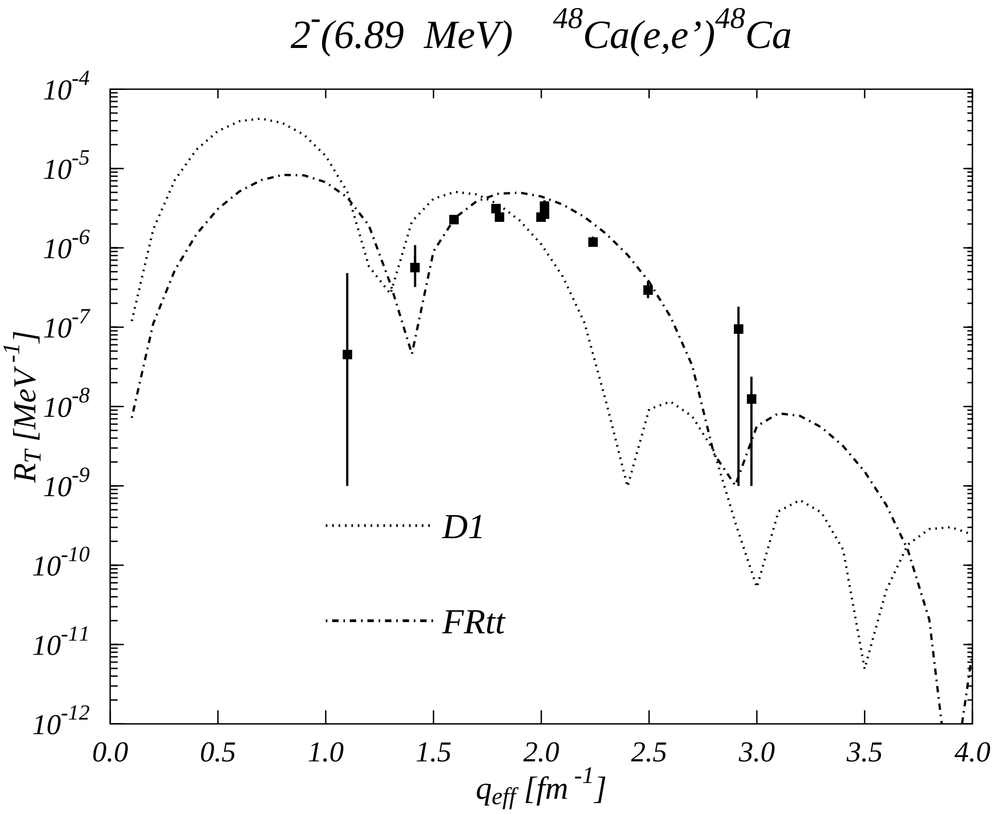

Figure 6.27: Transverse response for the 2^- excited state for ^{48}Ca compared with experimental data [58]

6.5.5 The ^{90}Zr nucleus

The spectrum of the ^{90}Zr nucleus is presented in Tab. 6.35 and in Fig. 6.28.

^{90}Zr			
excitation	D1	FRtt	exp
2^+	5.26	2.19	2.19
5^-	2.80	2.51	2.32
4^-	3.23	3.30	2.74
3^-	4.29	5.76	2.75
4^+	5.53	3.96	3.08
2^+	8.05	6.07	3.31
6^+	5.64	4.37	3.45
8^+	7.23	6.55	3.59
5^-	4.81	4.73	3.97
10^-	12.02	8.90	7.36

Table 6.35: Low excitated states energies of ^{90}Zr in MeV.

We observe the inversion of the first two states. This happens also in LMFFS calculations but here the difference between the two states is larger.

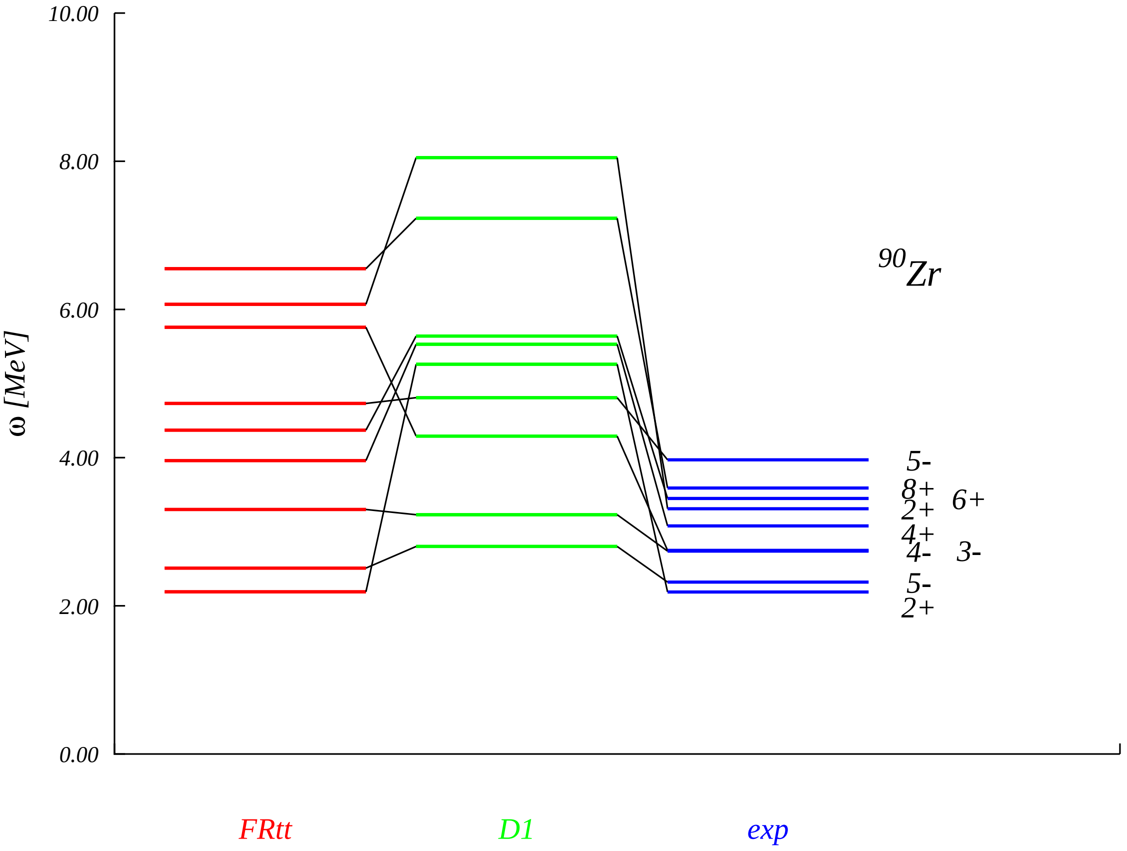

Figure 6.28: ^{90}Zr spectrum

We consider now the electric states 2^+ and 4^+. In Tab. 6.36 and Tab. 6.37 we show the contributions of ph pairs for the 2^+ excitation and in Tab. 6.38 those for the 4^+ state. All these states are dominated by single discrete excitation.

2^+ (2.19 MeV)		$D1$	
ω		5.26	
transition	ϵ_p -ϵ_h	X	Y
$[(2d_{5/2})(1g_{9/2})^{-1}]_\nu$	5.67	-0.99	-0.05

Table 6.36: Main ph pairs for the first 2^+ state and their X and Y amplitudes calculated with the D1 interaction.

2^+ (3.30 MeV)		$D1$	
ω		8.05	
transition	ϵ_p -ϵ_h	X	Y
$[(1g_{7/2})(1g_{9/2})^{-1}]_\nu$	7.42	0.99	0.23

Table 6.37: Main ph pairs for the second 2^+ state and their X and Y amplitudes calculated with the D1 interaction.

We show in Fig. 6.29 the transition densities of the two states 2^+ and we compare them with the empirical transition density. Both the calculations are in bad agreement with the empirical data.

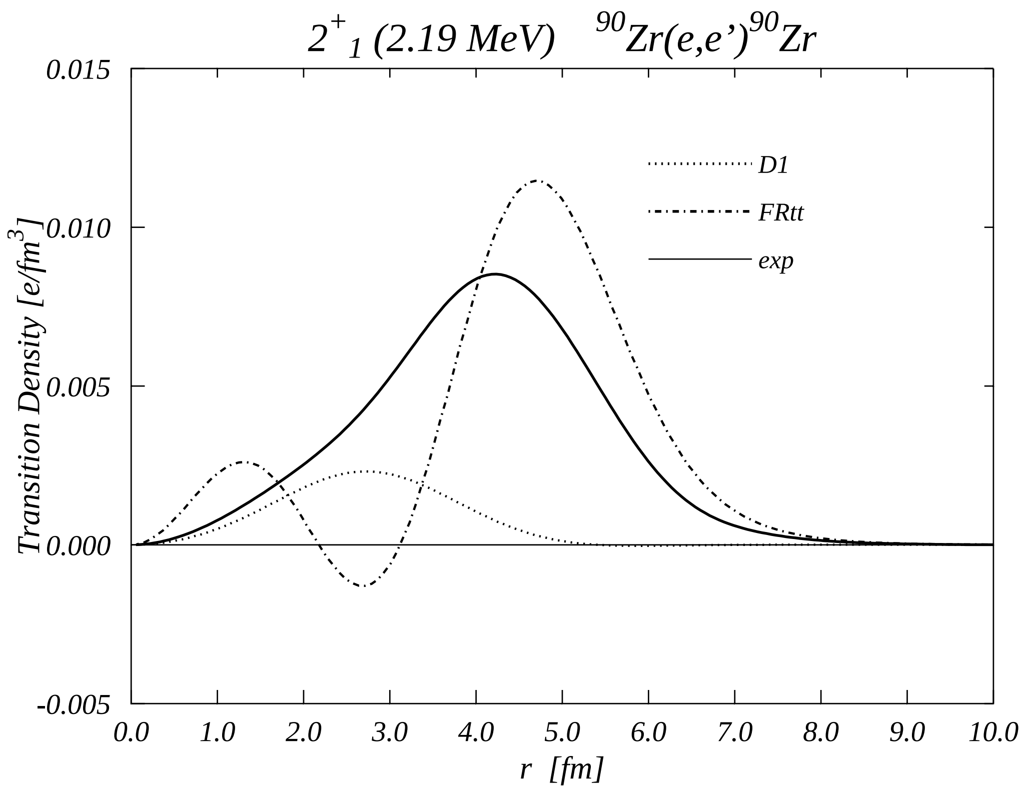

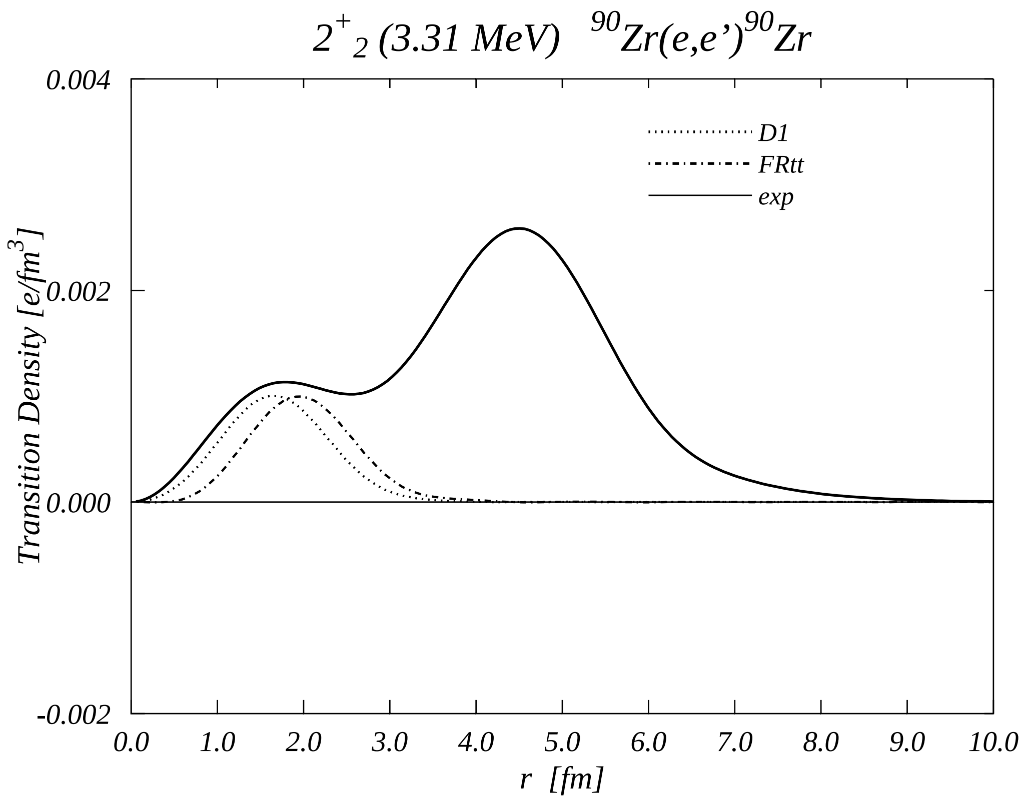

Figure 6.29: Transition density for the excited state 2^+ for ^{90}Zr compared with experimental data [59]

4^+ (3.08 MeV)		$D1$	
ω		5.53	
transition	ϵ_p -ϵ_h	X	Y
$[(2d_{5/2})(1g_{9/2})^{-1}]_\nu$	5.67	1.00	0.00

Table 6.38: Main ph pairs for the first 4^+ state and their X and Y amplitudes calculated with the D1 interaction.

Also in the case of 4^+ excited state (Fig. 6.30) there is no agreement with experimental data.

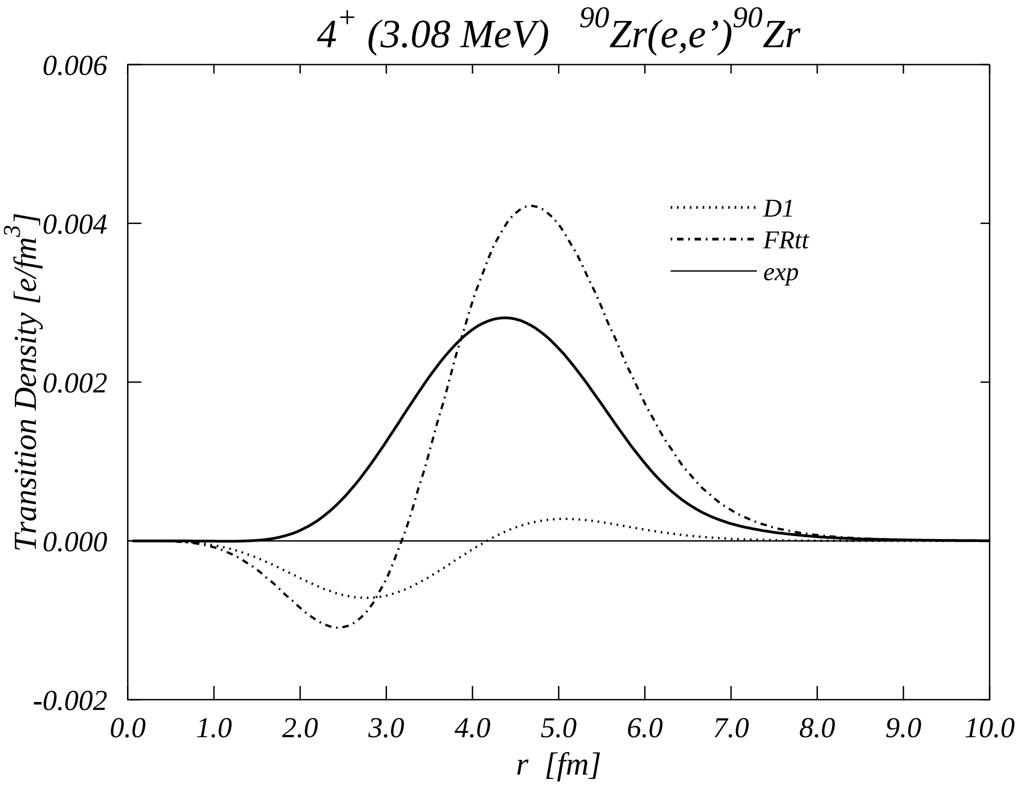

Figure 6.30: Transition density for the 4^+ excited state for ^{90}Zr compared to the experimental density [59].

We show in Fig. 6.31 the s.p. wave functions of the particle and hole states of Tab.6.38.

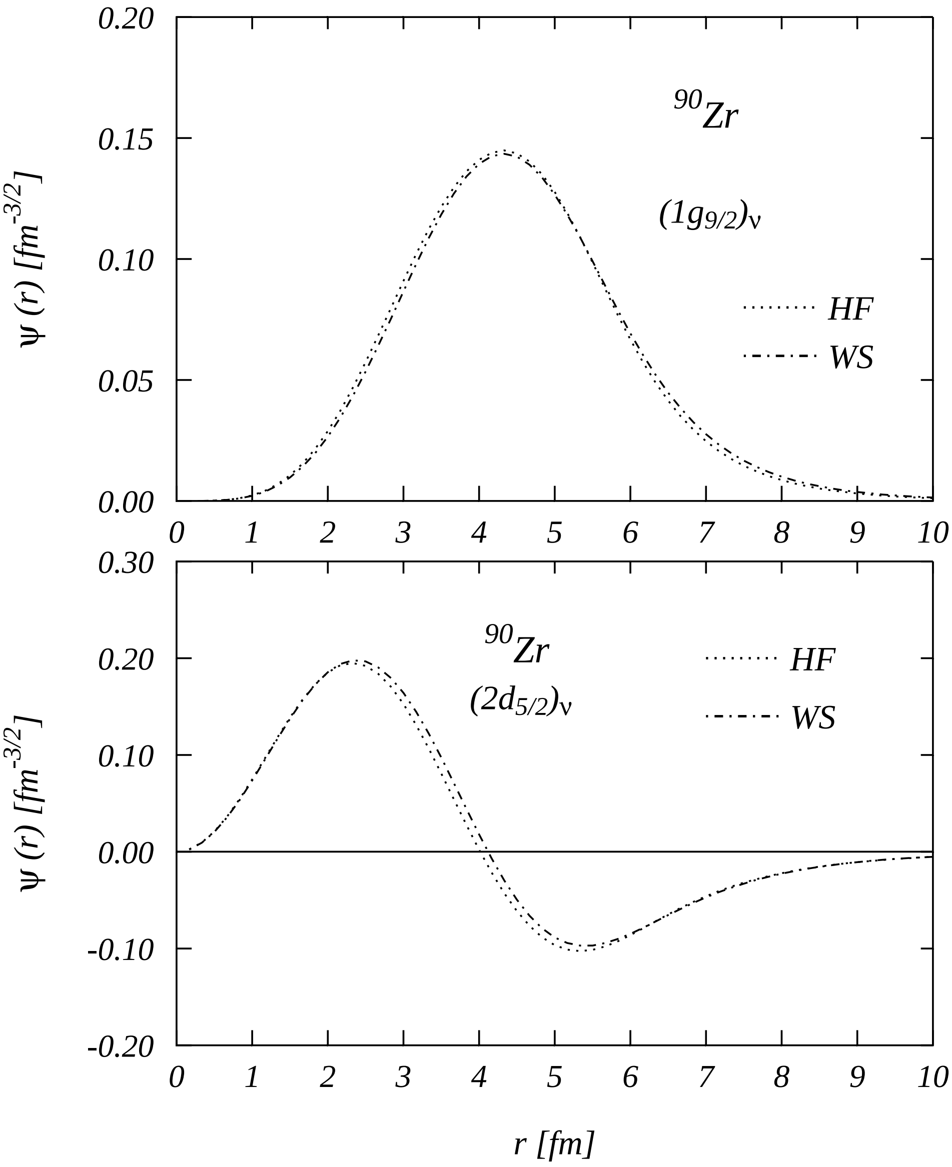

Figure 6.31: S.p. wave functions of the particle and hole states of Tab. 6.38.

As an example of magnetic state we consider the first 10^- state. It is dominated by a single ph excitation that, by HF calculation, is in the continuum with an energy of $0.39 MeV$ (Tab. 6.39). Its transverse response is given in Fig.6.32.

10^- (7.36 MeV)		$D1$	
ω		12.02	
transition	ϵ_p -ϵ_h	X	Y
$[(1h_{11/2})(1g_{9/2})^{-1}]_\nu$	11.46	1.00	-0.02

Table 6.39: Main ph pairs for the first 10^- state and their X and Y amplitudes calculated with the D1 interaction.

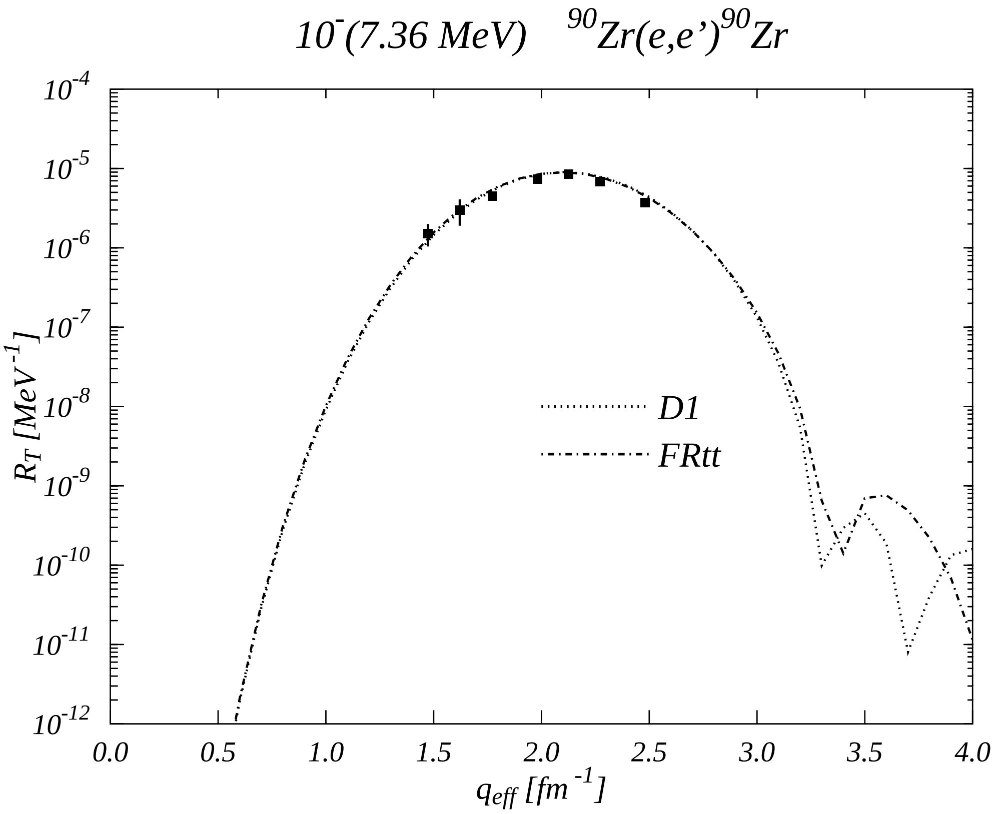

Figure 6.32: Transverse response of the 10^- state in ^{90}Zr compared with experimental data [60].

The agreement between the two calculations and with the experimental data is very good.

6.6 Conclusions

The comparison of the self consistent calculations with the results obtained within the LMFFS and with the experimental data gives an idea of the difficulties related to a complete self-consistent approach. It is evident, for example, in the transverse and longitudinal form factor of the 5^- excitation of ^{40}Ca. In these calculations we have studied the predictive capability of the Gogny interaction. For all the cases studied this interaction inverts the isospin doublets lowering the isovector state and increasing the isoscalar one. This fact indicates the presence of a problem in the isospin channel.

Chapter 7

Conclusions and perspectives

The work of this thesis consisted in developing the RPA formalism to deal with finite range interactions. In our calculations these interactions are composed by all the interaction channels up to the tensor ones. The RPA equations have been solved by using a fully discrete configuration space of s.p. wave functions, and also by treating the continuum exactly. While the solution of the discrete RPA secular equations has been obtained by using standard techniques, that of the continuum RPA equations required the development of a technology based on an expansion on a SB basis.

The results shown in the thesis are related to the application of the discrete RPA to the study of the low-lying excitation spectrum of some doubly closed shell nuclei. This technique has been extended to describe hypernuclei. The continuum RPA results presented in the thesis are related to the photoexcitation of the ^{16}O nucleus.

At the end of each chapter we have already summarized the main findings, regarding the results presented there. We do not repeat in this section what has already been stated. Here we would rather like to discuss the perspectives of our work. The short-term perspectives indicate what, we think, should be done to complete properly this thesis work and also the body of results we have presented. The medium-term perspectives, are straightforward applications of the techniques we have developed. Finally, in the long-term perspectives we indicate some extensions of our work, in the framework of the project we have outlined in the introduction, project aiming to provide a unitary description of bound and excited states of nuclei based on realistic NN interactions.

7.0.1 Short term perspectives

1. Study of the spectrum of the ^{208}Pb nucleus with the D1 interaction.

2. Study of the low-lying spectra of the nuclei we have considered, with a Gogny-type interaction which includes a tensor term [103].

3. Calculations of the continuum RPA spectra of other doubly magic nuclei.

7.0.2 Medium term perspectives

1. Self consistent calculations in the continuum. This type of calculations requires the construction of the Hartree-Fock mean field and the solution of the s.p. Schrödinger equation with continuum boundary conditions.

2. Study of the charge exchange excitation spectra. Since the tensor terms of the interaction are dominated by the one-pion exchange term which populates the tensor-isospin channel, we expect the charge exchange spectra to be more sensistive to this term of the interaction than the charge conserving excitations.

3. Use of the continuum RPA results to study electron and neutrino induced excitations, for both charge conserving and charge exchange excitations.

4. Use of the continuum RPA results to study nucleon knock-out processes. This is important in electron scattering where there are numerous (e,e'p) data. The extension of the knock-out study to the neutrino induced reactions is important since in this process the detected particle is usually the emitted nucleon.

5. Self-consistent calculations for hypernuclei. The use of the same interaction to describe with Hartree-Fock the hypernuclei ground states and with RPA the excitation spectra could put some severe constraint on the Λ-nucleon interaction.

7.0.3 Long term perspectives

1. Construction of the effective hamiltonian, and its use in self-consistent RPA calculations. We plan to construct an effective hamiltonian by starting from the CBF/FHNC approach to the description of finite nuclear systems [15].

2. Extension of the RPA. The relevance of phenomena which cannot be described in terms of RPA correlations is well known [42, 104, 105, 100]. We would like to extend the RPA by considering two-particle, two-hole degrees of freedom, in a fully self-consistent and parameter free manner. The extension of the RPA based on the phenomenological LMFFS [104, 100, 106] requires as input the experimental s.p. energies and uses an interaction whose parameters should be adjusted to reproduce some specific excited states. Self-consistent calculations use interactions constructed to reproduce at best the nuclear ground state within the Hartree-Fock theory. In our project, we plan to use microscopic NN interactions, in order to make parameter free calculations.

Appendix A

Woods-Saxon Eigenfunctions

We have defined the Woods-Saxon potential in Eq. (1.5) as:

$$V(r) = \frac{U_0}{1 + e^{\frac{r-R_0}{a_0}}} + \left(\frac{\hbar c}{m_\pi c^2}\right)^2 \frac{1}{r}\frac{U_{SO}}{a_{SO}} \frac{e^{\frac{r-R_{SO}}{a_{SO}}}}{(1 + e^{\frac{r-R_{SO}}{a_{SO}}})} \boldsymbol{l}\cdot\boldsymbol{\sigma} - V_C(r) \tag{A.1}$$

where:

$$m_\pi c^2 = 139.5669 MeV \tag{A.2}$$

is the mass of the pion and

$$\hbar c = 197.32858 MeV \cdot fm \tag{A.3}$$

$$\left(\frac{\hbar c}{m_\pi c^2}\right)^2 = 1.99901 fm^2 \tag{A.4}$$

The Coulomb potential is different from zero only for protons, and it is defined as

$$V_C(r) = \begin{cases} (Z-1)\frac{e^2}{r} & \text{if } r > R \\ \frac{(Z-1)e^2}{2R}\left[3 - \frac{r^2}{R^2}\right] & \text{if} r \leq R \end{cases} \tag{A.5}$$

with

$$e^2 = 1.44 MeV \cdot fm. \tag{A.6}$$

By defining:

$$V_0(r) = \frac{U_0}{1 + e^{\frac{r-R_0}{a_0}}} \tag{A.7}$$

$$V_{SO}(r) = \left(\frac{\hbar c}{m_\pi c^2}\right)^2 \frac{1}{r}\frac{U_{SO}}{a_{SO}} \frac{e^{\frac{r-R_{SO}}{a_{SO}}}}{(1 + e^{\frac{r-R_{SO}}{a_{SO}}})} \boldsymbol{l}\cdot\boldsymbol{\sigma} \tag{A.8}$$

we can rewrite the Woods-Saxon potential in compact way:

$$V(r) = V_{cent}(r) + V_{SO}(r) + V_C(r) \tag{A.9}$$

The Schrödinger equation for the radial part R of the s.p. wave functions is:

$$\left\{-\frac{\hbar^2}{2m_p}\left[\frac{1}{r^2}\frac{d}{dr}\left(r^2\frac{d}{dr}\right) - \frac{l(l+1)}{r^2}\right] + V_{cent}(r) + V_{SO}(r) + V_C(r)\right\} R_{nlj}(r) = E_{nlj}R_{nlj}(r) \tag{A.10}$$

where m_p and l are the values of the mass and angular momentum respectively. We expand the radial eigenfunctions $R_{nlj}(r)$ on a basis of harmonic oscillator eigenfunctions $R^{HO}_{ml}(r)$:

$$R_{nlj}(r) = \sum_{m=1}^{M} a_m(nlj) R^{HO}_{ml}(r) \tag{A.11}$$

that are solutions of the following Schrödinger equation:

$$\left\{ -\frac{\hbar^2}{2m_p} \left[\frac{1}{r^2} \frac{d}{dr} \left(r^2 \frac{d}{dr} \right) - \frac{l(l+1)}{r^2} \right] + \frac{1}{2} m_p \omega^2 r^2 \right\} R^{HO}_{ml}(r) = E^{HO}_{ml} R^{HO}_{ml}(r) \tag{A.12}$$

where

$$m = 1, 2, 3, 4, ... \tag{A.13}$$

is the principal quantum number indicating the number of nodes (minus one) of the wave function, and

$$E^{HO}_{ml} = \left(2m + l - \frac{1}{2} \right) \hbar\omega. \tag{A.14}$$

The explicit expression of the harmonic oscillator eigenfunctions is:

$$R^{HO}_{ml}(r) = \sqrt{\frac{2(m-1)!}{\Gamma\left(m + l + \frac{1}{2}\right) b^3}} \left(\frac{r}{b} \right)^l L^{l+\frac{1}{2}}_{m-1} \left(\frac{r^2}{b^2} \right) e^{-\frac{r^2}{2b^2}} \tag{A.15}$$

where we have indicated by L the Laguerre polynomial. In Eq. (A.10) we add and subtract the term $\frac{1}{2} m_p \omega^2 r^2$ and we insert the expansion (A.11), then we obtain

$$\begin{aligned} &\sum_{m=1}^{M} \left(V_{cent}(r) + V_{SO}(r) + V_C(r) - \frac{1}{2} m_p \omega^2 r^2 + E^{HO}_{ml} \right) a_m(nlj) R^{HO}_{ml}(r) = \\ &E_{nlj} \sum_{m=1}^{M} a_m(nlj) R^{HO}_{ml}(r) \end{aligned} \tag{A.16}$$

Multiplying by $R^{*HO}_{\mu l}$, integrating on the radial coordinate r the previous equation, and using the orthonormality relation between harmonic oscillator eigenstates we obtain:

$$\begin{aligned} \sum_{m=1}^{M} a_m(nlj) \Big\{ E^{HO}_{ml} \delta_{m\mu} &+ \int drr^2 R^{HO*}_{\mu l}(r) R^{HO}_{ml}(r) \\ &\left[V_{cen}(r) + V_{SO}(r) + V_C(r) - \frac{1}{2} m_p \omega^2 r^2 \right] \Big\} = \\ = E_{nlj} \sum_{m=1}^{M} a_m(nlj) \delta_{m\mu} &= E_{nlj} a_\mu(nlj) = E_{nlj} a_\mu(nlj) \end{aligned} \tag{A.17}$$

The problem is now the solution of the following eigenvalue equation:

$$H_{nlj} a(nlj) = E_{nlj} a(nlj) \tag{A.18}$$

with:

$$\begin{aligned} H^{nlj}_{m\mu} = E^{HO}_{ml} \delta_{m\mu} &+ \int drr^2 R^{HO*}_{\mu l}(r) R^{HO}_{ml}(r) \\ &\left[V_{cen}(r) + V_{SO}(r) + V_C(r) - \frac{1}{2} m_p \omega^2 r^2 \right]. \end{aligned} \tag{A.19}$$

The normalization relation between the Woods-Saxon eigenstates

$$\int drr^2 R^*_{nlj}(r)R_{nlj}(r) = 1 \tag{A.20}$$

implies the following relation between the $a(nlj)$ coefficients:

$$\begin{aligned}
&\int drr^2 \sum_{\mu=1}^{M} a_\mu(nlj)R^{HO*}_{\mu l}(r) \sum_{m=1}^{M} a_m(nlj)R^{HO}_{ml}(r) = \\
&= \sum_{\mu=1}^{M} a_\mu(nlj) \sum_{m=1}^{M} a_m(nlj) \int drr^2 R^{HO*}_{\mu l}(r)R^{HO}_{ml}(r) = \\
&= \sum_{\mu=1}^{M} a_\mu(nlj) \sum_{m=1}^{M} a_m(nlj)\delta_{m\mu} = \sum_{m=1}^{M} (a_m(nlj))^2 = 1
\end{aligned} \tag{A.21}$$

Appendix B

RPA equations

B 1 RPA equations

Starting from the Schrödinger equation (Eq. (2.1)) and from the operators $Q^\dagger_\nu$ and Q_ν described by equations (2.2) and (2.3) we obtain the expressions of the action of $[H, Q^\dagger_\nu]$ and $[H, Q_\nu]$ on the ground state

$$
\begin{aligned}
[H, Q^\dagger_\nu]|0\rangle &= \omega Q^\dagger_\nu|0\rangle && \text{(B.1)}\\
[H, Q_\nu]\,|0\rangle &= 0 && \text{(B.2)}
\end{aligned}
$$

It can be seen that for a generic operator A we can write:

$$
\begin{aligned}
&< 0|[A, [H, Q^\dagger_\nu]]|0\rangle = \\
&\quad = \omega\langle 0|AQ^\dagger_\nu|0\rangle - \langle|HQ^\dagger_\nu A|0\rangle + \langle 0|Q^\dagger_\nu HA|0\rangle = \\
&\quad = \omega\langle 0|[A, Q^\dagger_\nu]|0\rangle. && \text{(B.3)}
\end{aligned}
$$

Now, using as the operator A the variation:

$$
\delta Q_\nu = \sum_{mi}(\delta X^\nu_{mi} a^\dagger_i a_m - \delta Y^\nu_{mi} a^\dagger_m a_i) \tag{B.4}
$$

the equation of motion gives:

$$
\langle 0|[\delta q_\nu, [H, Q^\dagger_\nu]]|0\rangle = \omega\langle 0|[\delta Q_\nu, Q^\dagger_\nu]|0\rangle \tag{B.5}
$$

and we obtain

$$
\begin{aligned}
&\langle 0|[\sum_{mi}(\delta X^\nu_{mi} a^\dagger_i a_m - \delta Y^\nu_{mi} a^\dagger_m a_i), [H, Q^\dagger_\nu]]|0\rangle = \\
&\quad = \omega\langle 0|[\sum_{mi}(\delta X^\nu_{mi} a^\dagger_i a_m - \delta Y^\nu_{mi} a^\dagger_m a_i), Q^\dagger_\nu]|0\rangle && \text{(B.6)}
\end{aligned}
$$

Extracting the sums and the variations δX and δY from the brackets and inserting the RPA ground state $|\Psi_0\rangle$, separating the δX and the δY terms and considering that the variations δX and δY are linearly independent we obtain the following system of coupled equations:

$$
\begin{aligned}
\langle\Psi_0|[a^\dagger_i a_m, [H, Q^\dagger_\nu]]|\Psi_0\rangle &= \omega_\nu\langle\Psi_0|[a^\dagger_i a_m, Q^\dagger_\nu]|\Psi_0\rangle && \text{(B.7)}\\
\langle\Psi_0|[a^\dagger_m a_i, [H, Q^\dagger_\nu]]|\Psi_0\rangle &= \omega_\nu\langle\Psi_0|[a^\dagger_m a_i, Q^\dagger_\nu]|\Psi_0\rangle && \text{(B.8)}
\end{aligned}
$$

where ω_ν is the excitation energy $(E_\nu - E_0)$ of the $|\nu>$ state. Considering now the first member of Eq. (B.7), writing the expression of $Q^\dagger$ we obtain:

$$\langle\Psi_0|[a_i^\dagger a_m,[H,Q_\nu^\dagger]]|\Psi_0\rangle = \sum_{nj}(X_{nj}^\nu A_{minj} + Y_{nj}^\nu B_{minj}) \tag{B.9}$$

with

$$A_{minj} = \langle\Psi_0|[a_i^\dagger a_m,[H,a_n^\dagger a_j]]|\Psi_0\rangle \tag{B.10}$$

and

$$B_{minj} = -\langle\Psi_0|[a_i^\dagger a_m,[H,a_j^\dagger a_n]]|\Psi_0\rangle. \tag{B.11}$$

Writing the expression of $Q_\nu^\dagger$ in the second member of Eq. (B.7) we obtain:

$$\begin{aligned}&\langle\Psi_0|[a_i^\dagger a_m, Q_\nu^\dagger]|\Psi_0\rangle = \\ &= \sum_{nj}\left\{X_{nj}^\nu\langle\Psi_0|[a_i^\dagger a_m, a_n^\dagger a_j]|\Psi_0\rangle - Y_{nj}^\nu\langle\Psi_0|[a_i^\dagger a_m, a_j^\dagger a_n]|\Psi_0\rangle\right\}.\end{aligned} \tag{B.12}$$

Using the Quasi Boson Approximation that consists in approximating, in calculations of commutators, the RPA ground state $|\Psi_0\rangle$ with the Hartree-Fock ground state $|\Phi_0\rangle$, we obtain:

$$\begin{aligned}\langle\Psi_0|[a_i^\dagger a_m, a_n^\dagger a_j]\Psi_0\rangle &\approx \langle\Phi_0|[a_i^\dagger a_m, a_m^\dagger, a_n^\dagger a_j]|\Phi_0\rangle = \\ &= \langle\Phi_0|a_i^\dagger a_m a_n^\dagger a_j|\Phi_0\rangle = \delta_{nj}\delta_{mi}\end{aligned} \tag{B.13}$$

and

$$\begin{aligned}\langle\Psi_0|[a_i^\dagger a_m, a_j^\dagger a_n]|\Psi_0\rangle &\approx \langle\Phi_0|[a_i^\dagger a_m, a_j^\dagger a_n]|\Phi_0\rangle = \\ &= \langle\Phi_0|a_i^\dagger a_m a_j^\dagger a_n|\Phi_0\rangle = 0\end{aligned} \tag{B.14}$$

therefore for Eq. (B.8) we obtain:

$$\sum_{nj}[X_{nj}^\nu A_{minj} + Y_{nj}^\nu B_{minj}] = \omega_\nu X_{mi}^\nu. \tag{B.15}$$

For Eq. (B.8) we can proceed in an analogous way and we obtain:

$$\sum_{nj}[X_{nj}^\nu B_{minj}^* + Y_{nj}^\nu A_{minj}^*] = -\omega_\nu Y_{mi}^\nu. \tag{B.16}$$

B 2 Explicit expressions of coefficients A and B

In order to calculate the explicit expression of A we have to insert in (B.10) the expression of H in Occupation Numbers Representation:

$$H = \sum_{\alpha\beta} h_{\alpha\beta}a_\alpha^\dagger a_\beta - \frac{1}{2}\sum_{ijij}\overline{V}_{ijij} + \frac{1}{4}\sum \alpha\beta\alpha'\beta' N[a_\alpha^\dagger a_\beta^\dagger a_{\beta'} a_{\alpha'}]. \tag{B.17}$$

Applying the Quasi Boson Approximation we obtain

$$\begin{aligned}A_{minj} = \langle\Phi_0|\sum_{\alpha\beta} h_{\alpha\beta}[a_i^\dagger a_m,[a_\alpha^\dagger a_\beta, a_n^\dagger a_j]] + \\ -\frac{1}{2}[a_i^\dagger a_m,[\sum_{ijij}\overline{V}_{ijij}, a_n^\dagger a_j]] + \\ +\frac{1}{4}\sum_{\alpha\beta\alpha'\beta'}\overline{V}_{\alpha\beta\alpha'\beta'}[a_i^\dagger a_m,[N[a_\alpha^\dagger a_\beta^\dagger a_{\beta'} a_{\alpha'}], a_n^\dagger a_j]|\Phi_0\rangle.\end{aligned} \tag{B.18}$$

In the previous equation

$$[a^\dagger_\alpha a_\beta, a^\dagger_n a_j] = -a^\dagger_n a_\beta \delta_{j\alpha} + a^\dagger_\alpha a_j \delta_{n\beta} \tag{B.19}$$

so the first matrix element of Eq. (B.18), applying Wick's theorem, becomes:

$$\begin{aligned}\langle\Phi_0|[a^\dagger_i a_m, [a^\dagger_\alpha a_\beta, a^\dagger_n a_j]]|\Phi_0\rangle = \langle\Phi_0|[a^\dagger_i a_m, (-a^\dagger_n a_\beta \delta_{j\alpha} + a^\dagger_\alpha a_j \delta_{n\beta}]\Phi_0\rangle = \\ = \delta_{ij}\delta_{m\alpha}\delta_{\beta n} - \delta_{mn}\delta_{j\alpha}\delta_{i\beta}.\end{aligned} \tag{B.20}$$

Using the previous expression, the first term of Eq. (B.18) can be written as:

$$\langle\Phi_0|\sum_{\alpha\beta} h_{\alpha\beta}[a^\dagger_i a_m, [a^\dagger_\alpha a_\beta, a^\dagger_n a_j]]|\Phi_0\rangle = (\epsilon_m - \epsilon_i)\delta_{ij}\delta_{mn}. \tag{B.21}$$

The second term of Eq. (B.18) contains the scalar operator V_{ijij} that commutes with the creation and annihilation operators and, therefore, the matrix element is equal to zero. The third term of Eq. (B.18), applying Wick's theorem, can be written as:

$$\begin{aligned}\langle\Phi_0|[a^\dagger_i a_m, [N[a^\dagger_\alpha a^\dagger_\beta a_{\beta'} a_{\alpha'}], a^\dagger_n a_j]|\Phi_0\rangle = \\ = -\delta_{m\alpha}\delta_{j\beta}\delta_{n\alpha'} - \delta_{i\beta'} + \delta_{j\alpha}\delta_{m\beta}\delta_{n\alpha'}\delta_{i\beta'} - \delta_{j\alpha}\delta_{m\beta}\delta_{i\alpha'}\delta_{n\beta'} + \delta_{m\alpha}\delta_{j\beta}\delta_{i\alpha'}\delta_{n\beta'}\end{aligned} \tag{B.22}$$

and we obtain:

$$\begin{aligned}\langle\Phi_0|\frac{1}{4}\sum_{\alpha\beta\alpha'\beta'} \overline{V}_{\alpha\beta\alpha'\beta'}[a^\dagger_i a_m, [N[a^\dagger_\alpha a^\dagger_\beta a_{\beta'} a_{\alpha'}], a^\dagger_n a_j]|\Phi_0\rangle = \\ = \frac{1}{4}(\overline{V}_{mjin} + \overline{V}_{jmin} - \overline{V}_{mjin} - \overline{V}_{jmni}).\end{aligned} \tag{B.23}$$

Using Eq.(B.21) and Eq. (B.23) and the relations:

$$\overline{V}_{mjin} = -\overline{V}_{mjni} = \overline{V}_{jmni} = -\overline{V}_{jmin} \tag{B.24}$$

the expression of the coefficient A is:

$$A_{mijn} = (\epsilon_m - \epsilon_i)\delta_{ji}\delta_{nm} + \overline{V}_{mjin}. \tag{B.25}$$

In order to obtain the explicit expression of the coefficient B we proceed in the same way as for the A coefficient. In this case we obtain that only the term with the interaction is different from zero. It is:

$$\frac{1}{4}\sum_{\alpha\beta\alpha'\beta'} \overline{V}_{\alpha\beta\alpha'\beta'}\langle\Phi_0|[a^\dagger_i a_m, [N[a^\dagger_\alpha a^\dagger_\beta a_{\beta'} a_{\alpha'}], a^\dagger_j a_n]]|\Phi_0\rangle = \overline{V}_{mnij}. \tag{B.26}$$

Finally, the expression for the B coefficient is:

$$B_{mjin} = \overline{V}_{mnij}. \tag{B.27}$$

Appendix C

RPA equations in angular momentum coupling

In this appendix we show how the RPA equations can be rewritten in angular momentum coupling. In order to deal with irreducible spherical tensors we have to work with the operators $a^\dagger_{jm}$ and $\tilde{a}_{jm} = (-1)^{j+m} a_{j-m}$. The ph-state can be described by

$$|ph\rangle = a^\dagger_{jm}\tilde{a}_{jm}|0\rangle = (-1)^{j_h+j_m}|j_p m_p j_h - m_h\rangle \tag{C.1}$$

and the correspondens matrix elements of the interactions can be written as

$$\begin{aligned} v_{ph,p'h'} &= \langle ph'|V|hp'\rangle - \langle ph'|V|p'h\rangle = \\ = (-1)^{j_h+m_h}(-1)^{j_{h'}+m_{h'}} &\left[\langle p-h'|V|-hp'\rangle - \langle p-h'|V|p'-h\rangle\right] \end{aligned} \tag{C.2}$$

and:

$$\begin{aligned} u_{ph,p'h'} &= \langle pp'|V|hh'\rangle - \langle pp'|V|h'h\rangle = \\ = (-1)^{j_h+m_h}(-1)^{j_{h'}+m_{h'}} &\left[\langle pp'|V|-h-h'\rangle - \langle pp'|V|-h'h\rangle\right] \end{aligned} \tag{C.3}$$

where explicitally:

$$|ab\rangle = |j_a m_a j_b m_b\rangle. \tag{C.4}$$

Using completeness of the Clebsh-Gordan coefficients we can write, in general:

$$\begin{aligned} \langle j_a m_a j_b m_b|V|j_c m_c j_d m_d\rangle = \sum_{J_1 M_1 J_2 M_2} &\langle j_a m_a j_b m_b|J_1 M_1\rangle \\ \langle j_c m_c j_d m_d|J_2 M_2\rangle &\langle j_a j_b J_1 M_1|V|j_c j_d J_2 M_2\rangle. \end{aligned} \tag{C.5}$$

Applying the Wigner Eckart theorem we have:

$$\begin{aligned} &\langle j_a j_b J_1 M_1|V|j_c j_d J_2 M_2\rangle = \\ (-1)^{J_1-M_1} \begin{pmatrix} J_1 & 0 & J_2 \\ -M_1 & 0 & M_2 \end{pmatrix} &\langle j_a j_b J_1||V||j_c j_d J_2\rangle = \\ &= \frac{\langle j_a j_b J_1||V||j_c j_d J_2\rangle}{\hat{J}_1}\delta_{J_1,J_2}\delta_{M_1,M_2}. \end{aligned} \tag{C.6}$$

Here the reduced matrix element is calculated only for the angular part of the matrix element. Eq. (C.5) can be rewritten as:

$$\langle j_a m_a j_b m_b | V | j_c m_c j_d m_d \rangle = \sum_{JM} \langle j_a m_a j_b m_b | JM \rangle \langle j_c m_c j_d m_d | JM \rangle \frac{\langle j_a j_b J || V || j_c j_d J \rangle}{\hat{J}}. \tag{C.7}$$

By using Eq. (C.6) we can write Eq. (C.2) as

$$\begin{aligned} v_{ph,p'h'} &= (-1)^{j_h+m_h}(-1)^{j_{h'}+m_{h'}} \Bigg[\sum_{JM} \langle j_p m_p j_{h'} - m_{h'} | JM \rangle \\ &\quad \langle j_h - m_h j_{p'} m_{p'} | JM \rangle \frac{\langle j_p j_{h'} J || V || j_h j_{p'} J \rangle}{\hat{J}} + \\ &\quad - \sum_{JM} \langle j_p m_p j_{h'} - m_{h'} | JM \rangle \langle j_{p'} m_{p'} j_h - m_h | JM \rangle \frac{\langle j_p j_{h'} J || V || j_{p'} j_h J \rangle}{\hat{J}} \Bigg] = \\ &= (-1)^{j_h+m_h}(-1)^{j_{h'}+m_{h'}} \sum_{JM} \langle j_p m_p j_{h'} - m_{h'} | JM \rangle \langle j_h - m_h j_{p'} m_{p'} | JM \rangle \frac{1}{\hat{J}} \\ &\quad \left[\langle j_p j_{h'} J || V || j_h j_{p'} J \rangle - (-1)^{j_{p'}+j_h-J} \langle j_p j_{h'} J || V || j_{p'} j_h J \rangle \right] \end{aligned} \tag{C.8}$$

where in the last expression we have used the relation:

$$\langle j_a m_a j_b m_b | JM \rangle = (-1)^{j_a+j_b-J} \langle j_b m_b j_a m_a | JM \rangle. \tag{C.9}$$

To express the first RPA equation in angular momentum coupling we must multiply it by $\sum_{m_p m_h} \langle j_p m_p j_h m_h | J' M' \rangle$ and we obtain

$$\begin{aligned} &\sum_{m_p m_h} \langle j_p m_p j_h m_h | J' M' \rangle v_{ph,p'h'} = \\ &= \sum_{m_p m_h} \langle j_p m_p j_h m_h | J' M' \rangle (-1)^{j_h+m_h}(-1)^{j_{h'}+m_{h'}} \\ &\quad \sum_{JM} \langle j_{p'} m_{p'} j_h - m_h | JM \rangle \langle j_{h'} - m_{h'} j_p m_p | JM \rangle \frac{1}{\hat{J}} \\ &\quad \left[\langle j_{p'} j_h J || V || j_{h'} j_p J \rangle - (-1)^{j_p+j_{h'}-J} \langle j_{p'} j_h J || V || j_p j_{h'} J \rangle \right]. \end{aligned} \tag{C.10}$$

The sum of the CG coefficients is

$$\begin{aligned} &\sum_{m_p m_h M} (-1)^{j_h+m_h}(-1)^{j_{h'}+m_{h'}} \langle j_p m_p j_h m_h | J' M' \rangle \langle j_{p'} m_{p'} j_h - m_h | JM \rangle \\ &\quad \langle j_{h'} - m_{h'} j_p m_p | JM \rangle = \\ &= \sum_{m_p m_h M} (-1)^{j_h+m_h}(-1)^{j_{h'}+m_{h'}}(-1)^{j_p-j_h+M'} \hat{J}' \begin{pmatrix} j_p & j_h & J' \\ m_p & m_h & -M' \end{pmatrix} \\ &\quad (-1)^{j_{p'}-j_h+M} \hat{J} \begin{pmatrix} j_{p'} & j_h & J \\ m_{p'} & m_h & -M \end{pmatrix} (-1)^{j_{h'}+j_p+M} \hat{J} \begin{pmatrix} j_{h'} & j_p & J \\ -m_{h'} & m_p & -M \end{pmatrix} = \\ &= \sum_{m_p m_h M} (-1)^{j_p+j_{p'}+J+M'}(-1)^{j_p+j_h+J+m_p-m_h+M} \hat{J}' \hat{J}^2 \\ &\quad \begin{pmatrix} j_p & j_h & J' \\ m_p & m_h & -M' \end{pmatrix} \begin{pmatrix} j_h & J & j_{p'} \\ -m_h & -M & m_{p'} \end{pmatrix} \begin{pmatrix} J & j_p & j_{h'} \\ M & -m_p & m_{h'} \end{pmatrix} = \\ &= (-1)^{j_p+j_{p'}+J+M'} \hat{J}' \hat{J}^2 \begin{pmatrix} j_{p'} & j_{h'} & J' \\ m_{p'} & m_{h'} & -M' \end{pmatrix} \begin{Bmatrix} j_{p'} & j_{h'} & J' \\ j_p & j_h & J \end{Bmatrix}. \end{aligned} \tag{C.11}$$

In this way we can express Eq. (C.10)

$$
\begin{aligned}
&\sum_{m_p m_h M} \langle j_p m_p j_h m_h | J'M' \rangle v_{php'h'} = \\
&\sum_J \hat{J}'\hat{J}(-1)^{j_p+j_{p'}+J+M'} \begin{pmatrix} j_{p'} & j_{h'} & J' \\ m_{p'} & m_{h'} & -M' \end{pmatrix} \begin{Bmatrix} j_{p'} & j_{h'} & J' \\ j_p & j_h & J \end{Bmatrix} \\
&\left[\langle j_{p'} j_h J||V||j_{h'} j_p J\rangle - (-1)^{j_p+j_{h'}-J}\langle j_{p'} j_h J||V||j_p j_{h'} J\rangle\right] = \\
&= \langle j_{p'} m_{p'} j_{h'} m_{h'} | J'M' \rangle \sum_J \hat{J}(-1)^{j_p+j_{h'}+J} \begin{Bmatrix} j_{p'} & j_{h'} & J' \\ j_p & j_h & J \end{Bmatrix} \\
&\left[\langle j_{p'} j_h J||V||j_{h'} j_p J\rangle - (-1)^{j_p+j_{h'}-J}\langle j_{p'} j_h J||V||j_p j_{h'} J\rangle\right] = \\
&= \langle j_{p'} m_{p'} j_{h'} m_{h'} | J'M' \rangle v^{J'}_{php'h'}
\end{aligned}
\tag{C.12}
$$

where we have defined:

$$
\begin{aligned}
v^{J'}_{php'h'} = &\sum_J \hat{J}(-1)^{j_p+j_{h'}+J} \begin{Bmatrix} j_{p'} & j_{h'} & J' \\ j_p & j_h & J \end{Bmatrix} \\
&\left[\langle j_{p'} j_h J||V||j_{h'} j_p J\rangle - (-1)^{j_p+j_{h'}-J}\langle j_{p'} j_h J||V||j_p j_{h'} J\rangle\right].
\end{aligned}
\tag{C.13}
$$

In a similar way we find:

$$
\begin{aligned}
&\sum_{m_p m_h} \langle j_p m_p j_h m_h | J'M' \rangle u_{php'h'} = \\
&= (-1)^{J'+M'} \langle j_{p'} m_{p'} j_{h'} m_{h'} | J' - M' \rangle \\
&(-1)^{j_{h'}-j_{p'}-J'} \sum_J (-1)^{j_p+j_{p'}+J} \hat{J} \begin{Bmatrix} j_{h'} & j_{p'} & J' \\ j_p & j_h & J \end{Bmatrix} \\
&\left[\langle j_{h'} j_h J||V||j_{p'} j_p J\rangle - (-1)^{j_p+j_{p'}-J}\langle j_{h'} j_h J||V||j_p j_{p'} J\rangle\right] = \\
&= (-1)^{J'+M'} \langle j_{p'} m_{p'} j_{h'} m_{h'} | J' - M' \rangle u^{J'}_{php'h'}
\end{aligned}
\tag{C.14}
$$

where we have defined:

$$
\begin{aligned}
u^{J'}_{php'h'} = &(-1)^{j_{h'}-j_{p'}-J'} \sum_J (-1)^{j_p+j_{p'}+J} \hat{J} \begin{Bmatrix} j_{h'} & j_{p'} & J' \\ j_p & j_h & J \end{Bmatrix} \\
&\left[\langle j_{h'} j_h J||V||j_{p'} j_p J\rangle - (-1)^{j_p+j_{p'}-J}\langle j_{h'} j_h J||V||j_p j_{p'} J\rangle\right].
\end{aligned}
\tag{C.15}
$$

The last expression can be rewritten as:

$$
\begin{aligned}
&(-1)^{J'+M'} \langle j_{p'} m_{p'} j_{h'} m_{h'} | J' - M' \rangle u^{J'}_{php'h'} = \\
&(-1)^{J'+M'} \langle j_{p'} m_{p'} j_{h'} m_{h'} | J' - M' \rangle (-1)^{j'_h - j'_p - J'} v^{J'}_{phh'p'}.
\end{aligned}
\tag{C.16}
$$

To obtain the first RPA equation in angular momentum coupling we multiply Eq.(2.12) by

$$
\sum_{m_p m_h} \langle j_p m_p j_h m_h | JM \rangle \tag{C.17}
$$

$$
\sum_{m_p m_h} \langle j_p m_p j_h m_h | JM \rangle \left[(\epsilon_p - \epsilon_h - \omega) X_{ph} + \sum_{p'h'} (v_{php'h'} X_{p'h'} + u_{php'h' Y_{p'h'}}) \right] = 0 \tag{C.18}
$$

and defining:

$$
\begin{aligned}
X^J_{ph} &= \sum_{m_p m_h} \langle j_p m_p j_h m_h | JM \rangle X_{ph} \\
Y^J_{ph} &= \sum_{m_p m_h} (-1)^{J-M} \langle j_p m_p j_h m_h | J - M \rangle Y_{ph}
\end{aligned}
\tag{C.19}
$$

we obtain

$$(\epsilon_p - \epsilon_h - \omega)X^J_{ph} + \sum_{p'h'} \langle j_{p'} m_{p'} j_{h'} m_{h'} | JM \rangle v^J_{php'h'} X_{p'h'} +$$

$$+ \sum_{p'h'} \langle j_{p'} m_{p'} j_{h'} m_{h'} | J - M \rangle (-1)^{J+M} u^J_{php'h'} Y_{p'h'} = 0 \tag{C.20}$$

$$(\epsilon_p - \epsilon_h - \omega)X^J_{ph} + \sum_{\tilde{p'}\tilde{h'}} (v^J_{php'h'} X^J_{p'h'} + u^J_{php'h'} Y^J_{p'h'}) = 0 \tag{C.21}$$

where with $\tilde{p'}$ and $\tilde{h'}$ we indicate that there is no sum on m. The second RPA equation in angular momentum coupling is obtained by using an analogous method and by multiplying Eq.(2.13) by $\sum_{m_p m_h} \langle j_p m_p j_h m_h | J - M \rangle (-1)^{J-M}$

$$(\epsilon_p - \epsilon_h + \omega)Y^J_{ph} + \sum_{p'h'} (v^{J*}_{php'h'} Y^J_{p'h'} + u^{J*}_{php'h'} X^J_{p'h'}) = 0. \tag{C.22}$$

Appendix D

Matrix elements of the interaction

D 1 Matrix element for the central channel

The matrix element to be calculated is:

$$v^{JdirF}_{1,php'h'} = \sum_K (-1)^{K+j_h+j_{p'}} \hat{K}^2 \left\{ \begin{array}{ccc} j_p & j_h & J \\ j_{p'} & j_{h'} & K \end{array} \right\}$$
$$\langle ph'K|v_1(\boldsymbol{r}_1,\boldsymbol{r}_2)|hp'K\rangle \tag{D.1}$$

where:

$$v_1(\boldsymbol{r}_1,\boldsymbol{r}_2) = \frac{1}{(2\pi)^3} \int e^{i\boldsymbol{q}\cdot(\boldsymbol{r}_1-\boldsymbol{r}_2)} V_1(q) d\boldsymbol{q}. \tag{D.2}$$

We separate the exponentials depending on $\boldsymbol{r}_1$ and $\boldsymbol{r}_2$ and we expand them on a basis of spherical harmonics

$$v_1(\boldsymbol{r}_1,\boldsymbol{r}_2) = \frac{1}{(2\pi)^3} \int dq q^2 V_1(q) \int d\hat{q} 4\pi \sum_{l_1\mu_1} i^{l_1} j_{l_1}(qr_1)\, Y_{l_1\mu_1}(\hat{q})\, Y^*_{l_1\mu_1}(\hat{r}_1)$$
$$4\pi \sum_{l_2\mu_2} (-i)^{l_2} j_{l_2}(qr_2)\, Y^*_{l_2\mu_2}(\hat{q})\, Y_{l_2\mu_2}(\hat{r}_2). \tag{D.3}$$

By using the orthogonality relation between spherical harmonics we can write:

$$v_1(\boldsymbol{r}_1,\boldsymbol{r}_2) = \frac{(4\pi)^2}{(2\pi)^3} \int dq q^2 \sum_l j_l(qr_1) j_l(qr_2) \sum_\mu Y^*_{l\mu}(\hat{r}_1)\, Y_{l\mu}(\hat{r}_2) V_1(q). \tag{D.4}$$

We rewrite the product of spherical harmonics in terms of product of irreducible spherical tensors:

$$\sum_\mu Y^*_{l\mu}(\hat{r}_1)\, Y_{l\mu}(\hat{r}_2) = \sum_\mu (-1)^\mu\, Y_{l-\mu}(\hat{r}_1)\, Y_{l\mu}(\hat{r}_2) =$$
$$= \sum_\mu \hat{l}(-1)^l \frac{(-1)^{l+\mu}}{\hat{l}}\, Y_{l-\mu}(\hat{r}_1)\, Y_{l\mu}(\hat{r}_2) =$$
$$= (-1)^l \hat{l} \left[Y_l(\hat{r}_1) \otimes Y_l(\hat{r}_2) \right]^0_0 , \tag{D.5}$$

therefore we obtain

$$v_1(\boldsymbol{r}_1,\boldsymbol{r}_2) = \sum_l (-1)^l \hat{l} \left[Y_l(\hat{r}_1) \otimes Y_l(\hat{r}_2) \right]^0_0$$
$$\int dq q^2 \frac{2}{\pi} V_1(q) j_l(qr_1) j_l(qr_2). \tag{D.6}$$

We express the matrix element to be calculated as

$$v_{1,php'h'}^{JdirV_1} = \sum_K (-1)^{K+j_h+j_{p'}} \hat{K}^2 \left\{ \begin{array}{ccc} j_p & j_h & J \\ j_{p'} & j_{h'} & K \end{array} \right\}$$
$$\int dq q^2 \frac{2}{\pi} V_1(q) \langle ph'K | \sum_l (-1)^l \hat{l} \, [Y_l(\hat{r}_1) \otimes Y_l(\hat{r}_2)]_0^0 \, | hp'K \rangle \tag{D.7}$$

and we separate the angular coordinates from the radial ones:

$$v_{1,php'h'}^{JdirV_1} = \sum_l (-1)^l \hat{l} \sum_K (-1)^{K+j_h+j_{p'}} \hat{K}^2 \left\{ \begin{array}{ccc} j_p & j_h & J \\ j_{p'} & j_{h'} & K \end{array} \right\}$$
$$\langle j_p j_{h'} K | \, [Y_l(\hat{r}_1) \otimes Y_l(\hat{r}_2)]_0^0 \, | j_h j_{p'} K \rangle$$
$$\int dq q^2 \frac{2}{\pi} V_1(q) \int dr_1 r_1^2 R_p^*(r_1) R_h(r_1) j_l(qr_1) \int dr_2 r_2^2 R_{h'}^*(r_2) R_{p'}(r_2) j_l(qr_2). \tag{D.8}$$

In (D.8) we must calculate the following expression

$$\langle j_p j_{h'} K | \, [Y_l(\hat{r}_1) \otimes Y_l(\hat{r}_2)]_0^0 \, | j_h j_{p'} K \rangle =$$
$$= (-1)^{j_h+j_{h'}+K} \frac{(-1)^l}{\hat{l}} \left\{ \begin{array}{ccc} j_p & j_{h'} & K \\ j_{p'} & j_h & l \end{array} \right\} \langle j_p || \, Y_l(\hat{r}_1) || j_h \rangle \langle j_{h'} || \, Y_l(\hat{r}_2) || j_{p'} \rangle. \tag{D.9}$$

Inserting (D.9) in (D.8) we have to evaluate:

$$\sum_K \hat{K}^2 \left\{ \begin{array}{ccc} j_p & j_h & J \\ j_{p'} & j_{h'} & K \end{array} \right\} \left\{ \begin{array}{ccc} j_p & j_{h'} & K \\ j_{p'} & j_h & l \end{array} \right\} = \frac{\delta_{lJ}}{\hat{J}^2}. \tag{D.10}$$

Then we can write:

$$v_{1,php'h'}^{JdirV_1} = \frac{(-1)^{j_{p'}+j_{h'}+1}}{\hat{J}^2} \int dq q^2 \frac{2}{\pi} V_1(q) \int dr_1 r_1^2 R_p^*(r_1) R_h(r_1) j_J(qr_1)$$
$$\int dr_2 r_2^2 R_{h'}^*(r_2) R_{p'}(r_2) j_J(qr_2) \langle j_p || \, Y_J(\hat{r}_1) | j_h \rangle \langle j_{h'} || \, Y_J(\hat{r}_2) || j_{p'} \rangle \tag{D.11}$$

where:

$$\langle j_a || \, Y_J || j_b \rangle = (-1)^{j_a+\frac{1}{2}} \frac{\hat{j}_a \hat{j}_b \hat{J}}{\sqrt{4\pi}} \left(\begin{array}{ccc} j_a & J & j_b \\ \frac{1}{2} & 0 & -\frac{1}{2} \end{array} \right). \tag{D.12}$$

We use the expression (D.6) to obtain the exchange term

$$v_{1,php'h'}^{JexchV_1} = \sum_K \hat{K}^2 \left\{ \begin{array}{ccc} j_p & j_h & J \\ j_{p'} & j_{h'} & K \end{array} \right\} \langle ph'K | \sum_l (-1)^l \hat{l} \, [Y_l(\hat{r}_1) \otimes Y_l(\hat{r}_2)]_0^0$$
$$\int dq q^2 \frac{2}{\pi} V_1(q) j_l(qr_1) j_l(qr_2) | p'hK \rangle =$$
$$= \sum_l (-1)^l \hat{l} \sum_K \hat{K}^2 \left\{ \begin{array}{ccc} j_p & j_h & J \\ j_{p'} & j_{h'} & K \end{array} \right\} \langle j_p j_{h'} K | \, [Y_l(\hat{r}_1) \otimes Y_l(\hat{r}_2)]_0^0 \, | j_{p'} j_h K \rangle$$
$$\int dq q^2 V_1(q) \frac{2}{\pi} \int dr_1 r_1^2 R_p^*(r_1) R_{p'}(r_1) j_l(qr_1) \int dr_2 r_2^2 R_{h'}^*(r_2) R_h(r_2) j_l(qr_2). \tag{D.13}$$

Because:

$$\langle j_p j_{h'} K | \, [Y_l(\hat{r}_1) \otimes Y_l(\hat{r}_2)]_0^0 \, | j_{p'} j_h K \rangle =$$
$$= (-1)^{j_{p'}+j_{h'}+K} \frac{(-1)^l}{\hat{l}} \left\{ \begin{array}{ccc} j_p & j_{h'} & K \\ j_h & j_{p'} & l \end{array} \right\} \langle j_p || \, Y_l(\hat{r}_1) || j_{p'} \rangle \langle j_{h'} || \, Y_l(\hat{r}_2) || j_h \rangle, \tag{D.14}$$

in the above expression we find the term

$$\sum_K (-1)^{K+j_{h'}+j_{p'}} \hat{K}^2 \left\{ \begin{array}{ccc} j_p & j_h & J \\ j_{p'} & j_{h'} & K \end{array} \right\} \left\{ \begin{array}{ccc} j_p & j_{h'} & K \\ j_h & j_{p'} & l \end{array} \right\} = (-1)^{j_{h'}+j_{p'}+l+J} \left\{ \begin{array}{ccc} j_p & j_h & J \\ j_{h'} & j_{p'} & l \end{array} \right\}. \tag{D.15}$$

Finally we obtain:

$$v^{JexchV_1}_{1,php'h'} = \sum_l (-1)^{j_{p'}+j_{h'}+l+J} \left\{ \begin{array}{ccc} j_p & j_h & J \\ j_{h'} & j_{p'} & l \end{array} \right\} \langle j_p || Y_J | j_{p'} \rangle \langle j_{h'} || Y_J || j_h \rangle$$
$$\int dq q^2 \frac{2}{\pi} V_1(q) \int dr_1 r_1^2 R^*_p(r_1) R_{p'}(r_1) j_l(qr_1) \int dr_2 r_2^2 R^*_{h'}(r_2) R_h(r_2) j_l(qr_2). \tag{D.16}$$

D 2 Matrix elements for the spin channel

The spin-dependent interaction is:

$$v_3(\boldsymbol{r}_1, \boldsymbol{r}_2) = \frac{1}{(2\pi)^3} \int d\boldsymbol{q} e^{i\boldsymbol{q}\cdot(\boldsymbol{r}_1-\boldsymbol{r}_2)} V_3(q) \boldsymbol{\sigma}(1) \cdot \boldsymbol{\sigma}(2) \tag{D.17}$$

Using the multipole expansion we can rewrite the previous expression as:

$$v_3(\boldsymbol{r}_1, \boldsymbol{r}_2) = \int dq q^2 \frac{2}{\pi} V_3(q) \sum_l j_l(qr_1) j_l(qr_2) (-1)^l \hat{l} \left[Y_l(\hat{r}_1) \otimes Y_l(\hat{r}_2) \right]^0_0 \boldsymbol{\sigma}(1) \cdot \boldsymbol{\sigma}(2). \tag{D.18}$$

The operator term can be expressed as:

$$\begin{aligned} \left[Y_l(\hat{r}_1) \otimes Y_l(\hat{r}_2) \right]^0_0 \boldsymbol{\sigma}(1) \cdot \boldsymbol{\sigma}(2) &= \left[Y_l(\hat{r}_1) \otimes Y_l(\hat{r}_2) \right]^0_0 \left[\sigma(1) \otimes \sigma(2) \right]^0_0 (-1)\sqrt{3} = \\ &= -\sqrt{3} \left[\left[Y_l(\hat{r}_1) \otimes Y_l(\hat{r}_2) \right]^0 \otimes \left[\sigma(1) \otimes \sigma(2) \right]^0 \right]^0_0 = \\ = -\sqrt{3} \sum_L (-1)^{l+L+1} \hat{L} \left\{ \begin{array}{ccc} l & l & 0 \\ 1 & 1 & L \end{array} \right\} &\left[\left[Y_l(\hat{r}_1) \otimes \sigma(1) \right]^L \otimes \left[Y_l(\hat{r}_2) \otimes \sigma(2) \right]^L \right]^0_0 = \\ &= \frac{(-1)}{\hat{l}} \sum_L \hat{L} \left[\left[Y_l(\hat{r}_1) \otimes \sigma(1) \right]^L \otimes \left[Y_l(\hat{r}_2) \otimes \sigma(2) \right]^L \right]^0_0 . \end{aligned} \tag{D.19}$$

By using (D.19), we rewrite (D.18) as:

$$v_3(\boldsymbol{r}_1, \boldsymbol{r}_2) = \sum_l (-1)^{l+1} \sum_L \hat{L} \left[\left[Y_l(\hat{r}_1) \otimes \sigma(1) \right]^L \otimes \left[Y_l(\hat{r}_2) \otimes \sigma(2) \right]^L \right]^0_0$$
$$\int dq q^2 \frac{2}{\pi} V_3(q) j_l(qr_1) j_l(qr_2). \tag{D.20}$$

The matrix element to be calculated is

$$v^{JdirV_3}_{3,php'h'} = \sum_K (-1)^{K+j_h+j_{p'}} \hat{K}^2 \left\{ \begin{array}{ccc} j_p & j_h & J \\ j_{p'} & j_{h'} & K \end{array} \right\}$$
$$\langle ph'K | \sum_l (-1)^{l+1} \sum_L \hat{L} \left[\left[Y_l(\hat{r}_1) \otimes \sigma(1) \right]^L \otimes \left[Y_l(\hat{r}_2) \otimes \sigma(2) \right]^L \right]^0_0$$
$$\int dq q^2 \frac{2}{\pi} V_3(q) j_l(qr_1) j_l(qr_2) | hp'K \rangle. \tag{D.21}$$

Separating the angular part from the radial one we have:

$$v^{JdirV_3}_{3,php'h'} = \sum_l (-1)^{l+1} \sum_L \hat{L} \sum_K (-1)^{K+j_h+j_{p'}} \hat{K}^2 \left\{ \begin{array}{ccc} j_p & j_h & J \\ j_{p'} & j_{h'} & K \end{array} \right\}$$
$$\langle j_p j_{h'} K | \left[\left[Y_l(\hat{r}_1) \otimes \sigma(1) \right]^L \otimes \left[Y_l(\hat{r}_2) \otimes \sigma(2) \right]^L \right]^0_0 | j_h j_{p'} K \rangle$$
$$\int dq q^2 \frac{2}{\pi} V_3(q) \int dr_1 r_1^2 R^*_p(r_1) R_h(r_1) j_l(qr_1) \int dr_2 r_2^2 R^*_{h'}(r_2) R_{p'}(r_2) j_l(qr_2). \tag{D.22}$$

The angular momentum part is

$$\langle j_p j_{h'} K | \left[[Y_l(\hat{r}_1) \otimes \sigma(1)]^L \otimes [Y_l(\hat{r}_2) \otimes \sigma(2)]^L \right]_0^0 | j_h j_{p'} K \rangle =$$
$$= \frac{(-1)^L}{\hat{L}} (-1)^{j_h' + j_h + K} \left\{ \begin{array}{ccc} j_p & j_{h'} & K \\ j_{p'} & j_h & L \end{array} \right\} \langle j_p || [Y_l(\hat{r}_1) \otimes \sigma(1)]^L || j_h \rangle$$
$$\langle j_{h'} || [Y_l(\hat{r}_2) \otimes \sigma(2)]^L || j_{p'} \rangle. \tag{D.23}$$

In the calculation of $v_{3,php'h'}^{JdirV_3}$ we find:

$$\sum_K \hat{K}^2 \left\{ \begin{array}{ccc} j_p & j_h & J \\ j_{p'} & j_{h'} & K \end{array} \right\} \left\{ \begin{array}{ccc} j_p & j_{h'} & K \\ j_{p'} & j_h & L \end{array} \right\} = \frac{\delta_{LJ}}{\hat{L}^2}. \tag{D.24}$$

The final result is

$$v_{3,php'h'}^{JdirV_3} = \sum_l (-1)^{j_{p'} + j_{h'} + l} \frac{(-1)^J}{\hat{J}^2} \langle j_p || [Y_l(\hat{r}_1) \otimes \sigma(1)]^J || j_h \rangle \langle j_{h'} || [Y_l(\hat{r}_2) \otimes \sigma(2)]^J || j_{p'} \rangle$$
$$\int dq q^2 \frac{2}{\pi} V_3(q) \int dr_1 r_1^2 R_p^*(r_1) R_h(r_1) j_l(qr_1) \int dr_2 r_2^2 R_{h'}^*(r_2) R_{p'}(r_2) j_l(qr_2). \tag{D.25}$$

For the exchange term we have to calculate:

$$v_{3,php'h'}^{JexchV_3} = \sum_K \hat{K}^2 \left\{ \begin{array}{ccc} j_p & j_h & J \\ j_{p'} & j_{h'} & K \end{array} \right\}$$
$$\langle ph'K | \sum_l (-1)^{l+1} \sum_L \hat{L} \left[[Y_l(\hat{r}_1) \otimes \sigma(1)]^L \otimes [Y_l(\hat{r}_2) \otimes \sigma(2)]^L \right]_0^0$$
$$\int dq q^2 \frac{2}{\pi} V_3(q) j_l(qr_1) j_l(qr_2) | p'hK \rangle. \tag{D.26}$$

Separating the angular part from the radial one we have:

$$v_{3,php'h'}^{JexchV_3} = \sum_l (-1)^{l+1} \sum_L \hat{L} \sum_K \hat{K}^2 \left\{ \begin{array}{ccc} j_p & j_h & J \\ j_{p'} & j_{h'} & K \end{array} \right\}$$
$$\langle j_p j_{h'} K | \left[[Y_l(\hat{r}_1) \otimes \sigma(1)]^L \otimes [Y_l(\hat{r}_2) \otimes \sigma(2)]^L \right]_0^0 | j_{p'} j_h K \rangle$$
$$\int dq q^2 \frac{2}{\pi} V_3(q) \int dr_1 r_1^2 R_p^*(r_1) R_{p'}(r_1) j_l(qr_1) \int dr_2 r_2^2 R_{h'}^*(r_2) R_h(r_2) j_l(qr_2). \tag{D.27}$$

We express the angular momentum dependent term as

$$\langle j_p j_{h'} K | \left[[Y_l(\hat{r}_1) \otimes \sigma(1)]^L \otimes [Y_l(\hat{r}_2) \otimes \sigma(2)]^L \right]_0^0 | j_{p'} j_h K \rangle =$$
$$= \frac{(-1)^L}{\hat{L}} (-1)^{j_{h'} + j_{p'} + K} \left\{ \begin{array}{ccc} j_p & j_{h'} & K \\ j_h & j_{p'} & L \end{array} \right\} \langle j_p || [Y_l(\hat{r}_1) \otimes \sigma(1)]^L || j_{p'} \rangle \langle j_{h'} || [Y_l(\hat{r}_2) \otimes \sigma(2)]^L || j_h \rangle \tag{D.28}$$

In the evaluation of $v_{3,php'h'}^{JexchV_3}$ we find

$$\sum_K \hat{K}^2 \left\{ \begin{array}{ccc} j_p & j_h & J \\ j_{p'} & j_{h'} & K \end{array} \right\} \left\{ \begin{array}{ccc} j_p & j_{h'} & K \\ j_h & j_{p'} & L \end{array} \right\} (-1)^{L+K+j_{h'}+j_{p'}} =$$
$$= \left\{ \begin{array}{ccc} j_p & j_h & J \\ j_{h'} & j_{p'} & L \end{array} \right\} (-1)^{j_{p'} + j_{h'} + J}. \tag{D.29}$$

Using (D.29) we finally obtain:

$$v_{3,php'h'}^{JexchV_3} = \sum_{lL} (-1)^{l+1} (-1)^{j_{h'} + j_{p'} + J} \left\{ \begin{array}{ccc} j_p & j_h & J \\ j_{h'} & j_{p'} & L \end{array} \right\}$$
$$\langle j_p || [Y_l(\hat{r}_1) \otimes \sigma(1)]^L || j_{p'} \rangle \langle j_{h'} || [Y_l(\hat{r}_2) \otimes \sigma(2)]^L || j_h \rangle$$
$$\int dq q^2 \frac{2}{\pi} V_3(q) \int dr_1 r_1^2 R_p^*(r_1) R_{p'}(r_1) j_l(qr_1) \int dr_2 r_2^2 R_{h'}^*(r_2) R_h(r_2) j_l(qr_2). \tag{D.30}$$

In the previous expression there are matrix elements of the type

$$\begin{aligned}
&\langle l_a \frac{1}{2} j_a || (Y_l \otimes \sigma(1))^L || l_b \frac{1}{2} j_b \rangle = \\
&= \hat{j}_a \hat{j}_b \hat{L} \left\{ \begin{array}{ccc} l_a & \frac{1}{2} & j_a \\ l_b & \frac{1}{2} & j_b \\ l & 1 & L \end{array} \right\} \langle l_a || Y_l || l_b \rangle \langle \frac{1}{2} || \sigma || \frac{1}{2} \rangle = \\
&= \frac{(-1)^{l_a}}{\sqrt{4\pi}} \hat{l}_a \hat{l}_b \hat{l} \hat{j}_a \hat{j}_b \hat{L} \left\{ \begin{array}{ccc} l_a & \frac{1}{2} & j_a \\ l_b & \frac{1}{2} & j_b \\ l & 1 & L \end{array} \right\} \left(\begin{array}{ccc} l_a & l & l_b \\ 0 & 0 & 0 \end{array} \right) \sqrt{6}.
\end{aligned} \tag{D.31}$$

D 3 Matrix elements for the isospin channel

The treatment of the V_2 and V_4 terms is the same as V_1 and V_2: the only difference is the presence of the $\boldsymbol{\tau}(1) \cdot \boldsymbol{\tau}(2)$ term. For the direct matrix elements we have to calculate:

$$\begin{aligned}
\langle \tau_p \tau_{h'} | \tau(1) \cdot \tau(2) | \tau_h \tau_{p'} \rangle &= \sum_k (-1)^k \langle \tau_p \tau_{h'} | \tau_k \tau_{-k} | \tau_h \tau_{p'} \rangle = \\
&= \sum_k (-1)^k \langle \tau_p | \tau_k | \tau_h \rangle \langle \tau_{h'} | \tau_{-k} | \tau_{p'} \rangle
\end{aligned} \tag{D.32}$$

Using the Wigner-Eckart theorem we can rewrite the previous expression as:

$$\begin{aligned}
\langle \tau_p \tau_{h'} | \tau(1) \cdot \tau(2) | \tau_h \tau_{p'} \rangle = \sum_k (-1)^{\tau_p - \tau_p} \left(\begin{array}{ccc} \tau_p & 1 & \tau_h \\ -k_p & k & k_h \end{array} \right) \langle \tau_p || \tau_k || \tau_h \rangle \\
(-1)^{\tau_{h'} - k_{h'}} \left(\begin{array}{ccc} \tau_{h'} & 1 & \tau_{p'} \\ -k_{h'} & -k & k_{p'} \end{array} \right) \langle \tau_{h'} || \tau_{-k} || \tau_{p'} \rangle.
\end{aligned} \tag{D.33}$$

For charge conservation $k = 0$ and because we work only with nucleons we have: $\tau_p = \tau_h = \tau_{h'} = \tau_{p'} = \frac{1}{2}$. By using these considerations we can simplify the previous expression as:

$$\begin{aligned}
&\langle \tau_p \tau_{h'} | \tau(1) \cdot \tau(2) | \tau_h \tau_{p'} \rangle = \\
&(-1)^{1 - k_p - k_{h'}} \left(\begin{array}{ccc} \frac{1}{2} & 1 & \frac{1}{2} \\ -k_p & 0 & k_h \end{array} \right) \left(\begin{array}{ccc} \frac{1}{2} & 1 & \frac{1}{2} \\ -k_{h'} & 0 & k_{p'} \end{array} \right) \langle \frac{1}{2} || \tau || \frac{1}{2} \rangle \langle \frac{1}{2} || \tau || \frac{1}{2} \rangle.
\end{aligned} \tag{D.34}$$

In change conserving transitions there is no proton-neutron excitation, therefore $k_p = k_h$. Because:

$$\left(\begin{array}{ccc} \frac{1}{2} & 1 & \frac{1}{2} \\ -k_p & 0 & k_h \end{array} \right) = \frac{1}{\sqrt{6}} \tag{D.35}$$

we obtain:

$$\langle \tau_p \tau_{h'} | \tau(1) \cdot \tau(2) | \tau_h \tau_{p'} \rangle = (-1)^{1 - k_p - k_{h'}}. \tag{D.36}$$

In the calculation of the exchange part we follow what we have done for the direct term:

$$\langle \tau_p \tau_{h'} | \tau(1) \cdot \tau(2) | \tau_{p'} \tau_h \rangle = \sum_k (-1)^k \langle \tau_p | \tau_k | \tau_{p'} \rangle \langle \tau_{h'} | \tau_{-k} | \tau_h \rangle. \tag{D.37}$$

Applying the Wigner-Eckart theorem and considering that we work with nucleons and that we do not have proton-neutron mixing, we have $k_1 = k_p = k_h$ and $k_2 = k_{p'} = k_{h'}$, therefore we obtain

$$\begin{aligned}
\langle \tau_p \tau_{h'} | \tau(1) \cdot \tau(2) | \tau_{p'} \tau_h \rangle = \sum_k (-1)^k (-1)^{\frac{1}{2} - k_1} \left(\begin{array}{ccc} \frac{1}{2} & 1 & \frac{1}{2} \\ -k_1 & k & k_2 \end{array} \right) \langle \frac{1}{2} || \tau || \frac{1}{2} \rangle \\
(-1)^{\frac{1}{2} - k_2} \left(\begin{array}{ccc} \frac{1}{2} & 1 & \frac{1}{2} \\ -k_2 & -k & k_1 \end{array} \right) \langle \frac{1}{2} || \tau || \frac{1}{2} \rangle.
\end{aligned} \tag{D.38}$$

When ph and $p'h'$ are pairs of the same type of nucleons the value of the isospin matrix element is 1 for both direct and exchange terms. On the contrary when the ph and $p'h'$ pairs describe the excitation of different types of nucleons, the value of the matrix element is -1 for the direct term and $+2$ for the exchange term.

D 4 Matrix elements for the tensor channel

We define:

$$S_{12}(\hat{q}) = \sqrt{6}\sum_{\mu}\left[\sigma(1)\otimes\sigma(2)\right]^2_{-\mu}\sqrt{\frac{4\pi}{5}}(-1)^{\mu}\,Y_{2\mu}(\hat{q}) \tag{D.39}$$

and

$$V_t(q) = -\frac{4\pi}{(2\pi)^3}\int dr r^2 j_2(qr)V_t(r) \tag{D.40}$$

so we can rewrite:

$$V(q) = V_t(q)S_{12}(\hat{q}). \tag{D.41}$$

With definitions (D.39), (D.40), (D.41) we have to evaluate:

$$\begin{aligned} S(\boldsymbol{r}_1,\boldsymbol{r}_2) &= \frac{1}{(2\pi)^3}\int d\boldsymbol{q}e^{i\boldsymbol{q}\cdot(\boldsymbol{r}_1-\boldsymbol{r}_2)}V_t(q)S_{12}(\hat{q}) = \\ = \frac{1}{(2\pi)^3}\int dq q^2 V_t(q) &\int d\hat{q} 4\pi\sum_{l_1\mu_1}(i)^{l_1}j_{l_1}(qr_1)\,Y_{l_1\mu_1}(\hat{q})\,Y^*_{l_1\mu_1}(\hat{r}_1) \\ &4\pi\sum_{l_2\mu_2}(-i)^{l_2}j_{l_2}(qr_2)\,Y^*_{l_2\mu_2}(\hat{q})\,Y_{l_2\mu_2}(\hat{r}_2)S_{12}(\hat{q}). \end{aligned} \tag{D.42}$$

The operator $S_{12}(\hat{r})$ can be written as:

$$S_{12}(\hat{r}) = \sqrt{6}\sum_{\mu}[\sigma(1)\otimes\sigma(2)]^2_{\mu}\sqrt{\frac{4\pi}{5}}\,Y_{2-\mu}(\hat{r})(-1)^{\mu} \tag{D.43}$$

Replacing the operator with this expression and considering that:

$$\begin{aligned} &\int d\hat{q}\,Y_{l_1\mu_1}(\hat{q})\,Y^*_{l_2\mu_2}(\hat{q})\,Y_{2-\mu}(\hat{q}) = \\ &= (-1)^{\mu_2}\frac{\hat{l}_1\hat{l}_2\hat{2}}{\sqrt{4\pi}}\begin{pmatrix} l_1 & l_2 & 2 \\ \mu_1 & -\mu_2 & -\mu \end{pmatrix}\begin{pmatrix} l_1 & l_2 & 2 \\ 0 & 0 & 0 \end{pmatrix} = \\ &= (-1)^{\mu_2}\frac{\hat{l}_1\hat{l}_2\hat{2}}{\sqrt{4\pi}}\frac{\langle l_1-\mu_1 l_2\mu_2|2-\mu\rangle}{\hat{2}}(-1)^{l_1-l_2+\mu}\begin{pmatrix} l_1 & l_2 & 2 \\ 0 & 0 & 0 \end{pmatrix} \end{aligned} \tag{D.44}$$

we rewrite Eq. (D.42) as:

$$\begin{aligned} S(\boldsymbol{r}_1,\boldsymbol{r}_2) = \frac{1}{(2\pi)^3}\int dq q^2 V_t(q)16\pi^2 &\sum_{l_1 l_2}(i)^{l_1}j_{l_1}(qr_1)(-i)^{l_2}j_{l_2}(qr_2) \\ \sqrt{6}\sum_{\mu}[\sigma(1)\otimes\sigma(2)]^2_{\mu}&\begin{pmatrix} l_1 & l_2 & 2 \\ 0 & 0 & 0 \end{pmatrix}\hat{l}_1\hat{l}_2\sum_{\mu_1\mu_2}(-1)^{\mu}(-1)^{\mu_2} \\ &Y^*_{l_1\mu_1}(\hat{r}_1)\,Y_{l_2\mu_2}(\hat{r}_2)\frac{\langle l_1-\mu_1 l_2\mu_2|2-\mu\rangle}{\hat{2}}(-1)^{l_1-l_2+\mu}. \end{aligned} \tag{D.45}$$

Since

$$\begin{aligned} &\sum_{\mu_1\mu_2}(-1)^{\mu}(-1)^{\mu_2}\,Y^*_{l_1\mu_1}(\hat{r}_1)\,Y_{l_2\mu_2}(\hat{r}_2) = \\ &\frac{(-1)^{l_1-l_2+\mu}}{\sqrt{5}}\left[Y_{l_1}(\hat{r}_1)\otimes Y_{l_2}(\hat{r}_2)\right]^2_{-\mu} \end{aligned} \tag{D.46}$$

we can express $S(\boldsymbol{r}_1, \boldsymbol{r}_2)$ as

$$S(\boldsymbol{r}_1, \boldsymbol{r}_2) = \frac{16\pi^2}{(2\pi)^3} \int dq q^2 V_t(q) \sqrt{6} \sum_{l_1 l_2} i^{l_1} (-i)^{l_2} j_{l_1}(qr_1) j_{l_2}(qr_2) \begin{pmatrix} l_1 & l_2 & 2 \\ 0 & 0 & 0 \end{pmatrix} \hat{l}_1 \hat{l}_2 \frac{(-1)^{l_1-l_2}}{\sqrt{5}} \sum_{\mu} [\sigma(1) \otimes \sigma(2)]^2_{\mu} (-1)^{\mu} [Y_{l_1}(\hat{r}_1) \otimes Y_{l_2}(\hat{r}_2)]^2_{-\mu} . \tag{D.47}$$

The angular momentum part is

$$\begin{aligned} &\sum_{\mu} [\sigma(1) \otimes \sigma(2)]^2_{\mu} (-1)^{\mu} [Y_{l_1}(\hat{r}_1) \otimes Y_{l_2}(\hat{r}_2)]^2_{-\mu} = \\ &= \sqrt{5} \left[[\sigma(1) \otimes \sigma(2)]^2 \otimes [Y_{l_1}(\hat{r}_1) \otimes Y_{l_2}(\hat{r}_2)]^2 \right]^0_0 = \\ &= \sqrt{5} \sum_L \hat{L} \hat{2}^2 \begin{Bmatrix} l_1 & l_2 & 2 \\ 1 & 1 & 2 \\ L & L & 0 \end{Bmatrix} \left[[Y_{l_1}(\hat{r}_1) \otimes \sigma(1)]^L \otimes [Y_{l_2}(\hat{r}_2) \otimes \sigma(2)]^L \right]^0_0 = \\ &= \sqrt{5} \sum_L \hat{L} \hat{2}^2 \frac{(-1)^{l_2+1+L}}{\hat{2} \hat{L}} \begin{Bmatrix} l_1 & l_2 & 2 \\ 1 & 1 & L \end{Bmatrix} \\ &\left[[Y_{l_1}(\hat{r}_1) \otimes \sigma(1)]^L \otimes [Y_{l_2}(\hat{r}_2) \otimes \sigma(2)]^L \right]^0_0 . \end{aligned} \tag{D.48}$$

The final expression of $S(\boldsymbol{r}_1, \boldsymbol{r}_2)$ is

$$\begin{aligned} S(\boldsymbol{r}_1, \boldsymbol{r}_2) &= \frac{16\pi^2}{(2\pi)^3} \int dq q^2 V_t(q) \sqrt{6} \sum_{l_1 l_2} i^{l_1} (-i)^{l_2} j_{l_1}(qr_1) j_{l_2}(qr_2) \hat{l}_1 \hat{l}_2 (-1)^{l_1-l_2} \hat{2} \\ &\sum_L \hat{L} \begin{Bmatrix} l_1 & l_2 & 2 \\ 1 & 1 & L \end{Bmatrix} \begin{pmatrix} l_1 & l_2 & 2 \\ 0 & 0 & 0 \end{pmatrix} (-1)^{l_2+1+L} \\ &\left[[Y_{l_1}(\hat{r}_1) \otimes \sigma(1)]^L \otimes [Y_{l_2}(\hat{r}_2) \otimes \sigma(2)]^L \right]^0_0 . \end{aligned} \tag{D.49}$$

The expression of the tensor matrix element is

$$\begin{aligned} v^{JdirV_5}_{5,php'h'} &= \sum_K (-1)^{K+j_h+j_{p'}} \hat{K}^2 \begin{Bmatrix} j_p & j_h & J \\ j_{p'} & j_{h'} & K \end{Bmatrix} \\ &\langle ph'K | \frac{16\pi^2}{(2\pi)^3} \int dq q^2 V_t(q) \sqrt{6} \sum_{l_1 l_2} i^{l_1} (-i)^{l_2} j_{l_1}(qr_1) j_{l_2}(qr_2) \hat{l}_1 \hat{l}_2 (-1)^{l_1} \hat{2} \\ &\sum_L \hat{L} \begin{Bmatrix} l_1 & l_2 & 2 \\ 1 & 1 & L \end{Bmatrix} \begin{pmatrix} l_1 & l_2 & 2 \\ 0 & 0 & 0 \end{pmatrix} (-1)^{1+L} \\ &\left[[Y_{l_1}(\hat{r}_1) \otimes \sigma(1)]^L \otimes [Y_{l_2}(\hat{r}_2) \otimes \sigma(2)]^L \right]^0_0 | hp'K \rangle = \\ &= \sum_K (-1)^{K+j_h+j_{p'}} \hat{K} \begin{Bmatrix} j_p & j_h & J \\ j_{p'} & j_{h'} & K \end{Bmatrix} \frac{16\pi^2}{(2\pi)^3} \\ &\int dq q^2 V_t(q) \sqrt{6} \sum_{l_1 l_2} i^{l_1} (-i)^{l_2} \hat{l}_1 \hat{l}_2 (-1)^{l_1} \hat{2} \\ &\int dr_1 r_1^2 R^*_p(r_1) j_{l_1}(qr_1) R_h(r_1) \int dr_2 r_2^2 R^*_{h'}(r_2) j_{l_2}(qr_2) R_{p'}(r_2) \\ &\sum_L \hat{L} (-1)^{L+1} \begin{Bmatrix} l_1 & l_2 & 2 \\ 1 & 1 & L \end{Bmatrix} \begin{pmatrix} l_1 & l_2 & 2 \\ 0 & 0 & 0 \end{pmatrix} \\ &\langle j_p j_{h'} K || [[Y_{l_1}(\hat{r}_1) \otimes \sigma(1)]^L \otimes [Y_{l_2}(\hat{r}_2) \otimes \sigma(2)]^L]^0 || j_h j_{p'} K \rangle \end{aligned} \tag{D.50}$$

The angular momentum part of the previous expression is:

$$\begin{aligned}
&\langle j_p j_{h'} K||[[Y_{l_1}(\hat{r}_1)\otimes\sigma(1)]^L\otimes[Y_{l_2}(\hat{r}_2)\otimes\sigma(2)]^L]^0||j_h j_{p'} K\rangle = \\
&= (-1)^{j_{h'}+j_h+K}\frac{(-1)^L\hat{K}}{\hat{L}}\left\{\begin{array}{ccc} j_p & j_{h'} & K \\ j_{p'} & j_h & L\end{array}\right\} \\
&\langle j_p||[Y_{l_1}(\hat{r}_1)\otimes\sigma(1)]^L||j_h\rangle\langle j_{h'}||[Y_{l_2}(\hat{r}_2)\otimes\sigma(2)]^L||j_{p'}\rangle
\end{aligned} \tag{D.51}$$

and because

$$\begin{aligned}
&\langle j_p||[Y_{l_1}(\hat{r}_1)\otimes\sigma(1)]^L||j_h\rangle = \\
&= \hat{j}_p\hat{j}_h\hat{L}\left\{\begin{array}{ccc} l_p & \frac{1}{2} & j_p \\ l_h & \frac{1}{2} & j_h \\ l_1 & 1 & L\end{array}\right\}\langle l_p||Y_{l_1}(\hat{r}_1)||j_h\rangle\langle\frac{1}{2}||\sigma||\frac{1}{2}\rangle = \\
&= (-1)^{l_p}\sqrt{\frac{6}{4\pi}}\hat{j}_p\hat{j}_h\hat{l}_p\hat{l}_h\hat{l}_1\hat{L}\left\{\begin{array}{ccc} l_p & \frac{1}{2} & j_p \\ l_h & \frac{1}{2} & j_h \\ l_1 & 1 & L\end{array}\right\}\left(\begin{array}{ccc} l_p & l_1 & l_h \\ 0 & 0 & 0\end{array}\right)
\end{aligned} \tag{D.52}$$

we can rewrite Eq. (D.50) as

$$\begin{aligned}
v^{JdirV_5}_{5,php'h'} = & \sum_K(-1)^{K+j_h+j_{p'}}\hat{K}\left\{\begin{array}{ccc} j_p & j_h & J \\ j_{p'} & j_{h'} & K\end{array}\right\}\frac{16\pi^2}{(2\pi)^3}\int dqq^2V_t(q) \\
& \sqrt{6}\sum_{l_1l_2}i^{l_1}(-i)^{l_2}\hat{l}_1\hat{l}_2(-1)^{l_1}\hat{2}\int dr_1r_1^2R^*_p(r_1)j_{l_1}(qr_1)R_h(r_1) \\
& \int dr_2r_2^2R^*_{h'}(r_2)j_{l_2}(qr_2)R_{p'}(r_2) \\
& \sum_L\hat{L}(-1)^{L+1}\left\{\begin{array}{ccc} l_1 & l_2 & 2 \\ 1 & 1 & L\end{array}\right\}\left(\begin{array}{ccc} l_1 & l_2 & 2 \\ 0 & 0 & 0\end{array}\right) \\
& (-1)^{j_{h'}+j_h+K}\frac{(-1)^L\hat{K}}{\hat{L}}\left\{\begin{array}{ccc} j_p & j_{h'} & K \\ j_{p'} & j_h & L\end{array}\right\} \\
& (-1)^{l_p}\sqrt{\frac{6}{4\pi}}\hat{j}_p\hat{j}_h\hat{l}_p\hat{l}_h\hat{l}_1\hat{L}\left\{\begin{array}{ccc} l_p & \frac{1}{2} & j_p \\ l_h & \frac{1}{2} & j_h \\ l_1 & 1 & L\end{array}\right\}\left(\begin{array}{ccc} l_p & l_1 & l_h \\ 0 & 0 & 0\end{array}\right) \\
& (-1)^{l_{h'}}\sqrt{\frac{6}{4\pi}}\hat{j}_{p'}\hat{j}_{h'}\hat{l}_{p'}\hat{l}_{h'}\hat{l}_2\hat{L}\left\{\begin{array}{ccc} l_{h'} & \frac{1}{2} & j_{h'} \\ l_{p'} & \frac{1}{2} & j_{p'} \\ l_2 & 1 & L\end{array}\right\}\left(\begin{array}{ccc} l_{h'} & l_2 & l_{p'} \\ 0 & 0 & 0\end{array}\right).
\end{aligned} \tag{D.53}$$

Considering the relation:

$$\sum_K\hat{K}^2\left\{\begin{array}{ccc} j_p & j_h & J \\ j_{p'} & j_{h'} & K\end{array}\right\}\left\{\begin{array}{ccc} j_p & j_{h'} & K \\ j_{p'} & j_h & L\end{array}\right\} = \frac{\delta_{LJ}}{\hat{L}^2} \tag{D.54}$$

we obtain the expression

$$
\begin{aligned}
v_{5,php'h'}^{JdirV_5} \;=\;& (-1)^{j_{p'}+j_{h'}+l_p+l_{h'}} \frac{3\sqrt{30}}{\pi^2} \hat{j}_p \hat{j}_h \hat{j}_{p'} \hat{j}_{h'} \hat{l}_p \hat{l}_h \hat{l}_{p'} \hat{l}_{h'} \\
& \sum_{l_1 l_2} i^{l_1} (-i)^{l_2} \hat{l}_1^2 \hat{l}_2^2 (-1)^{l_1} \left\{ \begin{array}{ccc} l_1 & l_2 & 2 \\ 1 & 1 & J \end{array} \right\} \left(\begin{array}{ccc} l_1 & l_2 & 2 \\ 0 & 0 & 0 \end{array} \right) \\
& \left(\begin{array}{ccc} l_p & l_1 & l_h \\ 0 & 0 & 0 \end{array} \right) \left(\begin{array}{ccc} l_{h'} & l_2 & l_{p'} \\ 0 & 0 & 0 \end{array} \right) \left\{ \begin{array}{ccc} l_p & \frac{1}{2} & j_p \\ l_h & \frac{1}{2} & j_h \\ l_1 & 1 & J \end{array} \right\} \left\{ \begin{array}{ccc} l_{h'} & \frac{1}{2} & j_{h'} \\ l_{p'} & \frac{1}{2} & j_{p'} \\ l_2 & 1 & J \end{array} \right\} \\
& \int dq q^2 V_t(q) \int dr_1 r_1^2 R_p^*(r_1) j_{l_1}(qr_1) R_h(r_1) \\
& \int dr_2 r_2^2 R_{h'}^*(r_2) j_{l_2}(qr_2) R_{p'}(r_2).
\end{aligned} \tag{D.55}
$$

The exchange term is instead given by:

$$
\begin{aligned}
v_{5,php'h'}^{JexchV_5} \;=\;& \sum_K \hat{K}^3 \left\{ \begin{array}{ccc} j_p & j_h & J \\ j_{p'} & j_{h'} & K \end{array} \right\} \langle ph'K | \frac{16\pi^2}{(2\pi)^3} \int dq q^2 V_t(q) \sqrt{6} \\
& \sum_{l_1 l_2} i^{l_1} (-i)^{l_2} j_{l_1}(qr_1) j_{l_2}(qr_2) \hat{l}_1 \hat{l}_2 (-1)^{l_1 - l_2} \hat{2} \\
& \sum_L \hat{L} \left\{ \begin{array}{ccc} l_1 & l_2 & 2 \\ 1 & 1 & L \end{array} \right\} \left(\begin{array}{ccc} l_1 & l_2 & 2 \\ 0 & 0 & 0 \end{array} \right) (-1)^{l_2+1+L} \\
& \Big[[Y_{l_1}(\hat{r}_1) \otimes \sigma(1)]^L \otimes [Y_{l_2}(\hat{r}_2) \otimes \sigma(2)]^L \Big]_0^0 |p'hK\rangle = \\
=\;& \sum_K \hat{K} \left\{ \begin{array}{ccc} j_p & j_h & J \\ j_{p'} & j_{h'} & K \end{array} \right\} \frac{16\pi^2}{(2\pi)^3} \int dq q^2 V_t(q) \sqrt{6} \sum_{l_1 l_2} i^{l_1} (-i)^{l_2} \\
& \hat{l}_1 \hat{l}_2 (-1)^{l_1} \hat{2} \int dr_1 r_1^2 R_p^*(r_1) j_{l_1}(qr_1) R_{p'}(r_1) \\
& \int dr_2 r_2^2 R_{h'}^*(r_2) j_{l_2}(qr_2) R_h(r_2) \\
& \sum_L \hat{L} (-1)^{L+1} \left\{ \begin{array}{ccc} l_1 & l_2 & 2 \\ 1 & 1 & L \end{array} \right\} \left(\begin{array}{ccc} l_1 & l_2 & 2 \\ 0 & 0 & 0 \end{array} \right) \\
& \langle j_p j_{h'} K || [[Y_{l_1}(\hat{r}_1) \otimes \sigma(1)]^L \otimes [Y_{l_2}(\hat{r}_2) \otimes \sigma(2)]^L]^0 || j_p' j_h K \rangle.
\end{aligned} \tag{D.56}
$$

The angular momentum part is

$$
\begin{aligned}
& \langle j_p j_{h'} K || [[Y_{l_1}(\hat{r}_1) \otimes \sigma(1)]^L \otimes [Y_{l_2}(\hat{r}_2) \otimes \sigma(2)]^L]^0 || j_p' j_h K \rangle = \\
& = (-1)^{j_{h'}+j_{p'}+K} \frac{(-1)^L \hat{K}}{\hat{L}} \left\{ \begin{array}{ccc} j_p & j_{h'} & K \\ j_h & j_p & L \end{array} \right\} \\
& \langle j_p || [Y_{l_1}(\hat{r}_1) \otimes \sigma(1)]^L || j_{p'} \rangle \langle j_{h'} || [Y_{l_2}(\hat{r}_2) \otimes \sigma(2)]^L || j_h \rangle
\end{aligned} \tag{D.57}
$$

where:

$$
\begin{aligned}
& \langle j_p || [Y_{l_1}(\hat{r}_1) \otimes \sigma(1)]^L || j_{p'} \rangle = \\
& = \hat{j}_p \hat{j}_{p'} \hat{L} \left\{ \begin{array}{ccc} l_p & \frac{1}{2} & j_p \\ l_{p'} & \frac{1}{2} & j_{p'} \\ l_1 & 1 & L \end{array} \right\} \langle l_p || Y_{l_1}(\hat{r}_1) || j_{p'} \rangle \langle \frac{1}{2} || \sigma || \frac{1}{2} \rangle = \\
& = (-1)^{l_p} \sqrt{\frac{6}{4\pi}} \hat{j}_p \hat{j}_{p'} \hat{l}_p \hat{l}_{p'} \hat{l}_1 \hat{L} \left\{ \begin{array}{ccc} l_p & \frac{1}{2} & j_p \\ l_{p'} & \frac{1}{2} & j_{p'} \\ l_1 & 1 & L \end{array} \right\} \left(\begin{array}{ccc} l_p & l_1 & l_{p'} \\ 0 & 0 & 0 \end{array} \right).
\end{aligned} \tag{D.58}
$$

We then obtain

$$\begin{aligned}
v_{5,php'h'}^{JexchV_5} = & \sum_K \hat{K}^2 \left\{ \begin{array}{ccc} j_p & j_h & J \\ j_{p'} & j_{h'} & K \end{array} \right\} \frac{3}{\pi^2}\sqrt{30} \\
& \sum_{l_1 l_2} i^{l_1}(-i)^{l_2}\hat{l}_1\hat{l}_2(-1)^{l_1} \sum_L (-1)^1 \left\{ \begin{array}{ccc} l_1 & l_2 & 2 \\ 1 & 1 & L \end{array} \right\} \left(\begin{array}{ccc} l_1 & l_2 & 2 \\ 0 & 0 & 0 \end{array} \right) \\
& \left\{ \begin{array}{ccc} j_p & j_{h'} & K \\ j_h & j_{p'} & L \end{array} \right\} (-1)^{j_{h'}+j_{p'}+K} \hat{j}_p\hat{j}_{p'}\hat{j}_h\hat{j}_{h'}\hat{l}_p\hat{l}_{p'}\hat{l}_h\hat{l}_{h'}\hat{l}_1\hat{l}_2\hat{L}^2 \\
& (-1)^{l_p+l_{h'}} \left\{ \begin{array}{ccc} l_p & \frac{1}{2} & j_p \\ l_{p'} & \frac{1}{2} & j_{p'} \\ l_1 & 1 & L \end{array} \right\} \left(\begin{array}{ccc} l_p & l_1 & l_{p'} \\ 0 & 0 & 0 \end{array} \right) \left\{ \begin{array}{ccc} l_{h'} & \frac{1}{2} & j_{h'} \\ l_h & \frac{1}{2} & j_h \\ l_2 & 1 & L \end{array} \right\} \left(\begin{array}{ccc} l_{h'} & l_2 & l_h \\ 0 & 0 & 0 \end{array} \right) \\
& \int dq q^2 V_t(q) \int dr_1 r_1^2 R_p^*(r_1) j_{l_1}(qr_1) R_{p'}(r_1) \int dr_2 r_2^2 R_{h'}^*(r_2) j_{l_2}(qr_2) R_h(r_2).
\end{aligned} \tag{D.59}$$

We use the relation

$$\begin{aligned}
\sum_K \hat{K}^2 \left\{ \begin{array}{ccc} j_p & j_h & J \\ j_{p'} & j_{h'} & K \end{array} \right\} \left\{ \begin{array}{ccc} j_p & j_{h'} & J \\ j_h & j_{p'} & L \end{array} \right\} (-1)^{j_{h'}+j_{p'}+K} = \\
= \left\{ \begin{array}{ccc} j_p & j_h & J \\ j_{h'} & j_{p'} & L \end{array} \right\} (-1)^{j_{h'}+j_{p'}+L+J}
\end{aligned} \tag{D.60}$$

and for $v_{5,php'h'}^{JexchV_5}$ we obtain the expression:

$$\begin{aligned}
v_{5,php'h'}^{JexchV_5} = & -\frac{3}{\pi^2}\sqrt{30}(-1)^{j_{h'}+j_{p'}+J+l_p+l_{h'}} \hat{j}_p\hat{j}_{p'}\hat{j}_h\hat{j}_{h'}\hat{l}_p\hat{l}_{p'}\hat{l}_h\hat{l}_{h'} \\
& \sum_{l_1 l_2} i^{l_1}(-i)^{l_2}\hat{l}_1^2\hat{l}_2^2(-1)^{l_1} \left(\begin{array}{ccc} l_1 & l_2 & 2 \\ 0 & 0 & 0 \end{array} \right) \left(\begin{array}{ccc} l_p & l_1 & l_{p'} \\ 0 & 0 & 0 \end{array} \right) \left(\begin{array}{ccc} l_{h'} & l_2 & l_h \\ 0 & 0 & 0 \end{array} \right) \\
& \sum_L (-1)^L \hat{L}^2 \left\{ \begin{array}{ccc} l_1 & l_2 & 2 \\ 1 & 1 & L \end{array} \right\} \left\{ \begin{array}{ccc} l_p & \frac{1}{2} & j_p \\ l_{p'} & \frac{1}{2} & j_{p'} \\ l_1 & 1 & L \end{array} \right\} \left\{ \begin{array}{ccc} l_{h'} & \frac{1}{2} & j_{h'} \\ l_h & \frac{1}{2} & j_h \\ l_2 & 1 & L \end{array} \right\} \left\{ \begin{array}{ccc} j_p & j_h & J \\ j_{h'} & j_{p'} & L \end{array} \right\} \\
& \int dq q^2 V_t(q) \int dr_1 r_1^2 R_p^*(r_1) j_{l_1}(qr_1) R_{p'}(r_1) \int dr_2 r_2^2 R_{h'}^*(r_2) j_{l_2}(qr_2) R_h(r_2).
\end{aligned} \tag{D.61}$$

D 5 Charge changing matrix elements

In a charge changing process the terms without isospin contribution are equal to zero. The others are the same as in the charge conserving case but the multiplicative constants are different. In this section we want to evaluate them. For the direct terms we have to calculate:

$$\begin{aligned}
\langle \tau_p \tau_{h'} | \tau(1) \cdot \tau(2) | \tau_h \tau_{p'} \rangle = \sum_k (-1)^k \langle \tau_p \tau_{h'} | \tau_k \tau_{-k} | \tau_h \tau_{p'} \rangle = \\
= \sum_k (-1)^k \langle \tau_p | \tau_k | \tau_h \rangle \langle \tau_{h'} | \tau_{-k} | \tau_{p'} \rangle.
\end{aligned} \tag{D.62}$$

Using the Wigner-Eckart theorem we can rewrite the previous expression as:

$$\begin{aligned}
\langle \tau_p \tau_{h'} | \tau(1) \cdot \tau(2) | \tau_h \tau_{p'} \rangle = \sum_k (-1)^{\tau_p - \tau_p} \left(\begin{array}{ccc} \tau_p & 1 & \tau_h \\ -k_p & k & k_h \end{array} \right) \langle \tau_p || \tau_k || \tau_h \rangle \\
(-1)^{\tau_{h'} - k_{h'}} \left(\begin{array}{ccc} \tau_{h'} & 1 & \tau_{p'} \\ -k_{h'} & -k & k_{p'} \end{array} \right) \langle \tau_{h'} || \tau_{-k} || \tau_{p'} \rangle
\end{aligned} \tag{D.63}$$

If we consider processes where a neutron is transformed in a proton then $k = 1$, instead if a proton is transformed in a neutron we have $k = -1$. In both cases, expression (D.63) becomes:

$$\begin{aligned} &\langle \tau_p \tau_{h'} | \tau(1) \cdot \tau(2) | \tau_h \tau_{p'} \rangle = \\ (-1)^{\frac{1}{2}-\frac{1}{2}} \begin{pmatrix} \frac{1}{2} & 1 & \frac{1}{2} \\ -\frac{1}{2} & 1 & -\frac{1}{2} \end{pmatrix} (-1)^{\frac{1}{2}-\frac{1}{2}} \begin{pmatrix} \frac{1}{2} & 1 & \frac{1}{2} \\ \frac{1}{2} & -1 & \frac{1}{2} \end{pmatrix} &\langle \frac{1}{2} || \tau || \frac{1}{2} \rangle \langle \frac{1}{2} || \tau || \frac{1}{2} \rangle = \\ &= (-\frac{1}{\sqrt{3}})(-\frac{1}{\sqrt{3}}) 6 = 2. \end{aligned} \tag{D.64}$$

In the calculation of the exchange part we follow what we have done for the direct term:

$$\langle \tau_p \tau_{h'} | \tau(1) \cdot \tau(2) | \tau_{p'} \tau_h \rangle = \sum_k (-1)^k \langle \tau_p | \tau_k | \tau_{p'} \rangle \langle \tau_{h'} | \tau_{-k} | \tau_h \rangle . \tag{D.65}$$

Applying the Wigner-Eckart theorem and considering that in processes where a neutron is transformed in a proton all the particles are protons and all the holes are neutrons and on the contrary, when we consider processes where a proton is transformed in a neutron all the particles are neutrons and all the holes are protons, k is zero and we have to calculate:

$$\begin{aligned} \langle \tau_p \tau_{h'} | \tau(1) \cdot \tau(2) | \tau_{p'} \tau_h \rangle = (-1)^{\frac{1}{2}-\frac{1}{2}} &\begin{pmatrix} \frac{1}{2} & 1 & \frac{1}{2} \\ -\frac{1}{2} & 0 & \frac{1}{2} \end{pmatrix} \langle \frac{1}{2} || \tau || \frac{1}{2} \rangle \\ (-1)^{\frac{1}{2}+\frac{1}{2}} &\begin{pmatrix} \frac{1}{2} & 1 & \frac{1}{2} \\ \frac{1}{2} & 0 & -\frac{1}{2} \end{pmatrix} \langle \frac{1}{2} || \tau || \frac{1}{2} \rangle \\ &= (\frac{1}{\sqrt{6}})(-1)(\frac{1}{\sqrt{6}})(6) = -1. \end{aligned} \tag{D.66}$$

Appendix E

Electron Scattering formulas

In our approach the electron wave functions are plane wave solutions of the Dirac equation. In the process we want to describe, the electron is scattered through an angle θ from an initial state $k \equiv (\epsilon, \boldsymbol{k})$ to the final state $k' \equiv (\epsilon'\ ,\ \boldsymbol{k'}\ )$. In this process, a single virtual photon with four momentum $q_\mu \equiv (\omega, \boldsymbol{q}) = k - k'$ is exchanged with the nuclear target. The nucleus makes a transition from an initial state $|\Psi_0\rangle$ with four momentum P to a final state $|\Psi_f\rangle$ with $P' = P - q_\mu$. We consider that electron energies are large enough so that all terms depending upon the electron rest mass are neglected. If both the incident electron beam and the target nucleus are unpolarized and only the scattered electron is observed (inclusive experiment), the PWBA differential cross section in the laboratory frame is given by [107], [108]:

$$\frac{d\sigma}{d\Omega} = \sigma_M[v_L R_L(\boldsymbol{q}, \omega) + v_T R_T(\boldsymbol{q}, \omega)] \tag{E.1}$$

where we indicate with σ_M the Mott cross section:

$$\sigma_M = \left[\frac{\alpha cos(\frac{\theta}{2})}{2\epsilon sin^2(\frac{\theta}{2})}\right]^2 \tag{E.2}$$

The cross section is decomposed into longitudinal (Coulomb) R_L and transverse (electric and magnetic) R_T hadronic terms, multiplied by corresponding leptonic factors v that depend only on kinematic variables:

$$v_L = (\frac{q_\mu^2}{\boldsymbol{q}^2})^2 \tag{E.3}$$

$$v_T = tan^2\frac{\theta}{2} - \frac{1}{2}\frac{q_\mu^2}{\boldsymbol{q}^2} \tag{E.4}$$

The functions R_L and R_T represent longitudinal and transverse dynamic structure functions, respectively, or response functions that contain all the information on the distribution of the nuclear electromagnetic current density. Eq. (E.1) describes the inclusive inelastic electron scattering differential cross section in the general situation where the responses depend on both $q \equiv |\boldsymbol{q}|$ and ω. In case of inelastic scattering to discrete nuclear level, the energy transfer ω can assume only specific values and equals the nuclear excitation energy $E_f - E_0$ between the final and initial eigenstates. Electron scattering experiments in this region consist in selecting the excited state with the energy transfer and changing the momentum transfer. Because of the similarity with elastic scattering processes it is common practice to follow the elastic scattering nomenclature and to speak about form factors, instead of response functions. The response functions can be written in terms of longitudinal $F_L(q)$ and transverse electric $F_T^E(q)$ and magnetic $F_T^M(q)$ form factors as follows:

$$R_L(q, \omega) = |F_L(q)|^2 \delta(E_f - E_0 - \omega) \tag{E.5}$$

$$\begin{aligned} R_T(q, \omega) &= |F_T(q)|^2 \delta(E_f - E_0 - \omega) = \\ &= [|F_T^E(q)|^2 + |F_T^M(q)|^2]\delta(E_f - E_0 - \omega) \end{aligned} \tag{E.6}$$

where the longitudinal form factor and the transverse electric and magnetic form factor are simple Fourier Bessel transforms of the nuclear charge and current densities:

$$\rho(\boldsymbol{r}) = \sum_{k=1}^{A} \frac{1+\tau_k^3}{2}\delta(\boldsymbol{r}-\boldsymbol{r}_k) \tag{E.7}$$

$$\boldsymbol{J}(\boldsymbol{r}) = [\boldsymbol{J}^C(\boldsymbol{r}) + \boldsymbol{J}^M(\boldsymbol{r})]. \tag{E.8}$$

Here:

$$\boldsymbol{J}^C(\boldsymbol{r}) = \sum_{k=1}^{A} \frac{-i}{2M_k}\frac{1+\tau_k^3}{2}[\delta(\boldsymbol{r}-\boldsymbol{r}_k)\nabla_k + \nabla_k\delta(\boldsymbol{r}-\boldsymbol{r}_k)] \tag{E.9}$$

and:

$$\boldsymbol{J}^M(\boldsymbol{r}) = \sum_{k=1}^{A} \frac{1}{2M_k}(\mu^P\frac{1+\tau_k^3}{2} + \mu^N\frac{1-\tau_k^3}{2})\nabla_k \times \delta(\boldsymbol{r}-\boldsymbol{r}_k)\boldsymbol{\sigma}_k \tag{E.10}$$

where M_k indicates the rest mass of $k-th$ nucleon, μ^P and μ^N the anomalous magnetic moment of the proton and neutron respectively, $\boldsymbol{\sigma}_k$ is the Pauli spin matrix of the k-th nucleon and $\tau_k^3 = 1(-1)$ for protons (neutrons). Considering the nuclear transition between states with good initial $|\Psi_0\rangle \rightarrow |J_0M_0,\Pi_0\rangle$ and final $|\Psi_f\rangle \rightarrow |J_fM_f,\Pi_f\rangle$ angular momentum the form factors may be written as:

$$|F_L(q)|^2 = \frac{4\pi}{2J_0+1}\sum_{\lambda=0}^{\infty}|\langle J_f||M_\lambda(q)||J_0\rangle|^2 \tag{E.11}$$

$$|F_T(q)|^2 = \frac{4\pi}{2J_0+1}$$
$$\sum_{\lambda=1}^{\infty}[|\langle J_f||T_\lambda^E(q)||J_0\rangle|^2 + |\langle J_f||T_\lambda^M(q)||J_0\rangle|^2] \tag{E.12}$$

where $M_\lambda(q)$, $T_\lambda^E(q)$ and $T_\lambda^M(q)$ are the Coulomb, electric and magnetic operators that have the following expressions:

$$M_{\lambda\nu}(q) = \int d^3r j_\lambda(qr)Y_{\lambda\nu}(\hat{\boldsymbol{r}})\rho(\boldsymbol{r}) \tag{E.13}$$

$$T_{\lambda\nu}^E(q) = \frac{1}{q}\int d^3r\{\nabla \times [j_\lambda(qr)\boldsymbol{Y}_{\lambda\lambda}^{\nu}(\hat{\boldsymbol{r}})]\}\cdot\boldsymbol{J}(\boldsymbol{r}) \tag{E.14}$$

$$T_{\lambda\nu}^M(q) = \int d^3r j_\lambda(qr)\boldsymbol{Y}_{\lambda\lambda}^{\nu}(\hat{\boldsymbol{r}})\cdot\boldsymbol{J}(\boldsymbol{r}). \tag{E.15}$$

Here we have used the symbol $\boldsymbol{Y}_{LJ}^M$ to indicate the vector spherical harmonics [48]. We restrict our study for doubly closed shell nuclei, i.e. spin zero nuclei, with initial state with $J_0 = 0$ and final state with $J_f = J$. Then as a result of selection rules, the sums of Eqs. (E.11) and (E.12) will include only the single multipole term $\lambda = J$. Eqs. (E.11) and (E.12) may be rewritten as:

$$|F_L(q)|^2 = \frac{4\pi}{Z^2}|\langle||M_J(q)||0\rangle|^2 \tag{E.16}$$

$$|F_T(q)|^2 = \frac{4\pi}{Z^2}\left[|\langle J||T_J^E(q)||0\rangle|^2 + |\langle J||T_J^M(q)||0\rangle|^2\right] \tag{E.17}$$

The explicit form of the electro-magnetic reduced matrix element is the following:

$$M_J = G_E^p(q^2)\delta_{t_p,t_h}\gamma_{ph}^J I_J^{[ph]}(q) \tag{E.18}$$

where we have indicated by γ:

$$\gamma^{\lambda}_{\alpha\beta} = \langle l_\alpha \frac{1}{2} j_\alpha || Y_\lambda(\hat{\boldsymbol{r}}) || l_\beta \frac{1}{2} j_\beta \rangle =$$

$$= \frac{1}{\sqrt{4\pi}} (-1)^{j_\beta+\lambda-\frac{1}{2}} \xi(l_\alpha + l_\beta + \lambda) \hat{j}_\alpha \hat{j}_\beta \hat{\lambda} \begin{pmatrix} j_\alpha & j_\beta & \lambda \\ \frac{1}{2} & -\frac{1}{2} & 0 \end{pmatrix} \tag{E.19}$$

with $\xi(l_\alpha + l_\beta + \lambda) = 1$ if $l_\alpha + l_\beta + \lambda$ is even and $\xi(l_\alpha + l_\beta + \lambda) = 0$ otherwise. In (E.18) we have indicatet by $G^{\alpha}_{E}(q^2)$ the electric form factor of the nucleon in the s.p. state α and we have defined the integral:

$$I^{[\alpha\beta]}_{J}(q) = \int dr_1 r_1^2 j_J(qr_1) R^*_\alpha(r_1) R_\beta(r_1). \tag{E.20}$$

The transverse electric magnetization current matrix elements has instead the following form:

$$T^{E}_{J,M} = -q \frac{G^{p}_{M}(q^2)}{2M_p} \delta_{t_p,t_h} \gamma^{J}_{ph} \frac{\chi_p - \chi_h}{\sqrt{J(J+1)}} I^{[ph]}_{J}(q). \tag{E.21}$$

In the above equation we have indicated with $G^{\alpha}_{M}(q^2)$ the magnetic form factor [109] of the nucleon in the s.p. state α and with χ_α:

$$\chi_\alpha = (l_\alpha - j_\alpha)(2j_\alpha + 1). \tag{E.22}$$

For the transverse electric convection current matrix element we have:

$$T^{E}_{J,C} = \frac{G^{p}_{E}(q^2)}{2M_p} \delta_{t_p,t_h} \frac{\gamma^{J}_{ph}}{\hat{J}^2} \Bigg[\chi_{ph} \left(\frac{\sqrt{J}}{\sqrt{J+1}} I^{[\frac{1}{r}ph]}_{J+1}(q) - \frac{\sqrt{J+1}}{\sqrt{J}} I^{[\frac{1}{r}ph]}_{J-1}(q) \right) + \sqrt{J(J+1)} \left\{ I^{[ph'-p'h]}_{J+1}(q) \right\} \Bigg] \tag{E.23}$$

where we have indicated by $G^{\alpha}_{E}(q^2)$ the electric form factor of Höhler et al. [109]. In the above equation we have indicated:

$$\chi_{\alpha\beta} = (\chi_\alpha - \chi_\beta)(\chi_\alpha + \chi_\beta + 1) \tag{E.24}$$

and the integrals are defined as follow:

$$I^{[\frac{1}{r}\alpha\beta]}_{J_s}(q) = \int dr_1 r_1^2 j_{J_s}(qr_1) \frac{R^*_\alpha(r_1) R_\beta(r_1)}{r_1} \tag{E.25}$$

$$I^{[\alpha\beta'-\alpha'\beta]}_{J_s}(q) = \int dr_1 r_1^2 j_{J_s}(qr_1) \left[R^*_\alpha(r_1) \frac{dR_\beta(r_1)}{dr_1} - \frac{dR^*_\alpha(r_1)}{dr_1} R_\beta(r_1) \right]. \tag{E.26}$$

Again, since the transverse magnetic current has both magnetization and convection currents contributions, one should distinguish between them. The magnetic magnetization current matrix element is:

$$T^{M}_{J,M} = -iq \frac{G^{p}_{M}(q^2)}{2M_p} \delta_{t_p,t_h} \eta^{J}_{ph} \frac{1}{\hat{J}^2} \sum_{s=\pm1} s \sqrt{\frac{J+\delta_{s,-1}}{J+\delta_{s,1}}} (\chi_p + \chi_h + sJ + \delta_{s,1}) I^{[ph]}_{J_s}(q). \tag{E.27}$$

In the previous equation we have defined:

$$\eta^{\lambda}_{\alpha\beta} = \frac{1}{\sqrt{4\pi}} (-1)^{j_\beta+\lambda-\frac{1}{2}} \xi(l_\alpha + l_\beta + \lambda + 1) \hat{j_\alpha} \hat{j_\beta} \hat{\lambda} \begin{pmatrix} j_\alpha & j_\beta & \lambda \\ \frac{1}{2} & -\frac{1}{2} & 0 \end{pmatrix} \tag{E.28}$$

For the magnetic convention current matrix element we have:

$$T^{M}_{J,C} = -(i) \frac{G^{P}_{E}(q^2)}{2M_p} \delta_{t_p,t_h} \eta^{J}_{ph} \left[\frac{(\chi_p + \chi_h)(\chi_p + \chi_h + 1) - J(J+1)}{\sqrt{J(J+1)}} \right]. \tag{E.29}$$

Appendix F

Sturm-Bessel functions

The SB function basis is related to the regular solution of the equation:

$$\left[\frac{d^2}{dr^2} + k^2 - \frac{l(l+1)}{r^2}\right] f_{ln}(r) = \overline{U}_{ln}(r) f_{ln}(r), \tag{F.1}$$

where $k^2 = \frac{2\mu E}{\hbar^2}$,

$$\overline{U}_{ln}(r) = \begin{cases} \frac{2\mu}{\hbar^2}\left(\overline{V}_{ln} + i\overline{W}_{ln}\right) & \text{if } r \leq a \\ 0 & \text{if } r > a \end{cases},$$

and $\overline{V}_{ln}$ and $\overline{W}_{ln}$ are real constants determined by the boundary condition on f_{ln} at $r = a$; E is the center of mass energy in MeV of a particle with mass μ, and l refers to orbital angular momentum and assumes only integer values. The internal solution is:

$$f_{ln}(r) = K_{ln} r j_l(K_{ln} r), \tag{F.2}$$

where j_l is the spherical Bessel function of complex argument with:

$$K_{ln}^2 = k^2 - \frac{2\mu}{\hbar^2}\left(\overline{V}_{ln} + i\overline{W}_{ln}\right). \tag{F.3}$$

The subscript n in equations (F.2) and (F.3) indicates that equation (F.1) has solutions only for a discrete set of complex potentials $\overline{U}_{ln}$ for fixed l. This set is discrete because the boundary conditions on $f_{ln}(r)$ for $r = a$ are:

$$\left[\frac{1}{f_{ln}(r)}\frac{df_{ln}(r)}{dr}\right]_{r=a} = \left[\frac{1}{H_l^+(kr)}\frac{dH_l^+(kr)}{dr}\right]_{r=a} \tag{F.4}$$

where $H_l^+(kr)$ is a Hankel (or Coulomb) function. Eq. (F.4) is a complex transcendental equation with roots K_{ln}. At the matching point $r = a$, defining $Z = Ka$, the boundary condition of Eq. (F.4) can be written as:

$$Z\left[\frac{j_{l-1}(Z)}{j_l(Z)}\right] - (l + z_0) = 0 \tag{F.5}$$

where:

$$z_0 = \frac{a}{H_l^+(kr)}\frac{dH_l^+(kr)}{dr}\bigg|_{r=a} = x_0 + iy_0 \tag{F.6}$$

The roots $Z_{ln} = A_{ln} + iB_{ln}$ [110] are found by Newton's iteration method in the complex plane, using as starting values Z_{ln}. For large values of n and even l, A_{ln} is close to a half-integral multiple of π, while for odd l, A_{ln} lies close to an integral multiple of π. As n decreases, a bend in the trajectory of points (A_{ln}, B_{ln}) occurs (close to $A_{ln} \approx 2\pi$). This behaviour can be understood by examining the behaviour of the first part of equation (F.5). For large values of Z the asymptotic form of the Bessel functions can be used, and we find two branches for the solutions, denoted as $(+)$ and $(-)$. They lie close to the points a^+_{ln} and a^-_{ln} given by:

$$\begin{aligned} a^+_{ln} &= (2n+l-1)\frac{\pi}{2} \\ a^-_{ln} &= (2n+l)\frac{\pi}{2} \end{aligned} \tag{F.7}$$

For the minus branch the asymptotic solutions are:

$$A^-_{ln} = a^-_{ln} + \frac{y_0^2}{(a^-_{ln})^3} + \frac{l(l+1)}{2a^-_{ln}} \tag{F.8}$$

$$B^-_{ln} = -\frac{y_0}{a^-_{ln}}. \tag{F.9}$$

For the plus branch these solutions are:

$$\begin{aligned} A^+_{ln} &= a^+_{ln}(1 - \frac{1}{y_0^2}) \\ B^+_{ln} &= -\frac{a^+_{ln}}{y_0}. \end{aligned} \tag{F.10}$$

The numerical procedure consists in starting the iterative solutions at large values of n on the minus branch. The starting values Z_{ln} are taken from equations (F.8) and (F.9). The value of n is decreased successively by one unit, the previously found values of Z_{ln} serving to construct the guess for the next value of n. This procedure is continued until we arrive near the bend of the curve, where the plus branch of the solution is reached. The Sturm Bessel function basis ϕ^n_l, $n = 1, 2, ...$, is defined by:

$$\phi^n_l(r) = \begin{cases} N^n_l K_{ln} r j_l(K_{ln} r) & \text{if } r \leq a \\ N'_{ln} H^+_l(kr) & \text{if } r > a. \end{cases}$$

The basis is orthonormal, with the normalization constants N_{ln} chosen such that:

$$(\overline{V}_{ln} + i\overline{W}_{ln}) \int_0^a \phi^n_l(r)\phi^m_l(r)dr = \delta_{nm} \tag{F.11}$$

which follows from the boundary condition of f_{ln}. The functions Φ^l_n used in the expansion of the channel functions are linked to those described in this section by the following relation:

$$\Phi^l_\mu(r) = \frac{\phi^l_n(r)}{r}. \tag{F.12}$$

Appendix G

RPA equations with an expansion on the sturmian basis

We want to derive the first equation for the coefficients of the expansion of the channel functions [25]. First we calculate the following expression:

$$(h_0 - \epsilon_h - \omega) f_{[p]h}(r). \tag{G.1}$$

If $\epsilon_h + \omega > 0$ we expand $f_{[p]h}$ on the Sturm-Bessel basis and we obtain:

$$\begin{aligned}
(h_0 - \epsilon_h - \omega)\Big[R_{p_0}(r)\delta_{pp_0}\delta_{hh_0} + \sum_\mu c^{+\mu}_{[p]h}\widetilde{\Phi}^{+\mu}_p(r)\Big] \quad &= \\
= (h_0 - \epsilon_h - \omega)\Big[R_{p_0}(r)\delta_{pp_0}\delta_{hh_0} + \sum_\mu c^{+\mu}_{[p]h}\Phi^{+\mu}_p(r) \quad &+ \\
-\sum_\mu c^{+\mu}_{[p]h} \sum_{\substack{\epsilon_i < \epsilon_F \\ i = p}} R_i(r)\int dr' r'^2 R_i(r')\Phi^{+\mu}_p(r')\Big]. &
\end{aligned} \tag{G.2}$$

The first term is zero, so we can write (G.1) as:

$$\begin{aligned}
\sum_\mu c^{+\mu}_{[p]h}\left[h_0 - (\epsilon_h + \omega)\right]\Phi^{+\mu}_p(r) \quad + \\
-\sum_\mu c^{+\mu}_{[p]h} \sum_{\substack{\epsilon_i < \epsilon_F \\ i = p}} (h_0 - \epsilon_h - \omega)R_i(r)\int dr' r'^2 R_i(r')\Phi^{+\mu}_p(r') = \\
= -\sum_\mu c^{+\mu}_{[p]h}\frac{\hbar^2}{2m}\overline{U}^\mu_p(r)\Phi^{+\mu}_p(r) + \sum_\mu c^{+\mu}_{[p]h}V_{WS}(r)\Phi^{+\mu}_p(r) + \\
-\sum_\mu c^{+\mu}_{[p]h} \sum_{\substack{\epsilon_i < \epsilon_F \\ i = p}} (\epsilon_i - \epsilon_h - \omega)R_i(r)\int dr' r'^2 R_i(r')\Phi^{+\mu}_p(r')
\end{aligned}$$

where we have used the definition of radial part of wave function:

$$h_0 R_p(r) = \epsilon_p R_p(r) \tag{G.3}$$

and the definition of Sturm-Bessel functions:

$$(h_0 - V_{WS}(r) - \epsilon_p)\Phi^\mu_p(r) = -\frac{\hbar^2}{2m}\overline{U}(r)\Phi^\mu_p(r). \tag{G.4}$$

Multiplying the previous expression by $r^2\Phi_p^{+\nu}(r)$ and integrating on r we obtain:

$$
\begin{aligned}
-\sum_\mu c^{+\mu}_{[p]h}(\overline{V}+i\overline{W})\int_0^{r_a} drr^2\Phi_p^{+\nu}(r)\Phi_p^{+\mu}(r) + \\
+\sum_\mu c^{+\mu}_{[p]h}\int drr^2\Phi_p^{+\nu}(r)V_{WS}(r)\Phi_p^{+\mu}(r) + \\
-\sum_\mu c^{+\mu}_{[p]h}\int drr^2\Phi_p^{+\nu}(r)\sum_{\substack{\epsilon_i<\epsilon_F\\ i=p}}(\epsilon_i-\epsilon_h-\omega)R_i(r)\int dr'r'^2R_i(r')\Phi_p^{+\mu}(r').
\end{aligned}
$$

The extremes of the integration are, where not indicated, 0 and ∞. Remembering the orthogonality relation between sturmian functions the first term can be written as:

$$
\begin{aligned}
-\sum_\mu\Big[c^{+\mu}_{[p]h}\delta_{\mu\nu}-c^{\mu+}_{[p]h}\int drr^2V_{WS}(r)\Phi_p^{\nu+}(r)\Phi_p^{\mu+}(r) \\
-c^{\mu+}_{[p]h}\sum_{\substack{\epsilon_i<\epsilon_F\\ i=p}}(\epsilon_i-\epsilon_h-\omega)\int dr'r'^2R_i(r)\Phi_p^{+\nu}(r)\int dr'r'^2R_i(r')\Phi_p^{+\mu}(r')\Big].
\end{aligned}
\tag{G.5}
$$

Integrating also the other terms of the equation we obtain:

$$
\begin{aligned}
&-\sum_{p'h'}\int drr^2\int dr'r'^2R^*_{h'}(r')R_h(r)R_{p_0}(r')\delta_{p'p_0}\delta_{h'h_0}\Phi_p^{+\nu}(r)V(r,r')\langle v^{dir}_{php'h'}\rangle + \\
&+\sum_{p'h'}\int drr^2\int dr'r'^2R^*_{h'}(r')R_h(r')R_{p_0}(r)\delta_{p'p_0}\delta_{h'h_0}\Phi_p^{+\nu}(r)V(r,r')\langle v^{exch}_{php'h'}\rangle + \\
&-\sum_{p'h'}\sum_\mu c^{+\mu}_{[p']h'}\int drr^2\int dr'r'^2R^*_{h'}(r')R_h(r)\widetilde{\Phi}_{p'}^{+\mu}(r')\Phi_p^{+\nu}(r)V(r,r')\langle v^{dir}_{php'h'}\rangle + \\
&+\sum_{p'h'}\sum_\mu c^{+\mu}_{[p']h'}\int drr^2\int dr'r'^2R^*_{h'}(r')R_h(r')\widetilde{\Phi}_{p'}^{+\mu}(r)\Phi_p^{+\nu}(r)V(r,r')\langle v^{exch}_{php'h'}\rangle + \\
&-\sum_{p'h'}\sum_\mu c^{-\mu*}_{[p']h'}\int drr^2\int dr'r'^2\widetilde{\Phi}_{p'}^{-\mu*}(r')R_h(r)R_{h'}(r')\Phi_p^{+\nu}(r)V(r,r')\langle u^{dir}_{php'h'}\rangle + \\
&+\sum_{p'h'}\sum_\mu c^{-\mu*}_{[p']h'}\int drr^2\int dr'r'^2\widetilde{\Phi}_{p'}^{-\mu*}(r')R_h(r')R_{h'}(r)\Phi_p^{+\nu}(r)V(r,r')\langle u^{exch}_{php'h'}\rangle .
\end{aligned}
\tag{G.6}
$$

Doing the same for the BST terms we obtain:

$$
\begin{aligned}
&\sum_{p'h'}\sum_{\epsilon_p<\epsilon_F}\int drr^2\Phi_p^{+\nu}(r)\int dr_1r_1^2\int dr_2r_2^2R_p(r)R^*_p(r_1) \\
&\Big\{R^*_{h'}(r_2)\Big[R_h(r_1)R_{p_0}(r_2)\delta_{p'p_0}\delta_{h'h_0}v^{dir}_{php'h'}(r_1,r_2)-R_h(r_2)R_{p_0}\delta_{p'p_0}\delta_{h'h_0}(r_1)v^{exch}_{php'h'}(r_1,r_2)\Big] + \\
&R^*_{h'}(r_2)\Big[R_h(r_1)\sum_\mu c^{+\mu}_{[p']h'}\widetilde{\Phi}_{p'}^{+\mu}(r_2)v^{dir}_{php'h'}(r_1,r_2)-R_h(r_2)\sum_\mu c^{+\mu}_{[p']h'}\widetilde{\Phi}_{p'}^{+\mu}(r_1)v^{exch}_{php'h'}(r_1,r_2)\Big] + \\
&+\sum_\mu c^{-\mu*}_{[p']h'}\{\widetilde{\Phi}_{p'}^{-\mu*}(r_2)\Big[R_h(r_1)R_{h'}(r_2)u^{dir}_{php'h'}(r_1,r_2)-R_{h'}(r_1)R_h(r_2)u^{exch}_{php'h'}(r_1,r_2)\Big]\Big\}.
\end{aligned}
\tag{G.7}
$$

Remembering the definition of $\widetilde{\Phi}_p^\nu(r)$:

$$\widetilde{\Phi}_p^\mu(r) = \Phi_p^\mu(r) - \sum_{\substack{\epsilon_i < \epsilon_F \\ i=p}} R_i(r)\int dr' r'^2 R_i(r')\Phi_p^\mu(r'),$$

joining the terms of (G.6) that go from the 3-rd to the 6-th with the terms of (G.7) that go from the 3-rd to the 6-th and putting together the first two terms of (G.6) and of (G.7) we obtain:

$$\begin{aligned}
&\sum_\mu c_{[p]h}^{+\mu}\delta_{\mu\nu} + \sum_\mu c_{[p]h}^{+\mu} \sum_{\substack{\epsilon_i < \epsilon_F \\ i=p}} (\epsilon_p - \epsilon_h - \omega)\int drr^2 R_i(r)\Phi_p^{+\nu}(r)\int dr'r'^2 R_i(r')\Phi_p^{+\mu}(r') + \\
&\quad - \sum_{p'h'}\sum_\mu c_{[p']h'}^{+\mu}\int drr^2\int dr'r'^2 R_{h'}^*(r')R_h(r)\widetilde{\Phi}_{p'}^{+\mu}(r')\widetilde{\Phi}_p^{+\nu}(r)V(r,r')\langle v_{php'h'}^{dir}\rangle + \\
&\quad + \sum_{p'h'}\sum_\mu c_{[p']h'}^{+\mu}\int drr^2\int dr'r'^2 R_{h'}^*(r')R_h(r')\widetilde{\Phi}_{p'}^{+\mu}(r)\widetilde{\Phi}_p^{+\nu}(r)V(r,r')\langle v_{php'h'}^{exch}\rangle + \\
&\quad - \sum_{p'h'}\sum_\mu c_{[p']h'}^{-\mu*}\int drr^2\int dr'r'^2 \widetilde{\Phi}_{p'}^{-\mu*}(r')R_h(r)R_{h'}(r')\widetilde{\Phi}_p^{+\nu}(r)V(r,r')\langle u_{php'h'}^{dir}\rangle + \\
&\quad + \sum_{p'h'}\sum_\mu c_{[p']h'}^{-\mu*}\int drr^2\int dr'r'^2 \widetilde{\Phi}_{p'}^{-\mu*}(r')R_h(r')R_{h'}(r)\widetilde{\Phi}_p^{+\nu}(r)V(r,r')\langle u_{php'h'}^{exch}\rangle = \\
&\quad = \int drr^2\int dr'r'^2 R_{h_0}^*(r')R_h(r)R_{p_0}(r')\widetilde{\Phi}_p^{+\nu}(r)V(r,r')\langle v_{php_0h_0}^{dir}\rangle + \\
&\quad - \int drr^2\int dr'r'^2 R_{h_0}^*(r')R_h(r')R_{p_0}(r)\widetilde{\Phi}_p^{+\nu}(r)V(r,r')\langle v_{php_0h_0}^{exch}\rangle. \qquad \text{(G.8)}
\end{aligned}$$

If $\epsilon_h + \omega < 0$ then we have to expand $f_{[p]h}$ of (G.1) on the real sturmian basis. In this way we obtain:

$$\begin{aligned}
(h_0 - \epsilon_h - \omega)(R_{p_0}(r)\delta_{pp_0}\delta_{hh_0} + \sum_\mu c_{ph}^{+\mu}\widetilde{\Phi}_p^{+\mu}(r)) &= \\
= (h_0 - \epsilon_h - \omega)(R_{p_0}(r)\delta_{pp_0}\delta_{hh_0} + \sum_\mu c_{ph}^{+\mu}\Phi_p^{+\mu}(r) &+ \\
- \sum_\mu c_{ph}^{+\mu}\sum_{\substack{E_i < E_f \\ i=p}} R_i(r)\int dr'r'^2 R_i(r')\Phi_p^{+\mu}(r')) &= \\
= (\epsilon_{p_0} - \epsilon_{h_0} - \omega)R_{p_0}(r)\delta_{pp_0}\delta_{hh_0} + \sum_\mu c_{ph}^{+\mu}(h_0 - (\epsilon_h + \omega))\Phi_p^{+\mu}(r) &+ \\
- \sum_\mu c_{ph}^{+\mu}\sum_{\substack{\epsilon_i < \epsilon_F \\ i=p}} (h_0 - \epsilon_h - \omega)R_i(r)\int dr'r'^2 R_i(r')\Phi_p^{+\mu}(r'). & \qquad \text{(G.9)}
\end{aligned}$$

Also in this case the first term is zero, so we can write (G.1) as:

$$\begin{aligned}
&- \sum_\mu \alpha_p^\mu c_{ph}^{+\mu} V(r)\Phi_p^{+\mu}(r) \quad + \\
&- \sum_\mu c_{ph}^{+\mu}\sum_{\substack{\epsilon_i < \epsilon_F \\ i=p}} (\epsilon_i - \epsilon_h - \omega)R_i(r)\int dr'r'^2 R_i(r')\Phi_p^{+\mu}(r')
\end{aligned}$$

where we have used the definition of radial part of wave function:

$$h_0 R_p(r) = \epsilon_p R_p(r) \tag{G.10}$$

and the definition of Sturmian functions:

$$(h_0 - \epsilon_p)\Phi_p^{\mu}(r) = -\alpha_p^{\mu} V(r)\Phi_p^{\mu}(r).$$

Multiplying the previous expression by $r^2\Phi_p^{+\nu}(r)$ and integrating on r we obtain:

$$-\sum_{\mu} \alpha_p^{\mu} c_{ph}^{+\mu} \int dr r^2 \Phi_p^{+\nu}(r) V(r) \Phi_p^{+\mu}(r) +$$
$$-\sum_{\mu} c_{ph}^{+\mu} \int dr r^2 \Phi_p^{+\nu}(r) \sum_{\substack{\epsilon_i < \epsilon_F \\ i = p}} (\epsilon_i - \epsilon_h - \omega) R_i(r) \int dr' r'^2 R_i(r') \Phi_p^{+\mu}(r').$$

Remembering the orthogonality relation between real sturmian functions the first term can be written as:

$$-\sum_{\mu} \left[c_{ph}^{+\mu}\delta_{\mu\nu} - c_{ph}^{\mu+} \sum_{\substack{\epsilon_i < \epsilon_F \\ i = p}} (\epsilon_i - \epsilon_h - \omega) \int dr' r'^2 R_i(r) \Phi_p^{+\nu}(r) \int dr' r'^2 R_i(r') \Phi_p^{+\mu}(r') \right]. \tag{G.11}$$

Integrating also the other terms of the equation we obtain:

$$\begin{aligned}
&-\sum_{p'h'} \int dr r^2 \int dr' r'^2 R_{h'}^*(r') R_h(r) R_{p_0}(r') \delta_{p'p_0}\delta_{h'h_0} \Phi_p^{+\nu}(r) V(r,r') \langle v_{php'h'}^{dir} \rangle + \\
&+\sum_{p'h'} \int dr r^2 \int dr' r'^2 R_{h'}^*(r') R_h(r') R_{p_0}(r) \delta_{p'p_0}\delta_{h'h_0} \Phi_p^{+\nu}(r) V(r,r') \langle v_{php'h'}^{exch} \rangle + \\
&-\sum_{p'h'} \sum_{\mu} c_{p'h'}^{+\mu} \int dr r^2 \int dr' r'^2 R_{h'}^*(r') R_h(r) \widetilde{\Phi}_{p'}^{+\mu}(r') \Phi_p^{+\nu}(r) V(r,r') \langle v_{php'h'}^{dir} \rangle + \\
&+\sum_{p'h'} \sum_{\mu} c_{p'h'}^{+\mu} \int dr r^2 \int dr' r'^2 R_{h'}^*(r') R_h(r') \widetilde{\Phi}_{p'}^{+\mu}(r) \Phi_p^{+\nu}(r) V(r,r') \langle v_{php'h'}^{exch} \rangle + \\
&-\sum_{p'h'} \sum_{\mu} c_{p'h'}^{-\mu*} \int dr r^2 \int dr' r'^2 \widetilde{\Phi}_{p'}^{-\mu*}(r') R_h(r) R_{h'}(r') \Phi_p^{+\nu}(r) V(r,r') \langle u_{php'h'}^{dir} \rangle + \\
&+\sum_{p'h'} \sum_{\mu} c_{p'h'}^{-\mu*} \int dr r^2 \int dr' r'^2 \widetilde{\Phi}_{p'}^{-\mu*}(r') R_h(r') R_{h'}(r) \Phi_p^{+\nu}(r) V(r,r') \langle u_{php'h'}^{exch} \rangle.
\end{aligned} \tag{G.12}$$

Doing the same for the BST terms we obtain:

$$\begin{aligned}
&\sum_{p'h'} \sum_{\epsilon_p < \epsilon_F} \int dr r^2 \Phi_p^{+\nu}(r) \int dr_1 r_1^2 \int dr_2 r_2^2 R_p(r) R_p^*(r_1) \\
&\Big\{ R_{h'}^*(r_2) \left[R_h(r_1) R_{p_0}(r_2) \delta_{p'p_0}\delta_{h'h_0} v_{php'h'}^{dir}(r_1,r_2) - R_h(r_2) R_{p_0}\delta_{p'p_0}\delta_{h'h_0}(r_1) v_{php'h'}^{exch}(r_1,r_2) \right] + \\
&R_{h'}^*(r_2) \big[R_h(r_1) \sum_{\mu} c_{p'h'}^{+\mu} \widetilde{\Phi}_{p'}^{+\mu}(r_2) v_{php'h'}^{dir}(r_1,r_2) - R_h(r_2) \sum_{\mu} c_{p'h'}^{+\mu} \widetilde{\Phi}_{p'}^{+\mu}(r_1) v_{php'h'}^{exch}(r_1,r_2) \big] + \\
&+\sum_{\mu} c_{p'h'}^{-\mu*} \{ \widetilde{\Phi}_{p'}^{-\mu*}(r_2) \left[R_h(r_1) R_{h'}(r_2) u_{php'h'}^{dir}(r_1,r_2) - R_{h'}(r_1) R_h(r_2) u_{php'h'}^{exch}(r_1,r_2) \right] \Big\}
\end{aligned} \tag{G.13}$$

Remembering the definition of $\widetilde{\Phi}^{\nu}_{p}(r)$:

$$\widetilde{\Phi}^{\mu}_{p}(r) = \Phi^{\mu}_{p}(r) - \sum_{\substack{\epsilon_i < \epsilon_F \\ i = p}} R_i(r) \int dr' r'^2 R_i(r') \Phi^{\mu}_{p}(r')$$

joining the terms of (G.12) that go from the 3-rd to the 6-th with the terms of (G.13) that go from the 3-rd to the 6-th and joining the first two terms of (G.12) and of (G.13) we obtain:

$$\begin{aligned}
\sum_{\mu} c^{+\mu}_{ph} \delta_{\mu\nu} + \sum_{\mu} c^{+\mu}_{ph} \sum_{\substack{\epsilon_i < \epsilon_F \\ i = p}} (\epsilon_p - \epsilon_h - \omega) \int drr^2 R_i(r) \Phi^{+\nu}_{p}(r) \int dr' r'^2 R_i(r') \Phi^{+\mu}_{p}(r') + \\
- \sum_{p'h'} \sum_{\mu} c^{+\mu}_{p'h'} \int drr^2 \int dr' r'^2 R^*_{h'}(r') R_h(r) \widetilde{\Phi}^{+\mu}_{p'}(r') \widetilde{\Phi}^{+\nu}_{p}(r) V(r,r') \langle v^{dir}_{php'h'} \rangle + \\
+ \sum_{p'h'} \sum_{\mu} c^{+\mu}_{p'h'} \int drr^2 \int dr' r'^2 R^*_{h'}(r') R_h(r') \widetilde{\Phi}^{+\mu}_{p'}(r) \widetilde{\Phi}^{+\nu}_{p}(r) V(r,r') \langle v^{exch}_{php'h'} \rangle + \\
- \sum_{p'h'} \sum_{\mu} c^{-\mu *}_{p'h'} \int drr^2 \int dr' r'^2 \widetilde{\Phi}^{-\mu *}_{p'}(r') R_h(r) R_{h'}(r') \widetilde{\Phi}^{+\nu}_{p}(r) V(r,r') \langle u^{dir}_{php'h'} \rangle + \\
+ \sum_{p'h'} \sum_{\mu} c^{-\mu *}_{p'h'} \int drr^2 \int dr' r'^2 \widetilde{\Phi}^{-\mu *}_{p'}(r') R_h(r') R_{h'}(r) \widetilde{\Phi}^{+\nu}_{p}(r) V(r,r') \langle u^{exch}_{php'h'} \rangle = \\
= \int drr^2 \int dr' r'^2 R^*_{h_0}(r') R_h(r) R_{p_0}(r') \widetilde{\Phi}^{+\nu}_{p}(r) V(r,r') \langle v^{dir}_{php_0h_0} \rangle + \\
- \int drr^2 \int dr' r'^2 R^*_{h_0}(r') R_h(r') R_{p_0}(r) \widetilde{\Phi}^{+\nu}_{p}(r) V(r,r') \langle v^{exch}_{php_0h_0} \rangle . \quad \text{(G.14)}
\end{aligned}$$

In order to obtain the second RPA equation for the coefficients of the expansion of the channel functions we have to remember that the $g_{[p]h}$ channel function is always expanded on a real sturmian basis. So the procedure is analogous to the last shown.

Appendix H

Sum rules for nuclear collective excitations

The sum rules limit cross sections value on all the range of excitation energy.
They fix general rules on the cross section and depend on ground state properties only. The sum rule for photoreactions is defined as

$$S_J = \int dE \frac{1}{k^{2J-2}} \sigma_J(E). \tag{H.1}$$

For photoabsorption reaction for a nucleus that is excited from a state with angular momentum J_i and energy E_i to a final state with angular momentum J_f and energy E_f, remembering the expression of the cross section, the previous expression becomes:

$$S_J = 8\pi^3 \frac{J+1}{J} \frac{1}{[(2J+1)!!]^2} \frac{1}{2J_i+1} \sum_M \sum_{J_f M_f} \frac{E_f - E_i}{\hbar c} \left| \langle J_f M_f | Q_{JM} | J_i M_i \rangle \right|^2 . \tag{H.2}$$

with

$$Q_{JM} = \sum_{a=1}^{Z} e_a r_a^J Y_{JM}(\hat{r}_a). \tag{H.3}$$

Now we want to evaluate the sum in (H.2):

$$(E_f - E_i)| < f|Q_{JM}|i > |^2 = < i|Q^\dagger_{JM}|f > (E_f - E_i) < f|Q_{JM}|i > \tag{H.4}$$

where

$$|f >= |J_f M_f > \tag{H.5}$$

and

$$|i >= |J_i M_i > . \tag{H.6}$$

Considering the hamiltonian H such as:

$$H|i >= E_i|i > \tag{H.7}$$

and

$$H|f >= E_f|f > \tag{H.8}$$

expression (H.4) can be rewritten as:

$$
\begin{aligned}
(E_f - E_i)| < f|Q_{JM}|i > |^2 =& < i|Q^\dagger_{JM}|f > E_f < f|Q_{JM}|i > \\
& - < i|Q^\dagger_{JM}|f > E_i < f|Q_{JM}|i >= \\
\frac{1}{2}\Big\{ & < i|Q^\dagger_{JM}H|f >< f|Q_{JM}|i > - < i|HQ^\dagger_{JM}|f >< f|Q_{JM}|i > + \\
& + < i|Q^\dagger_{JM}|f >< f|HQ_{JM}|i > - < i|Q^\dagger_{JM}|f >< f|Q_{JM}H|i > \Big\} . \qquad (H.9)
\end{aligned}
$$

Inserting a completeness relation on final states (H.9) can has the following expression:

$$
\sum_{fM}(E_f - E_i)| < f|Q_{JM}|i > |^2 = \sum_M \frac{1}{2} < i|[Q^\dagger_{JM}, H]Q_{JM} + Q^\dagger_{JM}[H, Q_{JM}]|i > . \qquad (H.10)
$$

Eq. (H.10) depends only on properties of the ground state. Now we consider the hypothesis that the hamiltonian commutes with Q_{JM}. In general this does not happen. For example, an isospin dependent term in the interaction hamiltonian does not commute with Q_{JM}.

If $H = T + V$, where

$$
T = -\sum_{a=1}^{Z} \frac{\hbar^2}{2m}\nabla_a^2 + V, \qquad (H.11)
$$

Eq. (H.10) becomes:

$$
\begin{aligned}
&\sum_M \sum_f (E_f - E_i)| < f|Q_{JM}|i > |^2 = \\
= \sum_M \Big\{ -\frac{\hbar^2}{2m}\frac{1}{2} < i| & \sum_a e_a r_a^J Y^*_{JM}(\hat{r}_a) \sum_q \nabla_q^2 \sum_b r_b^J Y_{JM}(\hat{r}_b) e_b + \\
& - \sum_q \nabla_q^2 \sum_a e_a r_a^J Y^*_{JM}(\hat{r}_a) \sum_b e_b r_b^J Y_{JM}(\hat{r}_b) + \\
& + \sum_a e_a r_a^J Y^*_{JM}(\hat{r}_a) \sum_q \nabla_q^2 \sum_b r_b^J Y_{JM}(\hat{r}_b) e_b + \\
& - \sum_a e_a r_a^J Y^*_{JM}(\hat{r}_a) \sum_b e_b r_b^J Y_{JM}(\hat{r}_b) \sum_q \nabla_q^2 |i > \Big\} . \qquad (H.12)
\end{aligned}
$$

It can be seen that

$$
\begin{aligned}
\nabla_a(\phi(r_i)\mathcal{Y}_{l\mu}(\hat{r}_i)) &= \nabla_a(\phi(r_a)\mathcal{Y}_{l\mu}(\hat{r}_a))\delta_{ai} \qquad (H.13) \\
\nabla^2(r^l \mathcal{Y}_{l\mu}(\hat{r})) &= 0 \qquad (H.14) \\
\sum_a \nabla_a^2 |i > &= 0 \qquad (H.15)
\end{aligned}
$$

Because [48]:

$$
\boldsymbol{\nabla}\phi(r)\mathcal{Y}_{l\mu} = -(\frac{l+1}{2l+1})^{\frac{1}{2}}(\frac{d}{dr} - \frac{l}{r})\phi \boldsymbol{\mathcal{Y}}^{\boldsymbol{\mu}}_{\boldsymbol{l,l+1,1}} + (\frac{l}{2l+1})^{\frac{1}{2}}(\frac{d}{dr} + \frac{l+1}{r})\phi \boldsymbol{\mathcal{Y}}^{\boldsymbol{\mu}}_{\boldsymbol{l,l-1,1}} \qquad (H.16)
$$

with:

$$
\boldsymbol{\mathcal{Y}}^{\boldsymbol{M}}_{\boldsymbol{lJ1}} = \sum_{\mu\sigma} < l\mu|\sigma|JM > \mathcal{Y}_{l\mu}\boldsymbol{e}_\sigma \qquad (H.17)
$$

Eq. (H.14) becomes

$$
\boldsymbol{\nabla}(r^l \mathcal{Y}_{l\mu}) = -(\frac{l+1}{2l+1})^{\frac{1}{2}}(l-l)r^{l-1}\boldsymbol{\mathcal{Y}}^{\boldsymbol{\mu}}_{\boldsymbol{l,l+1,1}} + (\frac{l}{2l+1})^{\frac{1}{2}}(l+l+1)r^{l-1}\boldsymbol{\mathcal{Y}}^{\boldsymbol{\mu}}_{\boldsymbol{l,l-1,1}} . \qquad (H.18)
$$

Now, ([48]):

$$\boldsymbol{\nabla}\cdot(\phi\boldsymbol{\mathcal{Y}}^{\boldsymbol{\mu}}_{\boldsymbol{l},\boldsymbol{l-1},\boldsymbol{1}}) = (\frac{l}{2l+1})^{\frac{1}{2}}(\frac{d}{dr}-\frac{l-1}{r})\phi\mathcal{Y}_{l\mu}\boldsymbol{e_\sigma} \tag{H.19}$$

therefore

$$\nabla^2(r^l\mathcal{Y}_{l\mu}) = (\frac{l}{2l+1})^{\frac{1}{2}}(2l+1)(\frac{l}{2l+1})^{\frac{1}{2}}(l-1-(l-1))r^{l-2}\mathcal{Y}_{l\mu} = 0. \tag{H.20}$$

The (H.15) is right because the state is antisymmetrized.

Using (H.13), (H.14) and (H.15), Eq.(H.12) becomes:

$$\sum_{fM}(E_f-E_i)|<f|Q_{JM}|i>|^2 = \frac{\hbar^2}{2m}\frac{1}{2}\sum_M\sum_a e_a^2 <i|\boldsymbol{\nabla}_a(r_a^J\mathcal{Y}^*_{JM}(\hat{r}_a))\boldsymbol{\nabla}_a(r_a^J\mathcal{Y}_{JM}(\hat{r}_a))|i>. \tag{H.21}$$

It can be demonstrated that:

$$\sum_M(\boldsymbol{\nabla}\phi(r)\mathcal{Y}^*_{l\mu}(\hat{r})) = \frac{2l+1}{4\pi}\left[(\frac{d}{dr}\phi(r))^2+\frac{l(l+1)}{r^2}(\phi(r))^2\right] \tag{H.22}$$

so:

$$\begin{aligned}\sum_M(\boldsymbol{\nabla}r^J\mathcal{Y}^*_{JM}(\hat{r}))(\boldsymbol{\nabla}r^J\mathcal{Y}_{JM}(\hat{r})) &=\\ =\frac{2J+1}{4\pi}\left[(Jr^{J-1})^2+\frac{J(J+1)}{r^2}r^{2J}\right] &=\\ =\frac{J(2J+1)^2}{4\pi}r^{2J-2}&\end{aligned} \tag{H.23}$$

therefore:

$$\sum_{Mf}(E_f-E_i)|<f|Q_{JM}|i>|^2 = \frac{\hbar^2}{2m}\frac{J(2J+1)^2}{4\pi}\sum_a <i|r^{2J-2}|i>e_a^2. \tag{H.24}$$

Finally the sum rule can be rewritten as:

$$S_J = \frac{1}{2J_i+1}\left(\frac{1}{\hbar c}\right)\frac{(\hbar c)^2}{mc^2}\pi^2\frac{J+1}{[(2J-1)!!]^2}\sum_a <i|r_a^{2J-2}|i>e_a^2. \tag{H.25}$$

For completeness we derive (H.22):

$$\begin{aligned}&\sum_M(\boldsymbol{\nabla}\phi(r)\mathcal{Y}^*_{l\mu}(\hat{r}))(\boldsymbol{\nabla}\phi(r)\mathcal{Y}_{l\mu}(\hat{r})) =\\ =\sum_M&\left\{-(\frac{l+1}{2l+1})^{\frac{1}{2}}(\frac{d}{dr}-\frac{l}{r})\phi\boldsymbol{\mathcal{Y}}^{\boldsymbol{\mu}*}_{\boldsymbol{l},\boldsymbol{l+1},\boldsymbol{1}}+(\frac{l}{2l+1})^{\frac{1}{2}}(\frac{d}{dr}+\frac{l+1}{r})\phi\boldsymbol{\mathcal{Y}}^{\boldsymbol{\mu}*}_{\boldsymbol{l},\boldsymbol{l-1},\boldsymbol{1}}\right\}\\ &\left\{-(\frac{l+1}{2l+1})^{\frac{1}{2}}(\frac{d}{dr}-\frac{l}{r})\phi\boldsymbol{\mathcal{Y}}^{\boldsymbol{\mu}*}_{\boldsymbol{l},\boldsymbol{l+1},\boldsymbol{1}}+(\frac{l}{2l+1})^{\frac{1}{2}}(\frac{d}{dr}+\frac{l+1}{r})\phi\boldsymbol{\mathcal{Y}}^{\boldsymbol{\mu}*}_{\boldsymbol{l},\boldsymbol{l-1},\boldsymbol{1}}\right\}.\end{aligned} \tag{H.26}$$

Now the sum:

$$\begin{aligned}\sum_m\boldsymbol{\mathcal{Y}}_{\boldsymbol{j},\boldsymbol{l},\boldsymbol{1}}\boldsymbol{\mathcal{Y}}^*{}_{\boldsymbol{j},\boldsymbol{l'},\boldsymbol{1}} &= \sum_\mu(\sum_{m\nu}<l\mu1\nu|jm><l'\mu1\nu|jm>)\mathcal{Y}_{l\mu}\mathcal{Y}^*_{l'\mu} =\\ =\sum_\mu(\frac{2j+1}{\sqrt{(2l+1)(2l'+1)}}&\sum_{m\nu}<j-m|\nu|l-\mu><j-m|\nu|l'-\mu>)\mathcal{Y}_{l\mu}\mathcal{Y}^*_{l'\mu} =\\ &=\frac{2J+1}{4\pi}\delta_{ll'}.\end{aligned} \tag{H.27}$$

Using (H.27), (H.26) can be rewritten as:

$$\begin{aligned}
&\sum_M (\boldsymbol{\nabla}\phi\mathcal{Y}^*_{l\mu})(\boldsymbol{\nabla}\phi\mathcal{Y}_{l\mu}) = \\
&\frac{l+1}{2l+1}\left[\left(\frac{d}{dr}-\frac{l}{r}\right)\phi\right]^2\frac{2l+1}{4\pi}+\frac{l}{2l+1}\left[\left(\frac{d}{dr}+\frac{l+1}{r}\right)\phi\right]^2\frac{2l+1}{4\pi} = \\
&\frac{2l+1}{4\pi}\left[\left(\frac{d}{dr}\phi\right)^2+\frac{l(l+1)}{r^2}\phi^2\right].
\end{aligned} \tag{H.28}$$

Appendix I

List of Abbriviations

BST	Bound State term
CBF	Correlated Basis functions
CG	Clebsh-Gordan
CRPA	Continuum Random Phase Approximation
c.w.f.	continuum wave function
FHNC	Fermi Hypernetted Chain
HF	Hartree-Fock
HO	harmonic oscillator
IVGDR	Isovector giant dipole resonance
LMFFS	Landau-Migdal theory of finite Fermi systems
MF	mean field
NN	nucleon-nucleon
RPA	Random Phase Approximation
SB	Sturm Bessel
s.p.	single particle
WS	Woods-Saxon

Acknowledgement

I wish to express my deep thanks to my advisor Prof. Giampaolo Co' for the great opportunities he gave me during the PhD course to work and learn, for the continuous encouragement and discussions and for the autonomy he provided me in the scientific activity.

A particular thank is for my coadvisor Dr. Chiara Maieron for her help and supporting.

Many thanks to Prof. Antonio Miguel Lallena and Prof. Marta Anguiano, Department of Physics, University of Granada, Spain, for the valuable comments and discussions during the time I spent in Granada.

Many thanks to all my friends at the university: Barbara, Crisitan, Paola, Monica, Ilaria, Antonella, Adelaide, Enzo, Mariangela and to my friends outside the university: Roberta, Elisa, Anna, Ivan, Daniela, Giorgio, Roberta, Giorgio and my cousin Maria.

Finally, the most important thanks are to my parents for their support and unconditional love, to my sister Livia who is my best friend and her husband Giuseppe and especially to my great love Antonio.

Bibliography

[1] H. Kamada, et al., Phys. Rev. C 64 (2001) 044001.

[2] B. S. Pudliner, V. R. Pandharipande, J. Carlson, R. B. Wiringa, Phys. Rev. Lett. 74 (1995) 4396.

[3] B. S. Pudliner, V. R. Pandharipande, J. Carlson, S. C. Pieper, R. B. Wiringa, Phys. Rev. C 56 (1997) 1720.

[4] S. C. Pieper, R. B. Wiringa, Ann. Rev. Nucl. Part. Sc. 51 (2001) 53.

[5] S. C. Pieper, Nucl. Phys. A 751 (2005) 516.

[6] S. Gandolfi, F. Pederiva, S. Fantoni, K. E. Schmidt, Phys. Rev. C 73 (2006) 044304.

[7] K. A. Brueckner, C. A. Lewison, H. M. Mahmond, Phys. Rev. 97 (1954) 217.

[8] K. A. Brueckner, Phys. Rev. 97 (1955) 1353.

[9] J. E. Mayer, M. G. Mayer, Statistical Mechanics, Wiley, New York, 1940.

[10] J. M. J. van Leeuwen, Groeneveld, J. de Boer, Physica 25 (1959) 792.

[11] M. Gaudin, J. Gillespie, G. Ripka, Nucl. Phys. A 176 (1971) 273.

[12] S. Fantoni, S. Rosati, Nuovo Cimento A 20 (1974) 179.

[13] S. Fantoni, S. Rosati, Nuovo Cimento A 25 (1975) 593.

[14] S. Fantoni, S. Rosati, Nuov. Cim. A 43 (1978) 413.

[15] F. Arias de Saavedra, C. Bisconti, G. Co', A. Fabrocini, Phys. Rep. 450 (2007) 1.

[16] D. Pines, D. Bohm, Phys. Rev. 85 (1952) 338.

[17] D. Bohm, D. Pines, Phys. Rev. 92 (1952) 609.

[18] J. W. Clark, The many body problem, Jastrow vs Brueckner theory, R. Guardiola and J. Ros eds., Lectures Notes in Physics, 138, Berlin, 1981.

[19] A. de Florio, Sviluppo di una teoria a molticorpi per la descrizione di stati eccitati in base correlata, Master's thesis, Università di Lecce (Italy), unpublished (1998).

[20] G. F. Bertsch, S. F. Tsai, Phys. Rep. 18 (1975) 125.

[21] R. de Haro, S. Krewald, J. Speth, Nucl. Phys. A 388 (1982) 265.

[22] A. M. Saruis, Phys. Rep. 235 (1993) 57.

[23] G. Co', K. F. Quader, R. D. Smith, J. Wambach, Nucl. Phys. A 485 (1988) 61.

[24] T. Udagawa, B. T. Kim, Phys. Rev. C 40 (1989) 2271.

[25] M. Buballa, S. Drożdż, S. Krewald, J. Speth, Ann. of Phys. 208 (1991) 346.

[26] M. Rotenberg, Ann. Phys. 19 (1962) 262.

[27] S. Weinberg, Phys. Rev. B. 133 (1963) 232.

[28] S. Weinberg, Lectures on Particles and FIeld Theory, Brandeis Summer Institute in Theoretical Physics, S. Deser and K.W.Ford (Prentice-Hall, Egelwood Cliffs, 1964.

[29] G. Newton, Scattering theory of Waves and Prticles, McGraw-Hill, New York, 1966.

[30] G. H. Rawitscher, Phys. Rev. C 25 (1982) 2196.

[31] D. Gogny, Nuclear selfconsistent fields, G.Ripka and M.Porneuf, North Holland, 1975.

[32] J. Dechargè, D. Gogny, Phys. Rev. C 21 (1980) 1568.

[33] H. Feldmeier, T. Neff, R. Roth, J. Schnack, Nucl. Phys. A 632 (1998) 61.

[34] T. Neff, H. Feldmeier, Nucl. Phys. A 713 (2003) 311.

[35] R. Roth, T. Neff, H. Hergert, H. Feldmeier, Nucl. Phys. A 745 (2004) 3.

[36] N. Paar, P. Papakonstantinou, H. Hergert, R. Roth, Phys. Rev. C 74 (2006) 014318.

[37] P. Papakonstantinou, R. Roth, N. Paar, Phys. Rev. C 75 (2007) 014310.

[38] C. W. D. Jager, C. D. Vries, At. Data Nucl. Data Tables 36 (1987) 495.

[39] P. Ring, P. Schuck, The nuclear many-body problem, Springer, Berlin, 1980.

[40] C. M. Lederer, V. S. Shirley, Table of isotopes, 7th ed., John Wiley and sons, New York, 1978.

[41] J. Wambach, V. K. Mishra, L. Chu-Hsia, Nucl. Phys. A 380 (1982) 285.

[42] G. F. Bertsch, P. F. Bortignon, R. A. Broglia, Rev. Mod. Phys. 55 (1983) 287.

[43] A. Migdal, Theory of finite Fermi systems and applications to atomic nuclei, Interscience, London, 1967.

[44] J. Speth, E. Werner, W. Wild, Phys. Rep. 33 (1977) 127.

[45] D. J. Rowe, Nuclear collective motion, Methuen, London, 1970.

[46] A. L. Fetter, J. D. Walecka, Quantum theory of many-particle systems, McGraw-Hill, S. Francisco, 1971.

[47] J. P. Blaizot, D. Gogny, Nucl. Phys. A 284 (1977) 429.

[48] A. R. Edmonds, Angular momentum in quantum mechanics, Princeton University Press, Princeton, 1957.

[49] J. Speth, V. Klemt, J. Wambach, G. E. Brown, Nucl. Phys. A 343 (1980) 382.

[50] G. Co', A. M. Lallena, Nucl. Phys. A 510 (1990) 139.

[51] R. B. Wiringa, V. G. J. Stoks, R. Schiavilla, Phys. Rev. C 51 (1995) 38.

[52] Buti, et al., Phys. Rev. C 33 (1986) 755.

[53] Hyde-Wright, Ph.D. thesis, Massachusetts Institute of Technology, unpublished (1984).

[54] A. Botrugno, Interazione neutrino-nucleo, Ph.D. thesis, Università di Lecce, unpublished (2004).

[55] A. Botrugno, G. Co', Nucl. Phys. A 761 (2005) 203.

[56] Hicks, et al., Phys. Rev. C 30 (1984) 1.

[57] C. F. Williamson, et al., unpublished (1987).

[58] J. E. Wise, et al., Phys. Rev. C 31 (1985) 1699.

[59] J. Heisenberg, et al., Phys. Rev. C 29 (1984) 97.

[60] R. A. Lindgren, B. L. Clausen. http://galileo.phys.virginia.edu/.

[61] D. Goutte, et al., Phys. Rev. C 45 (1980) 1618.

[62] J. P. Connelly, et al., Phys. Rev. C 45 (1992) 2711.

[63] S. Müller, et al., Phys. Rev. Lett. 54 (1985) 293.

[64] J. Linchtenstadt, et al., Phys. Rev. C 20 (1979) 497.

[65] P. H. Pile, et al., Phys. Rev. Lett. 66 (1991) 2585.

[66] T. Hasegawa, et al., Phys. Rev. C 53 (1996) 1210.

[67] S. Ajimura, et al., Nucl. Phys. A 639 (1998) 93.

[68] H. Hotchi, et al., Phys. Rev. C 64 (2001) 044302.

[69] H. Tamura, R. S. Hayano, H. Outa, Y. Yamazaki, Prog. Theor. Phys. Suppl. 117 (1994) 1.

[70] M. Agnello, et al., Phys. Lett. B 622 (2005) 35.

[71] M. Agnello, et al., Nucl. Phys. A 754 (2005) 399c.

[72] T. Miyoshi, et al., Phys. Rev. Lett. 90 (2003) 232502.

[73] F. Garibaldi, Eur. Phys. J. A 24S1 (2005) 91.

[74] M. Iodice, et al., Phys. Rev. Lett. 99 (2007) 052501.

[75] O. Hashimoto, H. Tamura, Prog. Part. Nucl. Phys. 57 (2006) 564.

[76] Y. Ma, et. al., Eur. Phys. J. A 33 (2007) 243.

[77] D. J. Millener, C. B. Dover, A. Gal, Phys. Rev. C 38 (1988) 2700.

[78] N. Auerbach, N. V. Giai, S. Y. Lee, Phys. Lett. B 68 (1977) 225.

[79] M. T. López-Arias, Nucl. Phys. A 582 (1995) 440.

[80] J. Suhonen, From nucleons to nucleus, Springer, Berlin, 2007.

[81] J. M. Blatt, V. F. Weisskopf, Theoretical nuclear physics, John Wiley and sons, New York, 1952.

[82] D. J. Millener, Nucl. Phys. A 754 (2005) 48c.

[83] Y. Yamamoto, H. Bandō, Prog. Theor. Phys. 73 (1985) 905.

[84] H. Bandō, T. Motoba, J. Žofka, Int. J. Mod. Phys. A 5 (1990) 4021.

[85] M. Ukai, et al., Eur. Phys. J. A 33 (2007) 247.

[86] W. Bruckner, el al., Phys. Lett. B 79 (1978) 157.

[87] R. H. Dalitz, Nucl. Phys. A 450 (1986) 311c.

[88] M. M. Nagels, T. A. Rijken, J. J. de Swart, Phys. Rev. D 20 (1979) 1633.

[89] K. Nakayama, S. Krewald, J. Speth, Phys. Lett. B 148 (1984) 399.

[90] D. J. Millener, Topics in Strangeness Nuclear Physics, P. Bydžovský, A. Gal and J. Mareš (Eds.), Springer, Berlin, 2007.

[91] H. Tamura, et al., Nucl. Phys. A 754 (2005) 58c.

[92] K. Itonaga, T. Motoba, O. Richter, M. Sotona, Phys. Rev. C 49 (1994) 1045.

[93] D. J. Millener, Nucl. Phys. A 691 (2001) 93.

[94] R. H. Dalitz, A. Gal, Ann. Phys. (NY) 116 (1978) 167.

[95] Y. Tzeng, S. Y. T. Tzeng, T. T. S. Kuo, Phys. Rev. C 65 (2002) 047303.

[96] G. A. Rinker, J. Speth, Nucl. Phys. A 306 (1978) 360.

[97] S. S. B. K. Agrawal, A.I.Sanzhur, Phys. Rev. C 67 (2003) 034314.

[98] J. Ahrens, et al., Nucl. Phys. A 251 (1975) 479.

[99] G. Co', S. Krewald, Nucl. Phys. A 433 (1985) 392.

[100] S. Kamerdzhiev, J. Speth, G. Tertychny, Phys. Rep. 393 (2004) 1.

[101] A. R. Bautista, G. Co', A. M. Lallena, Nuov. Cim. A 112 (1999) 1117.

[102] G. Co', A. M. Lallena, Nuov. Cim. A 111 (1998) 527.

[103] T. Otsuka, T. Matsuo, D. Abe, Phys. Rev. Lett. 97 (2006) 162501.

[104] S. Drożdż, S. Nishizaki, J. Speth, J. Wambach, Phys. Rep. 197 (1990) 1.

[105] P. F. Bortignon, A. Bracco, R. A. Broglia, Giant resonances. Nuclear structure at finite temperature, Harwood Academic Press, New York, 1998.

[106] F. Grümmer, J. Speth, Jour. Phys. G 32 (2006) R193.

[107] T. de Forest Jr., J. D. Walecka, Adv. Phys. NY 45 (1966) 365.

[108] T. W. Donnely, J. D. Walecka, Nucl. Sci. 25 (1975) 329.

[109] G. Höler, et al., Nucl. Phys. B 114 (1976) 505.

[110] G. H. Rawitscher, G. Delic, J. Math. Phys. 27 (1986) 816.